Using Flow-Induced Crystallisation to Improve the Performance of High-Density Polyethylene Pipes

---

The University Of Sheffield.

Thomas William Franklin

Department of Chemistry, The University of Sheffield

Submitted to the University of Sheffield

In fulfilment of the requirements for the award of Doctor of Philosophy

May 2021

Declaration

The work described in this thesis was carried out at the University of Sheffield under the supervision of Professor Anthony J. Ryan OBE and Dr Oleksandr O. Mykhaylyk between October 2016 and May 2021 and has not been submitted, either wholly or in part, for this or any other degree. All of the work is the original work of the author, except when acknowledged by references.

Signature: 

Date: 08/10/2021

Thomas William Franklin

Abstract

This thesis describes two potential solutions to increase the mechanical and barrier properties (to hydrocarbons from contaminated soils) of PE-100 plastic pipes for water transportation. Both solutions exploit the melting and crystallisation behaviour of HDPE: flow-induced crystallisation (FIC) and single-polymer composites (SPCs).

Two commonly-used PE-100 HDPE resins manufactured by Ineos Group Ltd (UK) and Borealis AG (Austria) have been characterised by a range of rheological, rheo-optical and rheo-SAXS (small-angle X-ray scattering) techniques in order to measure key flow parameters, including critical specific work for the flow-enhanced nucleation of HDPE and Rouse polymer relaxation time, responsible for the formation of oriented morphologies such as distorted spherulites and *shish-kebabs*. The measured flow parameters have been explored further in polymer processing to produce homogeneous polymer films of various structural morphologies for establishing structure - property (mechanical and permeation) relationships. To enable this, a novel Couette shear-flow cell has been developed. The detachable body of the cell, consisting of an inner rotor and a disassembling removable outer stator, is mounted inside a high temperature oven. This design enables larger oriented polymer films to be produced and recovered from the cell after shear for further measurements. Mechanical testing of the FIC HDPEs and SPCs has been performed either by tensile testing or dynamic mechanical analysis. Permeation cells were fabricated and polymer samples subjected to permeation testing in similar accordance with the time-lag protocol.

It was found that both HDPE resins could form an oriented morphology under a moderate shear flow. Polymer with a greater fraction of high molecular weight displayed greater degrees of orientation and improved mechanical performance but an increased permeability to xylene vapour. The latter was related to the orientation of the oriented morphology relative to the permeant flux during measurements. SPCs showed a negligible impact upon the mechanical properties, which was thought to arise from poor adhesion at the fibre-matrix interface and thus poor load stress transfer. Decreased permeability compared to homopolymer samples was observed, especially those with a bi-layer construction. Both approaches studied in this work have been shown to offer viable alternatives to the aluminium foil used as a permeation barrier in the current manufacture of PE-100 pipes.

Acknowledgements

I am incredibly grateful to the countless friends, colleagues and mentors who have supported me through my undergraduate and postgraduate qualifications at the University of Sheffield. Firstly, I would like to thank my project supervisors, Prof. Tony Ryan and Dr Oleksandr Mykhaylyk, for their patience, guidance and enormous wealth of experience in guiding me through this process. Your meticulous proof-reading of this work has been especially appreciated. An additional thanks for the many extra-curricular opportunities facilitated by you both throughout this PhD.

A great deal of thanks must also be given to my industrial collaborators' Dr Julie Alves and Dr Keith Wilson. Thank you for extremely insightful and valuable discussions surrounding plastic pipe manufacture. I thoroughly enjoyed my time spent at Aliaxis R&D and meeting so many brilliant scientists. I thank Aliaxis R&D/GPS PE Pipe Systems, along with EPSRC, for their generous funding.

A huge thank you to every member of the Ryan-Mykhaylyk research group, past and present, with whom I have had the great privilege of working alongside – particular thanks to James C, Cate, Courtney, Harry and James J for your help in navigating this PhD and frequent trips to the pub.

Without the help and support of the technical and support staff, this project would have been considerably more difficult. Particular thanks to the staff in the Accounts office and Stores. I am indebted to each one of you for your technical wisdom and guidance, but particularly thanks to Garry Turner and Richard Trusswell for countless discussions and hours spent in the workshop fabricating the permeation cells and upgrades to the Couette cell. Your contributions have been especially valuable.

Finally, a great deal of thanks to my family and friends whose unconditional love and support has helped propel me forward when I found things particularly difficult. To Mum, Dad, Alex, Sarah and, in particular my wife Anna, I could not have achieved all that I have without you all. I know I can rely on your love and support for whatever the future holds.

List of Abbreviations and Symbols

Materials

PE1	HDPE resin supplied by Borealis
PE2	HDPE resin supplied by Ineos
500k	HDPE resin with M_w = 500 kDa
5M	UHMWPE resin with M_w = 5 MDa
TA23	UHMWPE tape supplied by Teijin
XF23	UHMWPE tape supplied by Teijin
S1	UHMWPE tape supplied by Teijin

Symbols and Abbreviations

$\Gamma_{(x)}$	Probability that a line of length x has equal electron scattering length density at either end
ΔG	Change in Gibbs free energy
ΔG_{bulk}	Change in Gibbs free energy of the bulk
ΔG_{melt}	Change in Gibbs free energy of the melt
ΔG_{nuclei}	Change in Gibbs free energy of the nuclei
$\Delta G_{surface}$	Change in Gibbs free energy of the surface
ΔH	Change in enthalpy
ΔH_v	Specific enthalpy of melting per unit volume of crystal
ΔS	Change in entropy
ΔT	Change in temperature
Θ	Time lag (see also (t_L)

ϕ	Specific surface energy
ϕ	Azimuthal angle
α	Solvent quality
γ	Strain
γ_c	Critical Strain
$\dot{\gamma}$	Shear rate
$\dot{\gamma}_c$	Critical shear rate
$\dot{\gamma}_{min}$	Minimum shear rate
δ	Phase angle
ε	Strain
η	Viscosity
η^*	Complex viscosity
η_0	Zero-shear viscosity
η_∞	Infinite-shear viscosity
θ	Cone angle
2θ	Scattering angle
λ	Wavelength
ν	Poisson's ratio
ξ	Friction coefficient
ρ	Density
σ_{11}	Normal stress component acting in the direction of shear/flow
σ_{22}	Normal stress component acting perpendicular to the shearing plane
σ_{33}	Normal stress component acting in the transverse direction to shearing
σ_e	Fold surface free energy

σ_f	Fold surface free energy per unit area
σ_l	Lateral surface free energy per unit area
τ	Shear stress
τ_d	Reptation time
τ_r	Relaxation time (Maxwell model)
τ_R	Rouse relaxation time
φ	Specific surface energy
ω	Angular shear rate
A	Surface area
a	Tube diameter
ASTM	American Society for Testing and Materials
b	Nucleus thickness *or* segment length (Rouse Model)
CST	Coil-Stretch Transition Model
C_p	Heat capacity
d	Inter-crystalline region length
D	Diffusion coefficient
DP	Differential pressure
DSC	Differential Scanning Calorimetry
E	Electric field vector
E	Young's Modulus
E_a	Activation energy
ERM	Entropic Reduction Model
F	Force
FIC	Flow-induced crystallisation

G	Spreading rate
G'	Storage (elastic) modulus
G''	Loss (viscous) modulus
GPC	Gel Permeation Chromatography
G_R	Spreading (growth) rate
GTR	Gas transmission rate
h	Sample thickness
HDPE	High-density polyethylene
HF-DSC	Heat-Flux Differential Scanning Calorimeter
HMW	High molecular weight
HMWT	High molecular weight tail
HT-GPC	High-temperature gel permeation chromatography
I	Nucleation Rate
ILT	Ideal Laminate Theory
ISO	International Organisation for Standardisation
J	Flux
JMAK	Johnson-Mehl-Avrami-Kolmogorov model
K	Consistency index
k_0	Non-scattered X-ray beam
k_B	Boltzmann constant
K_i	Incident X-ray beam
K_g	Nucleation Constant
K_p	Reciprocal of polymer chain size in solution
K_s	Scattered X-ray beam

L	Sample length
L_c	Crystal thickness
LCB	Long chain branching
LDPE	Low-density polyethylene
LH	Lauritzen-Hoffman Theory
L_i	Initial sample length
LLDPE	Linear low-density polyethylene
LMW	Low molecular weight
l_{min}	Minimum stable lamellar thickness
L_P	Nucleus length
LVR	Linear viscoelastic region
M	Molecular Weight
M_c	Critical weight for entanglement formation
M_e	Entanglement molecular weight
M_n	Number-average molecular weight
M_W	Weight-average molecular weight
M_z	Z-average molecular weight
MWD	Molecular weight distribution
n	Power law index *or* refractive index
n_1	Ordinary refractive index
n_2	Extraordinary refractive index
N_1	First normal stress difference
N_2	Second normal stress difference
P	Electron charge displacement vector

P	Permeability
p	Pressure
P_2	Herman's Orientation Function
PE	Polyethylene
P_i	Permeability of individual layers
P_L	Total permeability of a laminate
PLI	Polarised light image
Q	Quantity of penetrant
q	Scattering vector
R	Light ray retardation
r	Radius
R_g	Radius of gyration
R_h	Hydrodynamic radius
RI	Refractive index
S	Solubility
SANS	Small-angle neutron scattering
SAXS	Small-angle X-ray scattering
SCB	Short chain branching
SCG	Slow crack growth
SIC	Shear-induced crystallisation
SIPLI	Sher-induced polarised light imaging
SNM	Stretch Network Model
SPC	Single-polymer composite
T	Temperature

t	Time
t_L	Time-lag value
T_0	Reference temperature
T_c	Crystallisation temperature
T_m	Melting temperature
T_m^0	Equilibrium melting temperature
T_{mo}	Melting temperature of *shish* nuclei
T_{ms}	Melting temperature of spherulites
TR	Transmission rate
TTS	Time-Temperature Superposition
*U**	Activation of the segmental jump
UHMW	Ultra-high molecular weight
UHMWPE	Ultra-high molecular weight polyethylene
V	Volume
V_R	Retention time
w	Work
w_c	Critical work
WAXD	Wide-angle X-ray diffraction
WAXS	Wide-angle X-ray scattering
w_c	Critical work
X_c	Fraction of crystallinity
X_w	Normalised molecular weight (M_w/M_e)

Contents

Chapter 1: Background

Chapter 2: Methodology and Measurement Techniques

Chapter 3: Characterisation of the Polyethylene Used in the Study

Chapter 4: Controlling the Structural Morphology Through Shear-Induced Crystallisation

Chapter 5: Polymer Processing under Controlled Flow Conditions as a Means of Improving the Barrier and Mechanical Properties

Chapter 6: Single-Polymer Composites as a Means of Improving the Barrier and Mechanical Properties

Chapter 7: Conclusions and Future Work

Chapter 1

Background

1.1 Aims and Thesis Outline

HDPE pipes have become an essential part of water transportation infrastructure, and the current solution to transport potable water through land contaminated with hydrocarbons (PE pipes with an encapsulated-aluminium permeation-barrier) has been successful because of their relatively high mechanical strength, flexibility and permeation barrier properties. However, two alternative technologies will be investigated as a means to produce the next generation of water pipes to address coming limitations originating from sustainable material requirements.

It is well known that the final material properties of a polymer product depend greatly upon the structural morphology.[1] Under normal, quiescent crystallisation conditions, typical semi-crystalline polymers crystallise into spherulites. However, upon application of an external flow field, such as shear, polymer chains are aligned with the flow direction and a crystalline *shish-kebab* morphology is produced. For plastic pipes, conventional extrusion causes alignment along the axial length and correspondingly greater tensile strength in the axial direction than in the hoop direction - this can make the pipe liable to failure through SCG.[2]

Several methods of pipe reinforcement have been trialled over the years such as carbon/glass fibres, steel strip, rotating mandrel and aluminium foil wrapping but these increase production complexity and cost.[3,4] Two novel methods of reinforcement shall thus be introduced in this work: FIC and SPCs. FIC is a very well-researched field, but little work has been conducted exclusively for the plastic pipe extrusion process, compared to injection moulding for example. Specifically, the oriented crystalline morphology resulting from FIC of two current pipe manufacturing grades of HDPE will be investigated through parallel plate and Couette cell shear flow as a means of improving the mechanical strength and barrier properties. In addition, SPCs fabricated using oriented UHMWPE tapes will also be investigated as an alternative approach for achieving improvements in mechanical and permeation barrier properties. Therefore, this work will investigate whether FIC and SPCs can increase the mechanical strength of a pipe whilst also maintaining, or even, improving the barrier properties, compared to the current aluminium-foil reinforced pipe. If either technology is successful, this could lead to significant savings in material and energy costs.

A full description of all experimental techniques and measurement conditions will be provided in Chapter 2. Two commercial grades of HDPE, currently used in the manufacture of plastic pipes, have been supplied by Aliaxis R&D (Vernouillet, France) in addition to three UHMWPE highly-oriented tapes from Teijin (Endumax). Several analytical techniques will be utilised in

Chapter 3 to characterise the molecular characteristics of the materials used. The molecular weight of both HDPE blends will be determined by high-temperature gel permeation chromatography (HT-GPC) which will be outsourced to Smithers Rapra (Shawbury, UK). Characterisation of the viscoelastic behaviour of the two HDPE materials will be performed by rheology measurements. The peak melting and crystallisation temperatures and the degree of crystallinity will be obtained for all materials by DSC measurements. Additionally, small-angle X-ray scattering (SAXS), rheo-SAXS and rheo-optical measurements will be used to characterise the degree of orientation and crystalline morphology of the materials as received and, in subsequent chapters, after shearing experiments.

Chapter 4 explores the flow behaviour of both HDPE blends and determines and optimises some key parameters. Using previous DSC measurements, a temperature-shear profile will be created for future shearing experiments performed using a parallel plate shear cell. Therefore, shear pulses will be applied to PE disks with post-shear SAXS scans across the diameter of each disk to determine the degree of orientation.[5] The effects of altering shear parameters, such as shear time and temperature, upon the crystalline morphology will also be investigated by post-shear SAXS measurements. Key shear parameters such as the critical shear rate and critical work will be determined in conjunction with rheological measurements. The impact of shear upon the crystallisation kinetics will also be explored.

In Chapter 5, a novel Couette cell setup will be described and extensively used to produce larger samples with a homogeneous oriented morphology for further mechanical and permeation testing. By altering the shear conditions, samples of different degrees of orientation will be produced for both HDPE materials and specimens cut for further testing. Comparisons will also be made with unoriented specimens. Tensile testing will be outsourced to Aliaxis R&D to find the Young's Modulus, elongation to break and stress at yield. A series of permeation cells will be fabricated to allow for permeation testing in accordance with the vapour loss transmission method. Three specimens from each shear condition will be cut from the larger samples and barrier properties investigated by measuring the mass lost from each cell at regular intervals using xylene as a simulated fuel.

Finally in Chapter 6, multi-layer HDPE-UHMWPE SPCs will be investigated as a suitable replacement for the current aluminium foil barrier layer. Fabrication conditions will be optimised through the use of a novel vacuum compression moulding (VCM) apparatus. Using the obtained UHMWPE tapes, mono-layer and bi-layer (with fibre orientation crossed at 90°)

composites will be fabricated alongside non-composite samples and an aluminium foil-composite control group. Three samples per composite layup will be fabricated and the barrier properties measured in the same manner as mentioned previously. Mechanical properties will be measured by dynamic mechanical analysis (DMA) frequency sweeps and the effect of UHMWPE as a tape interlayer assessed.

Therefore, this work aims to study whether the permeation resistance to hydrocarbons and mechanical properties can be improved by controlling the crystallisation process and resulting morphology through two novel technologies: FIC through Couette shearing and SPC fabrication.

1.2 Materials for Pipe Manufacturing

Solid-wall pipes have a vast array of uses and offer a cost-effective method of transporting natural gas, oil, potable water, sewerage and communications cables.[6] Early pipes were restricted by materials, joining technologies and the capacity to pump the fluid at high pressure – some of the earliest pipes were constructed of wood, stone, lead and copper.[6,7] Joining these pipes together often proved the greatest challenge. Wax, tar, pitch and other materials were used to 'seal' the joints of early pipes, leading to inevitable leaking. One of the principal drivers for the expansion of pipeline networks was for the transport of crude and refined oils and, as towns and cities grew, the transport of drinking water.[7]

1.2.1 Metal Pipes

With the advent of wrought (< 0.5 % carbon) and cast (2 - 4 % carbon) iron and subsequently steel (Table 1.1), a cost-effective solution for fluid transport was available.[7] To seal the pipes together, the hot ends of both pipe sections could be hammered or welded together to create a leak-free joint and allow for higher transport pressures, compared to wood for example.[7] However, this could be time-consuming and at very high pressures the seams could burst and thus were prone to leaking.[7] Screwing threaded pipe ends together was an alternative option.[7] Cast iron is heavy, inflexible, brittle and cracks easily; wrought iron is also heavy, but ductile and malleable.[7] Iron pipes also displayed significant temperature effects: expansion in hot weather caused bending and buckling; in cold weather the pipes would contract, pulling the screw threads apart, therefore leaking significantly.[7] Laying these pipelines underground mitigated these issues, but did increase corrosion.[7,8]

Transport pressures were significantly lower than modern pipes (at just 12 MPa) due to poor materials and joining technologies. Transitioning to ductile, seamless, high toughness steel pipe and oxyacetylene welding to join pipe ends allowed for larger pipe diameters and increased pressures.[7] Nonetheless, poor joining technologies and damage by corrosion caused metal pipes to be highly susceptible to leaking and the ingress of contaminants.[9]

Material	Advantages	Disadvantages
Wrought iron	Higher pressures than concrete/ clay pipes, ductile	Malleable, heavy, susceptible to corrosion
Cast iron	Higher pressures than concrete/ clay pipes	Heavy, inflexible, brittle and cracks easily, susceptible to corrosion
Steel	Seamless, corrosion-resistant, tough, larger diameters	Heavy, inflexible, low-operating pressures, short lifespan

Table 1.1: Key advantages and disadvantages of historic materials used for pipe manufacture.[10]

1.2.2 Plastic Pipes

Polyethylene (PE) was first used as a pipe material in the 1950's, when the rapidly expanding oil and gas industry required a tough but lightweight and flexible pipeline to meet demands.[7] The performance benefits of this new material then spread into municipal water, sewerage and communications applications. The success of PE pipe can be attributed to its low weight, low cost, corrosion resistance and leak-free joints.[6] Small diameter pipe is even flexible enough to be coiled for easier transport and installation.[6] Other piping materials include polybutylene (PB), polyvinyl chloride (PVC) and chlorinated polyvinyl chloride (CPVC), polypropylene (PP) and cross-linked PE (PE-X) (Table 1.2). The major benefit of plastic pipe is its excellent corrosion resistance, with additional savings in the cost of installation, labour and equipment.[6]

Material	Advantages	Disadvantages
HDPE	Lightweight, flexible, leak-free joints	Sensitive to mechanical loading and temperature changes
PE-X	Flexible, corrosion-resistant, high-temperature applications	Damaged by UV
PP	Cheap, corrosion-resistant, impermeable to moisture, chemically inert, good processing	Damaged by UV and high temperatures
PVC	Inert, corrosion-resistant	Brittle, cannot be used for hot water distribution, prone to leaking as joints age, small-diameter only
CPVC	Corrosion-resistant, can withstand slightly higher temperatures than PVC	Brittle, cannot be used for high temperature fluid applications, high thermal expansion coefficient
PB	Lightweight, flexible, low thermal expansion/ contraction	Prone to joint leakage, damaged by chlorine

Table 1.2: Key advantages and disadvantages of common polymer materials used for pipe manufacture.[10]

Piping technology has adapted and significantly changed in line with the needs and demands of the industry it serves. Transport of potable water through contaminated brownfield sites requires particularly careful pipe design to prevent ingress of contaminants. The current solution is a multi-layered pipe: inner PE pipe, aluminium foil barrier layer, external PE pipe. This solution has proven extremely effective, however further advancements will be required to produce the next generation of water pipes to address coming limitations originating from sustainable material requirements.

1.3 Introduction to Polyolefins

Plastics over the years have been the source of many advances in technology and brought benefits to society.[6] Polyolefins, namely PE and polypropylene (PP), are widely regarded as two of the most useful commodity polymers with a wide variety of applications, such as food

packaging, carrier bags, toys, kitchen/home appliances, pipes, medical applications and countless more.[11] The success of these polymers can be attributed to the very low cost of production and low toxicity compared to other polymers.[12] More recently, however, they have become a source for concern amongst environmentalist groups and the general public. By 2015, an estimated 8.3 billion tonnes of plastic had been created.[13] Of this amount, approximately 6.3 billion tonnes of waste, the vast majority of which is plastic bottles, has been generated: 79% accumulated (landfill or the environment), 12% incinerated and 9% recycled (567 million tonnes).[13] However, the problem of recyclability is an issue for all plastic industries, including the plastic pipe manufacturing industry. Thus, any new piping technology that can be fabricated using less raw material and lower energy costs will be of great benefit to producers and consumers alike.

Plastic products can be classified into two main groups: thermosets and thermoplastics. Thermosets undergo an irreversible chemical change upon heating, for example, epoxy resins form cross-links and 'cure' when heated. Thermoplastics, conversely, undergo reversible changes upon heating and examples include PE and PP.[14] Both PE and PP can be subdivided into different grades depending on their application - this work has focussed solely on PE.

Now ubiquitous in everyday life, PE proved difficult to produce initially. It was first discovered at the end of the 19th century, as a by-product of the thermal decomposition of diazomethane, but was only identified in later years as a polymer.[15] Hermann Staudinger's concept of high molar mass macromolecules and the polymerisation process in the 1920s paved the way for a new branch of chemistry and the discovery and characterisation of PE.[16–18] Fawcett and Gibson, in ICIs Cheshire laboratories, are officially credited with the first successful, if unintentional, discovery in 1933 as part of a series of reactions investigating the effect of pressure upon chemical reactions.[19] A mixture of ethylene gas and benzaldehyde was subjected to 170 °C and 1400 atm but without any apparent reaction until the autoclave was opened, whereupon a white, waxy solid was discovered coated to the reactor walls.[19] Benzaldehyde was recovered unchanged and the white solid appeared to be a polymer of ethylene.[20] Further repetitions of the experiment gave very low product yields and the experiments were abandoned. PE was essentially rediscovered in 1935 when it was found that minute quantities of oxygen (<10 ppm) in the reactor were necessary for a stable reaction and good yield.[20,21] The conditions produced oxygen radicals which, when introduced to ethylene, caused polymerisation by a chain reaction and formed inter- and intra-molecular branching, thus producing low-density polyethylene (LDPE).[15] The industrial and commercial value of

this novel material was quickly realised, however commercialisation was suspended on the outbreak of World War II and it became a state secret. LDPE was an excellent high-frequency electrical insulator and was used in the production of the coaxial cables in radar sets. In common with many other polymers, there was a concerted research effort during WWII and by 1944, Du Pont and the Bakelite Corporation in the USA began large-scale commercial production under license from ICI.[19] Further advancements showed that varying the pressure, temperature and catalyst could have a big impact upon the structure of the final product and generate different grades of PE.

Despite a seemingly simple hydrocarbon structure, composed solely of carbon and hydrogen, the vast number of grades for diverse applications arises from different morphologies of this basic structure.[11] Three distinct morphologies can be identified, each with different material properties: highly-crystalline, semi-crystalline and amorphous.[19] Highly crystalline PE has very neatly ordered chains folded into lamellae and is often brittle. Amorphous PE is the exact opposite. Little to no order is found in the chain packing arrangement thus imparting flexible material properties. Semi-crystalline PE consists of at least two distinct phases of highly ordered and disordered chains with the resulting mechanical properties a blend of both morphologies.[19] It is impossible to prepare a sample of PE that is anything but semi-crystalline – all commercial PE products can be classified as such.[19] The extent to which crystalline or amorphous characteristics dominate depends upon the size, orientation and proportions of the two respective morphologies. [19]

Within this semi-crystalline classification, various material grades of PE can be found (Figure 1.1), notably low-density (LDPE), high-density (HDPE), linear low-density (LLDPE) and ultra-high molecular weight (UHMWPE). All have the same backbone structure of carbon and hydrogen; variations arise mainly due to synthesis conditions and the degree of branching, hence causing differences in density and crystallinity (Table 1.3).[11,19] Branches disrupt the packing to form an ordered crystal structure and hence contribute to a lower density; hydrocarbons of various lengths or even acid and ester functional groups can form branches.[19] A general rule is that as the concentration of branches increases, the density and crystallinity of the material decreases.[19] Conversely, fewer branches contribute to a much higher density due to more efficient chain packing in the crystal.[19,22]

	HDPE	LDPE	LLDPE	UHMWPE
Density (g cm^{-3})	0.93 – 0.97	0.91 – 0.94	0.90 – 0.94	0.94 – 0.98
Degree of crystallinity (% from DSC)	55 - 77	30 - 54	22 - 55	50 - 95

Table 1.3: Density and degree of crystallinity (as measured by DSC) for various types of PE.[19]

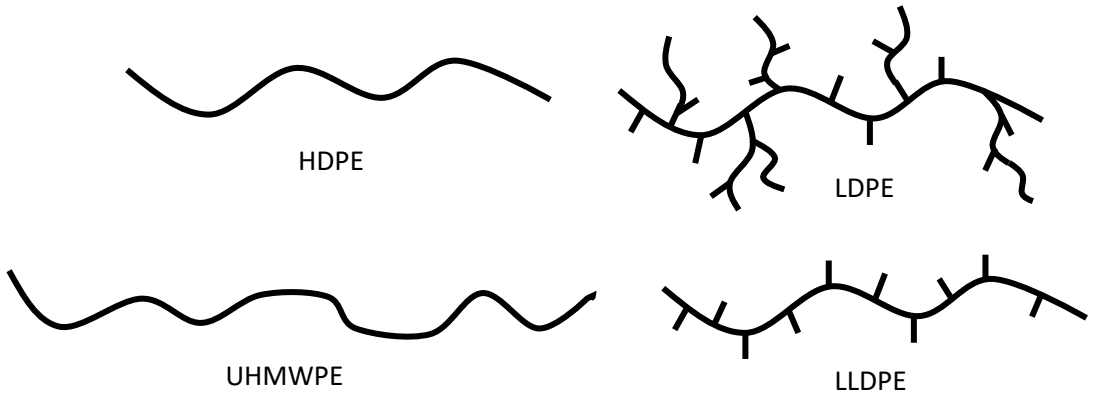

Figure 1.1: Simplified structures of HDPE, LDPE, LLDPE and UHMWPE. The chain length and degree of branching impact upon the physical properties and give rise to the different grades.

1.3.1 High-Density Polyethylene (HDPE)

HDPE produced by this route results in chains that are predominantly unbranched and therefore very linear (Figure 1.1).[15,19] The resulting morphology is consequently very organised and highly crystalline. HDPE is one of the stiffest grades available and is therefore used for high stress environments, such as pipe manufacture, where maintaining structural integrity is very important.[19]

1.3.2 Low-Density Polyethylene (LDPE)

LDPE on the other hand shows significant branching with a mixture of randomly located short and long chain branches, as a result of its free radical synthesis (Figure 1.1 and Section 1.2.5.2).[19] These long chain branches can in turn be subjected to further branching. The high degree of branching prevents close chain packing and therefore the recorded density of the material is much lower relative to HDPE.[19]

1.3.3 Linear Low-Density Polyethylene (LLDPE)

LLDPE also shows random branching, but with fewer long chains, and is synthesised by coordination catalysis (Figure 1.1).[19] Generally, this material is produced by co-polymerising ethylene with a number of 1-alkenes, mainly, ethyl, butyl and hexyl chains. The greater regularity of the branches hinders crystallinity to some extent, but is not as extreme as LDPE. Therefore, the density is somewhere between that of HDPE and LDPE.

1.3.4 Ultra-High Molecular Weight Polyethylene (UHMWPE)

UHMWPE has a molecular weight $>10^6$ g/mol and shows excellent chemical inertness, lubricity and mechanical strength (Figure 1.1). The latter property cannot be surpassed by any other grade owing to effective load transfer along the long chains. As such, UHMWPE finds extensive use in medical implants and ballistic protection.[23]

The high melt viscosity arising from the high molecular weight of the chains means that UHMWPE cannot be formed into products using conventional processing methods.[24] Typically, UHMWPE is often drawn into fibres or tapes via a process of gel-spinning and post-drawing.[25] In the former process, a dilute polymer solution is extruded through a nozzle with subsequent solvent evaporation or extraction.[25] This as-spun crystalline fibre is drawn under a tensile stress, at temperatures below the fibre melting point, to the desired draw ratio which produces fibres with greatly increased tensile modulus and break strength.[25] Highly orientating the fibres in this manner has a corresponding effect of greatly increasing the degree of crystallinity due to the closer chain packing in the crystalline regions.[26]

1.3.5 Polymer Synthesis

The reactor and catalyst system used will depend upon the grade of PE required: free radical, high-pressure synthesis produces LDPE, whereas Ziegler-Natta, low-pressure synthesis produces HDPE, for example.[19] The reactor at the centre of the process can either be an autoclave or a tubular reactor with the starting materials fed either in solution, slurry or gas phase.[19] Early catalysts contained many active sites, leading to PE resins with very broad molecular weight distributions (MWDs).[19] The resulting high and low molecular weight tails had a significant impact upon the physical properties: an excessive high molecular weight tail increased processing difficulty; an excessive low molecular weight tail exacerbated stress cracking.[19] Tighter control of polymerisation conditions and new generations of catalyst narrowed the MWD, but at the expense of easier overall processability of the resin.[19] Both

Ziegler-Natta[27] and metallocene[15] catalysis can be used during commercial PE synthesis, however the single-site nature of the latter leads to reduced branching of the chains.[15]

By installing multi-reactor systems, broad MWDs can be achieved and even tailored to specific applications (Figure 1.2) without negatively affecting the processing behaviour. The resulting MWD, measured by gel permeation chromatography (GPC), is an amalgamation of both individual MWDs. The result is a material with properties somewhere between those of the two individual component blends. The homo-polymer with the lower molecular weight is typically synthesised first. Clearly, different conditions and catalysts are required in each reactor in order to synthesise the desired homopolymer for the final blend.[19] Without the advancement in catalyst technology seen over the years, these types of blends would be much more difficult, if not impossible, to produce consistently.[28]

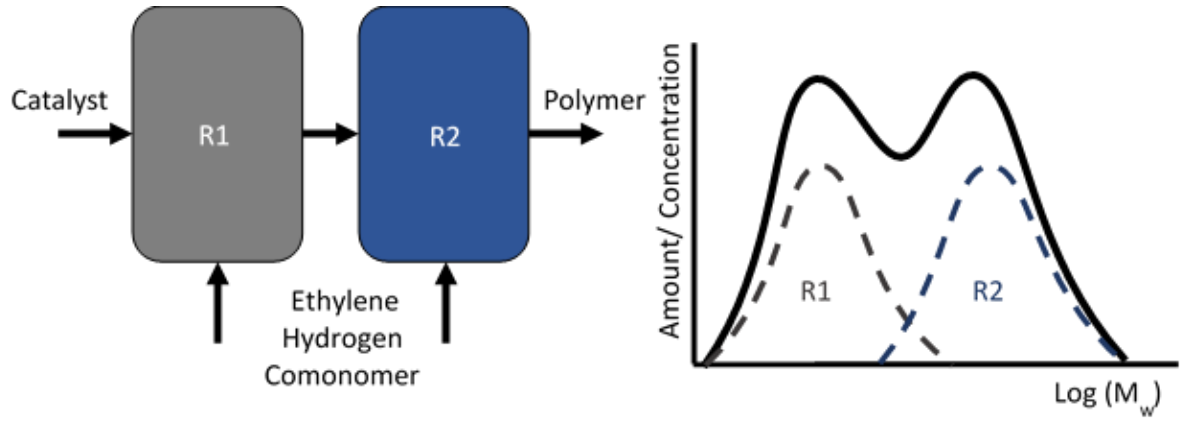

Figure 1.2: Multi-stage reactor for producing a bimodal distribution of HDPE/LDPE polymer. The final molecular weight distribution is a blend of the individual molecular weight distributions of the two components.

1.3.5.1 Ziegler-Natta Catalysis

Ziegler-Natta synthesis is the most common commercial production method for PE, owing to the flexibility of the catalyst system.[19] These catalysts are expensive to produce and so, highly active catalysts are desirable; by limiting the number of such active sites, the polymerisation can be closely controlled by reaction conditions. Typically, relatively low temperature and pressure conditions are required, compared to free radical polymerisation. Generally, the molecular weight of the final polymer increases as temperature decreases because of the decreased rate of chain transfer relative to chain propagation, the former being the primary limit to molecular weight.[19,29]

The catalyst system consists of a base metal halide or alkyl complex with a transition metal salt – for PE, a classic example is triethyl aluminium ($AlEt_3$) with titanium tetrachloride ($TiCl_4$).[19,30] The active centre is postulated to comprise of a Ti atom coordinated with an alkyl group and four Cl atoms in an octahedral arrangement, with one vacant site (Figure 1.3). An ethylene molecule coordinates at this vacant site, subsequently inserting between the alkyl and metal and creating a new vacancy. Repeat additions in this manner grow the polymer chain.[19]

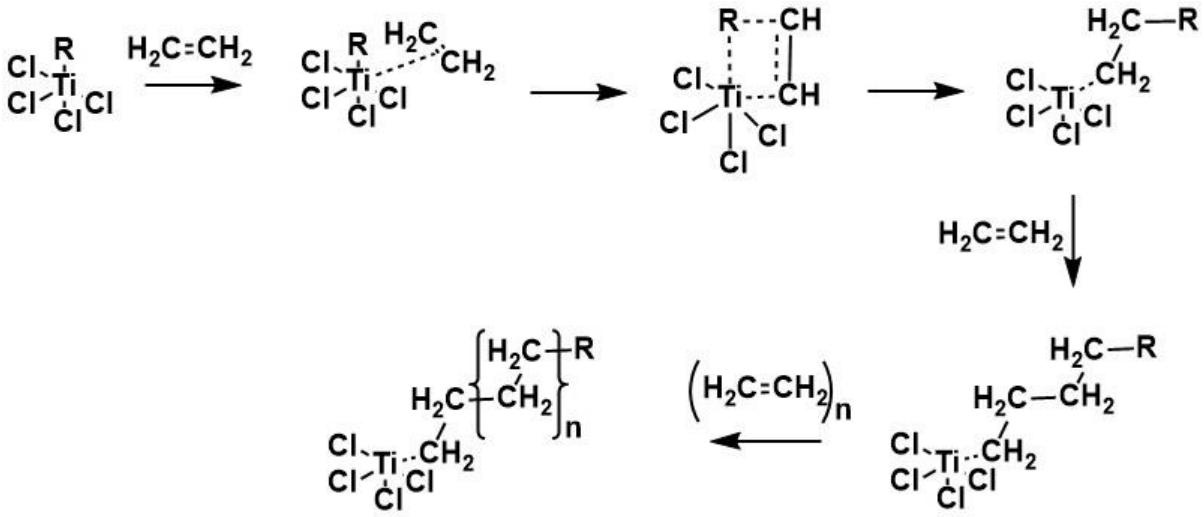

Figure 1.3: Mechanism of Ziegler-Natta polymerisation of ethylene.[19]

1.3.5.2 Free Radical Polymerisation

LDPE is produced exclusively by high-pressure free radical polymerisation, requiring an appropriate free radical source, ethylene monomer and high temperature (180 – 300 °C) and pressure (1000 – 4000 bar).[19,29] Conditions similar to those used initially by Fawcett and Gibson are still used today: 200 – 300 °C and 1000 – 1550 bar.[15] Typical free radical initiators include oxygen, organic peroxides and azo compounds and they initiate polymerisation by decomposition under the reaction conditions to form the radical (Figure 1.4).[19,29] Subsequent abstraction of a hydrogen atom from a nearby ethylene monomer (brought into close contact by the high pressure) propagates the chain growth.[19] Termination of the radical occurs either by quenching with another radical or when the radical on the growing chain is transferred to another chain. Thus, there are many competing side reactions which results in premature chain termination or branching.[19]

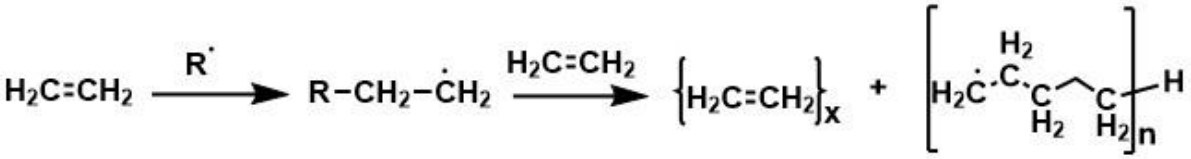

Figure 1.4: Mechanism of free-radical polymerisation of ethylene. R denotes a radical initiator such as oxygen, an organic peroxide or azo compound.[19]

Branching arises when a propagating chain radical abstracts a hydrogen from an existing polymer chain and can occur either intramolecularly, resulting in short chain branching (SCB), or intermolecularly, resulting in long chain branching (LCB).[19,29] SCB refers to branches of only a few carbon atoms much smaller than the backbone, whereas LCB refers to branches that are comparable in length to the backbone.[31] The frequency and type of branching can be controlled somewhat by reaction conditions, and the probability of LCB increases proportionally as the molecular weight of the chain increases.[19] SCB arises when the propagating chain end 'back-bites' and abstracts a hydrogen only several bonds away from the growing chain end, leading mainly to butyl SCB. Chain growth continues from this new radical centre, leaving the original chain end as a short branch.[19]

1.3.5.3 Metallocene Synthesis

Polymerisation using metallocene catalysts produces ethylene-α-olefin copolymers with narrow polydispersity, primarily LLDPE.[19] This can be achieved due to the single active site present in each catalyst, hence monomer polymerisation occurs identically resulting in fewer long chain branches.[19,29]

Generally, metallocene catalysts consist of a Group IV metal atom (Ti, Zr, Hf) attached to two substituted cyclopentadienyl ligands and two alkyl or halide ligands (Figure 1.5a).[19] Several variants of this generic metallocene catalyst are available (Figure 1.5b-d) and a methylalumoxane ([$(MeAlO)_n$], MAO) co-catalyst is also typically used in order to obtain a high catalytic activity.[19]

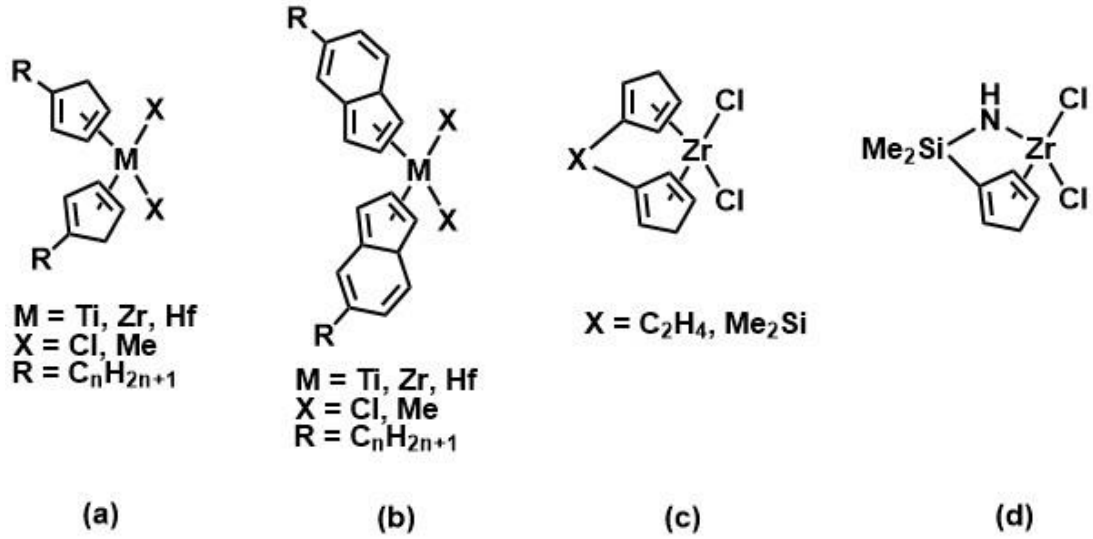

Figure 1.5: Example structures of (a) generic metallocene; (b) generic metallocene with indenyl substituents; (c) bridged metallocene; (d) constrained geometry catalyst.[19]

1.4 Polymer Processing

Polymers are often supplied as pellets or powders and in order to create a product, heat and pressure need to be applied.[19] Over the years, numerous processing techniques have been developed to process polymers in different ways depending on the desired product outcome. Techniques such as extrusion,[32] blown film moulding,[33] injection moulding[34] and calendering[35] are some of the most common. For the purpose of PE pipe manufacture, single-screw extrusion is exclusively used and so shall be the focus of further discussion.[32,36]

1.4.1 Fundamentals of Flow

The molecular structure of a polymer determines the processing behaviour.[36] The typical, and much simplified, procedure for thermoplastic processing is to heat the material to the molten state, rapidly shape into the desired product and subsequently cool to solidify. Due to the long chain nature of thermoplastics and the inevitable entanglement points between chains, the molten material has a much higher viscosity compared to low molecular weight materials.[37] For commercial processes, fast production is desirable. As such, when the high viscosity melt is moved rapidly, a large amount of frictional interaction and heating occurs.[38] This heat is due to the dissipation of mechanical energy and the process is known as viscous dissipation or 'shear heating'.

Viscosity and MWD are intrinsically linked due to polymer chain entanglements.[37] A plot by Berry and Fox[39] (Figure 1.6) of zero-shear viscosity, η_0 (the apparent viscosity of the material at zero shear rate, measured by extrapolation backwards from observed viscosities)[37], against the normalised molecular weight ($X_w = M_w/M_e$, where M_w is the molecular weight and M_e is the entanglement molecular weight, defined as the average molecular weight between topological constraints[40]) demonstrates that η_0 increases proportionally to the molecular weight, until it reaches M_c, the critical molecular weight for entanglement formation.[41,42] After this point, the dependence of viscosity on molecular weight, M, changes to the power of 3.4 – 3.5. These two regimes of molecular weight dependence on viscosity point to the existence of polymer chain entanglements.[41] Below a critical value, chains are too short to entangle but still have high viscosities. Doubling the molecular weight in this region only doubles the viscosity since $\eta_0 \propto M^1$. Above this threshold value, entanglements can form and the viscosity increases sharply.[39,41] This can cause problems for polymer processing if not taken into consideration.

Flow during these processes in the molten state also imparts orientation to the melt. This increases the stiffness and strength in the orientation direction because the force is borne mainly

along the chain axis and intramolecular bonds are much stronger than intermolecular bonds between chains.[19] Mechanical properties perpendicular to the direction of orientation are reduced however.

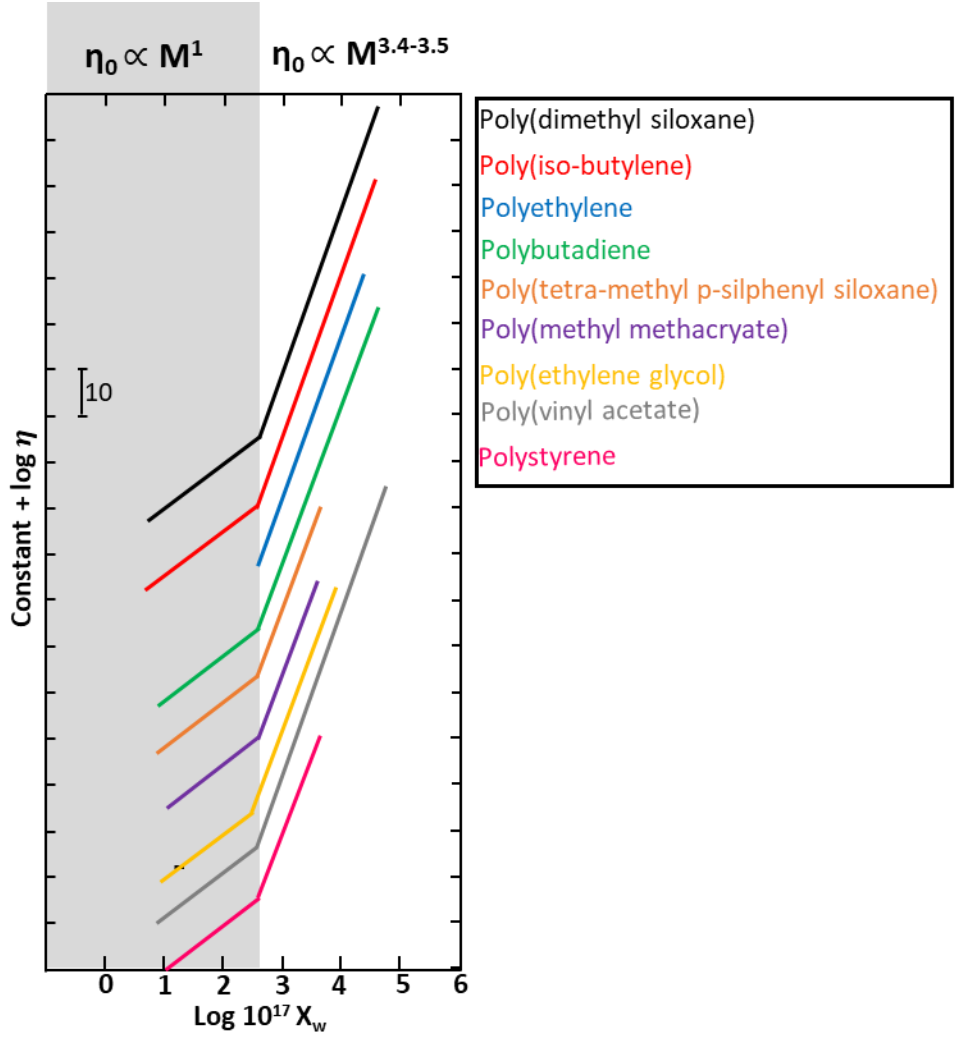

Figure 1.6: A plot of zero-shear viscosity, $\eta_{0,}$ against molecular weight showing the effect of entanglements between polymer chains on viscosity.[39] The low molecular weight lines in the grey zone correspond to unentangled samples while the high molecular weight lines correspond to entangled polymers. The dependence of viscosity upon molecular weight changes to the power of 3.4-3.5 after the entanglement point. $X_w = M_w/M_e$ where M_w is the weight-average molecular weight and M_e is the entanglement molecular weight.

1.4.2 Extrusion

The first thermoplastic extruder was designed in 1935 by Paul Troester in Germany and is arguably the most important tool in the polymer processing industry.[32] Material is extruded when it is pushed out of an opening from a tube – plastics, metals, ceramics and even foodstuffs

are all common extrudate materials (Figure 1.7).[32,38] Both solid and molten state extrusion are known, with the latter being the most common for thermoplastic processing. Generally, solid particulates or powder are fed into the extruder and melted within the extruder barrel in a process known as plasticating extrusion.[32,36] Continuous and batch extruders can be found, with the former using a rotating screw to maintain a constant flow of material. Batch extruders utilise a ram or piston and are commonly used for solid state extrusion or injection moulding. Both single- and twin-screw extruders are used in industry, with further sub-categories of twin-screw extruders depending on the process.[32] The advantages of single screw extruders are the relatively low cost, rugged design and good performance and reliability.[32] For PE pipe manufacture, single-screw extruders are exclusively used primarily due to the lower cost, but also because the good plasticising function ensures a stable and high-speed extrusion.[32] Another point of comparison is the mixing vs pumping ability. Twin-screw extruders offer superior mixing of the melt, whereas the single-screw can tolerate higher barrel pressures and, therefore, a greater pumping of the melt through the die head.[32] Twin-screw extruders are likely to be more expensive and are mainly used for PVC pipes because this material degrades very easily at high temperatures and two screws that are constantly 'cleaning' each other helps prevent any material stagnation and degradation.

Whether single- or twin-screw, the basics of any extruder are much the same (Figure 1.7).[36] Solid material is fed into a hopper where it enters a heated metal barrel and is conveyed forward by the rotating screw. At the other end of the screw is a screen and breaker plate assembly before the molten polymer passes into the die head.[32] Once out of the die, the polymer product is cooled either in air or with water jets. The vertical feed hopper shown (Figure 1.7) is the most common type and relies on gravity to feed the extruder. Other designs, such as vibrating hoppers, crammer hoppers and vacuum hoppers, allow for a more controlled rate of feed. They can also be used for material with a low bulk density that would cause 'bridging' in the feed throat causing a blockage.[36] Often the feed throat is water cooled to prevent premature melting of the material before it enters the barrel. The barrel itself must be able to resist internal pressures of up to 70 MPa, and the inner surface is often coated to prevent abrasive damage.[19] Electrical band heaters surrounding the barrel are used mainly to maintain the temperature, not to melt the material in the first instance which is caused by shear heating.[32]

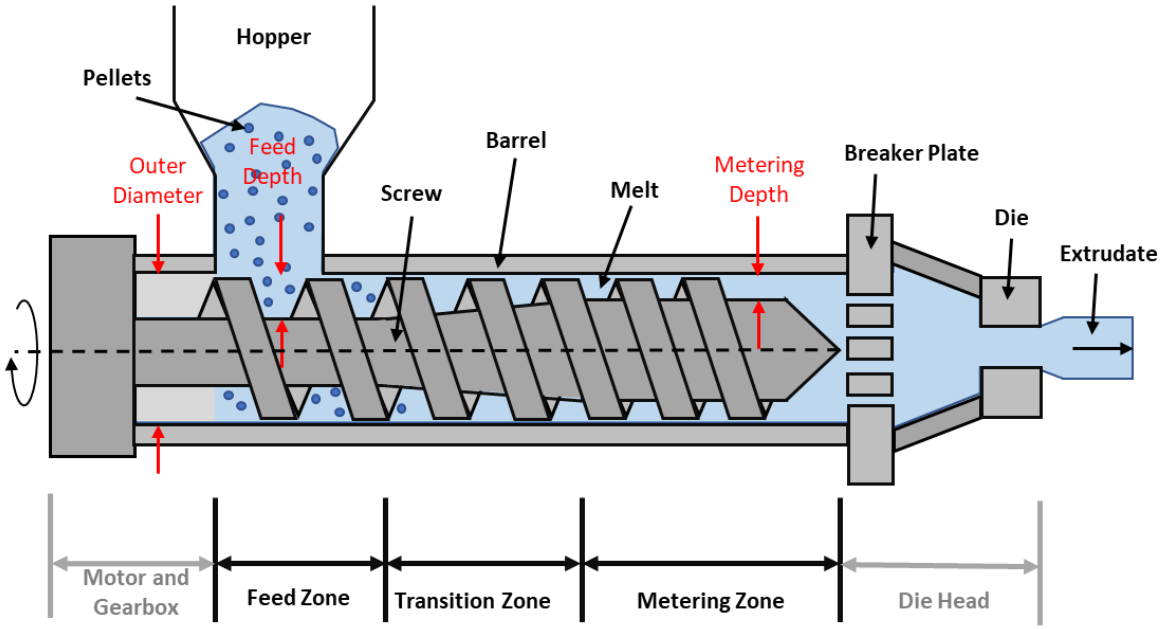

Figure 1.7: A schematic of a typical single screw extruder. Raw material, in the form of pellets, is fed into the hopper and conveyed forward by the screw, melting as a result of friction caused by shearing. The melt is forced through a breaker plate, which arrests the spiral motion of the melt, and a die to form the final product dimensions. Three zones are identifiable along the barrel, defined by the screw channel depth: 1) feed zone, raw material enters here and the channel depth is at its largest; 2) transition zone, the channel depth decreases and the pellets begin to melt; 3) metering zone, the channel depth decreases to its smallest point to homogenise the melt and pump it into the die head.

Three distinct, overlapping regions related to the screw geometry can be found in a conventional screw (Figure 1.7). The feed zone is directly underneath the hopper and has deep flight channels to accommodate the incoming feed at a high rate. The second zone is the compression or transition zone, in which the channel depth gradually decreases and the polymer begins to melt. This compression increases the pressure within the barrel and helps to homogenise the melt. The third and final section is the metering zone, which fully homogenises the melt and pumps it into the die head.[32,38]

Between the metering zone and die head, a breaker plate and screen pack can be installed. The breaker plate is a thick metal disk with many holes drilled through it parallel to the screw direction. This arrests the spiral motion of the melt arising from the screw rotation and forces the material into a linear flow to prevent extrudate distortions.[32,38] Wire mesh screens are used to filter out contaminants and/or gels but can also be used to increase die head pressure to further improve the mixing efficiency.[32] The die is responsible for shaping the polymer melt

into the final product - the function of the rest of the machine is simply to melt and transport the initial solid material to the die head as a homogeneous melt.[32]

1.4.3 Pipe and Tubing Dies

The difference between a pipe and a tube is usually size. It is generally accepted that tubing is a small diameter product of less than 10 mm, whereas pipes are much larger (generally larger than 20 mm).[32] In both cases, however, an annular die is used to shape them (Figure 1.8).[32] Die design is complex and must take into account heat flow, viscoelastic behaviour (different for each polymer) and extrudate swell.[32] This latter issue is a problem for profile extrusion where swelling can yield parts that are significantly outside the specified product dimensions. For pipe extrusion, shrinkage on cooling is usually uniform around the circumference but sagging becomes an issue for very large diameter, thick-walled pipes.[19]

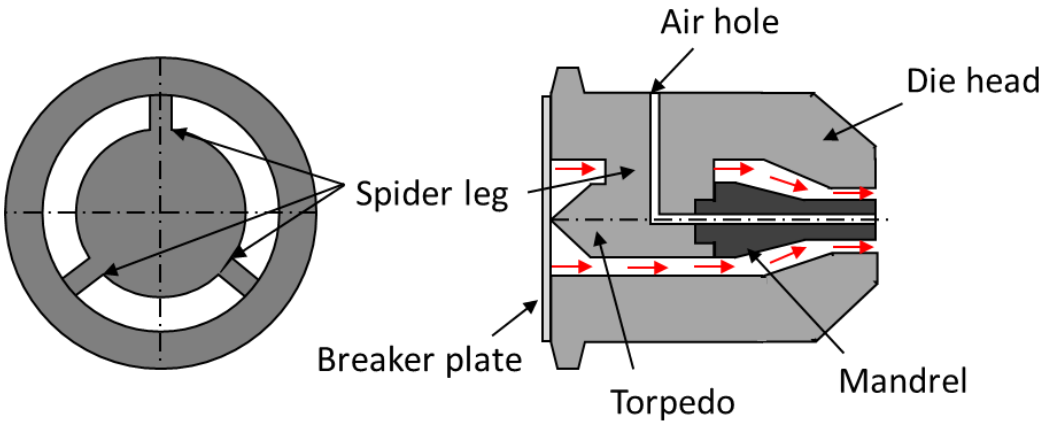

Figure 1.8: Cross-section of an annular die head highlighting the location of the spider legs, torpedo and mandrel. The red arrows indicate the direction of melt flow through the die head assembly.[32]

Weld lines are characteristic of annular die extrusion and significant effort has been conducted to minimise or remove these defects.[43,44] In order to form hollow products, the centre of the die must 'float' and the melt flow around it. A streamlined torpedo, supported by a number of 'spider legs' is the best solution (Figure 1.8).[32] The torpedo shape allows the melt to flow, without creating any dead spots, and converge again. The spider legs are also streamlined to aid this process. However, weld lines are still found despite the most streamlined torpedoes and spider legs possible. Sufficient time is needed after the flow converges for polymer chains to re-entangle and 'heal' the weld lines.[19] Therefore, the spider legs must be far enough away from the die exit to allow this, which is the drawback of annular die heads for pipe extrusion. These resulting changes in the polymer structure, which are not always immediately visible,

can have a detrimental effect upon the strength characteristics in certain areas.[19] For example, in the case of pipes, weld lines running the axial length of the pipe will decrease crack resistance in this direction. [45] A number of modifications to die heads have been used to reduce the unwanted effect of weld lines. Rotating the die head and mandrel to twist the weld lines off-centre;[3,4] coating the spider leg with PTFE to prevent adhesion, but these coatings soon wear;[32] heating the spider legs, which requires complex engineering solutions;[32] lengthening the die head after the spider legs, which considerably increases cost.[45] Research has been undertaken on mandrel/die rotation with favourable resulting mechanical properties.[4,46,47]

A common feature of all extrusion head dies is that the polymer flow is parallel in a zone of constant dimensions.[45] This region sets the final dimensions of the product, accounting for stress relaxation, and is always the last zone in the die. A supplementary channel is found in some mandrels for the inlet of low-pressure air (Figure 1.8). This allows for a more controlled cooling of both the outer and inner walls resulting in less sagging or product deformation.[45]

One of the most successful die heads for eliminating weld lines is the spiral mandrel die.[32,45] A spiral mandrel creates flow in the helical direction by forcing the polymer melt through a number of spiral channels of decreasing depth (Figure 1.9). This causes some circumferential orientation and an increased hoop stress performance. A series of deep channels arranged in a star pattern perpendicular to the flow carry the melt initially into the mandrel. As the melt progresses, the channels get progressively shallower and more polymer begins to flow over the top. Thus, at the end of the mandrel, the channels are at their narrowest with the bulk of the material flowing freely over the top. The spiral motion removes weld lines, and the gradual convergence to a single flow front homogenises the melt.

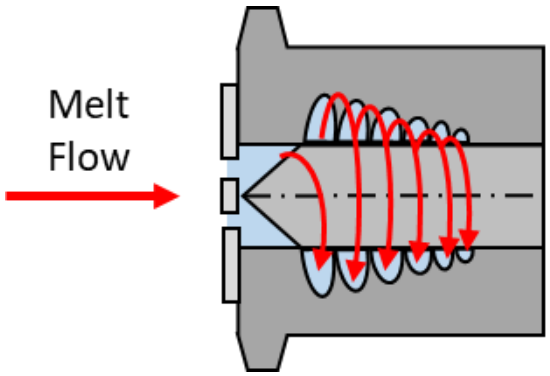

Figure 1.9: A cross-section schematic of a spiral mandrel die. The decreasing channel depth of the spiral flow lines is highlighted by the red arrows to indicate the melt flow direction.

1.5 Polymer Crystallisation

The crystallisation mechanism of polymers is complex and not fully understood,[48] but can be simplified into two main features: formation of a small seed crystal (nucleation)[49,50] and subsequent growth of the crystal by chain attachment to the primary nucleus.[49,50] This initial nucleation step can either be homogeneous or heterogeneous (Section 1.4.3.1).[51,52] Such is the complexity, that debate over the exact details of the process continues and, over the years, numerous theories have been put forward to try and clarify the issue. Several key features are essential for every crystallisation event. Firstly, polymer chains must partially disentangle from their surrounding neighbours.[49] Secondly, any entropy of conformation must be foregone in order to form crystals.[49] Finally, as cooling continues, the chains must arrange themselves into an ordered, periodic lamella structure.[49]

In polymer crystals, the chains are longer than the parameters of the unit cell with each chain often passing through many unit cells.[19] Accordingly, an ideal polymer crystal is impossible to come by, requiring infinite molecular weight, regular structure of the chains, regular conformation of the unit cells and completely regular chain conformation.[49] Therefore, the general requirements for any chain to crystallise are regular chemical structure and regular conformation of monomers.[49]

1.5.1 Morphology

Crystallisation is a phase transition process from the disordered, isotropic melt to the ordered semi-crystalline phase.[52] Disorder in the melt is characterised by random coils of polymer chains, but the semi-crystalline phase is more complex.[52] Consisting of amorphous, crystalline and interfacial regions, the relative volumes of each part determines the final macroscopic properties.[19] This interfacial transition zone ties the amorphous and crystalline regions together and could arguably be the most important region in determining final properties.[19]

The first solution-grown PE single crystals were reported in 1957,[53] but issues arose regarding the structure. Firstly, the chains were known to be longer than 1000 Å but the crystal was only 100 Å thick. Secondly, the calculated density was much higher than that measured experimentally.[53] A suitable structure to account for these observations was the chain-folded lamella as proposed by Keller (Figure 1.10).[54]

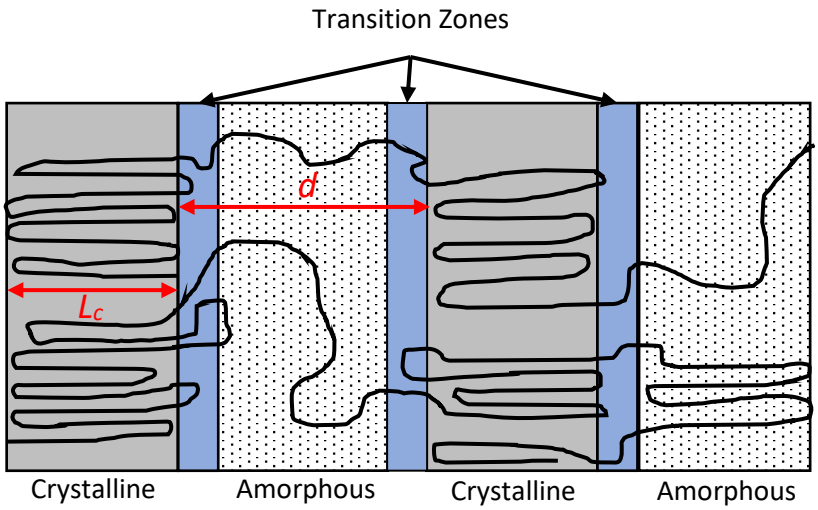

Figure 1.10: Example sketch of chain-folded lamella (in the grey crystalline regions) and a representative diagram of crystalline and amorphous regions, linked by tie-chains in the transition zones, in a semi-crystalline polymer.[29] A single polymer chain can cross several crystalline and amorphous boundaries. *d* is the distance between crystalline regions and L_c is the thickness of the lamellar structure.

Crystalline polymers always have a density that is lower than that of the fully crystalline material estimated from the unit cell of the crystal structure; this means that non-crystalline, amorphous material must be present in the structure. Moreover, the periodic nature of the morphology formed suggests that the non-crystalline component resides in between the crystalline layers as an amorphous layer, linked by tie-chains (Figure 1.10).[52] Small angle neutron scattering (SANS) experiments have shown that a single polymer chain can be included in different layers, with the tie chains between these layers forming the amorphous and non-crystallised regions (Figure 1.10). These chain-folded lamellae crystals are nonequilibrium, meta-stable structures and may rearrange or modify their structure over time.[52]

The surfaces of these solution-grown crystals were observed to be microscopically smooth, suggesting the crystals were composed of crystalline rods linked by tight folds to the next chain.[54] There is still debate over the exact method of chain re-entry into the lamellae. Adjacent re-entry (with tight or loose folds) and the switchboard model are the two most common explanations, with the latter the most popular (Figure 1.11).[54]

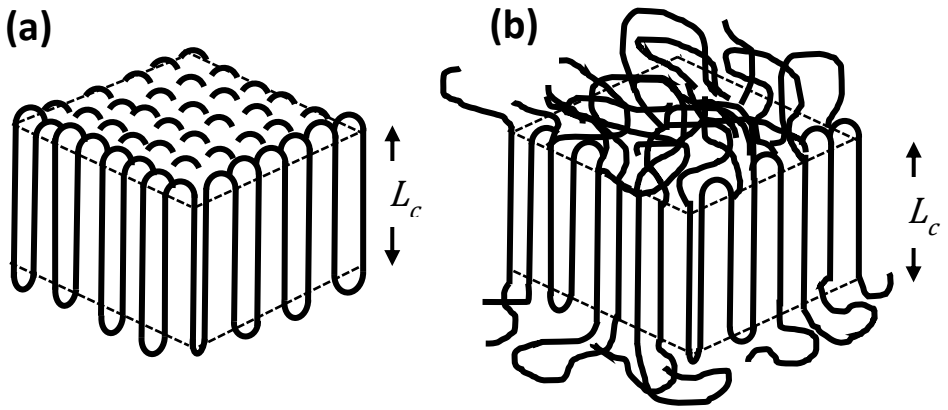

Figure 1.11: Sketches of adjacent re-entry (a) and switchboard models (b) for lamellae crystallisation.[19,55] L_c is the thickness of the crystalline domain.

Under quiescent crystallisation conditions, most polymers will crystallise from the melt into spherulites.[56] These symmetrical, spherical crystalline entities of chain-folded lamellae are a commonly observed feature of semi-crystalline polymer crystallisation with interesting optical properties.[48,49,57–61]

There are two requirements for spherulite morphology (Figure 1.12) formation: moderate or large undercooling and unrestricted growth.[49] It is important that the melt is cooled slowly to allow time for nuclei to generate randomly and subsequently grow radially. Fast cooling results in the random coils gathering together in the amorphous phase; therefore, the growth rate is dependent on the crystallisation temperature.[19] From a central nucleation point, a growth front radiates outwards only stopping upon impingement with a neighbouring spherulite.[49] Only pure material is crystallised, any impurities (such as dust particles or similar contaminants) are excreted ahead of the growth front.

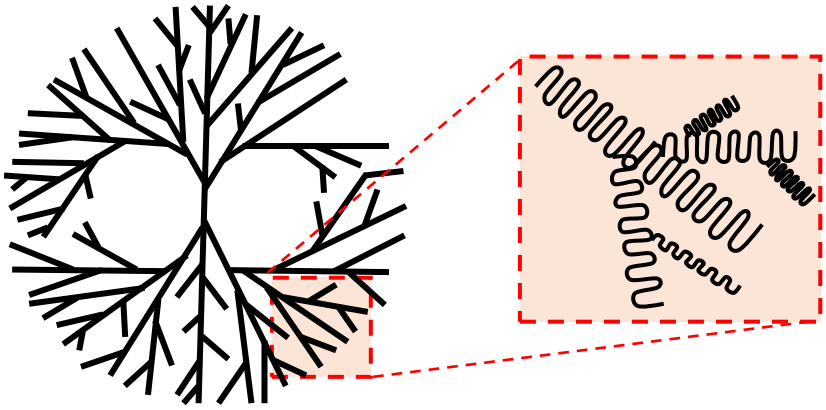

Figure 1.12: A schematic sketch of a spherulite demonstrating the radial growth from a central nucleation point. The inset image displays a sketch of the folded-chain arrangement to form lamellae.[62]

Initial crystal growth is restricted to three-dimensional growth of the lamellae away from the nucleation point.[52] This primary crystallisation is marked by linear lamellae growth rates, with splitting/branching occurring to fill the crystallisable space through the formation of a spherulitic superstructure consisting of lamellae stacks and amorphous regions.[52] This radial growth occurs until spherulite impingement, after which secondary crystallisation can occur in the intra-spherulitic regions.[52]

The chain stereochemistry and conformation also play an important part in crystal formation. Upon cooling, there is a tendency for chains to adopt the lowest energy conformation which favours co-operatively ordered chains and the formation of nuclei.[63] For polymer chains to crystallise, a basic requirement is for chains to adopt an ordered form, from which a crystal lattice can be created by orienting and packing chains regularly and uniformly.[64] Structure determinations and energy calculations have concluded that the conformation adopted by a polymer chain in the crystalline state is very close to the lowest energy conformation.[64] Despite a very simple polymer structure, constructing an energy level diagram for the chain conformations of PE reveals the all-*trans* conformation to be the lowest in energy, similar to that for butane (Figure 1.13).[19] Therefore, the planar zig-zag, all-trans conformation is present in the crystalline state which gives rise to the orthorhombic unit cell (the unit cell is the smallest chain segment arrangement that can be repeated in three dimensions to form the larger crystal[19]) as the most common crystalline unit cell.[64] This unit cell is a cuboid with axes of differing lengths and a 90° angle between each axis (Figure 1.14).[19] PE can arrange into different unit cells, such as monoclinic and hexagonal, under conditions of elongation or higher temperatures (Section 3.3.2).[19]

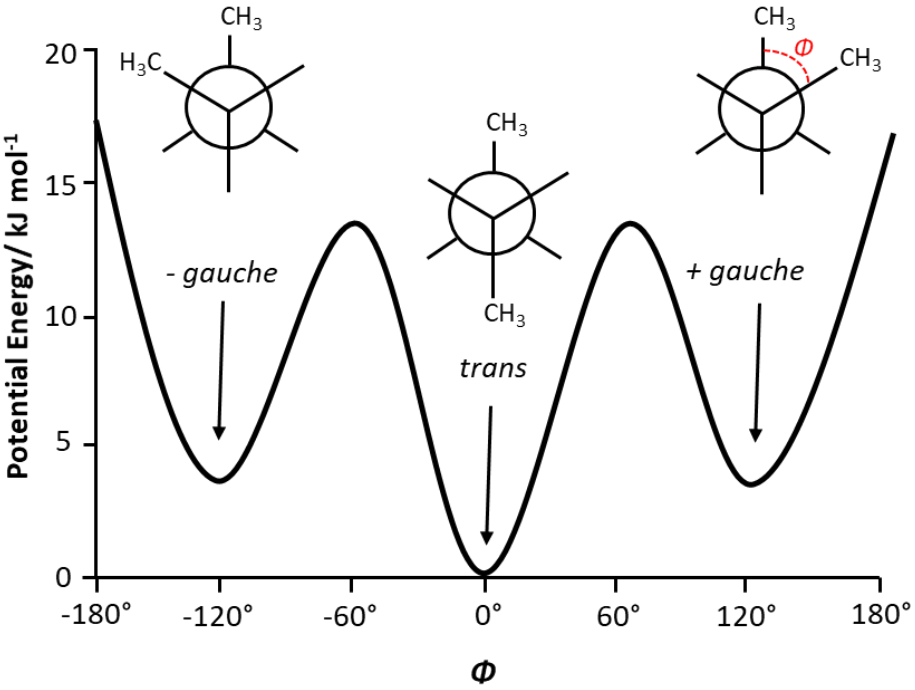

Figure 1.13: Potential energies associated with the rotation along the central C-C bond for an ethane sub-unit of a PE chain. The lowest energy conformation is the all-trans conformer.[64] The inset figures depict the conformation when viewed along the C-C bond axis. Φ is the rotation angle along the C-C bond.

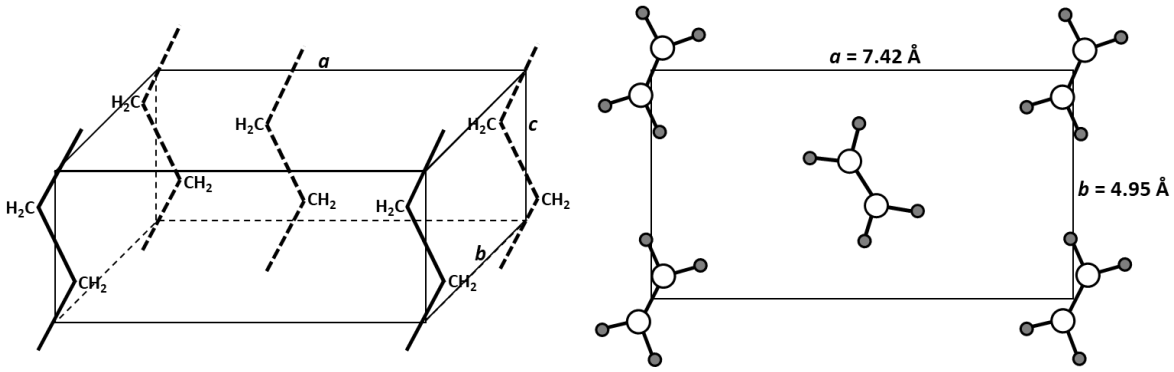

Figure 1.14: The orthorhombic unit cell of PE depicted in three-dimensions (left) and along the c-axis (right). The white circles represent carbon atoms and the grey circles represent hydrogen atoms. The lengths of each axis in an unperturbed unit cell are typically: a = 7.42 Å, b = 4.95 Å, c = 2.55 Å.

The observed macroscopic properties of a polymer are largely determined by the shape, size and inter-connectivity of the crystallites.[1] Therefore, good understanding of polymer crystallisation allows for control of the physical properties of these materials and possibilities for tuning the properties for a particular application.[1,65]

1.5.2 Thermodynamics

As with all thermodynamic processes, the Gibbs free energy (ΔG) dictates the direction of change and the spontaneity of the process (Eq. 1.1).

$$\Delta G = \Delta H - T\Delta S \quad 1.1$$

For crystallisation from the melt, ΔG will be negative (and therefore the process favourable) when the enthalpy released upon crystallisation exceeds the entropy loss at a given temperature: $\Delta H > T\Delta S$. As such, crystallisation is a delicate balance between thermodynamic and kinetic factors.[19] At high temperatures, the rate of crystallisation will be low due to little thermodynamic driving force. At low temperatures, the rate will be suppressed by kinetic factors hindering chain movement.[19]

All crystallisation events rely upon a two-step process, according to classical crystallisation theory: nucleation and growth. To initiate crystallisation, stable nuclei are required. Forming such nuclei requires a negative Gibbs free energy change from the melt to nuclei: $\Delta G = \Delta G_{nuclei} - \Delta G_{melt}$. An alternative way of thinking about this process is the competition between bulk (a negative value) and surface free energy changes (a positive value), the former of which must overcome the latter at a certain critical size of the nuclei to generate an energetically favourable stable nuclei: $\Delta G = \Delta G_{bulk} + \Delta G_{surface}$.[66]

1.5.3 Kinetics and Growth

It is widely accepted that the crystallisation process is kinetically-controlled[51] and therefore kinetics are governed by the rate of nucleation and the rate of crystal growth.[19] In addition, the conditions under which PE crystallises (i.e. the rate of crystallisation) can influence the final mechanical properties within limits imposed by molecular characteristics.[19] Hence the rate at which a PE resin crystallises can determine its suitability for certain industrial processes – for example, fast crystallisation may be more beneficial for injection moulding applications.[19] Molecular characteristics that influence the morphology can also influence the rate of crystallisation – for example, a high melt viscosity hinders chain mobility during crystallisation and so the rate decreases and also inhibits the formation of thick lamellae.[19] Thus, the conditions of crystallisation and molecular characteristics determine the final physical properties.[19,52]

Arguably one of the largest influences upon lamellae thickness is temperature, but molecular architecture such as branches and entanglements can hinder the crystallisation process. The

temperature at which lamellae are stable is a complex function of thickness and interfacial free energy and it has been observed that thinner lamellae melt at lower temperatures.[67] The greater the thickness, the higher the temperature it can exist at.[19] The Gibbs-Thomson equation (Eq. 1.2) helps to explain this:

$$T_m = T_m^0 \left(1 - \frac{2\sigma_e}{L_c \Delta H_v}\right) \qquad 1.2$$

where T_m is the actual melting temperature of a crystal of thickness L_c, T_m^0 is the equilibrium melting temperature, σ_e is the fold surface free energy, and ΔH_v is the specific enthalpy of melting per unit volume of crystal.[68] Thin lamellae have a very large surface-to-volume ratio, with the surface atoms at a higher energy than those within the bulk of the lamellae. Therefore, surface energy terms must be added to the Gibbs potential for the interior crystalline material. Consequently, melting points are depressed from T_m^0, for infinite thickness, to T_m with smaller lamellae thickness.

1.5.3.1 Primary Nucleation

Primary nucleation is the process by which new crystallites are formed when a bundle of chain stems adopts adjacent, parallel and linear configurations and packs together into a unit cell exceeding a critical size.[19,49,52] This process can either occur homogeneously or heterogeneously.[51,52] Homogeneous nucleation requires the sporadic and spontaneous generation of crystal nuclei, often from solution.[69–71] To do so, a free energy barrier must be overcome from an initially stable system to one that is meta-stable arising from thermal or density fluctuations – hence a large driving force, such as large undercooling, is necessary.[50,58,72] Density fluctuations arise from the Brownian motion of chain segments to form short-lived clusters.[58] Heterogeneous nucleation, on the other hand, occurs on a surface: the reactor wall, catalyst particles or even rogue dust particles.[19] This latter type of crystallisation occurs almost exclusively in quiescently-cooled PE melts.[58] The addition of foreign particles adds extra surface area and hence lowers the nucleation barrier – nucleating agents are often purposefully added to increase crystallisation rates by generating large numbers of nuclei.[19] In a polymer melt, the surface free energy is given as the sum of the contribution of all surfaces, assuming there are no foreign particles: $\Delta G_s = \Sigma \varphi A$ (where φ is the specific surface energy and A the surface area).

An additional mode of heterogeneous nucleation (termed athermal or self-nucleation) exists when a previously highly oriented polymer is melted, whereby the nucleation process is

initiated by nuclei which survive the melting process.[19,50] Upon cooling, these preserved nuclei help to initiate crystallisation and thus are an important feature of crystallisation memory effects.[52] An example of such self-nucleation is when highly oriented PE samples are melted and thermally stable oriented nuclei remain in the melt.[5,50]

As such, nucleation can be defined as the creation of a new solid phase, with lower free energy, from an old phase (molten) with a higher free energy.[72] The lower free energy of the newly formed phase arises due to the inevitable ordering that occurs during crystallisation.[19,48,49] The system is always striving to achieve the lowest possible energy state and a crystal is in a lower free energy state than its liquid when below the melting temperature.[48]

Nucleation and growth processes are marked by their occurrence when a homogeneous phase becomes metastable – an energy barrier thus must be overcome to initiate this.[51] Spinodal decomposition occurs when one phase spontaneously separates into two phases, thus negating the need for an energy barrier,[73–75] and has been shown to occur for HDPE.[63,76] However, it is difficult to make a distinction between the two processes (spinodal decomposition or nucleation and growth) when the nucleation barriers are below k_BT and, furthermore, it is difficult to separate the nucleation and growth processes due to the low concentrations of nuclei.[63,75] Phase separation via spinodal decomposition is known to occur below a stability limit – the temperature at which spontaneous phase separation occurs.[63,76] One phase contains polymers of the correct chain conformation for crystallisation and the other forms the amorphous phase upon crystallisation.[63,76] In particular, this mechanism of crystallisation has been seen for melts crystallised under shear because flow aligns the chains into the correct conformation and thus increases the density of appropriate chains for nuclei formation.[63]

1.5.3.2 Secondary Nucleation

Secondary nucleation refers to the two-dimensional nucleation on the surface of the newly formed primary nuclei,[19,52] and it plays a vital role in determining lamellae thickness and radial growth rates.[77] The Lauritzen-Hoffman (LH) theory provides a simple and analytical method of describing polymer crystallisation, in addition to the physical need for polymer chains to fold during the process.[19,49,51,78] The elementary unit in the LH theory is a crystal stem which attaches and detaches to the crystal front.[77] It assumes that the initial critical nucleus is longer than the minimum stable lamellar thickness, l_{min}, at the chosen crystallisation temperature,[77] created by random fluctuations. The rate-limiting step is the attachment of the first crystal stem to the growth front, therefore an enthalpic barrier for secondary nucleation exists and originates

from the surface free energy of the first crystal stem on the growth front.[77] Additional stems deposit onto the crystal growth front which results in lateral spreading and new layer formation before the next nucleation event.[51] Thus two parameters can be identified to characterise the process: the nucleation rate I, defined as the net rate of deposition on the surface per unit substrate length; the lateral growth rate G_R, defined as the difference between the arrival and departure of stems at the crystal surface.[51,78] Thus three regimes of nucleation and crystal growth can be identified depending upon the ratio of I to G_R (Figure 1.15 and Table 1.4) with the following parameters: b is the nucleus thickness, L_p is the nucleus length; K_g is the nucleation constant[77] where σ_l is the lateral surface free energy per unit area, σ_f is the fold surface free energy per unit area, T_m^0 is the equilibrium melting temperature, k_B is the Boltzmann constant, ΔH is the enthalpy change of fusion per repeat unit.[51,78,79] Despite wide acceptance, a number of challenges have been raised which has resulted in the development of several new kinetic models and modification of the original LH theory.[77]

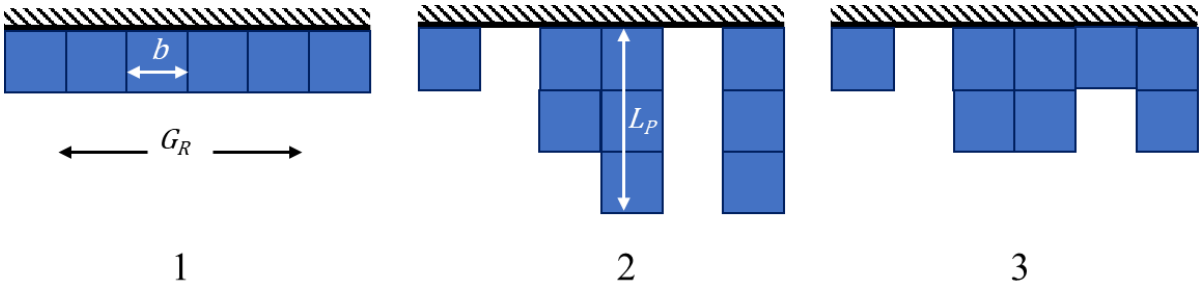

Figure 1.15: Three regimes of crystallisation kinetics, depending upon the ratio of the nucleation rate to the growth rate, as defined by the Lauritzen-Hoffman Nucleation Theory.[51]

	Regime	Lateral Growth Rate, G_R	Nucleation rate, I	K_g
1	$I << G_R$	$G_{R,1} = bIL_p$	$I_{1,n} = e^{-(K_g/T\Delta T)}$	$K_g = \frac{4b\sigma_l\sigma_f T_m^0}{k_B \Delta H}$
2	$I \approx G_R$	$G_{R,2} = b\sqrt{Ig}$	$I_{2,n} = e^{-(K_g'/T\Delta T)}$	$K_g = \frac{2b\sigma_l\sigma_f T_m^0}{k_B \Delta H}$
3	$I >> G_R$	$G_{R,3,n} = bIL_p = G_3^o e^{-U^*/k(T-T_0)-(K_g/T\Delta T)}$		

Table 1.4: Equations governing the growth and nucleation of the crystallisation regimes identified by the Lauritzen-Hoffman Secondary Nucleation Theory. U^* is the activation energy of the segmental jump.[79]

1.5.4 Flow-Induced Crystallisation

Flow-induced crystallisation (FIC) is of great industrial importance for polymer processing. Mechanical properties are linked intrinsically to the morphology, therefore any morphological change (such as crystal structure) will have a profound effect upon a polymeric material.[56,80]

The entropy of long chain molecules depends upon several factors, including pressure, temperature and degree of orientation. The thermodynamic consequence of stretching these molecules under flow is a reduction in entropy and a corresponding increase in the rate of polymer crystallisation.[81] The work of Pennings, Keller and others in the 1950 - 60s led to the discovery of the '*shish-kebab*' structure (Figure 1.14).[82–86] Developments in X-ray scattering techniques in the 1990s contributed to a second surge which has largely continued into the present day.[87–93]

Experiments on the effect of FIC can be divided into two categories: those performed in processing equipment to observe the effect of FIC for a particular process[33,94,95] and those performed under carefully controlled laboratory conditions using shear cells or rheometers.[88,96–98] There are advantages to both, however, laboratory experiments are preferred to elucidate and separate the roles of flow and temperature which is much harder to do in processing equipment.[98]

1.5.4.1 FIC Research Landscape

Pennings and Kiel observed an unusual fibrillar morphological structure upon stirring dilute PE solutions in xylene.[82] They were able to show that fibrillar crystals could be grown in flowing solutions under simple laminar flow.[83] Dilute solutions were used to minimise the effect of macromolecular interactions - isolated molecules in a flow field could more easily be studied, chain extension could be more easily observed and single crystal recovery for further analysis made easier.[81,82] Thin rings of crystalline PE, with high tensile strengths and strong birefringence, were deposited upon the stirrer and electron micrographs showed ribbon-like extended chain crystals with significant lamellae growing from them (Figure 1.14).[82] Significant orientation along the fibre axis was also observed.[82]

Subsequent salient work by Keller and Machin developed the mechanism of formation of oriented polymer crystals, building upon earlier work by Lindenmeyer who first coined the term *shish-kebabs*.[99,100] Normally, a nucleus is the origin from which crystal growth radiates, leading to a spherulitic structure.[1] At a surface, however, growth can only occur perpendicular to that surface, never through it and the same effect was seen upon 'flow lines' which originated

during injection-moulding.[100] This model of 'flow-line nucleated crystallisation' was extended to extruded PE and termed 'row-structure'.[100,101] It was shown that the extension of long chains promoted the crystallisation of long, thread-like precursors oriented parallel to the direction of flow. These precursors in turn acted as nucleating agents and a surface for the radial growth of folded lamella by lowering the energy for crysatallisation.[81,99,101] As such, a high molecular weight tail (HMWT) in the MWD (i.e. the longest chains) was deemed necessary for an enhancement of crystallisation kinetics.[98,102,103] Blackadder and Schlenitz showed that ultrasonic agitation could also form *shish-kebabs*.[104] This somewhat unusual observation is, however, consistent with the view that *shish-kebabs* are more frequently observed in solutions that are disturbed during crystallisation.[81,105]

Pennings built upon this work in his paper on the hydrodynamic effects of flow upon crystallisation.[85] He crystallised PE using a Couette cell: two concentric cylinders, the inner of which could rotate at a set shear rate. Under these conditions, the polymer crystallised at a higher temperature than was possible quiescently and, in similar solution experiments, the resulting PE crystal attached itself to the stirrer. It was also noted that only the high molecular weight (HMW) chains crystallised, leaving the low molecular weight (LMW) chains in solution.[101,106] Hydrodynamically, the origin of enhanced crystallisation was traced to the extensional flow component. Simple shear flow proved incapable of promoting primary nucleation, but proved extremely good at enhancing the growth of existing primary nuclei into macroscopic structures. [80,81,85] In other words, extensional flow accelerated primary nucleation, whereas shear flow accelerated secondary nucleation and growth.[81,106] A single molecule in simple shear flow, as is likely in the dilute solutions used, would simply rotate about its centre of gravity. The necessary conformation change to accelerate crystallisation kinetics could only be achieved with combined shear and extensional flow components.[80,106] Pennings, Keller and their associates produced numerous papers on the subject and helped to advance this emerging research field.[82–86,100–102,106–116]

Further study since then has confirmed that increasing the shear rate induces a change in the crystal morphology from spherulitic at low shear to *shish-kebab* at high shear.[117–121] Further increases in shear rate cause an increase in orientation and change in PE crystal orientation from isotropic to anisotropic, aligned along the flow direction.[122] Binsbergen noted that row-nuclei formed in sheared PP melts which disappeared only when heated to high temperature.[118] These observations were in accordance with Hill and Keller who demonstrated that such row-nuclei crystals caused nucleation and growth of lamellae oriented transversely to the row-

nuclei.[107,116] This was exploited by Odell *et al.* and Bashir *et al*. to produce extremely high-modulus PE fibres with an inter-locking *shish-kebab* structure through capillary extrusion.[123–125] Mykhaylyk *et al*. crucially demonstrated that the longest chains in a melt were stretched by shear flow to form stable nuclei along the flow direction from which the oriented lamellae morphology subsequently crystallised.[5] In order to achieve the initial stretching of the longest chains, shear needs to be applied at rates greater than the inverse relaxation time of the longest chains in the melt.[5,121] Similarly, Maxwell and Lagasse showed that enhancement of the crystallisation kinetics only occurred at shear rates greater than a critical shear rate.[81,126]

A number of theories have been presented to try and explain why the energy of crystallisation is lowered by flow-induced orientation.[80,81,85] The coil-stretch transition model (CST) first proposed by de Gennes[127] was developed further by Keller and Kolnaar[128] to account for the formation of the *shish-kebab* structure. Flory proposed the entropic reduction model (ERM)[129] for explaining the acceleration of crystallisation kinetics. This model proved extremely insightful by proposing that shearing and extending the chains reduces their conformational entropy.[129] Less entropy is therefore sacrificed when passing into the crystalline state, where the configurational entropy is taken as zero. When $T\Delta S < \Delta H$, crystallisation will occur. Therefore, providing $T\Delta S$ is smaller than the enthalpic term, crystallisation can occur at a higher temperature as ΔS becomes smaller due to chain extension.[129] Both of these models were theoretical efforts to try and interpret the observed effects of imposing flow on a polymer. The vast body of observations led to some general conclusions: enhanced crystallisation kinetics, new crystal forms and crystal morphology modified from spherulite to *shish-kebab*.[130]

More recently, a large body of work has been undertaken by various groups, that builds upon the models proposed previously, to elucidate the formation of *shish-kebabs* from crystallisation under flow.[130] Hsiao *et al*. concluded that the *shish* were composed of multiple entangled long chains and linked to coiled sections via a combination of in-situ SAXS and wide-angle x-ray diffraction (WAXD).[119,131] Kimata *et al*. postulated that the long chains in the melt played a catalytic role in recruiting surrounding chains in the formation of *shish* entities, but their concentration was not over-represented in the *shish* compared to the quiescent melt.[120] Alternatively, Han proposed that the cores of *shish-kebab*-like cylinders originated from stretched bundles of deformed entangled network strands and not extended single chains.[132,133] The effect of different flow conditions upon the morphology and enhanced crystallisation kinetics, which stems from an enhanced nucleation density, has also been extensively investigated.[134] Increasing the flow rate, strain, molecular weight and concentration of long

chains in the MWD enhance both the nucleation and degree of orientation.[121,135–137] Keum *et al*. found that the stability of *shish* induced by flow could be improved with an increased concentration of long chains in the melt.[138] Furthermore, the crystal structures induced by flow have been shown to survive for some time at temperatures above the quiescent melting temperature.[121,139,140]

Additional models have also been proposed which differ fundamentally from the CST model.[141] Most notably, the stretched network model (SNM) can be applied to entangled melts.[142] Pennings and Smook proposed that the entangled network of polymer chains during flow was responsible for *shish-kebab* formation during gel spinning.[143,144] During extrusion also, an inhomogeneous distribution of entanglement relaxation times was apparent: those with a short lifetime relaxed quickly, whereas those with a long lifetime had greater relaxation times and could thus maintain chain orientation after flow had ceased.[142] Janeshitz-Kriegl *et al*. introduced the concept of dormant nuclei for a polymer melt under flow.[145,146] These dormant nuclei would transform into point-like nuclei only above a critical value of the flow strength and align along the flow direction. Additional increases in flow strength would cause these nuclei to merge into *shish*-like nuclei.[142] Kornfield *et al*. built upon this and proposed that point-like precursors form initially during flow, from which adjacent chains adsorb to the surface causing the free chain velocity to reduce and thus stretch.[135,147] Mykhaylyk *et al*. proposed that point-like nuclei were directly aligned along the flow direction and aggregated into row nuclei, but an additional growth step was necessary for the final *shish* structures to form.[56,148,149] A 'ghost nucleation model' was proposed by Cui *et al*. whereby the movement of point-like precursors creates a new surface along their movement trails from which secondary nuclei promote the formation of row-nuclei.[150] Therefore, for polymer melts, the network of entanglements, rather than single chain dynamics, are responsible for the formation of *shish-kebabs* under flow.[142]

1.5.4.2 Crystalline Morphology and Mechanism of Formation

Penning's seminal work was the first to display the crystalline structure resulting from FIC.[82] The *shish-kebab* morphology is constructed of a thin central core fibre (*shish*) from which lamellae grow epitaxially to form rough disks (*kebabs*) (Figure 1.16). The central core is composed mainly of the longest chains in the melt or solution and crystallises first with shorter chains crystallising subsequently onto the fibre to form the lamella overgrowths.[106] The central core fibre thickness has been calculated to be approximately 1000 Å[151] with the lamellae ranging from 1000 - 3000 Å in thickness at a spacing of 1000 Å.[82]

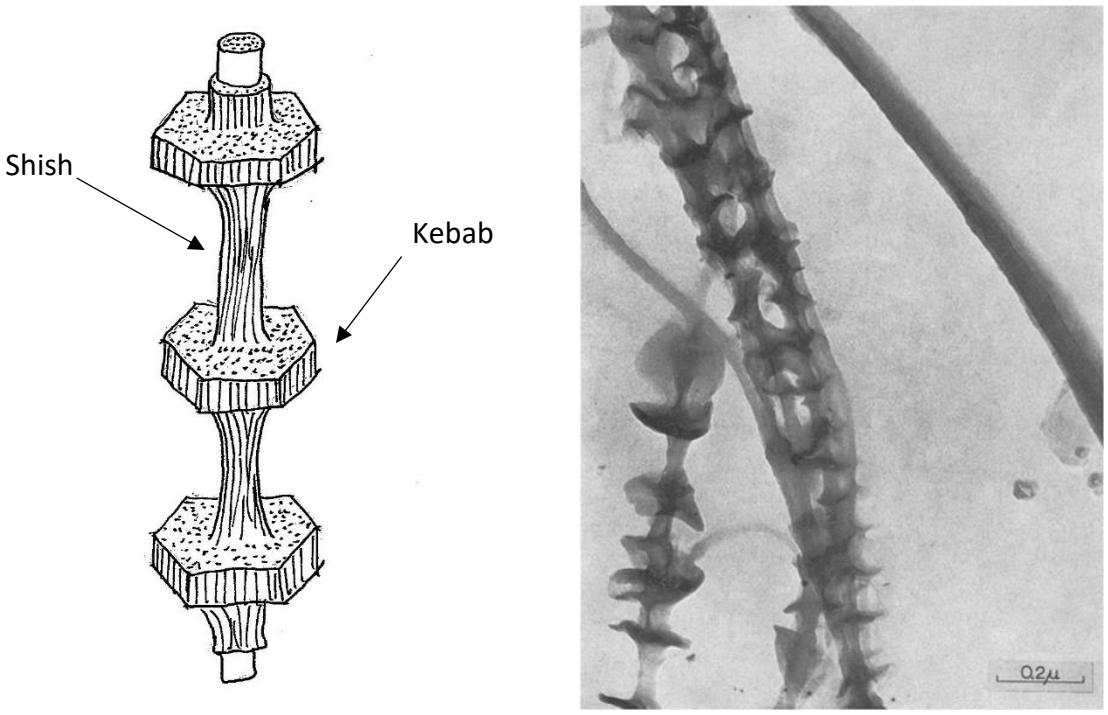

Figure 1.16: Sketch of a *shish-kebab* (L) and images of *shish-kebabs* (R) from the work of Pennings et al.[85]

A mechanism for the formation of *shish-kebabs* by shear flow has been proposed (Figure 1.17 – for clarity, entanglements between chains have been omitted).[149] In the quiescent state, polymer chains are entangled and coiled (Figure 1.17A). Upon application of shear flow, the longest chains are stretched and begin to align once a specific amount of work has been applied at shear rates greater than the inverse Rouse relaxation time ($\dot{\gamma} = 1/\tau_R$) of the longest chains in the melt (Figures 1.17B and 1.17C).[5] With continued shearing, these stretched and oriented bundles nucleate to form a row of nuclei and, subsequently, a *shish* fibre (Figure 1.17D). After the cessation of shear, cooling the melt initiates thermal crystallisation (Figure 1.17E) and the remaining chains in the melt use the newly formed *shish* fibre to crystallise epitaxially into chain-folded lamellae *kebabs* (Figure 1.17F) via a diffusion-controlled mechanism.[138,151] Crucially, the flow time must be applied for a sufficiently long time in order to orient and stretch the longest chains enough to induce *shish* formation.[149,152]

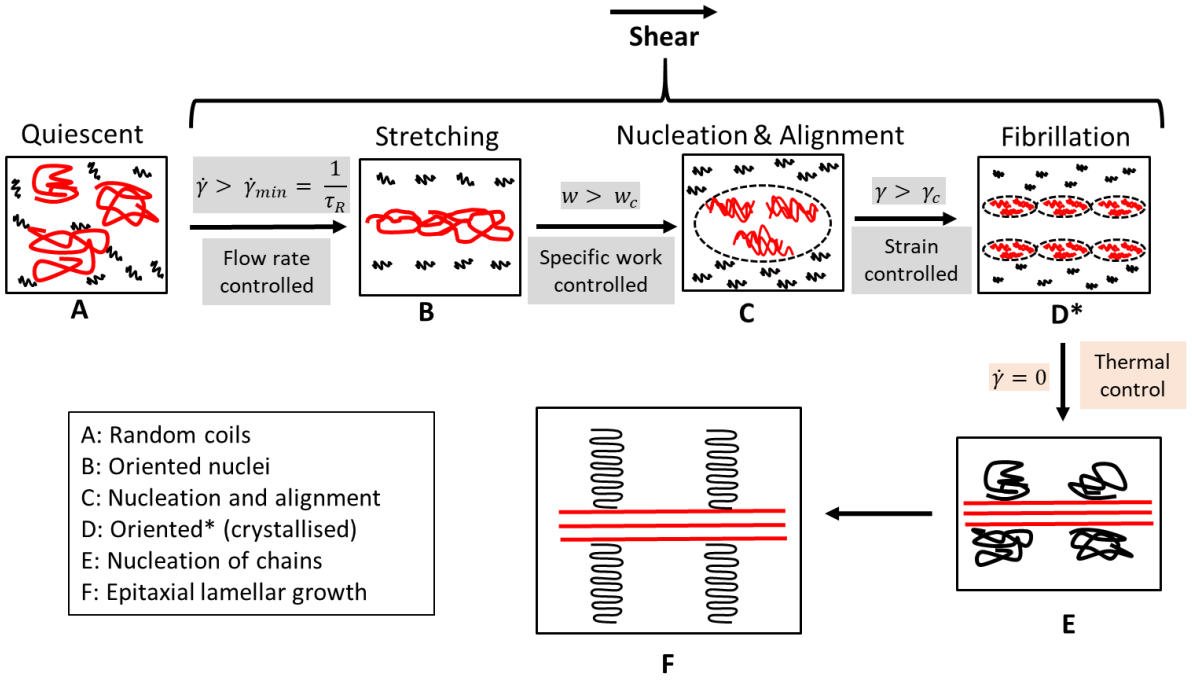

Figure 1.17: A schematic diagram of the formation of shear-induced structural morphologies in polymers: a four-stage model of *shish* formation in a quiescent polymer melt (A) under shear conditions consisting of stretching of long-chain molecules (stage 1, B), nucleation (stage 2, C), alignment of shish nuclei (stage 3, D) and fibrillation (stage 4, D). After the cessation of shear and starting to cool the melt, shorter chains use the newly formed shish as a nucleation point (E) from which to grow into chain-folded lamellae kebabs (F).[149]

Keller and Machin discovered that nitric acid washing could remove an outer part of the *shish-kebab* to yield a thinner ribbon-like fibre, measured to be 20 - 30 Å thick and 70 Å wide.[100] However, this fibre was not a smooth ribbon; it too contained lamellae overgrowths and was thus itself a *shish-kebab* (Figure 1.18). This finding was also confirmed by Pennings.[84] This leads to a classification of micro and macro *shish-kebabs* and would suggest that a micro *shish-kebab* resides within the core of the much larger macro *shish-kebab*. Nitric acid can remove the lamellae from the macro-*shish*, but not from the micro-*shish*, the lamellae of which are permanent. This not only suggests that this is the smallest entity present in these structures, but also that there is molecular connectivity at the micro-level.[153]

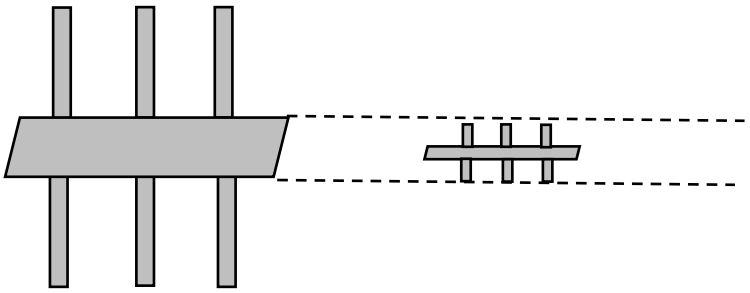

Figure 1.18: The lamellae of the macro-*shish* (left) can be removed to reveal a much smaller micro-*shish-kebab* (right).

1.5.4.3 Mechanical Properties

The formation of *shish-kebabs* has been shown to increase the mechanical properties of polymer products.[154] More specifically, the tensile strength, fracture toughness, flexural modulus and elongation to break can all be increased.[154] Research suggests that the *shish-kebab* structure can dissipate the energy of deformation along the length of the *shish*, thus providing an enhancement over spherulites.[154] The drawback, however, is a corresponding decrease in ductility which can make processing difficult.[154] By forming *shish-kebabs*, the crystallinity of a sample is increased. Since more energy input is required to deform a crystalline (compared to an amorphous) region, the net result is an observable enhancement in properties.[154] For example, work by Bai *et al.* showed that increasing the crystallinity, by the formation of *shish-kebabs*, of injection moulded samples resulted in an increase in yield strength, amongst other properties.[155]

Most of the mechanical enhancement via *shish-kebabs* occurs in the direction of the fibre, which grows parallel to the direction of the flow. As such, uniaxially oriented fibres prove extremely strong when pulled in the *shish* direction.[49] Conversely, if a stress is applied perpendicularly to the fibre direction (transverse), the mechanical enhancement is not as readily observed. Keller *et al.* explained that much of the axial strength arises due to covalent bonding along the chain axis which is much stronger than intermolecular chain bonding.[125] They also observed that the *kebabs* interlocked, thus preventing crystal slippage and increasing stiffness and strength along the *shish* direction.[125]

This transverse (or radial) stress can cause serious problems for pipe manufacture, where slow crack growth (SCG) along the pipe length is the principal mechanism of pipe failure.[47] Through the manufacturing process, polymer chains are naturally oriented along the pipe length resulting in very strong axial strength, but weaker transverse radial strength. Much research has been undertaken to try and solve this problem, and it was discovered that rotating the pipe

through the die head and/ or mandrel correspondingly twisted the oriented structures around the pipe diameter in a spiral fashion; therefore orientation was no longer parallel to the pipe longitudinal axis alleviating the SCG failure mechanism.[4,46,47,156,157]

1.6 Single-Polymer Composites

Composite technology has revolutionised many key industrial applications, most notably in aircraft manufacture. Their key properties of high strength and low weight have led to many new developments that would not have been possible with conventional materials, such as steel, wood, glass or ceramics. Bulk plastics typically suffer from low elastic moduli when compared to metal counterparts, however reinforcement of these bulk plastics can redress this imbalance. In particular, continuous fibre-reinforced composites comprise a great number of applications. Key properties, and advantages over conventional metals for example, include higher stiffness, improved corrosion resistance and greater fatigue strength.[158] The typical construction of such composites involves a continuous fibre, such as carbon, glass or aramid, often in a woven fabric impregnated in a continuous matrix phase, such as epoxy resin.[158,159]

The primary aim of any fibre-reinforced composite is to obtain materials with both high strength and elastic modulus.[160] Typically, very strong materials are brittle and do not exhibit elasticity, whereas elastic materials do not have the necessary strength requirements for load bearing applications. Fibre-reinforced composites negate this issue with a high strength fibre and more elastic reinforcing matrix. Single-polymer composites (SPCs), also known as polymer self-composites, are an exciting and interesting new development in fibre-reinforced polymer materials. Typical composites comprise two different materials, e.g. a glass- or carbon-fibre embedded into an epoxy resin.[160] SPCs use a matrix and fibre reinforcement of the same material, for example HDPE matrix and UHMWPE fibre.

A common issue with traditional composites is their end-of-life disposal because the matrix (for example, epoxy resin) and fibre reinforcement (for example, carbon fibre) are typically not compatible to be recycled in the same waste streams.[161] Therefore, an extra step, and added expense, is the separation of the matrix from the fibre typically by milling or chipping. Thus, another key advantage of SPCs lies in their inherent recyclability, as both the fibre and the matrix are fully compatible in the same waste streams.[161]

1.6.1 Composite Technology

The mechanical behaviour of fibre-reinforced composites depends predominantly on the ability for stress transfer from the matrix to the fibre. This in turn depends on a number of parameters, including matrix strength, fibre strength and the fibre/matrix interfacial adhesion. Thus, the use of stronger fibres and matrices leads ultimately to stronger composites.[161]

The 1930s are often heralded as the start of the fibre-reinforced composite industry with the advent of glass fibres and fibreglass – typically SiO_2-based with small amounts of other metal/non-metal oxides. Typical tensile strengths of these fibres in commercial applications are of the order 2.8 – 4.8 GPa.[160] It was not until 1964, that carbon-fibre was first discovered and subsequently applied to composite materials, specifically in aircraft components where high strength-to-weight ratios and fatigue resistance are crucial.[159] Importantly, carbon fibres are relatively inert, resistant to moisture and thermal expansion and have high thermal and electrical conductivity. Of all the reinforcing fibres, carbon fibre offers the highest tensile strength, with a maximum of 7 GPa, and elastic moduli between 200 – 400 GPa.[160] In the decade that followed, aramid and UHMWPE fibres were also incorporated and led to remarkable breakthroughs in aircraft and automotive transportation, sporting equipment, body armour and much more.[161]

1.6.2 UHMWPE Composites

Aside from the issues surrounding end-of-life disposal, another inherent problem with conventional composites, is achieving a strong and stable interface between chemically different fibre- reinforcement and matrix.[162] Not so with SPCs, as both the fibre and matrix are chemically identical. The manufacture of these composites exploits a narrow temperature window between the melting points of the two materials caused by the orientation of the UHMWPE chains.[163] Ideally, the matrix needs to melt and fully wet the fibres without thermal relaxation destroying any of the orientation in the reinforcing fibre. Typically, this temperature window is 10 - 20 °C, depending on melting temperatures of the components, so careful temperature control is required.

Capiati and Porter first published findings of HDPE reinforced with UHMWPE fibres – the first SPCs.[162] Their findings showed that extended and aligned chain crystals had a higher melting point, due to the greater thermodynamic stability of extended chains, than conventional crystals. Hine *et al.* explored different melt pressing techniques in order to ascertain the optimal route.[164] Hot compaction and film stacking were combined with woven and non-woven tapes

to allow the comparison of traditional hot compaction, traditional film stacking and a combined approach. Their results showed that the combined approach gave the greatest mechanical properties and a larger temperature processing window, likely due to the partial melting and wetting of the fibre surface allowing for a better interface.[164] Followed by Deng and Shallaby, SPCs of UHMWPE fibre and matrix gave favourable tensile strength and creep resistance, but no change in wear properties, with specific focus on load-bearing biomedical applications.[165] Guan *et al.* reported on mould temperature effects in an oscillating stress field, with specific focus on measuring the resulting improved mechanical properties.[166] Differential scanning calorimetry (DSC) measurements revealed a double peak melting endotherm, which was attributed to the presence of spherulites at the lower temperature and *shish-kebabs* at the higher temperature - the orientation of these *shish-kebabs* was determined by WAXD.[166] The presence of the latter helped to explain the increased mechanical performance.

Huang *et al.* used continuous extrusion to produce self-reinforced sheets of HDPE, the tensile properties of which were improved.[167] By careful design and control of the die head pressure at the die exit, FIC was successfully used to produce these samples. The increasing extensional strain rate as the melt approached the die exit was sufficient to increase the crystallisation rate. Zhang *et al.* used oscillating packing injection moulding to produce SPCs of HDPE/LDPE with improved tensile strength and modulus.[168] This was attributed to the orientation of the chains and resulting *shish-kebab* crystal structures with DSC and WAXD measurements revealing some co-crystallisation between HDPE and LDPE. Amer and Ganapathiraju investigated the effects of common processing parameters (cooling rate, temperature, processing pressure and duration) on the elastic modulus of self-reinforced HDPE.[169] Optimum parameters were shown to be matrix-dependent with higher moduli achieved for slower HDPE matrix cooling rates.

Similarly to Zhang *et al.*, Lei *et al.* focussed on dynamic packing injection moulding to produce uni- and bi-axially oriented specimens.[170] Both the flow direction and transverse direction were studied, with a 42 % increase in tensile strength in both directions for the bi-axially oriented samples.[170] DSC, SAXS, WAXD and electron microscopy revealed an inter-locking *shish-kebab* structure which explained the improved mechanical properties. Further work revealed the presence of a transcrystalline layer between the matrix and fibre reinforcement.[171] The work of Stern *et al.* showed that this layer was not produced using amorphous fibres, such as glass, because a sufficiently high heterogeneous nucleation density could not be achieved along the fibre surface. Subsequent crystal growth was restricted in the lateral direction, hence the

transcrystalline layer.[171] SPCs from PP, polyester and cellulose have also been fabricated over the years.[172]

1.7 References

1 T. Verho, A. Paajanen, J. Vaari and A. Laukkanen, *Macromolecules*, 2018, **51**, 4865–4873.

2 H. Yang, X. Luo, K. Shen, Y. Yuan, Q. Fu, X. Gao and L. Jiang, *Polymer (Guildf).*, 2019, **184**, 121915.

3 J. Long, S. Kaizhi, J. I. Jiliang and G. Qing, *J. Appl. Polym. Sci.*, 1998, **69**, 323–328.

4 N. Intawong, A. Darajang, S. Udomsom, T. Yoochooshai and C. Kantala, *Int. J. Plast. Technol.*, 2014, **18**, 241–251.

5 O. O. Mykhaylyk, P. Chambon, C. Impradice, J. P. A. Fairclough, N. J. Terrill and A. J. Ryan, *Macromolecules*, 2010, **43**, 2389–2405.

6 Plastics Pipe Institute (PPI), in *PPI Handbook of Polyethylene Pipe*, 2nd edn., 1950, pp. 5–13.

7 P. Hopkins, in *The 5th Asian Pacific IIW International Congress*, Sydney, 2001, p. 27.

8 M. Wasim, S. Shoaib, N. M. Mubarak, Inamuddin and A. M. Asiri, 2018, **16**, 861–879.

9 J. Mora-Rodríguez, X. Delgado-Galván, H. M. Ramos and P. A. López-Jiménez, *Urban Water J.*, 2014, **11**, 1–10.

10 E. Vahidi, E. Jin, M. Das, M. Singh and F. Zhao, *Sustain. Cities Soc.*, 2016, **27**, 167–174.

11 J. B. P. Soares and T. F. L. McKenna, *Polyolefin React. Eng. First Ed.*, 2012, **14**.

12 M. D. Tabone, J. J. Cregg, E. J. Beckman and A. E. Landis, *Environ. Sci. Technol.*, 2010, **44**, 8264–8269.

13 R. Geyer, J. R. Jambeck and K. L. Law, *Sci. Adv.*, 2017, **3**, e1700782.

14 C. L. Beyler and M. M. Hirschler, in *SFPE Handbook of Fire Protection Engineering*, National Fire Protection Assciation, Quincy, Massachusetts, 3rd edn., 2005, pp. 110–131.

15 D. W. Sauter, M. Taoufik and C. Boisson, *Polymers (Basel).*, 2017, **9**, 1–13.

16 H. Staudinger, *Berichte der Dtsch. Chem. Gesellschaft (A B Ser.*, 1920, **53**, 1073–1085.

17 H. Staudinger and J. Fritschi, *Helv. Chim. Acta*, 1922, **5**, 785–806.

18 H. Staudinger, *Berichte der Dtsch. Chem. Gesellschaft (A B Ser.*, 1924, **57**, 1203–1208.

19 A. J. Peacock, *Handbook of Polyethylene*, Marcel Dekker, New York, 2000.

20 S. L. Aggarwal and O. J. Sweeting, *Chem Rev.*, 1957, **57**, 665–742.

21 P. Lepoutre, *New Zeal. Inst. Chem.*, 2013, 1–5.

22 F. M. Rugg, J. J. Smith and L. H. Wartman, *Ann. N. Y. Acad. Sci.*, 1953, **57**, 398–416.

23 T. A. Sherazi, in *Encyclopedia of Membranes*, eds. E. Drioli and L. Giorno, 2016, pp. 1–2.

24 D. Romano, N. Tops, J. Bos and S. Rastogi, *Macromolecules*, 2017, **50**, 2033–2042.

25 C. K. Henry, G. R. Palmese and N. J. Alvarez, *Soft Matter*, 2018, **14**, 8974–8985.

26 L. Balzano, Eindhoven University of Technology, 2008.

27 S. Padmanabhan, K. R. Sarma and S. Sharma, *Ind. Eng. Chem. Res.*, 2009, **48**, 4866–4871.

28 M. Gahleitner, L. Resconi and P. Doshev, *MRS Bull.*, 2013, **38**, 229–233.

29 G. Odian, *Principles of Polymerisation*, John Wiley & Sons, Inc., Hoboken, New Jersey, 4th edn., 2004.

30 J. P. Claverie and F. Schaper, *MRS Bull.*, 2013, **38**, 213–218.

31 R. Ramachandran, G. Beaucage, A. S. Kulkarni, D. McFaddin, J. Merrick-Mack and V. Galiatsatos, *Macromolecules*, 2008, **41**, 9802–9806.

32 Chris Rauwendaal, *Polymer Extrusion*, Hanser Publishers, Munich, 5th edn., 2014.

33 X. . Zhang, S. Elkoun, A. Ajji and M. . Huneault, *Polymer (Guildf).*, 2004, **45**, 217–229.

34 A. Kelly, T. Gough, B. Whiteside, P. D. Coates and M. Zatloukal, in *AIP Conference Proceedings*, AIP, 2009, vol. 1152, pp. 161–167.

35 J. M. Coburn, in *SPI Plastics Engineering Handbook of the Society of the Plastics Industry, Inc.*, Springer US, Boston, MA, 1991, pp. 441–446.

36 A. N. Wilkinson and A. J. Ryan, *Polymer Processing and Strucure Development*, Kluwer Academic Publishers, London, 1998.

37 C. Macosko, *Rheology: Principles, Measurements and Applications*, Wiley VCH, New York, 1996, vol. 86.

38 A. N. Wilkinson and A. J. Ryan, *Polymer processing and structure development*, Kluwer Academic Publishers, Dordrecht, 1999.

39 G. C. Berry and T. . Fox, *Fortschritte der Hochpolym.*, 1968, **5**, 261–357.

40 P. G. de Gennes, *Phys. Today*, 1983, **36**, 33–39.

41 F. A. Morrison, *Understanding Rheology*, Oxford Univesity Press, Oxford, 2001.

42 J. M. Dealy and J. Wang, *Melt Rheology and its Applications in the Plastics Industry*, 2013.

43 Y. Huang and P. Prentice, *Polym. Eng. Sci.*, 1998, **38**, 1506–1522.

44 L. L. Ferrás, Y. Sitotaw, C. Fernandes, J. M. Nóbrega and O. S. Carneiro, *Polym. Eng. Sci.*, 2017, **58**, 249–260.

45 J. Sikora, Thesis, Lublin University of Technology, 2008.

46 M. Nie and Q. Wang, *J. Appl. Polym. Sci.*, 2013, **128**, 3149–3155.

47 M. Nie, S. B. Bai and Q. Wang, *Polym. Bull.*, 2010, **65**, 609–621.

48 G. Schuur, *J. Polym. Sci.*, 1953, **11**, 385–398.

49 E. Piorkowska and G. C. Rutledge, *Handbook of Polymer Crystallization*, Wiley, Hoboken, NJ, USA, 2013.

50 J. D. Menczel and R. B. Prime, *Thermal Analysis of Polymers: Fundamentals and Applications*, Wiley, Hoboken, New Jersey, 2009.

51 M. Zhang, B.-H. Guo and J. Xu, *A Review on Polymer Crystallization Theories*, 2017,

vol. 7.

52 Q. Guo, *Polymer Morphology: Principles, Characterisation and Processing*, Wiley, Hoboken, NJ, USA, 2016.

53 P. H. Till, *J. Polym. Sci.*, 1957, **24**, 519–529.

54 A. Keller, *Philos. Mag.*, 1957, **2**, 1171–1175.

55 J. D. Hoffman and R. L. Miller, *Polymer (Guildf).*, 1997, **38**, 3151–3212.

56 Z. Wang, Z. Ma and L. Li, *Macromolecules*, 2016, **49**, 1505–1517.

57 F. Ebert and T. Thurn-Albrecht, *Macromolecules*, 2003, **36**, 8685–8694.

58 L. Balzano, S. Rastogi and G. Peters, *Macromolecules*, 2011, **44**, 2926–2933.

59 T. Yamamoto, *Polymer (Guildf).*, 2009, **50**, 1975–1985.

60 H. Janeschitz-Kriegl, E. Ratajski and M. Stadlbauer, *Rheol. Acta*, 2003, **42**, 355–364.

61 V. Ratta, *Crystallization Morphology, Thermal Stability and Adhesive Properties of Novel High Performance Semicrystalline Polyimides*, PhD Thesis, Virginia Tech, 1999.

62 K. Okada, K. Watanabe, I. Wataoka, A. Toda, S. Sasaki, K. Inoue and M. Hikosaka, *Polymer (Guildf).*, 2007, **48**, 382–392.

63 A. J. Ryan, J. P. A. Fairclough, N. J. Terrill, P. D. Olmsted and W. C. K. Poon, *Faraday Discuss.*, 1999, **112**, 13–29.

64 G. Strobl, *The Physics of Polymers*, Springer, 3rd edn., 2007.

65 W. H. Carothers and J. W. Hill, *J. Am. Chem. Soc.*, 1932, **54**, 1579–1587.

66 Z. Ma, Technische Universiteit Eindhoven, 2012.

67 B. Wunderlich, L. Melillo, C. M. Cormier, T. Davidson and G. Snyder, *J. Macromol. Sci. Part B*, 1967, **1**, 485–516.

68 C. Androsch, R.; Schick, *Polymer Crystallization II: From Chain Microstructure to Processing*, Springer, 2017, vol. 277.

69 D. W. Oxtoby, *J. Phys. Condens. Matter*, 1992, **4**, 7627–7650.

70 P. E. Wagner and R. Strey, *J. Chem. Phys.*, 1984, **80**, 5266–5275.

71 C. Hung, M. J. Krasnopoler and J. L. Katz, *J. Chem. Phys.*, 1989, **90**, 1856–1865.

72 S. Karthika, T. K. Radhakrishnan and P. Kalaichelvi, *Cryst. Growth Des.*, 2016, **16**, 6663–6681.

73 M. Imai, K. Mori, T. Mizukami, K. Kaji and T. Kanaya, *Polymer (Guildf).*, 1992, **33**, 4451–4456.

74 J. W. Cahn, *Acta Metall.*, 1961, **9**, 795–801.

75 J. W. Cahn and J. E. Hilliard, *J. Chem. Phys.*, 1958, **28**, 258–267.

76 N. J. Terrill, P. A. Fairclough, E. Towns-Andrews, B. U. Komanschek, R. J. Young and A. J. Ryan, *Polymer (Guildf).*, 1998, **39**, 2381–2385.

77 S. Zhang, Z. Wang, B. Guo and J. Xu, *Polym. Cryst.*, 2021, **e10173**, 15.

78 J. I. Lauritzen and J. D. Hoffman, *J. Res. Natl. Bur. Stand. Phys. Chem.*, 1960, **64A**, 73–102.

79 S. Vyazovkin, J. Stone and N. Sbirrazzuoli, *J. Therm. Anal. Calorim.*, 2005, **80**, 177–180.

80 G. Lamberti, *Chem. Soc. Rev.*, 2014, **43**, 2240–52.

81 R. R. Lagasse and B. Maxwell, *Polym. Eng. Sci.*, 1976, **16**, 189–199.

82 A. J. Pennings and A. M. Kiel, *Kolloid-Zeitschrift Zeitschrift fur Polym.*, 1965, **205**, 160–162.

83 A. Zwijnenburg and A. J. Pennings, *Colloid Polym. Sci.*, 1976, **254**, 868–881.

84 A. Zwijnenburg, P. F. van Hutten, A. J. Pennings and H. D. Chanzy, *Colloid Polym. Sci. Kolloid Zeitschrift Zeitschrift für Polym.*, 1978, **256**, 729–740.

85 A. J. Pennings, J. M. A. A. van der Mark and A. M. Kiel, *Kolloid-Zeitschrift Zeitschrift fur Polym.*, 1970, **237**, 336–358.

86 A. J. Pennings and A. Zwijnenburg, *J. Polym. Sci. Polym. Phys. Ed.*, 1979, **17**, 1011–1932.

87 R. H. Somani, L. Yang, B. S. Hsiao, P. K. Agarwal, H. A. Fruitwala and A. H. Tsou, *Macromolecules*, 2002, **35**, 9096–9104.

88 G. Kumaraswamy, R. K. Verma, J. A. Kornfield, F. Yeh and B. S. Hsiao, *Macromolecules*, 2004, **37**, 9005–9017.

89 J. K. Keum, F. Zuo and B. S. Hsiao, *J. Appl. Crystallogr.*, 2007, **40**, 48–51.

90 J. K. Keum, C. Burger, B. S. Hsiao, R. Somani, L. Yang, B. Chu, R. Kolb, H. Chen and C. T. Lue, *Prog. Colloid Polym. Sci.*, 2005, **130**, 114–126.

91 E. L. Heeley, T. Gough, D. J. Hughes, W. Bras, J. Rieger and A. J. Ryan, *Polym. (United Kingdom)*, 2013, **54**, 6580–6588.

92 S. Fischer, O. Marti, T. Diesner and B. Rieger, *Macromolecules*, 2010, **43**, 5009–5015.

93 L. Boldon, F. Laliberte and L. Liu, *Nano Rev.*, 2015, **6**, 25661.

94 J. K. Keum, R. H. Somani, F. Zuo, C. Burger, I. Sics, B. S. Hsiao, H. Chen, R. Kolb and C.-T. Lue, *Macromolecules*, 2005, **38**, 5128–5136.

95 G. Lamberti, V. Brucato and G. Titomanlio, *J. Appl. Polym. Sci.*, 2002, **84**, 1981–1992.

96 B. Shen, Y. Liang, J. A. Kornfield and C. C. Han, *Macromolecules*, 2013, **46**, 1528–1542.

97 G. Kumaraswamy, R. K. Verma and J. A. Kornfield, *Rev. Sci. Instrum.*, 1999, **70**, 2097–2104.

98 J. A. Kornfield, G. Kumaraswamy and A. M. Issaian, *Ind. Eng. Chem. Res.*, 2002, **41**, 6383–6392.

99 P. H. Lindenmeyer, *J. Polym. Sci. Part C Polym. Symp.*, 1967, **20**, 145–158.

100 A. Keller and M. J. Machin, *J. Macromol. Sci. Part B Phys.*, 1967, **1**, 47–91.

101 A. Keller, *J. Polym. Sci.*, 1955, **15**, 31–49.

102 J. C. M. Torfs and A. J. Pennings, *J. Appl. Polym. Sci.*, 1983, **28**, 77–85.

103 G. Eder and H. Janeschitz-Kriegl, in *Materials science and technology : a comprehensive treatment*, eds. R. W. Cahn, P. Haasen, E. J. Kramer and H. E. H. Meijer, VCH, 18th edn., 1991, pp. 270–340.

104 D. A. Blackadder and H. M. Schleiniz, *Nature*, 1963, **200**, 778–779.

105 A. Keller and M. J. Machin, *J. Macromol. Sci. Part B*, 1967, **1**, 41–91.

106 A. J. Pennings, J. M. A. A. van der Mark and A. M. Kiel, *Kolloid-Zeitschrift Zeitschrift f??r Polym.*, 1970, **237**, 336–358.

107 M. J. Hill and A. Keller, *J. Macromol. Sci. Part B*, 1969, **3**, 153–169.

108 A. J. Pennings, *J. Polym. Sci. Polym. Symp.*, 1977, **59**, 86.

109 A. Zwijnenburg and A. J. Pennings, *Colloid Polym. Sci.*, 1975, **253**, 452–461.

110 A. J. Pennings and A. Zwijnenburg, *J. Polym. Sci. Polym. Phys. Ed.*, 1979, **17**, 1011–1032.

111 A. J. Pennings and J. Torfs, *Colloid Polym. Sci.*, 1979, **257**, 547–549.

112 J. C. M. Torfs, J. Smook and A. J. Pennings, *J. Appl. Polym. Sci.*, 1983, **28**, 57–75.

113 J. C. M. Torfs and A. J. Pennings, *J. Appl. Polym. Sci.*, 1981, **26**, 303–320.

114 A. Zwijnenburg and A. J. Pennings, *J. Polym. Sci. Polym. Lett. Ed.*, 1976, **14**, 339–346.

115 B. Kalb and A. J. Pennings, *J. Mater. Sci.*, 1980, **15**, 2584–2590.

116 M. J. Hill and A. Keller, *J. Macromol. Sci. Part B*, 1971, **5**, 591–615.

117 B. Monasse, *J. Mater. Sci.*, 1995, **30**, 5002–5012.

118 F. L. Binsbergen, *Nature*, 1966, **211**, 516–517.

119 R. H. Somani, L. Yang, L. Zhu and B. S. Hsiao, *Polymer (Guildf).*, 2005, **46**, 8587–8623.

120 S. Kimata, T. Sakurai, Y. Nozue, T. Kasahara, N. Yamaguchi, T. Karino, M. Shibayama and J. A. Kornfield, *Science (80-.).*, 2007, **316**, 1014–1017.

121 O. O. Mykhaylyk, P. Chambon, R. S. Graham, J. P. A. Fairclough, P. D. Olmsted and A. J. Ryan, *Macromolecules*, 2008, **41**, 1901–1904.

122 K. Kobayashi and T. Nagasawa, *J. Macromolecualr Sci. Part B Phys.*, 1970, **4**, 331–345.

123 Z. Bashir, J. A. Odell and A. Keller, *J. Mater. Sci.*, 1986, **21**, 3993–4002.

124 Z. Bashir, J. A. Odell and A. Keller, *J. Mater. Sci.*, 1984, **19**, 3713–3725.

125 J. A. Odell, D. T. Grubb and A. Keller, *Polymer (Guildf).*, 1978, **19**, 617–626.

126 J. van Meerveld, G. W. M. Peters and M. Hütter, *Rheol. Acta*, 2004, **44**, 119–134.

127 P. G. De Gennes, *J. Chem. Phys.*, 1974, **60**, 5030–5042.

128 H. . H. Meijer, in *Materials Science and Technology Part II: Structure Development During Processing*, ed. H. E. H. Meijer, WILEY-VCH Verlag GmbH & Co, 2006, p. 762.

129 P. J. Flory, *J. Chem. Phys.*, 1947, **15**, 397–408.

130 Z. Jiang, Y. Tang, J. Rieger, H. F. Enderle, D. Lilge, S. V. Roth, R. Gehrke, Z. Wu, Z. Li, X. Li and Y. Men, *Eur. Polym. J.*, 2010, **46**, 1866–1877.

131 B. S. Hsiao, L. Yang, R. H. Somani, C. A. Avila-Orta and L. Zhu, *Phys. Rev. Lett.*, 2005, **94**, 1–4.

132 C. Zhang, H. Hu, X. Wang, Y. Yao, X. Dong, D. Wang, Z. Wang and C. C. Han, *Polymer (Guildf).*, 2007, **48**, 1105–1115.

133 C. Zhang, H. Hu, D. Wang, S. Yan and C. C. Han, *Polymer (Guildf).*, 2005, **46**, 8157–8161.

134 R. S. Graham, *J. Rheol. (N. Y. N. Y).*, 2019, **63**, 203.

135 M. Seki, D. W. Thurman, J. P. Oberhauser and J. A. Kornfield, 2002, 2583–2594.

136 E. L. Heeley, C. M. Fernyhough, R. S. Graham, P. D. Olmsted, N. J. Inkson, J. Embery, D. J. Groves, T. C. B. McLeish, A. C. Morgovan, F. Meneau, W. Bras and A. J. Ryan, *Macromolecules*, 2006, **39**, 5058–5071.

137 G. Kumaraswamy, A. M. Issaian and J. A. Kornfield, *Macromolecules*, 1999, **32**, 7537–7547.

138 J. K. Keum, F. Zuo and B. S. Hsiao, *Macromolecules*, 2008, **41**, 4766–4776.

139 L. Balzano, N. Kukalyekar, S. Rastogi, G. W. M. Peters and J. C. Chadwick, *Phys. Rev. Lett.*, 2008, **100**, 1–4.

140 F. Azzurri and G. C. Alfonso, *Macromolecules*, 2005, **38**, 1723–1728.

141 G. Kumaraswamy, *J. Macromol. Sci. - Polym. Rev.*, 2005, **45**, 375–397.

142 W. Chen, Q. Zhang, J. Zhao and L. Li, *J. Appl. Phys.*, 2020, **127**, 241101.

143 J. Smook and A. J. Pennings, 1984, **19**, 31–43.

144 J. Smook and J. Pennings, *Colloid Polym. Sci.*, 1984, **262**, 712–722.

145 H. Janeschitz-Kriegl and E. Ratajski, *Polymer (Guildf).*, 2005, **46**, 3856–3870.

146 H. Janeschitz-Kriegl, *J. Rheol. (N. Y.).*, 2013, **57**, 1057.

147 L. Fernandez-ballester, D. W. Thurman, W. Zhou and J. A. Kornfield, *Macromolecules*, 2012, **45**, 6557–6570.

148 R. Zhao, Z. Chu and Z. Ma, *Polym.*, 2020, **12**, 2571–2582.

149 O. O. Mykhaylyk, C. M. Fernyhough, M. Okura, J. P. A. Fairclough, A. J. Ryan and R. Graham, *Eur. Polym. J.*, 2011, **47**, 447–464.

150 K. Cui, L. Meng, N. Tian, W. Zhou, Y. Liu, Z. Wang, J. He and L. Li, *Macromolecules*, 2012, **45**, 5477–5486.

151 A. Keller and H. W. H. Kolnaar, in *Materials Science and Technology: Processing of Polymers*, ed. H. E. H. Meijer, Wiley-VCH, Weinheim, 1997, vol. 18, pp. 191–266.

152 J. W. Housmans, G. W. M. Peters and H. E. H. Meijer, *J. Therm. Anal. Calorim.*, 2009, **98**, 693–705.

153 I. M. Ward, *Structure and Properties of Oriented Polymers*, Springer, Dordrecht, 2nd edn., 1997.

154 D. Mi, C. Xia, M. Jin, F. Wang, K. Shen and J. Zhang, *Macromolecules*, 2016, **49**, 4571–4578.

155 H. Bai, H. Deng, Q. Zhang, K. Wang, Q. Fu, Z. Zhang and Y. Men, *Polym Int*, 2012, **61**, 252–258.

156 M. Nie, X. Li, X. Hu and Q. Wang, *J. Macromol. Sci. Part B*, 2014, **53**, 1442–1452.

157 M. Nie, Q. Wang and S. Bai, *Polym. Eng. Sci.*, 2010, **50**, 1743–1750.

158 W. J. Cantwell and J. Morton, *Composites*, 1991, **22**, 347–362.

159 C. Soutis, *Prog. Aerosp. Sci.*, 2005, **41**, 143–151.

160 S. Prashanth, S. K. M, K. Nithin and S. Sachhidananda, *J. Mater. Sci. Eng.*, 2017, **V**, 594–595.

161 M. Kuzmanovic, L. Delva, L. Cardon and K. Ragaert, *Adv. Mater.*, 2020, **32**, 2003938.

162 N. J. Capiati and R. S. Porter, *J. Mater. Sci.*, 1975, **10**, 1671–1677.

163 Á. Kmetty, T. Bárány and J. Karger-Kocsis, *Prog. Polym. Sci.*, 2010, **35**, 1288–1310.

164 P. J. Hine, R. H. Olley and I. M. Ward, *Compos. Sci. Technol.*, 2008, **68**, 1413–1421.

165 M. Deng and S. W. Shalaby, *Biomaterials*, 1997, **18**, 645–655.

166 Q. Guan, F. S. Lai, S. P. McCarthy, D. Chiu, X. Zhu and K. Shen, *Polymer (Guildf).*, 1997, **38**, 5251–5253.

167 H. X. Huang, *Polym. Eng. Sci.*, 1998, **38**, 1805–1811.

168 G. Zhang, L. Jiang, K. Z. Shen and Q. Guan, *Acta Polym. Sin.*, 1998, 591–594.

169 M. S. Amer and S. Ganapathiraju, *J. Appl. Polym. Sci.*, 2001, **81**, 1136–1141.

170 J. Lei, C. Jiang and K. Shen, *J. Appl. Polym. Sci.*, 2004, **93**, 1584–1590.

171 T. Stern, G. Marom and E. Wachtel, *J. Compos. Part A*, 1997, **444**, 437–444.

172 C. Gao, L. Yu, H. Liu and L. Chen, *Prog. Polym. Sci.*, 2012, **37**, 767–780.

Chapter 2

Methodology and Measurement Techniques

2.1 Preparation of Polyethylene Disks

HDPE pellets were supplied by Borealis (HE3490-LS,) and Ineos (B4922N3004), designated in the subsequent text as PE1 and PE2 respectively. Both materials were designed for use in pressure pipes for water transport, offering excellent resistance to stress crack propagation and good processing properties through extrusion.[1,2] For the purpose of this study, unpigmented resins were supplied to prevent potential additional nucleation effects and in order to utilise polarised light imaging.

HDPE pellets were first heated to 150 °C, above the melting temperature of spherulites, in a vacuum oven for 12 - 24 hours to degas the material for future processing and measurements. This was subsequently transferred to a Moore hot press and pressed between 2 steel plates with 0.55 mm spacers at 150 °C. The press was closed and a force applied to approximately 2 tons. The heating element was switched off and the press cooled to 100 °C to solidify the polymer below the spherulitic crystallisation temperature, after which point the steel plates were extracted, opened and the sample removed. Disks of various diameters were cut from the larger film using a manual hand press. Disks of 25 mm diameter were also prepared via VCM using the MeltPrep apparatus, full operational details of which are given in Section 2.10.1.

2.2 Apparatus for Shearing Experiments

2.2.1 Shear Geometry Selection

A number of available geometries are capable of shearing a polymer sample, each imparting different flow. Typically, the four most commonly used are cone-plate,[3] rectilinear parallel plates,[4] slot flow[5] and torsional parallel-plates.[6] A uniform shear rate is obtained for cone-plate and rectilinear parallel plates, whereas a linear distribution of shear rate is obtained with slot flow and parallel plates. A fifth geometry is also available, which also imparts a uniform shear rate – the concentric cylinder Couette flow.[6,7]

2.2.2 Cone-Plate and Parallel-Plate Geometries

Typically, rotational rheometers have two fixtures, one of which rotates whilst the other remains stationary; the rotating fixture can either be a cone or parallel (Figure 2.1).[4]

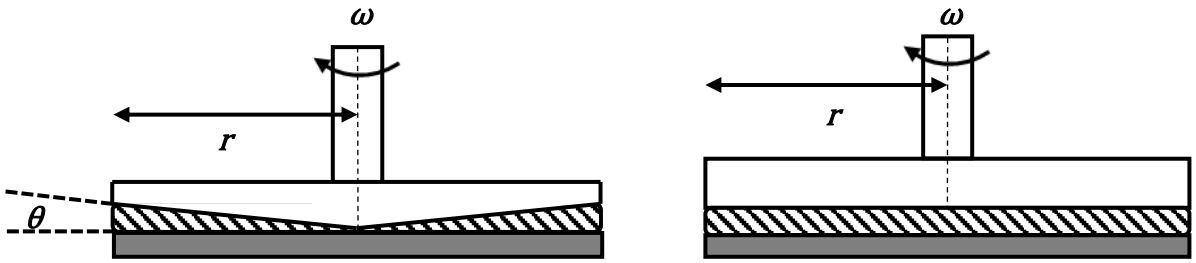

Figure 2.1: Two types of rheometer fixture: cone-plate (left) and parallel-plate (right). The cone-plate fixture has an associated cone angle, θ, which makes the shear rate across the sample radius, r, constant at a defined angular speed, ω. The parallel-plate fixture results in a radial distribution of shear rates across the sample, changing linearly from zero at the centre to maximum at the fixture edge. The sample is represented with dashed lines, the fixture in white and the base in grey.

The results of a test performed with either fixture will generally be consistent, however, the difference lies in the shear rate distribution across the sample. The shear rate is determined by:

$$\dot{\gamma} = \frac{\omega r}{h} \qquad 2.1$$

where $\dot{\gamma}$ is the shear rate, ω is the angular speed, r is the distance from the centre of rotation and h is the sample thickness. For a cone-plate fixture, the sample gap increases radially towards the edge and $\omega r/h$ ratio remains constant; therefore, for a given angular speed and radius, the shear rate (reported as that at the disk edge for both cone-plate and parallel plate) remains constant over the whole sample.[4] For a parallel-plate fixture, the sample thickness h is constant and, therefore, a distribution of shear rates is obtained from zero at the centre to $\dot{\gamma}_{max}$ at the edge (Figure 2.2).[4] For shear thinning materials in a parallel plate, it is therefore possible that a corresponding distribution in the magnitude of shear-thinning could also occur across the diameter, with the greatest shear-thinning occurring at the disk edge with maximum shear rate ($\dot{\gamma}_{max}$). Hence, small diameter plates and low oscillation amplitude measurements are used to help minimise this effect.[4] For steady-state parallel plate shear flow, the Weissenberg-Rabinowitsch correction takes account of the higher shear rates at the disk edge and thus can be applied to account for the non-linear flow behaviour.[4]

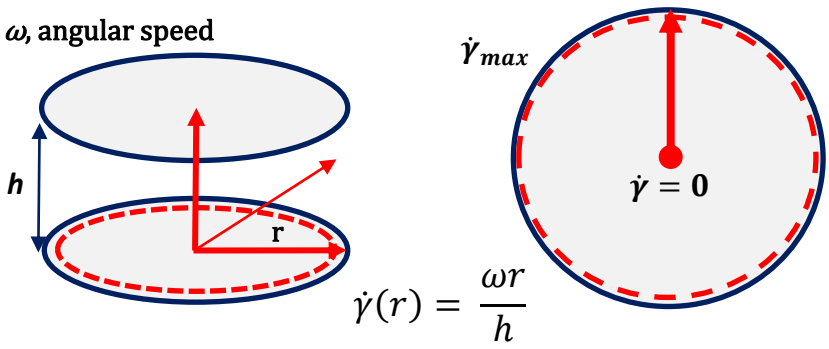

Figure 2.2: A linear distribution of shear rates is observed across parallel-plate shear with the shear rate equal to zero at the centre and maximum ($\dot{\gamma}_{max}$) at the disk edge. The shear rate can be calculated from the disk radius (r), the gap between plates (h), and the angular speed (ω).[8]

When trying to ascertain boundary conditions for nucleation and flow experiments, a distribution of shear rates is most beneficial – especially if flow conditions are unknown.[8] Therefore, a torsional parallel-plate shearing device was selected for use in this work (Figure 2.1). However, subsequent work required larger oriented samples with a uniform orientation, for mechanical testing and permeation measurements, and so a novel Couette cell shearing device was developed and utilised. By shearing under a number of different conditions, and hence producing different degrees of polymer chain orientation, subsequent tensile testing would give the modulus for each set of conditions to show the effect of orientation upon mechanical properties.[9]

2.2.3 Couette Geometry

Shear rheometers can be divided into two categories: drag-flow and pressure-driven flow. Drag-flow rheometers, such as Couette fixtures, generate shear between moving and fixed solid surfaces, whereas pressure-driven rheometers use a pressure difference over a closed channel to generate shear (Figure 2.3).[6]

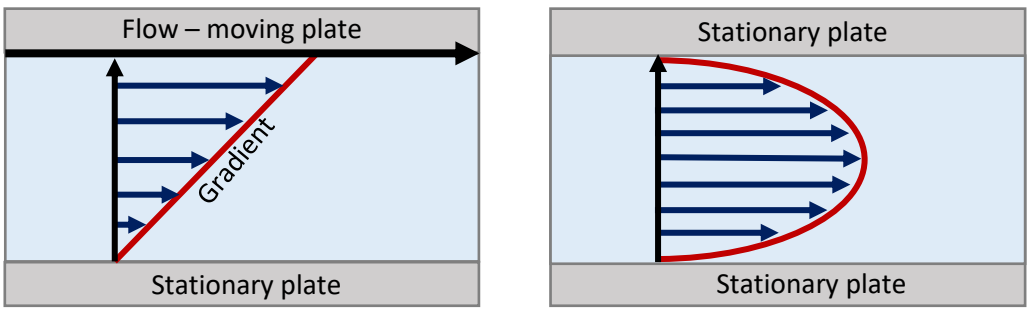

Figure 2.3: Diagrams depicting drag-flow (left) and pressure-driven flow (right).

The Couette viscometer is a rotational, drag-flow rheometer, but differs significantly from the fixtures previously described. Also known as a 'cup and bob' or 'concentric cylinder', this particular fixture uses two concentric cylinders with one or both able to rotate. Typically, the outer cylinder is fixed (the stator) whilst the inner cylinder (rotor) rotates (Figure 2.4). If the stator-rotor gap is small enough, the curvature can be neglected and the fluid under investigation is considered to experience a constant shear rate.[10]

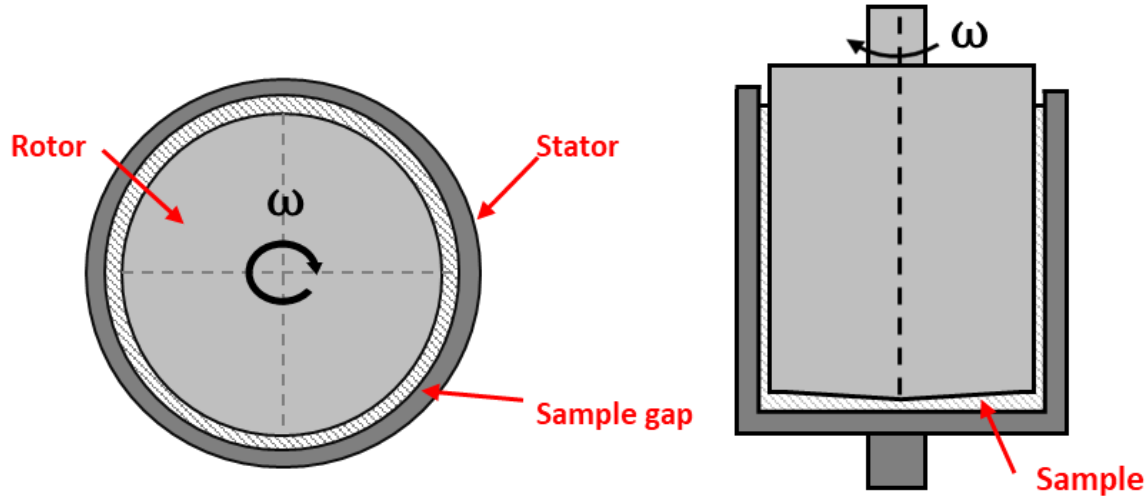

Figure 2.4: A cross-section (left) schematic of the rotor and stator assembly showing the small sample gap. An example (right) schematic of an angled Couette fixture. The sample is highlighted by the dashed lines between the rotor (light grey) and stator (dark grey) gap. ω is the angular rotation of the rotor.

2.2.4 Instrument Selection

Whilst rheometers can impart very accurate flow fields, temperature control is more accurate with shear devices such as a Linkam CSS450 shear cell, fitted with silver block heaters.[8] Previous work by Mykhaylyk *et al.* has shown that, even for the Linkam device, a temperature gradient of 1 °C exists across the sample plates at a radius exceeding 10 mm from the centre point.[8] Thus, it was necessary to use small samples for these shear experiments with a gap of 0.5 mm chosen. In order to provide accurate flow fields, some modifications were made by Mykhaylyk *et al.* to stabilise the motors and handle the normal forces produced when shearing viscous materials.[8]

A novel Couette cell was constructed by previous members of the research group, and modified during the course of this research, to enable shearing of larger polymer films in order to obtain

uniformly oriented specimens for mechanical testing. Crucially, the outer stator could be disassembled and removed to retrieve the crystallised samples.

2.3 Gel Permeation Chromatography

2.3.1 Background & Theory

Polymers, regardless of polymerisation route, always contain a mixture of chains of different molecular weights. The reason for the inherent dispersity of polymers arises due to the statistical variations in common polymerisation processes, such as free radical or step growth.[11] GPC is an extremely valuable tool for characterising this MWD. The basic apparatus consists of a series of reference and measurement columns packed with porous beads, a detector for measuring the concentration of polymer within the eluent over time and a system for recording the eluent volume.[12]

The columns contain porous, crosslinked polystyrene beads with pores ranging in diameter from 60 Å - 10^7 Å.[13] Only solubilised polymer can be measured, so any insoluble gel must be removed prior to the measurement. For successful characterisation, each polymer chain must form a random coil and the solution be sufficiently dilute so as to avoid polymer-polymer interactions. Different solvents will cause different degrees of solvation and swelling of the polymer, resulting in different hydrodynamic radii (R_h). Other effects, such as conformational changes, resonance forms, steric bulk of branches and degree of branching, can all affect the R_h.[11] A solution of the sample polymer, dissolved in the column eluent, flows through the column at a known and controlled rate, whereby interaction between the beads and solvated polymer molecules causes fractionation of the material according to size exclusion of certain molecular dimensions.[14] Longer chains will have a larger R_h value and thus will elute much quicker than shorter chains with lower R_h values as the latter chains will have greater interaction with the pores in the separation columns, therefore producing a distribution in elution times.[12,13]

Calibration should be performed ideally using fractions of known molecular weight and narrow MWD of the polymer under investigation. Since such fractions are generally not available, a universal calibration method is employed whereby the elution volume of a polymer fraction can be related to the intrinsic viscosity of a solution at a certain molecular weight, $[\eta]M$, to produce a calibration curve plot (Figure 2.5).

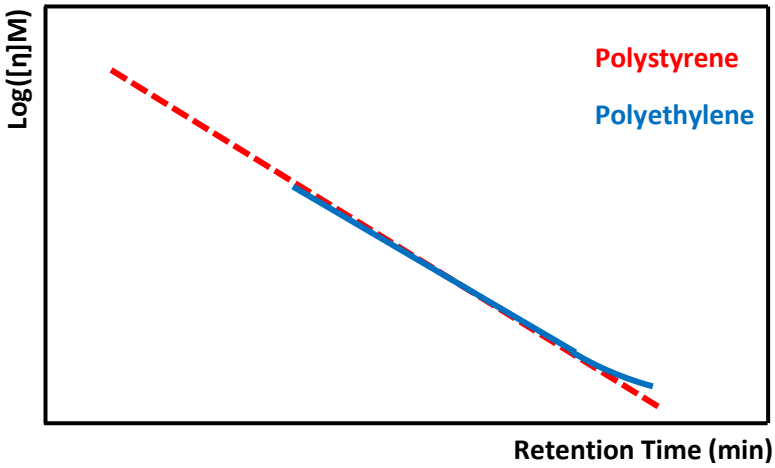

Figure 2.5: Example sketch of universal calibration curves for polystyrene and polyethylene narrow standards. Information obtained from Agilent Technologies Application Note.[15]

It has been shown that when a calibration plot of $log[\eta]M$ vs retention time (V_R) is made, many different polymer types, including branched polymers, fall upon this single curve where η is the intrinsic viscosity (the relative viscosity increase of a solvent resulting from the addition of polymer molecules[14]) for a specific M.[12,16] Therefore, the calibration plot provides a relation between intrinsic viscosity and M of a polymer solution through the Mark-Houwink equation (Eq. 2.2):[13]

$$[\eta] = K_p M^{\alpha} \qquad 2.2$$

where the values of K_p and α are related to a specific polymer-solvent system.[16] The reciprocal function of the size of the polymer in solution is proportional to K_p and α describes the quality of the solvent.[16] As viscosity is a function of polymer chain size (the hydrodynamic radius), and not strictly M, the viscosity-average molecular weight depends strongly upon polymer-solvent interactions.[17] Typically, narrow MWD polystyrenes are used and, providing the K_p and α values of both polymers are known (typically found in the literature), a good calibration can be made and the molecular weight of the sample polymer can be obtained.[12,13,16–18]

2.3.2 Measurement Conditions

HDPE is sparingly soluble in organic solvents and only in those at elevated temperatures close to or above its melting point. In particular, HDPE can only be solubilised by 1,2,4-trichlorobenzene at 138 °C or xylene above 100 °C.[13,17,19–22] Thus, the MWD of HDPE was measured by conventional HT-GPC at 160 °C using 1,2,4-trichlorobenzene as the eluent by outsourcing to Smithers Rapra, Shawbury, UK.

A solution of each polymer was prepared by adding 15 mL of eluent to 15 mg of sample and heating at 190 °C for 20 minutes with shaking to aid dissolution. The solutions were allowed to cool to 160 °C and subsequently filtered through a 1.0 μm mesh of glass-fibres directly into autosampler vials with automatic sample injection.

The measurement was performed using an Agilent Technologies PL GPC220 with Agilent Technologies Olexis columns (PLgel Olexis guard plus 3 x Olexis, 30 cm, 13 μm) at a flow rate of 1.0 mL/minute at 160 °C. All data acquisition and handling were performed by Agilent Technologies *Cirrus* software. A differential refractive index (RI) detector (effectively measuring concentration) and on-line differential pressure (DP) detector were used to obtain the chromatograms. This latter detector is more sensitive to high M_w polymers as the response is a function of intrinsic viscosity (effectively M_w) and concentration. However, providing that measured samples are of the same chemical structure and composition, RI detectors allow for better comparison of MWD as the response is proportional to M_w and concentration of the eluted sample.[13]

By using known polystyrene calibration standards with a narrow MWD in the same eluent, the chromatograms obtained through RI detectors can be converted to MWDs.[21] Calibration was undertaken using a series of Agilent/Polymer Laboratories EasiVial PS-H polystyrene calibrants with further mathematical procedures involving literature viscosity constants (Mark-Houwink parameters) applied to express the results for linear HDPE (Table 2.1).[21]

	Polystyrene (calibrants)	**Polyethylene (samples)**
α	0.707	0.725
$\boldsymbol{K_p}$ **x** $\mathbf{10^{-4}}$	1.21	4.06

Table 2.1: Mark-Houwink parameters used to calibrate the HT-GPC for linear polyethylene using polystyrene calibrants.

2.4 Differential Scanning Calorimetry

Thermal properties and transitions, such as melting and crystallisation, can be obtained through DSC and it was used in this work to select the temperature ranges used in the rheological measurements and shearing experiments.

2.4.1 Background & Theory

A typical heat flux-DSC (HF-DSC) consists of a furnace and two sample environments, each connected to a thermocouple (Figure 2.6). Above each thermocouple sits either an empty reference pan or a sample pan, both typically made from aluminium. Providing each pan is made from the same material, thermal effects arising from this material can be discounted.[23]

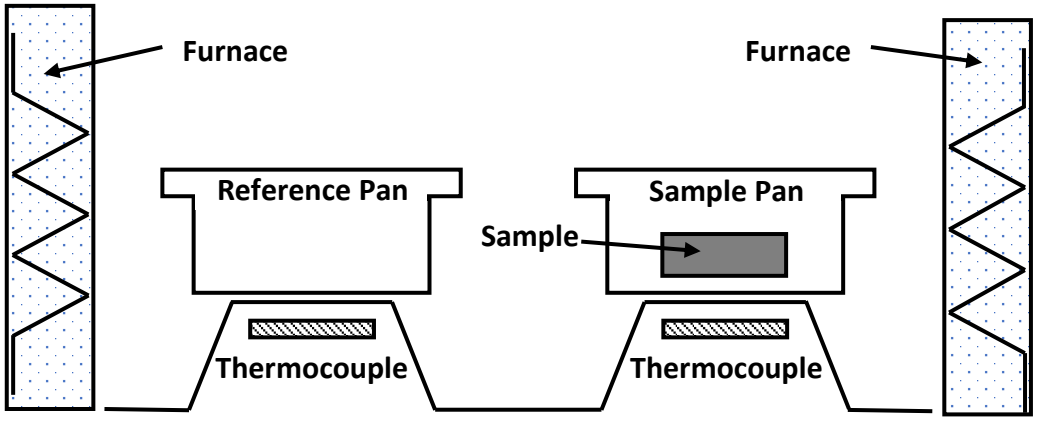

Figure 2.6: A schematic of a typical heat-flux differential scanning calorimeter. Sample and empty reference pans rest upon individual thermocouples with heating supplied at a controlled rate via the furnace. The resulting discrepancies in heat flow in the sample pan are recorded.

During a DSC measurement, a sample and reference are subjected to a controlled temperature program and the resulting difference in the heat flow, and hence the enthalpy, between the two is measured.[24,25] The resulting DSC curve expresses heat flow over time (or temperature) with heat flow given by:

$$\frac{dH}{dT} = C_P \frac{dT}{dt} + f(T,t) \qquad 2.3$$

where $\frac{dH}{dT}$ is the heat flow (W g^{-1} or mW g^{-1}), C_P is the specific heat capacity (J g^{-1} K^{-1}), $\frac{dT}{dt}$ is the heating rate (°C min^{-1}) and $f(T,t)$ is a (kinetic) function of time and temperature and is strongly affected by phase transitions (e.g. melting, crystallisation etc.).[26] Recall that enthalpy can be defined thermodynamically by:

$$H = \int_0^T C_P dT \qquad 2.4$$

Hence, knowledge of C_P from zero Kelvin up to the relevant temperature of interest allows for accurate material property determination.[23] For endothermic transitions (such as melting), the enthalpy of the system increases, whereas for exothermic transitions (such as crystallisation),

the enthalpy of the system decreases.[23,27,28] In the absence of any phase transitions, and therefore enthalpy changes, the amplitude of the DSC curve is proportional to the heat capacity at constant ambient pressure.[25] For both endothermic and exothermic peaks, integration of the peak will yield the enthalpy of the transition, provided that an accurate baseline calibration (to obtain C_P) has been performed.[29]

When analysing DSC curves for semicrystalline polymers, there are some important temperatures and associated considerations. Upon melting there are two melting points: a lower transition corresponding to the spherulitic melting temperature, T_{ms}, and an upper transition, known as the equilibrium melting temperature, T_m^0 - the melting point of an infinitely thick crystal.[8,25,30,31] For HDPE, this value is 145.5 °C.[25] T_{ms} is often simply referred to as the melting point (or nominal melting point) of the polymer and is associated with quiescently cooled polymer melts (from which spherulites are the dominant morphology).[8] Additionally, the onset and end points of crystallisation and melting can be determined.

In all DSC measurements performed in this work, a cyclic heating-cooling protocol was employed, unless stated otherwise (Table 2.2). The temperature of the first heating exceeded T_m^0 and was held isothermally for 10 minutes to ensure complete erasing of the thermal and processing history. The first cooling, in particular the cooling rate, depends largely upon the information required. Under slow cooling, high crystallinities can be achieved as the polymer chains have sufficient time to arrange into an optimal state.[32–36] Fast cooling, however, can effectively quench the amorphous state or be useful when performing isothermal crystallisation studies.[25] The second heating provides information regarding the thermal behaviour of the polymer and the structure obtained during the previous cooling, hence the importance of cooling rate selection.[25] Thus, this step provides information upon the material without processing history effects. The second cooling step is not strictly necessary, however can be useful for comparison to the first cooling.

2.4.2 Degree of Crystallinity

Several methods have been developed to measure the degree of crystallinity in polyolefins, such as density measurements, Raman spectroscopy, SAXS, WAXS and DSC.[32] From a practical perspective, DSC offers a balance of simplicity and valuable quantitative information, providing special attention is paid to heating rate and baseline calibrations.[23,32,37]

By quantifying the heat associated with fusion (melting) of the polymer, polymer crystallinity, X_c, can be determined. This value is typically reported as a percentage and is obtained by

normalising the obtained heat of fusion against that for a 100 % crystalline polymer sample.[25,37,38] For PE, such crystals cannot be produced and, therefore, theoretical values must be used.[25,32,37,39] Wunderlich and colleagues estimated this value to be 293 J g^{-1} by extrapolation from an almost completely crystalline PE formed via high-pressure crystallisation.[39–45] A further complication is the broadening of the melting endotherm of polymeric species due to the distribution of crystal stem lengths present.[25,46–49]

2.4.3 Measurement Conditions

A TA Instruments DSC25 was used, with temperature and heat capacity calibrations performed prior to measurement using indium standards. All measurements were performed under a nitrogen atmosphere, to avoid oxidative sample degradation.[25] The polymer sample weights ranged between 5 - 10 mg (in order to minimise any thermal gradient in the sample), measured using a 4 decimal point balance and encapsulated in high-purity aluminium pans with a hole punched into the lid to maintain atmospheric pressure during heating.[25] A 4-step heating and cooling protocol at 10 °C min^{-1} was applied to each sample (Table 2.2). All measurements and data analysis were performed using TA instruments *Trios* software.

Step	Initial Temperature (°C)	Final Temperature (°C)
1	40	180
2	180	40
3	40	180
4	180	40

Table 2.2: Initial and final temperatures at each step of the DSC temperature program for the measurement of melting and crystallisation enthalpies and temperatures of HDPE samples. All heating and cooling rates were 10 °C min^{-1}.

The measurement of isothermal crystallisation kinetics required a modified temperature protocol, with all other calibrations and instrumentation the same. Samples were heated at 10 °C min^{-1} to 136 °C and maintained isothermally for 1 minute at this temperature. The samples were next cooled at a rate of 100 °C min^{-1} to the crystallisation temperature and maintained isothermally at this temperature for 10 minutes before cooling to room temperature at 20 °C min^{-1}. Crystallisation temperatures for each successive measurement were between 120 – 110 °C in 2 °C increments with a new sample used each time.

2.5 Rheology

2.5.1 Background & Theory

Rheology is the study of the deformation and flow of matter, and is often dominated by studying complex fluids such as polymers, suspensions and slurries. Early theories of elasticity and viscosity were developed by Hooke and Newton: Hooke's theory of elasticity states that force is directly proportional to deflection;[50] Newton established viscosity relationships for normal liquids - applying only to fluids with Newtonian behaviour, viscosity is constant regardless of shear rate (i.e. shear rate-independent).[3,51] A liquid showing any deviation from these conditions is non-Newtonian or viscoelastic, such as a PE melt.[10]

In the 19th century, Navier and Stokes presented a consistent theory for a Newtonian viscous liquid (named such in honour of Newton). For simple shear, a shear stress, σ, results in a shear flow which persists as long as stress is applied, in the case of a Newtonian liquid.[10] With respect to both of these theories, complex, non-Newtonian fluids, such as polymer melts, do not obey either of them. Polymers show non-linear behaviour, whereby a material property can change as the applied stress also changes – but not in a linear fashion. An example is shear-thinning viscosity behaviour with increasing shear rate. Thus, there are elements of both viscous and elastic components to the behaviour.

Thinking in terms of the earliest definitions for material classification, the Newtonian fluid and Hookean solid, it is apparent that there are two types of behaviour resulting from an applied stress. A classical fluid will flow under stress, but a solid will deform under that same stress. Polymers exhibit both flow and deformation, depending on the type of polymer and applied shear stress. Therefore, rheology is an important tool to understand material behaviour, both during flow and/or deformation. Viscosity is an extremely important material parameter. As polymers display non-Newtonian (viscoelastic) behaviour, parameters such as shear rate and temperature can affect the measured viscosity and is thus an important consideration when designing polymer processing techniques.[3,6]

2.5.2 Rheometers

One of the simplest types of rheometer is the viscometer, which consists of a spindle dipped into the test liquid. By rotating this spindle, and measuring the torque required to do so, the viscosity of the liquid can be obtained.[3] This technique forms the basis of the rotational rheometer, used to generate torsional shear flows. In the majority of rotational tests, the imposed stress and strain may be kept constant (i.e. steady shear) or oscillate sinusoidally (i.e.

oscillatory shear) with time.[6] For Newtonian liquids, rotational steady-shear measurements can be used to obtain the viscosity.[6] However, as non-Newtonian liquids display viscoelastic behaviour, sinusoidal oscillatory measurements are capable of detecting the influence of both viscous and elastic components upon the material response.[6] Additionally, oscillatory tests are regarded as non-destructive when performed in the linear viscoelastic region (LVR) as the microstructure is not destroyed by the applied deformation.[6] When a sinusoidal stress is applied to a material, a corresponding sinusoidal strain response is observed, measured as torque by the rheometer[52]. The strain of a viscoelastic material is out of phase with the applied stress by the phase angle, δ, due to the extra time necessary for molecular motions and relaxations to occur (Figure 2.7).[20]

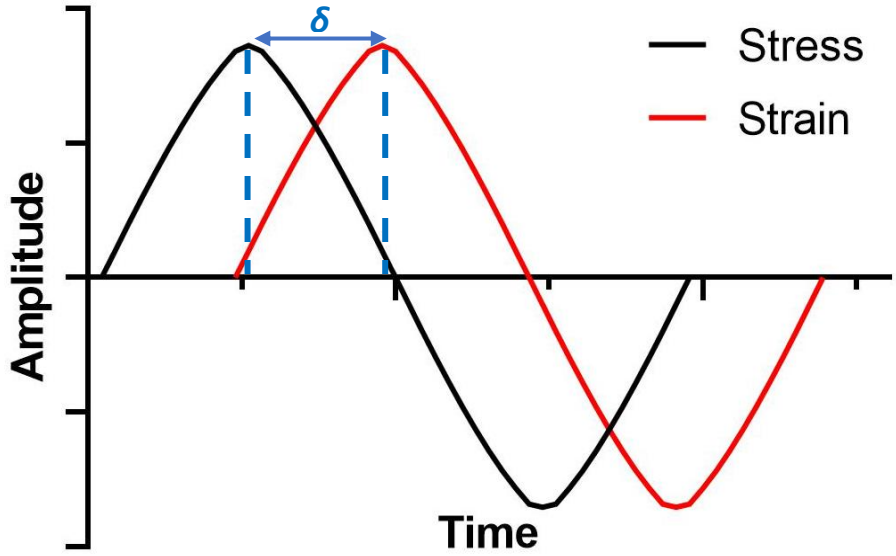

Figure 2.7: Sinusoidal waveforms for stress and strain functions during a rheology measurement with associated phase shift, δ, between the respective waveforms.

Viscoelastic materials exhibit both viscous and elastic behaviour and the measurement response reflects this with an elastic component, *G'*, and a viscous component, *G''*.[3,6,53] These are often referred to as the storage modulus and loss modulus respectively. The amplitude of the strain and stress gives *G';* the phase difference combined with the amplitude of strain and stress gives *G''*.[52] A further component, complex viscosity (η^*), can be calculated from the storage and loss moduli and angular frequency of oscillations, ω:

$$|\eta^*| = \sqrt{\left(\frac{G'}{\omega}\right)^2 + \left(\frac{G''}{\omega}\right)^2} \qquad 2.5$$

Consider the case of a spindle dipped into a Newtonian liquid; upon rotation, this purely viscous, inelastic liquid will display a concave surface due to centripetal force pushing the liquid away from the axis of rotation.[54] Conversely, a non-Newtonian, viscoelastic liquid will be observed 'climbing' up the rod – this free surface climbing is known as the normal stress (Weissenberg) effect.[54–56] The rod climbing is caused by normal stresses generated by shear.[57] When a viscoelastic liquid undergoes shear flow, an additional normal stress arises in the flow direction due to the stretching and orientation of the entangled network, in addition to the usual shearing stress.[54,58] A normal stress alone has little rheological significance, since if the stress is isotropic no deformation will occur, however a normal stress difference can cause deformation.[59] Two, independent normal stress differences are apparent (termed the first and second normal stress difference, N_1 and N_2 respectively) which, in conjunction with the viscosity, are functions of shear rate and are called the viscometric functions (Eq. 2.6 – 2.8):

$$\eta(\dot{\gamma}) \equiv \sigma/\gamma \tag{2.6}$$

$$N_1(\dot{\gamma}) \equiv \sigma_{11} - \sigma_{22} \tag{2.7}$$

$$N_2(\dot{\gamma}) \equiv \sigma_{22} - \sigma_{33} \tag{2.8}$$

where σ is the shear stress, γ is the shear strain, σ_{11} is the normal stress component acting in the direction of shear/flow, σ_{22} is the normal stress component acting perpendicular to the shearing plane and σ_{33} is the normal stress component acting in the transverse direction to shearing.[60]

These normal forces have been studied in detail for polymer melts for two principal reasons. Firstly, these elastic stresses give rise to interesting flow behaviour, such as rod climbing and extrudate swell. Secondly, they have proven important in determining the constitutive equations for general flow that provide relations between the applied stress and resulting deformation rate.[58,61] Thus, for high viscosity, polymer melts oscillatory measurements are favoured over rotational measurements to minimise the Weissenberg effect. Whilst the sample under investigation in a rheometer is confined underneath the plate fixture, the same 'climbing' effect occurs, exhibited as an axial 'normal force' against the fixture, measured by an axial force sensor. The sensitive nature of rheometer components necessitates normal force limits to be placed on the motors to prevent damage, which are swiftly reached with viscous materials.

2.5.3 Variation with Shear Rate

Situation	Shear Rate (s^{-1})	Application
Sedimentation of fine powder in liquid	$10^{-6} – 10^{-4}$	Medicines, paints
Levelling due to surface tension	$10^{-2} – 10^{-1}$	Paints, printing inks
Draining under gravity	$10^{-1} – 10^{1}$	Painting and coating
Extruders	$10^{0} – 10^{2}$	Polymers
Mixing and stirring	$10^{1} – 10^{3}$	Liquid manufacture
Pipe flow	$10^{0} – 10^{3}$	Pumping, blood flow
Spraying and brushing	$10^{3} – 10^{4}$	Spray-painting, brushing
Lubrication	$10^{3} – 10^{7}$	Internal-combustion engine

Table 2.3: Typical shear rate ranges for common industrial and household processes.

A wide range of shear rates (Table 2.3) can be encountered in industrial and everyday situations, demonstrating the varying conditions a polymer melt might be subjected to. [10] The approximate shear rate for any operation can be estimated by dividing the average velocity of the liquid by a characteristic dimension (such as the radius of the tube the liquid flows through).[10]

PE melts are viscoelastic and exhibit shear-thinning, a reduction in the measured viscosity as the shear rate increases (Figure 2.8). Generally speaking, shear-thinning is a characteristic of non-Newtonian liquids, enhanced by a broad MWD, and arises from the alignment of the entangled network (at rest, no shear applied) with the flow direction under applied shear.[4]

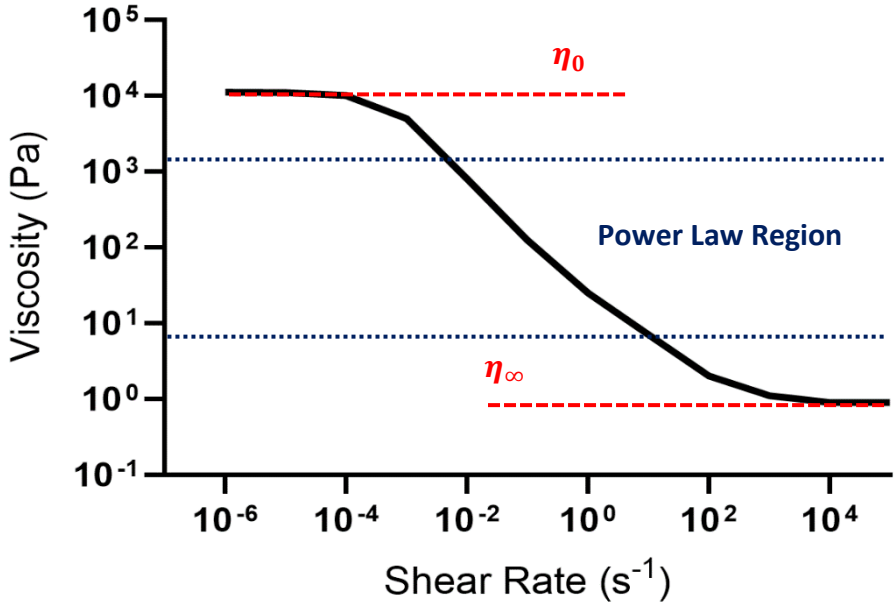

Figure 2.8: A plot of shear rate against viscosity showing a typical shear-thinning curve for a non-Newtonian liquid with the Power Law region, zero-shear (η_0) and infinite-shear (η_∞) plateaus indicated.

Note that plateaus are found at the lowest and highest shear rate regions. These signify the zero-shear viscosity, η_0, at low shear rate when the limit tends to zero,[62] and infinite-shear viscosity, η_∞, at high shear rate when the limit tends to infinity.[63] Historically, these have also been called the 1st and 2nd Newtonian plateaus respectively. In order to obtain a complete flow curve, two or often three different viscosity measurement techniques are needed to access a wide shear rate range as these different techniques often have over-lapping shear rate regions. Once generated, there are a number of equations that can be used to model this flow curve and obtain values for η_0 and η_∞.

The Power Law Model, which describes the relationship between shear rate and viscosity, can be defined:

$$\eta = K\dot{\gamma}^{n-1} \qquad 2.9$$

where n is the power law index and K is the consistency index. For most polymer melts, the power law region describes the characteristic shear-thinning behaviour.[63] The limitation of this model is that it can only fit the linear part of the double logarithmic flow curve where the fluid shows power law behaviour and cannot capture the Newtonian plateaus.

Polymer melts display complex flow behaviour and therefore require complex models to adequately describe this behaviour. The Power Law Model is applicable within the range

$\eta_\infty \ll \eta \ll \eta_0$, however outside of this range, it can be expanded to the empirical Cross Model:

$$|\eta(\dot{\gamma})| = \eta_\infty + \frac{(\eta_0 - \eta_\infty)}{1 + (K\dot{\gamma})^n} \qquad 2.10$$

where $\eta(\dot{\gamma})$ is the shear rate-dependent viscosity, η_0 and η_∞ are the zero-shear and infinite-shear viscosities respectively, $\dot{\gamma}$ is the shear rate, K is the consistency index and n is the power law index.[64,65] One disadvantage of this model, however, is the difficulty in measuring η_∞ experimentally and, as such, is often set to a small value or discounted as negligible.[65] By also utilising the Cox-Merz rule, which correlates dynamic and steady-flow measurements, $\dot{\gamma}$ and ω can be directly interchanged:

$$|\eta^*(\omega)| = \eta(\dot{\gamma}) \qquad \text{for } \omega = \dot{\gamma} \qquad 2.11$$

A major benefit of this rule is the ability to predict $\eta^*(\dot{\gamma})$ from oscillatory measurements.[66,67]

2.5.6 Rheological Models

Several rheological models are useful for describing and understanding the linear viscoelastic and relaxation behaviour of polymer melts.

2.5.6.1 Maxwell Model

A fundamental mathematical model for describing stress relaxation from rheological data is the Maxwell Model.[4,68] It describes linear viscoelastic behaviour by considering both the elastic and viscous components of a material, represented by the spring (elastic) and dashpot (viscous) connected in series (Figure 2.9).[10]

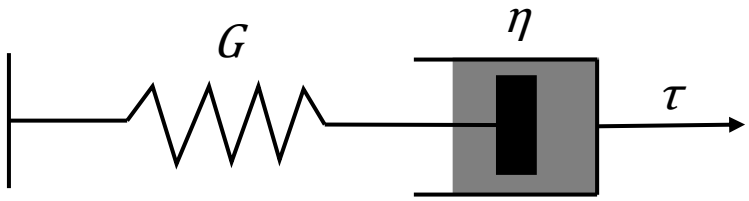

Figure 2.9: A diagram depicting a spring and dashpot in series to represent one of the simplest linear viscoelastic models, the Maxwell Model. When a stress (τ) is applied, the measured response can be modelled by the spring and dashpot connected in series. The viscous component is represented by the dashpot (η) and the elastic component by the spring (G).

Upon application of a constant strain, only the spring deforms initially followed by the time-dependent dashpot response, which deforms under the same strain. As the stress relaxes to

zero, the deformation is transferred to the dashpot leading to a loss of energy as this latter deformation is irreversible.[68] For slow motions, viscous Newtonian behaviour dominates, whereas elastic behaviour dominates at rapidly changing stresses.[6]

The general constitutive equation for the Maxwell model is given by:

$$\eta\dot{\gamma} = \tau_r \frac{d\sigma}{dt} + \sigma \qquad 2.12$$

where τ_r is the relaxation time of the material. For oscillatory motion, a constitutive equation can be formulated:

$$\frac{\sigma}{\gamma_0} = G' \sin(\omega t) + G"cos(\omega t) \qquad 2.13$$

where $G' = G\frac{(\omega t)^2}{1+(\omega t)^2}$ and $G" = \eta\frac{\omega}{1+(\omega t)^2}$

At sufficiently low frequencies ($\omega << 1/\tau_r$), these reduce further to:

$$G' = G_0(\omega\tau_r)^2 \text{ and } G" = \eta\omega \qquad 2.14a \quad 2.14b$$

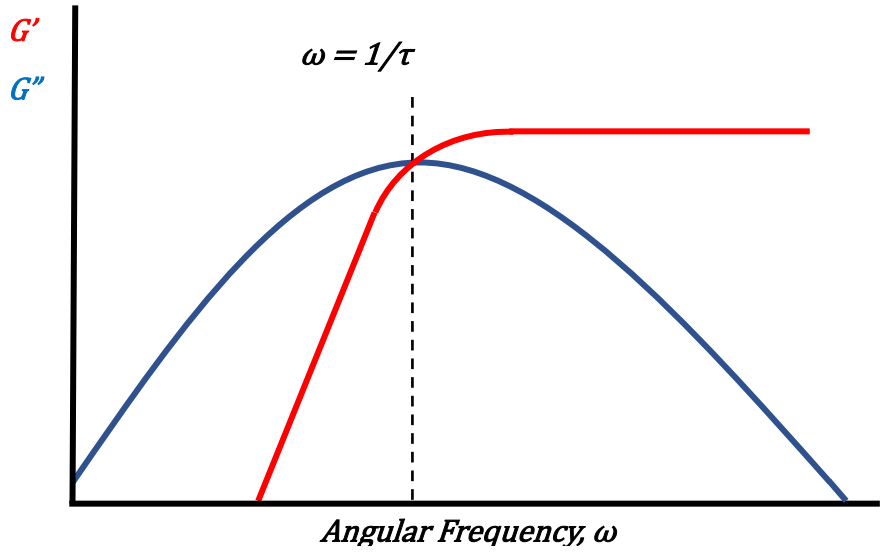

Figure 2.10: A typical Maxwellian response of the storage modulus, *G'*, and loss modulus, *G"*, against angular frequency, ω, on a double logarithmic scale.

For a typical Maxwellian oscillatory response (Figure 2.10), *G"* is much larger than *G'* at low frequencies and, therefore, liquid-like behaviour dominates. As the oscillatory frequency increases, *G'* increases to an extent that solid-like behaviour dominates. At the maximum of

G", *G'* is equal to *G"* - this critical crossover frequency is the inverse of the relaxation time, $\omega = 1/\tau_r$.[4]

By utilising multiple Maxwell models in parallel, the dynamic response of a viscoelastic material over a range of frequencies can be modelled providing that suitable values for *G* and τ_r are selected to cover the entire frequency range of measurement. The values of the overall *G'* and *G"* at any frequency, ω, can be obtained from the sum of *i* contributions from *i* Maxwell elements:[4]

$$G'(\omega) = \sum_i G_i \frac{\omega^2 \tau_{ri}^2}{1 + \omega^2 \tau_{ri}^2} \quad \text{and} \quad G'' = \sum_i \eta_i \frac{\omega \tau_r}{1 + \omega^2 \tau_{ri}^2} \qquad \begin{matrix} 2.15a \\ 2.15b \end{matrix}$$

2.5.6.2 Boltzmann Superposition

According to Boltzmann's superposition principle, the influence of strains applied at different times can be superposed – the deformation of a polymer is the sum, or superposition, of all strains that results from various deformations acting at different times.[68,69] Therefore, the material response to a certain strain is independent of any existing strain.[68]

If, at a particular time t_i a strain $\Delta\gamma(t_i)$ is applied, the resulting stress can be expressed by:

$$\tau_{xy_i}(t) = G(t - t_i)\Delta\gamma_{xy_i}(t_i) \qquad 2.16$$

where τ is the stress and *G* is the relaxation modulus. Therefore, the stress within a specimen exposed to several different strains at different time points can be found by the sum of all stress responses when $t > t_i$:

$$\tau_{xy}(t) = \sum_{i=1}^{n} G\,(t - t_i)\Delta\gamma_{xy_i}(t_i) \qquad 2.17$$

2.5.6.3 Time-Temperature Superposition

For a Newtonian liquid, viscosity decreases as temperature increases according to the Arrhenius equation:

$$\eta = Ae^{B/T} \qquad 2.18$$

where *T* is the absolute temperature and *A* and *B* are constants of the liquid.

Non-Newtonian liquids, similarly, show a strong dependence upon temperature due to several reasons. The dominating factor is the strong decrease of relaxation times with increasing temperature; less importantly, the moduli associated with such relaxation processes and

absolute temperature are proportional.[3] Thus another superposition is the time-temperature superposition (TTS). By shifting the data obtained at several different temperatures to a common reference temperature, the viscoelastic behaviour of a material over a broad range of times or frequencies can be described.[70] It requires the use of temperature-dependent (vertical), and time-dependent (horizontal), shift factors (a_T and b_T respectively) on double-logarithmic plots of, for example, *G'/G"* against angular frequency, ω. A mastercurve can be generated through the use of these shift factors to give a data range covering several decades that cannot be measured on any one single rheometer at any one temperature.

In generating the mastercurve, two relationships can be used along with the temperature-dependent shift factor, a_T. By studying the temperature dependence of liquid viscosity, the empirical Arrhenius relationship can be proposed in terms of a_T:

$$a_T\,(T) = exp\left[\frac{E_a}{R}\left(\frac{1}{T} - \frac{1}{T_0}\right)\right] \qquad 2.19$$

where E_a is the activation energy for flow, R the gas constant and T and T_0 the measurement and reference temperatures respectively. Providing the temperature is above the T_g, this relationship holds for linear polymers in the plateau zones.[70] If the temperature is much closer to the T_g, then the model proposed by Williams, Landel and Ferry (WLF) is preferred:

$$log a_T = \frac{-c_1(T - T_0)}{[c_2 + (T - T_0]} \qquad 2.20$$

with T and T_0 defined as previously and C_1 and C_2 as empirical constants.[71,72]

2.5.6.4 Rouse Model

Rouse developed a simple spring and bead model (Figure 2.11) to describe the relaxation behaviour of a local part of the chain.[73]

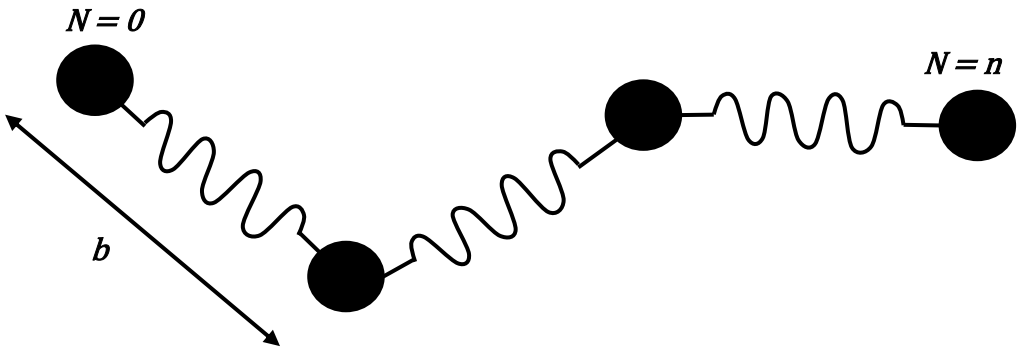

Figure 2.11: Representative sketch of the Rouse Model which describes the relaxation behaviour of *n* number of polymer chains. The segment length is denoted by *b* and the number of segments by *N*.[52]

In creating this model, Rouse made three assumptions: 1) both the springs and beads have no volume; 2) all springs have the same spring constant; 3) no interaction exists between the springs or beads. If an external stress is applied to this model polymer, relaxation of the spring occurs after a certain time, known as the Rouse relaxation time, τ_R, and is defined as:

$$\tau_R = \frac{\xi N^2 b^2}{3\pi^2 k_B T} \qquad 2.21$$

where ξ is the friction coefficient, b is the segment length, N is number of segments, k_B is the Boltzmann constant and T is the temperature.

2.5.6.5 Tube Model

De Gennes proposed the tube model as a way of taking into account the interactions of surrounding entanglements and the restriction of movement upon relaxation behaviour (Figure 2.12).[74]

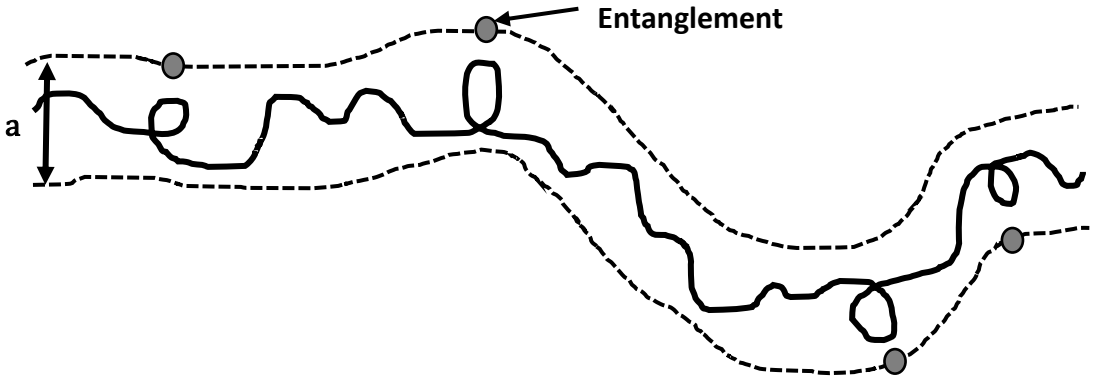

Figure 2.12: A representative sketch of the Tube Model which describes chain interactions and surrounding entanglements (indicated by the grey circles) associated with relaxation. The tube diameter is denoted by *a*.[52]

The polymer chains can only move parallel to the tube direction and, as such, the relaxation time is equal to the time necessary for the chain to slip through the tube. This is known as the reptation time, τ_d and is represented by:

$$\tau_d = \frac{\xi N^3 b^4}{3\pi^2 k_B T a^2} \qquad 2.22$$

with all terms as defined previously and *a* as the tube diameter.

2.5.7 Measurement Conditions

Amplitude and frequency sweeps were performed using a TA instruments AR-G2 rheometer fitted with a high temperature furnace and 8 mm parallel steel plates.[52] Prior to all measurements, zeroing of the fixture-plate gap and normal force was performed at the measurement temperature to ensure that the measured response was a product of the sample and not a machine artefact. All measurements and subsequent data analysis were performed using TA instruments *Rheology Advantage* and *Data Analysis* software systems respectively.

In all measurements, the following preliminary preparation steps were undertaken. The sample was heated to the required measurement temperature (under nitrogen flow to prevent oxidative thermal decomposition[75,76]) and the rheometer fixture lowered to a gap of 500 μm. Excess material was trimmed and a relaxation period applied in order for the chains to relax and the normal force to reduce to zero prior to starting measurements. Sample trimming was a necessary and important step to prevent errors in the measurements: overfilling, resulting in excess melt outside of the tool, causes an addition to the torque signal;[77] underfilling, resulting

in incomplete filling of the fixture-plate gap, causes a large error similar to edge fracture instability ('edge effects') at the fluid-air interface.[6,78,79]

Amplitude (% strain) oscillation sweeps were first performed to determine the LVR, the area in which the material responds linearly to the magnitudes of stress and strain over time.[4,80] Measurements were performed at angular frequencies 0.06283 rad s^{-1}, 6.283 rad s^{-1}, 62.83 rad s^{-1}, 100 rad $s^{-1}$and 628.3 rad $s^{-1}$and across the range of percentage oscillation strains 0.01 – 100 %, repeated in duplicate. Each suite of measurements was performed at temperatures of 150, 170 and 190 °C in order to understand the material rheological response across a range of strains and temperatures. A strain of 1 % fell within the LVR and was used for further measurements.

Frequency oscillation sweeps were carried out at 1 % strain, between 100 – 0.06283 rad s^{-1} and at temperatures of 150 – 200 °C. At least three viscosity curves were measured at different temperatures and merged to create a mastercurve by means of the TTS using TA instruments *Trios* software. The viscosity curve at the temperature of interest (130 °C) was then calculated by shifting the mastercurve using TTS coefficients and fitted with the empirical Cross model to obtain the shear rate-dependence of the viscosity, $\eta(\dot{\gamma})$.[3,6,52,81]

2.6 Sample Preparation via Couette Cell Shearing

A custom-built co-axial cylinder (Couette) shearing cell was used, consisting of an inner rotating cylinder (rotor) and stationary outer cylinder (stator), to obtain large samples with homogeneously-distributed oriented morphology for mechanical testing and permeation measurements.

The most significant aspect of this apparatus was the unique design of the stator, such that it was assembled of four equal segments comprising a circle (Figure 2.14, image b). This allowed the outer stator to be disassembled and removed and the crystallised material to be recovered for further measurements. The main body of the cell was constructed from stainless steel and the stator and rotor from brass to exploit the strength and heat conductive properties of the metal and alloy respectively. A bearing system was installed between the rotor and shaft coupling to reduce friction and ensure free rotation around a fixed axis.

The cell (Figure 2.13 and 2.14) was connected via steel shafts (diameter 10 mm) and a rigid shaft coupling (Ruland, 45 mm length, 29 mm outer diameter, 10 mm inner diameter) to an inline spur gear reducer (Ondrives NH92-20, 15mm output shaft, 17 - 40 Nm output torque,

ratio 20:1) and high torque stepper motor (Pacific Scientific, T23NRHK-LDF-C5-00) with closed loop encoder (Pacific Scientific, PD2406-DI-001E) programmed from a computer through *ToolPac* software. A 90 L oven with CAL 3300 PID temperature controller and i-Autoc KSIM series single phase AC output solid state relay was used to heat the sample.

The whole cell was located within a natural convection oven, with the gearbox and motor assembly fixed atop the oven. Steel shafts connecting the motor and cell ran through an opening in the oven roof. 12 Nm of torque was required to initiate rotation of the shaft, as measured by a manual torque wrench, however the torque from the motor output alone was 2.68 Nm and thus insufficient to initiate rotation of the cell. Therefore, a gearbox was installed to increase the torque output to 29.5 Nm.

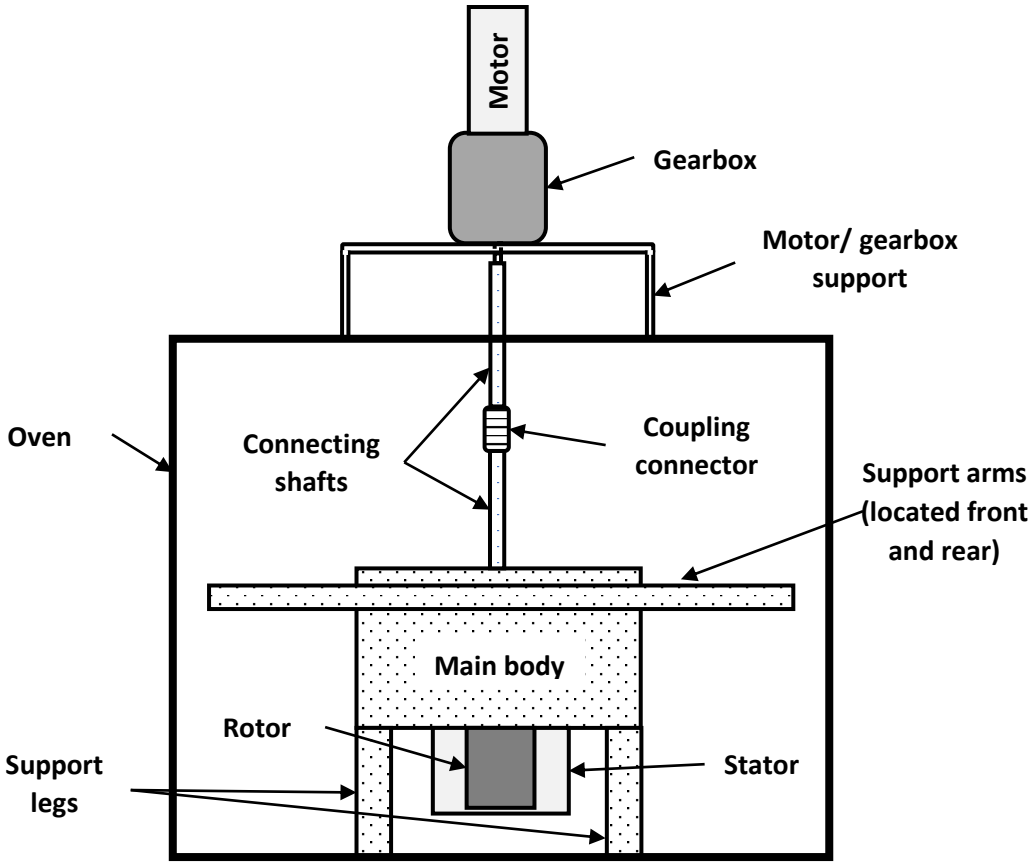

Figure 2.13: A schematic of the novel Couette cell used to obtain large samples with homogeneously-distributed oriented morphology for mechanical testing and permeation measurements.

Samples of 60 mm x 160 mm were cut and clamped around the rotor by the stator with a sample gap of 0.5 mm (Figure 2.14). The cell was heated in the oven to 150 °C, briefly removed to tighten all bolts and fixings and placed back into the oven for 30 minutes to achieve thermal

equilibrium. The oven was subsequently cooled to 130 °C and a shear pulse applied by the external motor and gear reduction assembly, fitted atop the oven. The motor and cell were disconnected, removed from the oven and submerged in a large cold-water bath to complete the crystallisation. The stator was disassembled and the sample removed.

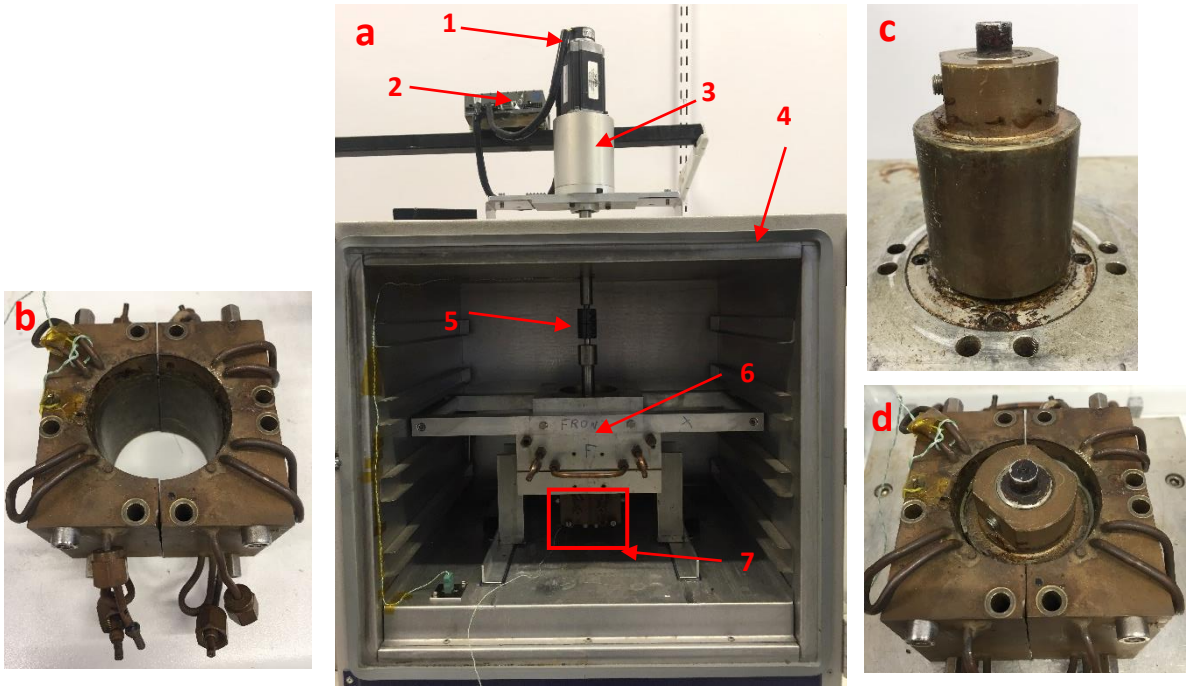

Figure 2.14: Images of the Couette cell: a) whole assembly; b) stator cylinder, the stator is composed of four equal quadrants to remove the sample; c) rotor cylinder; d) rotor and stator with crystallised HDPE present in the sample gap. The numbers correspond to: 1) motor, 2) control box, 3) gearbox, 4) oven, 5) shaft coupling, 6) main body (bearing housing), 7) stator and rotor assembly (also in images b-d).

2.7 Shear-Induced Polarised Light Imaging of PE disks

2.7.1 Background & Theory

Polarised light imaging is a valuable tool to study the oriented morphology of polymers by observing the retardation of incident light caused by the birefringence of oriented molecular chains.[52,82] Birefringence has been shown to be directly proportional to stress and, therefore, is a valuable yet non-invasive method of measuring flow fields and the stresses generated during shear.[3,83] In particular, flow birefringence techniques have become an essential tool in understanding polymer fluid dynamics. By subjecting a polymeric liquid to an external flow field, the applied stress causes the refractive index to display anisotropy, thus connecting fluid

motion and structural response.[82] Upon interaction with a birefringent object, the incident light is separated into two rays: ordinary and extraordinary. By using the refractive indices corresponding to each ray, n_1 (ordinary) and n_2 (extraordinary) the retardation of incident light can be quantified as:

$$R = h(n_1 - n_2) \qquad 2.23$$

where R = retardation, h = sample thickness.[52]

Typically, to obtain polarised light images (PLIs), a sample is placed between 90° crossed polariser and analyser with a white light source and images acquired through a CCD or CMOS camera (Figure 2.15). If the sample is birefringent and the light is linearly polarized by a polariser, then the refracted light emerges with an altered polarisation due to a phase shift by the different refractive indices of ordinary and extraordinary components of the incident light. This altered polarisation allows the light to pass through the analyser crossed with the polariser at 90° to give a PLI containing sample structural information. Non-birefringent samples generate a dark image because the light retains its incident polarisation, therefore it cannot pass through the "crossed" analyser.[82,84]

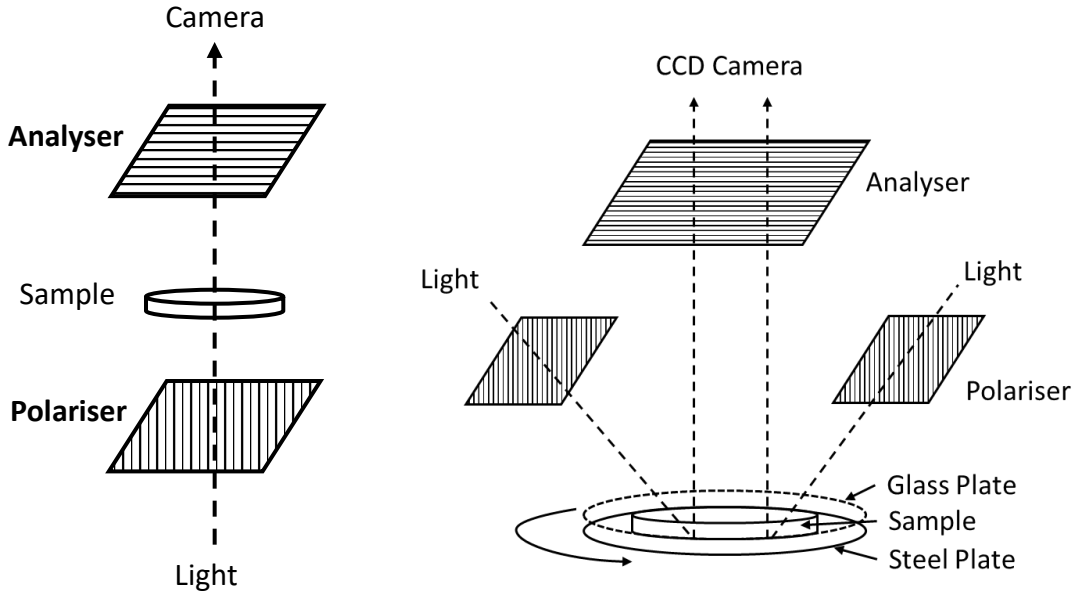

Figure 2.15: Optical arrangements of PLI acquisition. Left: basic method; Right: In-situ method. The hatched lines give an approximation of the polariser directions.

An advance to this technique developed by Mykhaylyk is the acquisition of *in-situ* images, typically under shear (Figure 2.16), and is known as shear-induced polarised light imaging (SIPLI).[82] Coupling the basic technique with torsional parallel plates produces a shear rate

distribution across the sample and therefore a direct insight into the shear process. Another major advantage of this technique is the ability to perform time-resolved experiments and track the formation of oriented nuclei and subsequent crystallisation during shear-induced crystallisation (SIC).[82]

A common feature of any PLI, regardless of the method to obtain it, is the Maltese cross (arising from the circumferentially aligned birefringence axis) which is indicative of oriented morphology.[82,84] The interaction of light with a medium causes electrons to be displaced. This electron charge displacement, **P**, is generally not parallel with the electric field vector, **E**, due to the anisotropy of electron clouds. The greater the interaction between the light wave and the medium, the greater the refractive index, *n*, and the smaller the wavelength, λ. Refractive index can be defined by:

$$n_1 sin\theta_1 = n_2 sin\theta_2 \qquad 2.24$$

where *n* is the refractive index of the medium and θ is the angle of the propagating light wave measured from the normal of the boundary.[6] All transparent, non-cubic crystals are birefringent because the polarisation caused by a light ray depends on the **E** vector direction, which is perpendicular to the propagation direction. An important consequence of this is that the polarisation state of an incident ray is changed upon interaction with the medium, thus forming the basis for polarised light microscopy.[85]

Consider a polymer chain as an optical indicatrix, the imaginary surface of which can be described by the refractive indices of light rays propagating in different directions.[84] Viscoelastic liquids, under quiescent conditions, are optically isotropic - they form a spherical indicatrix caused by light rays propagating equally in all directions.[82,84,85] Under the influence of shearing, stretching, deformation and/or orientation, this spherical indicatrix is stretched into an ellipsoidal indicatrix, which is associated with birefringence. The refractive indices become uniaxially oriented along the direction of flow, with its semi-axis length proportional to the principal refractive indices (Figure 2.16).[84]

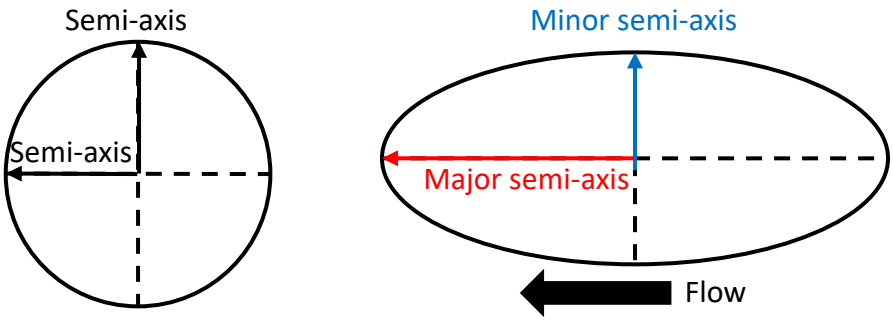

Figure 2.16: 2D representations of the optical indicatrix of a polymer chain under no flow (left) and flow (right). The semi-axes are equal in the case of no flow, however major and minor semi-axes arise under flow. The major semi-axis is in the flow direction.[86]

Zero birefringence, and hence a dark field image, is obtained when the sample is isotropic or if the crystal is viewed along its optic axis.[85] Rotating the sample has no effect as the indicatrix is spherical. Alternating dark and light segments are observed when crystal orientation is such that the projected indicatrix is a major ellipse. The dark regions are the result of either principal indicatrix axis coinciding with the vector of the propagating ray.[85] Crystals within a spherulite have a common radially-pointing crystallographic direction, thus setting the indicatrix pattern. Two examples are presented (Figure 2.17) where the principal indicatrix axis is tangential or radial to the incident ray. Considering the direction of the incident ray to be vertical, the region appears dark as E is parallel to a semi-axis and therefore transmitted rays have the same field direction and are thus blocked by the analyser.[85]

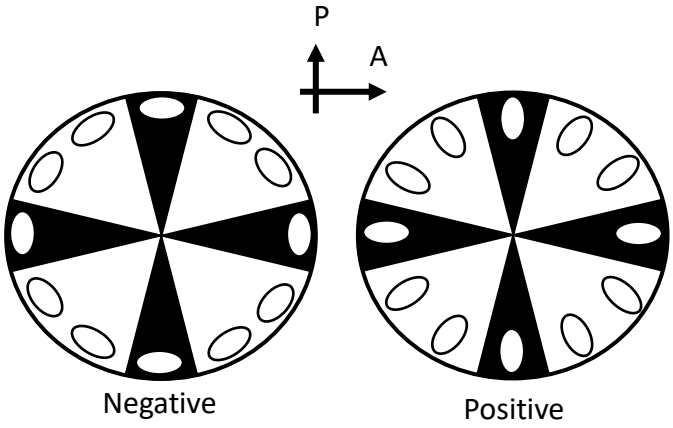

Figure 2.17: Maltese cross patterns observed from negatively and positively birefringent spherulites. The indicatrix has the largest semi-axis in the tangential direction for negative spherulites, while the largest semi-axis is radial in a positive spherulite. Rotating the spherulite about the viewing direction or by interchanging the directions of polarizer (P) and analyser (A), does not change the pattern.[85]

2.7.2 Measurement Conditions

Two methods of gathering *in-situ* PLIs were used to observe the formation of oriented morphology in polymer melts.

2.7.2.1 Linkam CSS450 Shear Cell

This setup can be described as a torsional parallel plate shear device coupled to a reflection polariscope, with a key feature being the use of reflected light to gather PLIs. A Linkam CSS450 shear cell was modified by attaching an external high torque stepper motor (Pacific Scientific, T23NRHK-LDF-C5-00) and closed loop encoder (Pacific Scientific, PD2406-DI-001E) programmed from a computer. A fixed glass top plate was used as a viewing window and a polished steel rotating bottom plate was used both to shear the sample and act as a mirror for the polarised light (Figure 2.18). Mounted coaxially was a polariscope setup: StockerYale Model 21AC quartz halogen white light source attached to a fibre optic ring light guide, two linear polarisers (a ring-shaped polariser and disk-shaped analyser) and CMOS camera (IDS GmbH, UI-3860CP-C-HQ Rev.2, Sony IMX290 CMOS Colour Sensor, 1945x1097 Pixel) with a lens (17.6 mm focal length, Xenoplan 1.4/17-0903). The disk-shaped analyser could be rotated through 360° allowing for a 90° crossed polariser-analyser setup. An additional heat source, supplied by an electronic temperature-programmable heat gun (Steinel HG2320E) supplied additional heating alongside the bottom heater of the shear device to compensate for heat loss (due to the removal and replacement of the top heater plate with a glass plate) and maintain the required temperature within the sample. All heating, cooling, and gap setting was performed using *LinkSys* software and all shearing through *ToolPac* software. Image capture was performed using *uEye Cockpit* software.[82]

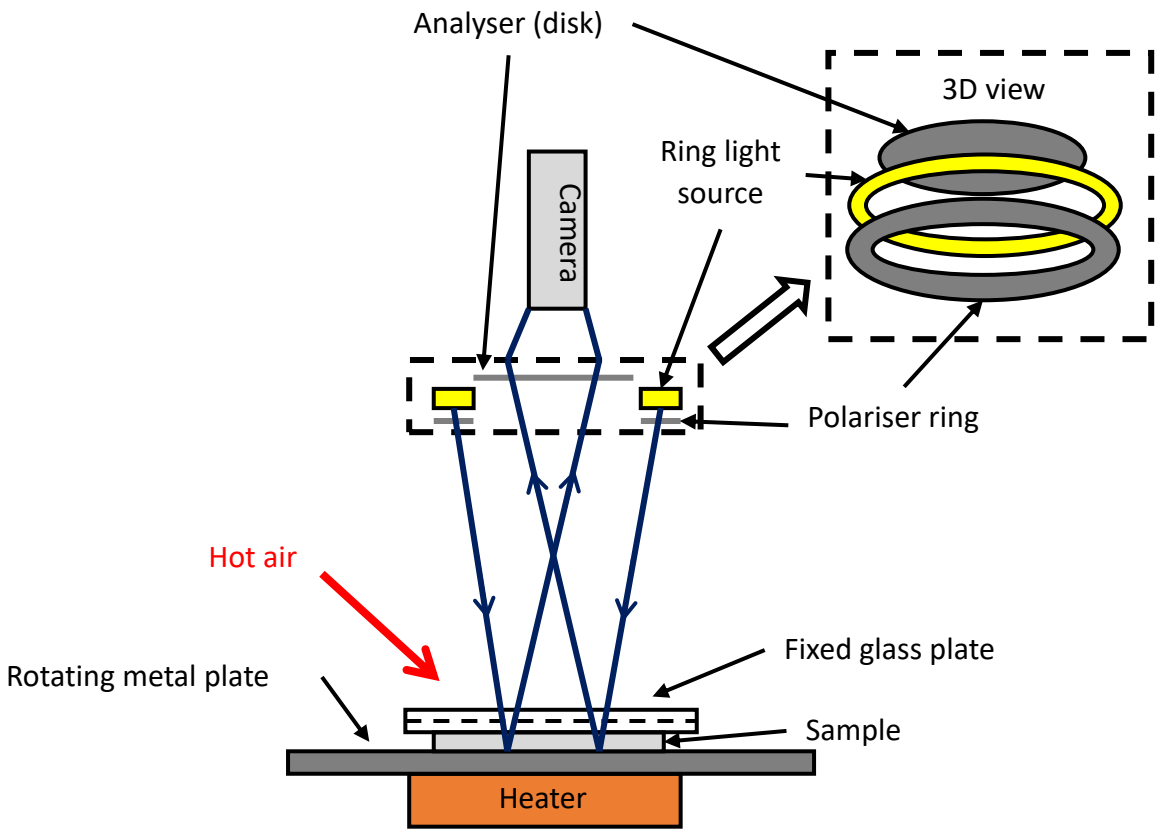

Figure 2.18: A schematic of the Linkam CSS450 shear cell with coaxially mounted polariscope setup. The inset figure (dashed lines) shows the polarisation setup consisting of polariser ring, ring light and analyser disk. Blue lines with arrows indicate the light path from the source, reflected back through the sample to the analyser and camera.[82]

Pre-cut 16 mm diameter PE disks were placed inside the shear device and heated at 10 °C min^{-1} to 150 °C and held isothermally for 10 minutes. The sample was cooled to 130 °C at 1 °C min^{-1} and held for 5 minutes, during which time a shear pulse was applied with simultaneous video capture using a CMOS camera. The sample was subsequently cooled at 20 °C min^{-1} to room temperature and removed (Figure 2.19).

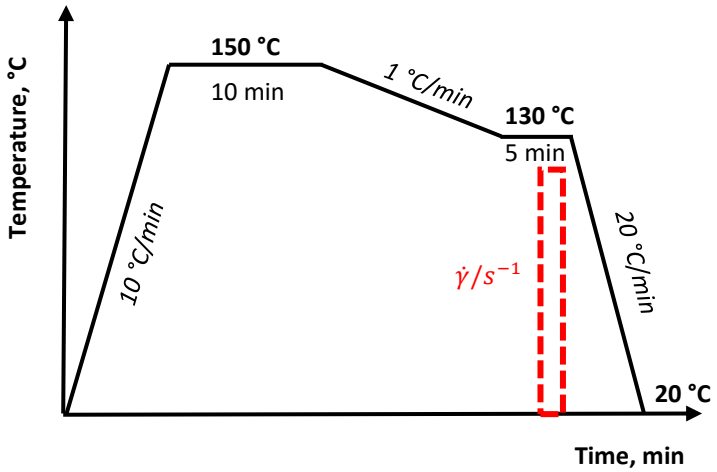

Figure 2.19: The temperature-shear protocol for SIPLI using a Linkam CSS450 shear cell. An initial heating step to 150 °C at 10 °C min^{-1} was followed by a 10-minute isothermal hold to erase thermal history. Cooling at 1 °C min^{-1} to the shear temperature of 130 °C, with a 5-minute isothermal hold, during which time a shear pulse was applied. The final cooling step to room temperature occurred at 20 °C min^{-1}.

2.7.2.2 SIPLI Rheometer

A 25 mm diameter disk of PE was placed between parallel plates of a modified Anton Paar MCR301 mechano-optical rheometer (Figure 2.20) connected to a variable temperature Peltier system, with Peltier hood for better temperature control. The modifications allowed for in-situ image capture of shear-induced PLIs. A rotating, polished steel parallel plate fixture was used to shear the sample and act as a mirror for the reflected polarised light. A transparent, fused quartz bottom plate was used as viewing window to allow polarised light to pass through the sample and record an image on the camera below. The parallel plate fixture was highly polished with diamond paste to create a reflective surface with a surface roughness of approximately 1 μm, which was comparable with the wavelength of light but larger than the radius of gyration of polymer chains.[84]

The optics consisted of an Edmund Optics 150 W MI-150 high intensity fibre optic white light source as the incident light, polariser and analyser disks "crossed" 90° with a colour CCD camera (Lumenera Lu165c) to capture the images. Images were acquired every 500 ms for the duration of the experiment using software supplied with the camera. The optical path can be described as follows. Light rays from the source are plane-polarised upon passing through the polariser, reflected off the beam splitter up into the sample at an angle perpendicular to the sample surface. The light is then reflected by the highly polished fixture back through the sample (thus creating a double pass through the sample and glass disk), through the beam

splitter and analyser before reaching the camera. The state of polarisation does not change upon reflection by the mirror, only the sample.[84]

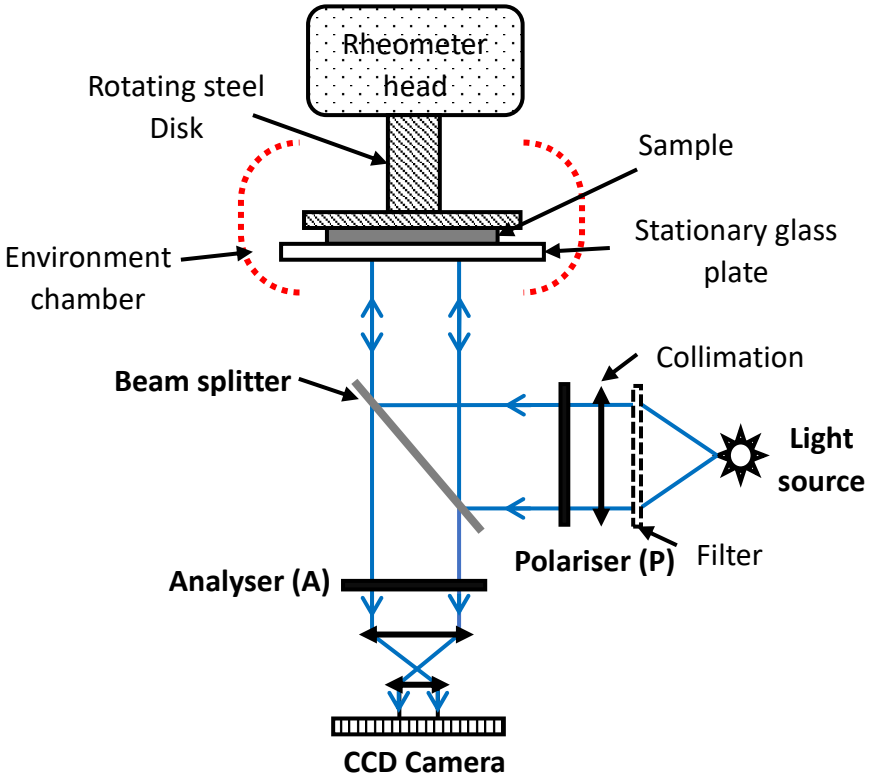

Figure 2.20: A schematic of the mechano-optical rheometer setup used for simultaneous rheology and SIPLI measurements. The main components of the optical setup are written in bold text with the blue arrows representing the light path.[84]

The sample was heated to 150 °C and a gap of 0.5 mm was selected. After sample trimming and sufficient time had elapsed to allow for the material normal stresses to reach as close to zero as possible (after 1 hour the normal forces had decreased to 10^{-2} – 10^{-3} Pa and after 2 hours, the normal forces had not reduced further which indicated a limit of relaxation), the sample was cooled to 130 °C. After 5 minutes, a continuous shear pulse was applied (using a range between $\dot{\gamma}$ = 0.5 - 10 s^{-1}; t_s = 10 - 30 s), after which the sample was cooled to room temperature and removed.

2.8 Linkam CSS450 Shear Experiments for *ex-situ* SAXS

A modified Linkam CSS450 shear cell (as described in Section 2.7.2.1) was used to shear samples. The samples were also to be unloaded from the cell after completion of the temperature-shear protocol, thus requiring rigid fixtures, and so the original glass plates were substituted for steel and the heating performance of the device was appropriately calibrated.

Controlled heating was supplied by silver heating blocks located in both upper and lower plates and controlled cooling by an external liquid nitrogen cylinder and pump assembly. All heating, cooling, and gap setting was performed using *LinkSys* software and all shearing through *ToolPac* software.

Pre-cut 16 mm diameter PE disks of 0.55 mm thickness were placed between the plates of the device and a temperature-shear protocol analogous to that used for SIPLI measurements (Section 2.7.2.2) was applied.

2.9 Small-Angle X-Ray Scattering of Sheared PE disks

2.9.1 SAXS Instrumentation

SAXS is a technique widely used to study structural features on a sub-micrometre scale.[87] Normally a sample is exposed to an X-ray beam in transmission mode and any particles or features within the beam scatter X-rays and are recorded by a detector. Thus, SAXS displays the averaged structure of selected particles within the bulk material.[88]

The basic components of any SAXS instrument are largely the same: source, monochromator/X-ray mirror, collimator, sample holder, beam stop and detector (Figure 2.21). X-rays are generated by the source and propagate towards the sample and, upon interaction with the electrons in the sample, scattered waves carrying information about the structural morphology of the material are produced. All components of the setup are held under vacuum to prevent unwanted scattering from the air.

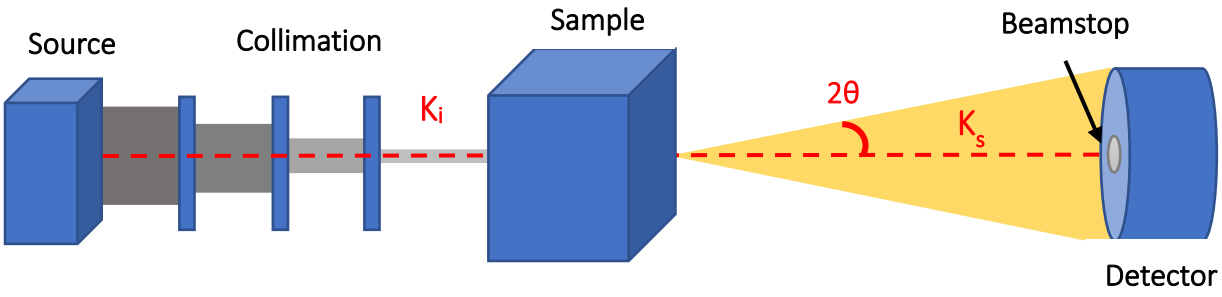

Figure 2.21: A typical setup for a SAXS measurement. K_i is the incident X-ray beam and K_s is the scattered beam.

2.9.2 Basic Scattering Theory

X-rays are electromagnetic radiation with a wavelength of 10^{-2} – 10^{2} Å on the electromagnetic spectrum. Typically, a wavelength range of 0.5 – 2.5 Å[89] is used because the X-ray wavelength

is comparable to interatomic bond distances and is ideal for structural characterisation.[87] Polymer studies can be performed using a copper anode tube, characteristic Kα radiation of 1.54 Å, or a gallium liquid metal jet anode, λ = 1.34 Å.

When X-rays interact with matter, both scattering and absorption processes occur. The majority of the radiation is simply transmitted.[88] Electrons within the irradiated sample scatter incoming waves of radiation, the intensity of which is measured by the detector. Two types of scattering can occur: elastic and inelastic scattering (Figure 2.22). Elastic scattering (Rayleigh or Thompson scattering) results in no energy transfer from the wave to the particle and occurs during SAXS. Inelastic scattering (or Compton scattering) occurs when energy is transferred to the particle, thus reducing the energy of the scattered wave accordingly.

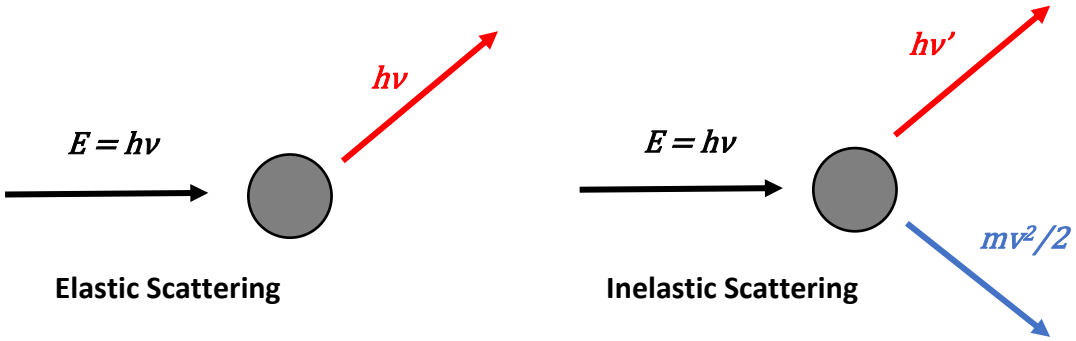

Figure 2.22: Scattering from a particle can be elastic (left) or inelastic (right). Elastic scattering occurs when X-rays interact with particles.

Scattering methods can provide information about structure and morphology, movement and molecular mass.[88] However, the result of any scattering experiment will be ambiguous and, as such, prior knowledge of the sample (an approximate idea of the structure or microscopy images) is necessary to assist with analysis.[88] Commonly, if a studied sample is isotropic, the scattering pattern is the averaged result of all material in the sample, therefore the recorded two-dimensional (2D) scattering data are reduced to one-dimensional (1D) patterns. The resulting 1D curve can be fitted with various models and thus the size, shape and ordering of objects within the sample can be elucidated.

Important to any scattering experiment is the magnitude and direction by which waves are scattered, called the scattering vector, *q*, which can be derived from scattering angles (Figure 2.23 and Eqs. 2.25 – 2.27). The dimensions are the reciprocal of length, hence scattering patterns show structures in reciprocal space. Particles obviously have real structures with real

dimensions and are said to exist in real space.[88] Since elastic scattering is occurring, k and k_0 have the same magnitude.

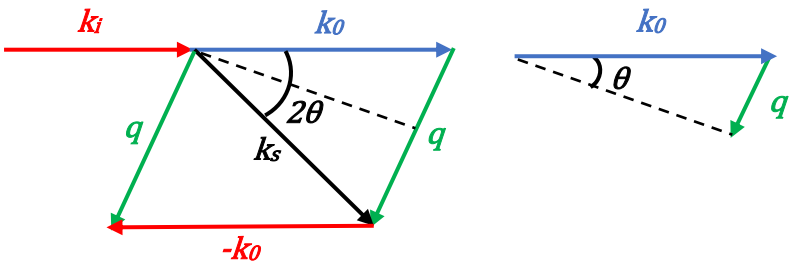

$$|k_0| = |k_s| = \frac{2\pi}{\lambda} \qquad 2.25$$

$$q = k_s - k_0 \qquad 2.26$$

$$|q| = \frac{4\pi}{\lambda}\sin\theta \qquad 2.27$$

Figure 2.23: Schematic diagram of the interaction of an electron with incident X-rays. The vector k_i represents the incoming X-rays, k_0 represents the non-scattered X-rays, k_s represents the scattered X-rays, q represents the scattering vector and θ is one-half of the scattering angle.

2.9.3 Structure Determination

Correlation Function analysis (Figure 2.24) is commonly applied to semi-crystalline polymers exhibiting a two-phase (crystalline and amorphous) structure, assuming a lamellar morphology (see Section 1.4.1, Figure 1.10).[90]

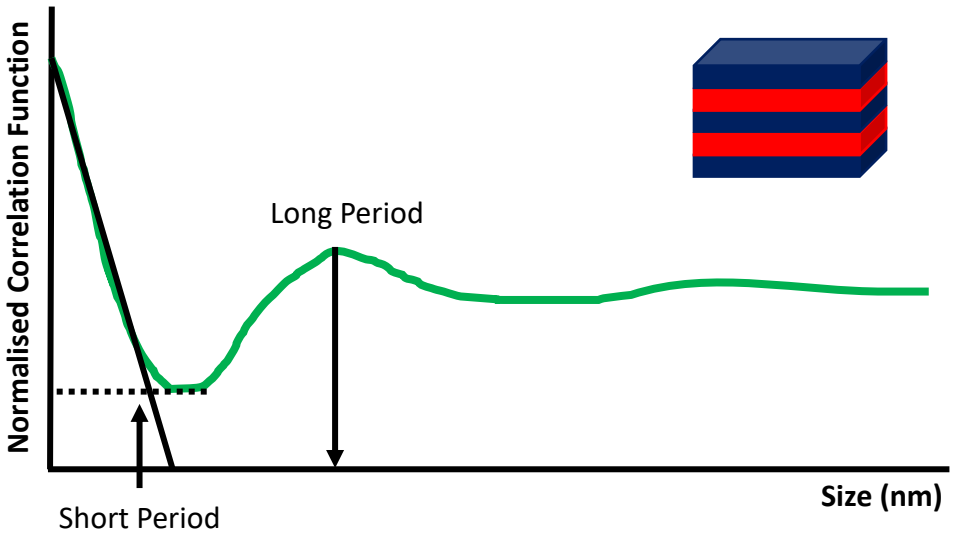

Figure 2.24: An example sketch of a correlation function of the electron density in a semi-crystalline lamellae morphology, as a function of size. Analysis of this correlation function provides information regarding the short and long-periods of the lamellae morphology.

From the correlation function, information such as crystallinity, average lamellae thickness, long spacing and, if absolute scattering intensities are measured, the difference in electron

density between amorphous and crystalline regions.[90] The main assumption is that scattering is due to a linear arrangement of lamellae stacks with sharp boundaries between the phases.[90] In reality, they consist of folded chains and a small transition region between the crystalline and amorphous domains.[91] In addition, a range of lamellae thicknesses are possible resulting in broad SAXS peaks.[90,91]

The position of the diffraction peak maximum is related to the lamellae d-spacing (the distance between planes of atoms that give rise to diffraction peaks[92]) with a larger d-spacing appearing at smaller scattering angles. To gather further information from the scattering, an electron density correlation function can be obtained by subjecting the scattering function to a Fourier transformation.[91]

2.9.4 Data Analysis

The relative electron density distributions determine how strongly or weakly a particular object will scatter. Weakly scattering objects, such as dilute polymer solutions, will require much longer exposure times compared to stronger scatterers, such as polymer films. The amount of data in a 2D scattering pattern (Figure 2.25) can be reduced by averaging to give a 1D pattern. Typically, averages are either linear (box average) or circular (pie and arc average) depending on the investigation and instrument type.[88] For assessing the degree of orientation in a sample, an arc average, termed azimuthal integration, is performed around the 2D scattering pattern with its centre at the direct x-ray beam position. Partially oriented artefacts, such as fibres and sheared solutions, are identified by an intensity spike in the azimuthal profile. From such an integration, it is also possible to identify isotropic and crystalline samples.

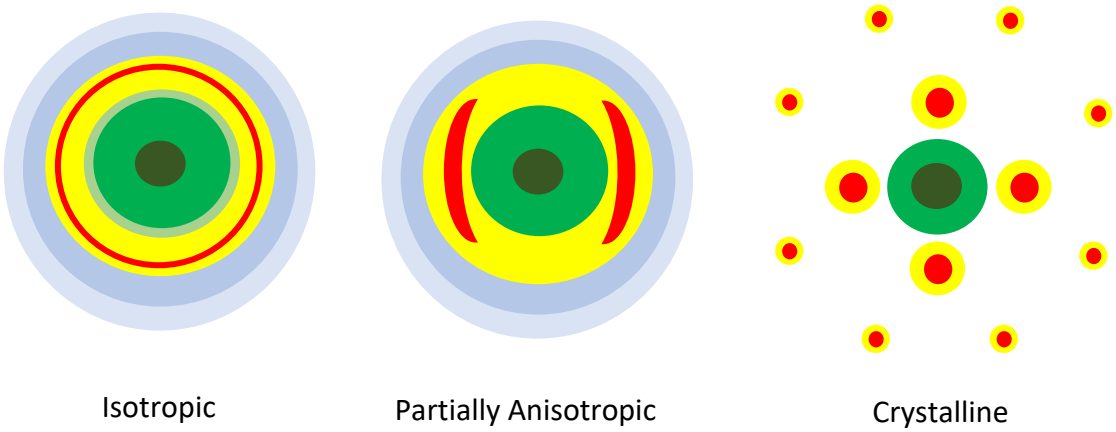

Figure 2.25: Representative 2D SAXS patterns resulting from different degrees of orientation within a sample.[88]

2.9.5 Measurement Conditions

Throughout this work, SAXS patterns were collected using laboratory instruments. A Bruker AXS NanoStar (equipped with a 2D Hi-STAR multi-wire gas detector and modified with Xenocs GeniX 3D X-ray source [CuKα radiation, X-ray wavelength λ = 1.54 Å] and motorised collimating scatterless slits) was used at a sample-detector distance of 147 cm. Samples of sheared PE disks (16 mm diameter) were mounted normal to the X-ray beam and fixed in place with Kapton tape at the edges. Once the edges of the sample had been identified, the disk was scanned at 0.5 mm intervals for acquisitions of 120 seconds each.

All data collection was performed using software supplied with the instrumentation. 1D scattering curves were obtained by an azimuthal integration of the 2D scattering patterns using Irena SAS and Nika SAS2D macros for Igor Pro.[93,94] Further data analysis to quantify the degree of orientation was applied through a custom-written program (by O. Mykhaylyk). The obtained azimuthal intensity distribution patterns, $I(\phi)$, (ϕ is the azimuthal angle) were used to calculate Herman's Orientation Function (P_2), defined as:

$$P_2 = \frac{3\langle cos^2\phi\rangle - 1}{2} \qquad 2.28$$

where

$$\langle cos^2\phi\rangle = \frac{\int_0^{\pi/2} I(\phi) cos^2\phi \; sin\phi \; d\phi}{\int_0^{\pi/2} I(\phi) \; sin\phi \; d\phi} \qquad 2.29$$

is the average angle that the polymer chain axis (lamellae normal) makes with a chosen direction, which in this case is associated with the deformation direction.[8]

2.10 Preparation of Single-Polymer Composites via MeltPrep VCM

2.10.1 MeltPrep VCM Apparatus

MeltPrep™ is a commercial vacuum compression moulding (VCM) apparatus for making homogeneous, defect-free samples from powder or pellet starting materials (Figure 2.26). Common applications include sample preparation for rheology, tensile/extensional testing, shear experiments and DSC. In this work it was used to fabricate SPC samples in both disk and bar configurations.

The apparatus consists of a heating plate, cooling plate, VCM tool and vacuum pump with a four-way manifold controlled by sliding valves. Two manifold valves are for the heating and cooling plates and two for sample tools. Both heating and cooling plates have been modified to accommodate a Viton O-ring and small aperture to draw a vacuum to hold the sample tool securely in place and maintain consistent thermal contact across all sample preparations. A supply of compressed air is fed in a ring around the sample tool to cool it (Figure 2.26).

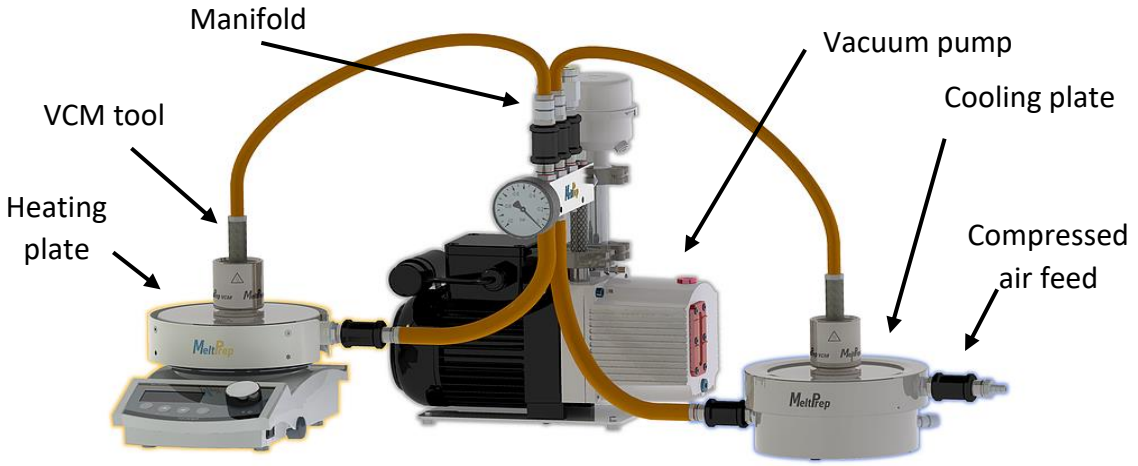

Figure 2.26: A photograph of the MeltPrep vacuum compression moulding (VCM) apparatus used for the fabrication of single-polymer composite samples. ©MeltPrep GmbH

The VCM sample tool (Figures 2.27 and 2.28) consists of a base plate, sample chamber (known as the VCM insert), outer jacket and lid with a vacuum outlet. The VCM insert consists of a base plate, PTFE separation foils, VCM chamber and piston. This also has Viton O-rings located on the VCM chamber, outer jacket and lid to ensure a tight vacuum seal.

Figure 2.27: Photographs of the 25 mm diameter VCM tool (left and top) supplied with the MeltPrep apparatus consisting of a lid, outer jacket and VCM chamber. The bottom image shows the 10 mm x 40 mm bar tool. ©MeltPrep GmbH

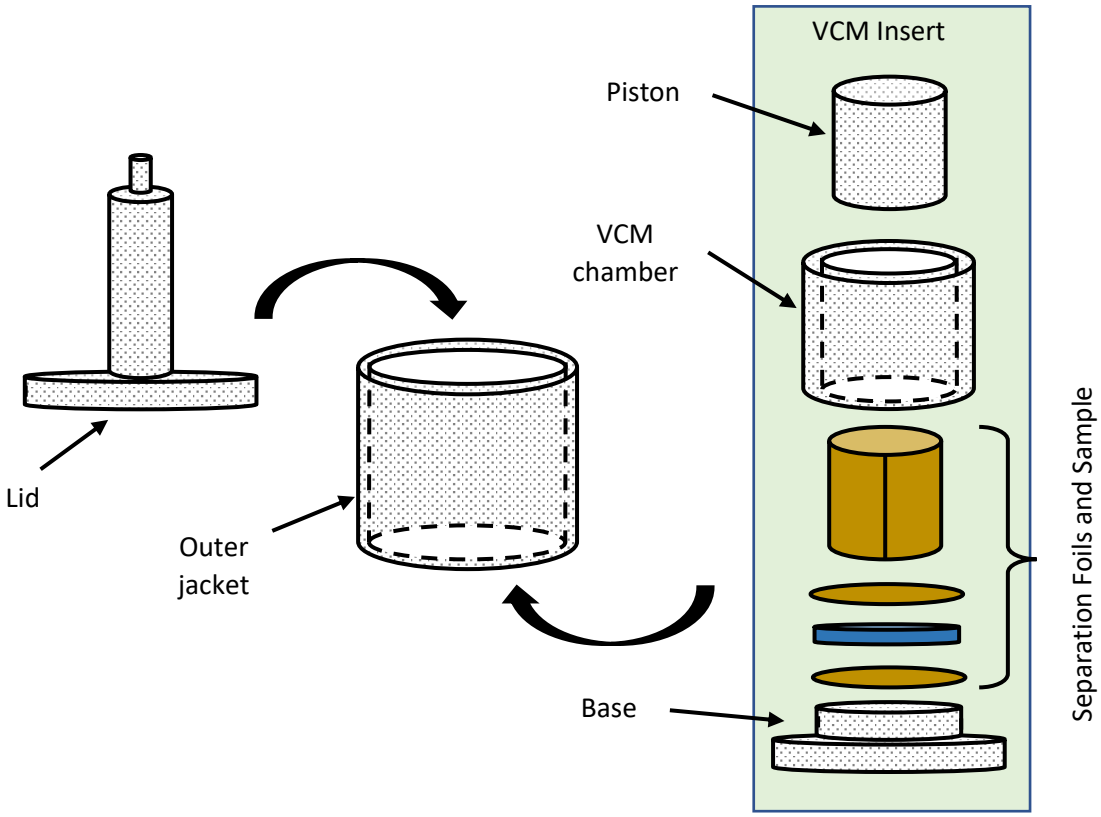

Figure 2.28: A schematic of the VCM tool supplied with the MeltPrep apparatus. The exploded view details the inner components of the VCM tool insert showing the layering of the separation foils and sample. Viton O-rings have been omitted for clarity.

A number of tool dimensions are available in various disk diameters, and for this work the 25 mm diameter disk tool and 10 mm x 40 mm bar tool were selected (Figure 2.27). To ensure that any sample residue did not stick to the chamber walls, polytetrafluorethylene (PTFE) foils were placed on the bottom and top of the sample and also wrapped around the VCM chamber (Figures 2.28 and 2.29), which could be easily removed from the sample upon unloading.

Figure 2.29: PTFE separation foils used to encase the sample within the MeltPrep VCM tool to prevent any sample material sticking to the chamber walls and thus allowing for easy sample removal. ©MeltPrep GmbH

2.10.2 Preparation Conditions

The versatility of the MeltPrep system is that any sample thickness can be prepared with knowledge of the density of the material and the volume of the tool sample chamber. As the radius of the tool is fixed, and the required sample thickness is known, the volume of the sample

can be determined. Then, by exploiting the relationship between volume, density and mass, the mass of required starting material can be determined. For this work, HDPE disks of 0.5 mm thickness and 25 mm diameter were required. Therefore, the volume of the 25 mm diameter sample was:

$$V_{cyclinder} = \pi r^2 h = \pi([12.5\ mm]^2 \text{ x } 0.50\ mm) = 245.44\ mm^3 \qquad 2.30$$

where r = cylinder radius (mm) and h = height (mm).

Assuming a density of 0.931 g cm^{-3} (9.31 x 10^{-4} g mm^{-3}), the mass of HDPE required was:

$$M = V\rho = (245.44\ mm^3 \text{ x } [9.31 \text{ x } 10^{-4} g\ mm^{-3}]) = 0.2285\ g \qquad 2.31$$

where M = mass (g), V = volume (mm^3) and ρ = density (g mm^{-3}).

HDPE bar samples, with dimensions 10 mm x 40 mm, were also required. In this instance, the volume of the rectangular sample was first determined before applying the density-volume-mass relationship as before:

$$V_{bar} = (l \times w \times h) = (40\ mm \times 10\ mm \times 0.5\ mm) = 200.00\ mm^3 \qquad 2.32$$

where l = bar length (mm), w = bar width (mm) and h = height (mm).

Assuming a density of 0.931 g cm^{-3} (9.31 x 10^{-4} g mm^{-3}), the mass of HDPE required was:

$$M = V\rho = (200.00\ mm^3 \text{ x } [9.31 \text{ x } 10^{-4} g\ mm^{-3}]) = 0.1862\ g \qquad 2.33$$

with all terms as defined previously.

For preparation of the HDPE disks, the hot plate was set to 195 °C. The HDPE pellets were weighed and loaded into the sample chamber, along with PTFE foils; the tool was assembled and a vacuum applied. The tool was placed onto the hot plate and the vacuum ring engaged to secure it. Once the sample temperature was 195 °C (as measured by a thermocouple), the tool was kept in place for 5 minutes to ensure homogeneous melting. After the elapsed time, the VCM tool was transferred to the cooling ring and compressed air applied to the base. Once at room temperature, the tool was disassembled and the sample removed.

For preparation of SPCs, careful temperature control was required. The optimum temperature window was determined by DSC to be 136 – 144 °C and a hot plate temperature of 140 °C was chosen. As before, the sample was loaded into the chamber, the tool assembled and placed on the hot plate. Once at temperature, the tool was left for 10 minutes to allow complete melting

of the necessary components. Attempts with just 5 minutes resulted in non-uniform melting and/or delamination. After 10 minutes, the tool was transferred to the cooling ring until at room temperature.

2.11 Permeation Testing of Polymer Films

2.11.1 Permeation Theory

In order to understand the permeation of fuel vapour (typically low molecular weight species) through a polymer, both solution and diffusion mechanisms need to be considered. In a typical cup-based permeation test, each face of the polymer sample encounters different atmospheres – the upstream side facing the solvent reservoir, and the downstream side open to the atmosphere (Figure 2.30).

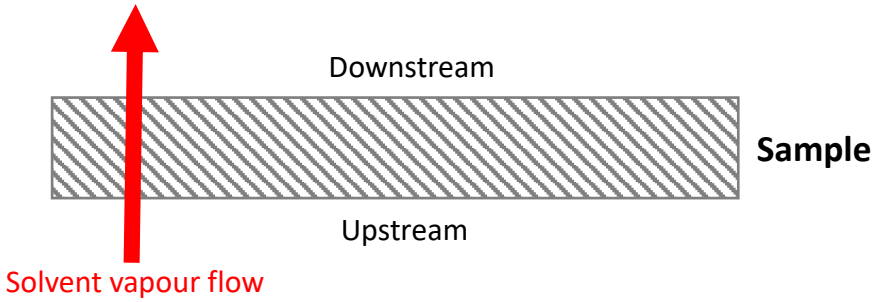

Figure 2.30: The two faces of a sample under permeation testing experience different atmospheres. The upstream side faces the solvent reservoir and the downstream side faces the open atmosphere. A permeant solvent molecule must first dissolve into the upstream side, diffuse through the sample and then evaporate from the downstream side into the atmosphere.

For effective permeation, a solvent molecule must first dissolve into the upstream face of the polymer. From there, it must diffuse through the solid bulk to the downstream face where it is free to evaporate back into the atmosphere.[95] Once this dissolution, diffusion and evaporation has occurred, the sample is said to be in a steady state of permeation. Hence, thicker samples under testing require longer measurement times in order to reach this steady state – the diffusion through the sample is the rate-limiting step.[20,96] This primary mechanism of vapour flow, in a defect-free polymer film, is called activated diffusion, driven by a concentration gradient experienced by the opposing film surfaces.[97]

This solution-diffusion mechanism can be described in terms of permeability (P), solubility (S) and diffusion (D); their relationship can be expressed as:

$$P = D \times S \qquad 2.34$$

The diffusion coefficient, *D*, is a kinetic term that describes the molecular mobility of a solute through the polymer phase, also known as the flux.[96] It can generally be determined by Fick's first law of diffusion[98] (the flux of the permeate is proportional to the local concentration gradient) and describes the ability of a solvent molecule (permeate) to move along the polymer segments:

$$J_x = -D\left(\frac{\partial c}{\partial x}\right) \qquad 2.35$$

where J_x is the flux in the x-direction, *D* is the diffusion coefficient and $\frac{\partial c}{\partial x}$ is the concentration gradient.[98,99] This first law assumes that the flux is constant in the given direction and is time-independent. Therefore, it can only be applied to the steady state regime.[99] For one-dimensional permeation through a polymer membrane, Eq. 2.35 can be rewritten in the form:

$$J = -D\left(\frac{\Delta c}{l}\right) \qquad 2.36$$

with all terms as defined previously and l as the sample thickness. The units for the preceding terms are given as: *J* (mol cm^{-2} s^{-1}); *D* (cm^2 s^{-1}); Δc (mol cm^{-3}); l (cm)

Diffusion occurs when a dissolved molecule moves from one 'hole' to another, which is a condition of the new hole being of sufficient size (and also the path to said hole) to accommodate the molecule. As the chain segments vibrate and rotate according to their degree of thermal excitation, holes form and collapse and are therefore transient in nature. Therefore, larger and more numerous holes result in faster diffusion; larger diffusant molecules result in slower diffusion. An energetic barrier, similar to an activation energy, must also be overcome for molecular transport via the holes.[20] Therefore, *D* effectively measures the speed at which a permeant diffuses through the polymer. Henry's Law (in which solubility is proportional to pressure[100]) is obeyed once the steady state is reached – the gas partial pressure and concentration at the surface are in equilibrium.[97]

The solubility, *S*, is thermodynamic in nature; dependent upon the ability of the permeant gas to condense, and also of polymer-solute interactions. It can be defined as the ratio between the equilibrium concentration of the dissolved solvent molecule in the polymer (*C*) and the gas phase partial pressure (*p*) by:[95,96,101]

$$S = \frac{C}{p} \qquad 2.37$$

As Eq. 2.34 shows, if the solubility of a molecule in PE is low, the corresponding permeation will be proportionally reduced.[20] The majority of organic solvents are sparingly soluble in PE, however, the less polar the nature of the solvent, the greater the solubility and hence permeability.[19] PE is therefore a good barrier against polar molecules because of their reduced affinity for the nonpolar polymer.[20] Therefore, in decreasing order of PE permeation by organic solvents: halogenated hydrocarbons, hydrocarbons, ethers, esters, aldehydes and ketones, nitrogen-derivatives and acids.[20]

Michaels *et al*. proposed and developed a two-phase model for studying gas transport through semi-crystalline polymers.[100–102] It was shown, for isotropic HDPE with spherulites, that both sorption and diffusion occurred exclusively in the amorphous regions with the crystalline regions acting as impermeable barriers, by decreasing the available polymer volume for sorption and also by forming a tortuous path for the penetrant molecule.[96,103] In addition, it was shown that solubility constants of gases were proportional to the amorphous volume fraction in the polymer, and thus independent of the degree of crystallinity, given by:[102]

$$S = \alpha S^* \qquad 2.38$$

where S is the solubility under investigation, α is the volume fraction of amorphous material and S^* is the solubility of a 100 % amorphous, hypothetical PE.[100] It was also shown that the solubility behaviour of the amorphous phase was similar to that of a LMW, homogeneous liquid and independent of polymerisation route, degree of crystallinity and thermal history.[100]

If the permeant is a gas, it is more convenient to measure the vapour pressure, p, then Eq. 2.36 becomes:

$$J = -D\left(\frac{S\Delta p}{l}\right) \qquad 2.39$$

The product DS still equates to the permeability, P.[97]

Consider the case whereby S is independent of concentration, thus resulting in a linear distance-concentration relationship. P, can therefore be defined as follows, with the ratio P/l given as the permeance, indicated by the symbol q.[97]

$$P = -\frac{Jl}{\Delta p} = DS \qquad 2.40$$

These idealised cases, displaying Fickian behaviour assume little to no interaction between permeant and polymer. Non-Fickian behaviour, as seen for water and hydrophilic polymers or solvent vapour diffusing through polymer films, requires separate consideration.[97]

A laminate sample, consisting of more than one polymer layer, can be described by the Ideal Laminate Theory (ILT), as proposed by Grüniger and von Rohr.[104] The total permeability of the laminate, P_L, is a function of the individual thickness, l_i, and permeability, P_i, of each layer, L:[97,104]

$$\frac{P_L}{\Sigma l_i} = \frac{1}{\Sigma(l_i/P_i)} = \frac{TR_L}{\Delta p} \qquad 2.41$$

The transmission rate, *TR*, is often a more convenient quantity to use instead of *P*, especially for laminates (hence the subscript *L* in Eq. 2.41) and is defined as the quantity of permeant passing through a membrane, per unit of time, per unit of area, at steady state.[97,104] This model only holds for samples without defects, such as cracks or pinholes, as the lateral spreading of the concentration profile around the defect results in the transport becoming a three-dimensional (3D), instead of a 1D problem.[97,104] Another quantity is the gas transmission rate, GTR, (also called permeance, *q*) expressed in the same way as for the ILT but with the *volume* of permeant measured:[97]

$$GTR\ (or\ q) = k_1 \left(\frac{V}{T[N - t_L]}\right) \qquad 2.42$$

where $k_1 = 9.89 \times 10^8$, *V* is the measured volume (mL), *N* is the slope of the measured curve (s), *T* is the temperature (K) and t_L is the time-lag value (s).[97]

2.11.2 Time-Lag Method

Numerous ASTM and ISO standard test methods exist (ISO 12572, ISO 2528, ASTM E96/E96M) for determining the rate of vapour transmission through a thin film sample.[105–107] Perhaps the simplest is the rate of weight loss over time when using a sample fuel, for example 50:50 toluene:iso-octane (also known as fuel C). A concern with this fuel mixture was the difference in vapour pressures, and hence evaporation rates, as a high vapour pressure equates to increased volatility.[108] Considering toluene (b.p. 110.6 °C; P_{vap} = 3.96 kPa at 25 °C)[109] and iso-octane (b.p. 99.3 °C; P_{vap} = 6.03 kPa at 25 °C)[109], iso-octane will evaporate at a faster rate than toluene potentially leading to a double plateau in the steady state permeation rate data. Instead, xylene (mixed isomers) was used for these experiments. However, a limitation of this test method is that the vapour transmission rate is directly linked to the testing conditions

(temperature, pressure, humidity) and so values obtained under one set of conditions are not comparable to those at another, unless the conditions are identical. The future application of this technology will be in underground water transport pipes, so ideally the permeation test should be performed as such. This was not feasible, however a good insight into permeation rates was still obtained.

Owing to the solubility-diffusion mechanism discussed previously, there is a time interval before the steady state is reached. This time-lag, described in seminal work by Barrer, and developed further Amerongen, showed that the values of *P* and *D* could be obtained from the same method.[110,111] By representing the quantity of penetrants passing through the membrane as a function of time, a straight line is obtained for the steady state region, indicating the flux of penetrant is constant across the entire membrane face (Figure 2.31).[96]

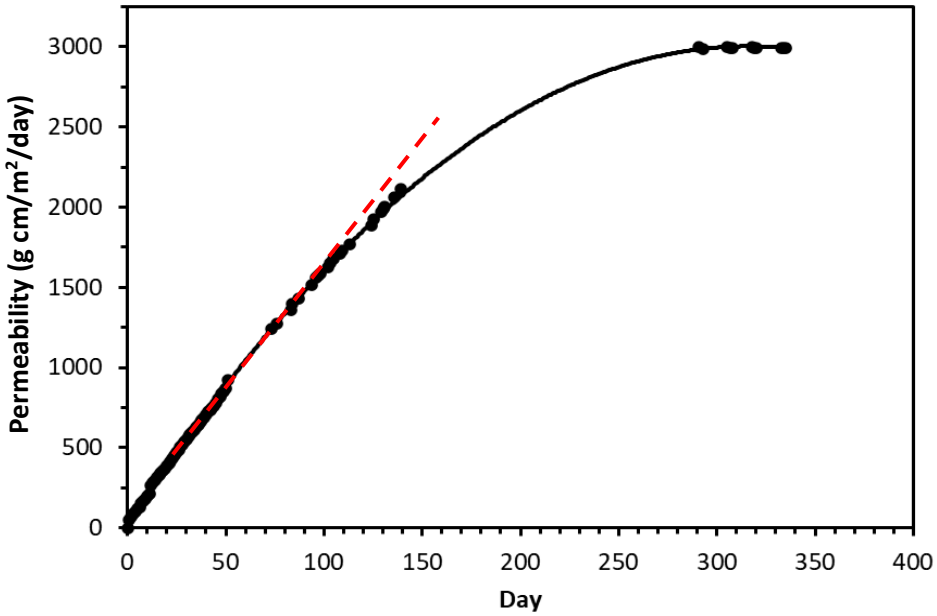

Figure 2.31: An example of a permeability curve showing the permeability (calculated by measuring the mass of the test cell at regular intervals to determine the mass of xylene lost) plotted against time, from which the steady state region, indicated by the red dashed line, can be determined. The plateau region at longer times indicates that the fuel reservoir is empty.

The permeability coefficient, *P*, is then directly proportional to this straight line by:

$$P = \frac{Ql}{Atp} \qquad 2.43$$

where *Q* is the quantity of penetrant, *l* the sample thickness, *A* is the sample area, *t* is the time and *p* is the pressure. Since the flux, *J*, is a product of the penetrant quantity, sample area and time, this equation can be rewritten as:[96,111,112]

$$P = \frac{Jl}{p} \qquad 2.44$$

Extrapolating this linear steady state region to intercept with the time axis is called the time lag, *Θ*, and is proportional to sample thickness and the diffusion coefficient, *D*, by:[96]

$$D = \frac{l^2}{6\Theta} \qquad 2.45$$

From this, the solubility coefficient, *S*, can be obtained from Eq. 2.34.

It is important to distinguish between permeance and permeability. Under specified temperature and humidity conditions, permeance relates to the rate of vapor transmission through unit area of flat material caused by the difference in unit vapor pressure between two specific surfaces. Permeance is therefore a performance evaluation and not a property of a material. Transmission relates to the steady state flow of vapour through a flat sample of unit area in unit time. Permeability is a material property and is the product of permeance and thickness.[106]

The purpose of these tests was to establish values for the rate of fuel vapour transmission through unoriented and oriented HDPE, and HDPE/UHMWPE SPC samples. By testing under identical conditions, it would be possible to draw a comparison between the samples and thus observe any changes in permeability by using an oriented morphology or HDPE/UHMWPE composite construction for pipe manufacture.

2.11.3 Measurement Conditions

A custom-built stainless-steel permeation cell was fabricated consisting of a solvent reservoir, sample loading area and sealing lid (Figure 2.32). 5 mL of xylene was added into the reservoir, a thin copper washer placed into the loading area and then a sample, prepared via MeltPrep or cut from Couette specimens, positioned on top. Silicone vacuum grease was applied to the screw thread of the lid and then screwed down onto the base, tightening securely. All samples were measured simultaneously across 40 permeation cells with mass measurements taken at regular intervals on a four decimal point balance.

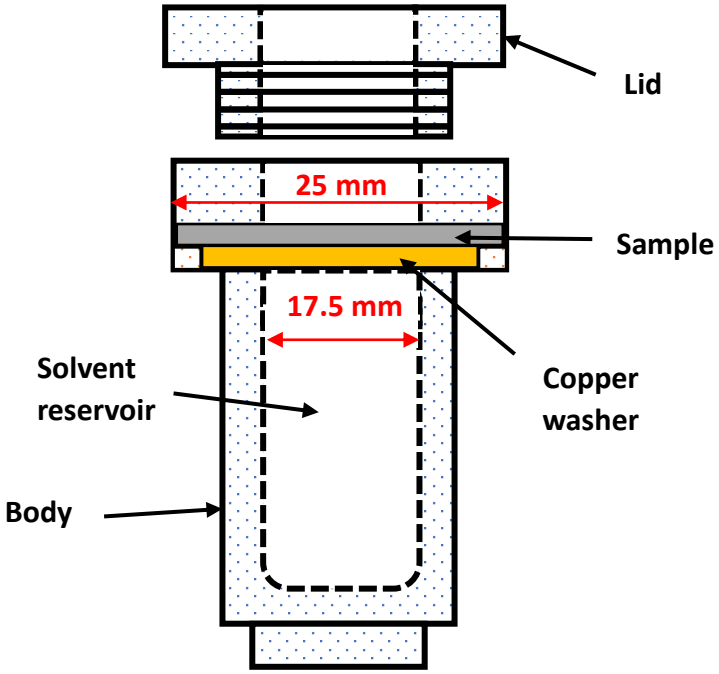

Figure 2.32: A schematic of the permeation cells fabricated for this work consisting of a solvent reservoir, notches for a sealing copper washer, sample and a screw-down lid to ensure tight sealing. The cells were designed for 25 mm diameter samples with a permeation aperture of 17.5 mm diameter.

2.12 Mechanical Testing

2.12.1 Background & Theory

The MWD plays a crucial role in determining the end-use properties of a resin, displaying a balanced performance in terms of processing and mechanical properties.[113] The LMW chains promote flowability and hence better processing whereas the HMW chains improve the mechanical properties of the melt.[114]

In addition to the MWD, the semi-crystalline morphology of PE is responsible for the physical properties observed.[20] Amorphous domains impart ductility, whereas crystalline domains impart hard and brittle properties, constraining the amorphous phases between them and acting as reinforcing points.[115] Thus changing the degree of crystallinity can have a profound effect upon mechanical properties.[115] The inter-lamellae connections (Section 1.4.1, Figure 1.10) are crucial to understanding the effect of morphology on mechanical properties as they transmit forces between the phases.[20] *Shish-kebab*s in semi-crystalline polymers have been shown to further improve the mechanical properties, such as stiffness, of end-use products compared to unoriented spherulitic material.[116,117] Therefore mechanical tests were performed to establish structure-property relationships for *shish-kebab* morphology and SPCs.

2.12.1.1 Tensile Testing

The stress-strain behaviour of polymeric materials depends upon several factors including molecular weight, microstructure, testing rate and temperature. Stress and strain can be defined by (Eqs. 2.46 and 2.47 respectively):

$$\sigma = \frac{L - L_i}{L_i} \qquad 2.46$$

$$\varepsilon = \frac{F}{A_i} \qquad 2.47$$

where F is the force, A_i is the initial cross-sectional area, L_i is the initial sample length and L is the length at which the force is F.[118] Consider a typical stress-strain curve for PE (Figure 2.33).

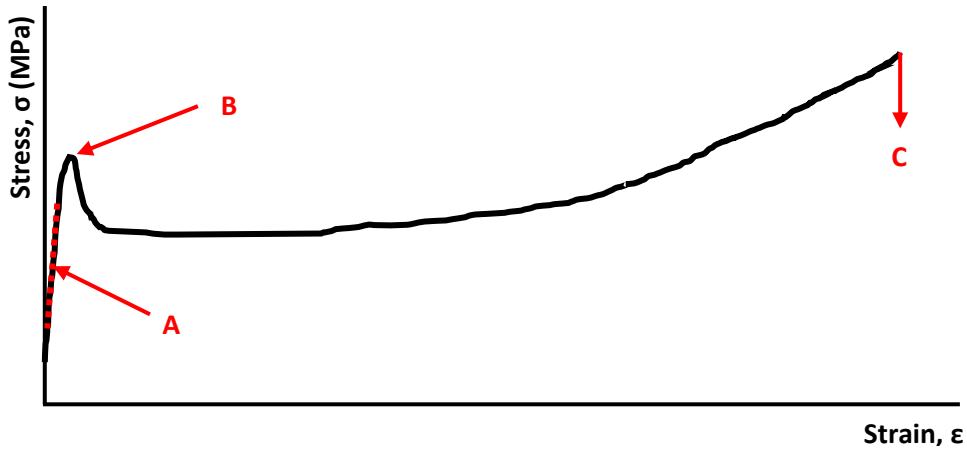

Figure 2.33: An example stress-strain curve for a semi-crystalline polymer. Points indicated are the Young's Modulus region (A and red dashed line), Yield Point (B) and Break Point (C). Strain hardening often occurs between points B and C.

At sufficiently low stresses and strains, the behaviour can be described as that of a linear elastic solid characterised by the Young's Modulus (A):

$$E = \sigma/\varepsilon \qquad 2.48$$

As stress and strain increase, the peak maximum indicates the Yield Point (B) at which the onset of permanent, plastic deformation occurs and the behaviour could hence be described as non-linear.[118,119] Below this point, strain is recoverable.[119] The corresponding stress and elongation are known as the Yield Stress and Yield Elongation respectively.[118] Beyond point B, the sample enters a region of plastic deformation which is characterised by considerable

stretching and the formation of a 'neck'. The neck is stabilised by drawing new material in from the surrounding regions until the entire section of the sample has reached the Yield Point.[118] At this point, strain hardening, caused by the alignment and orientation of polymer chains, occurs until the sample ruptures at a point termed the Break Point (C). The stress and strain at this point are known as the ultimate strength and elongation at break respectively.[118,119]

2.12.1.2 Dynamic Mechanical Analysis

The basic principles of Dynamic Mechanical Analysis (DMA) are the same as those described in Section 2.5.2 and Figure 2.7.[20,52] It is a term loosely used to describe a broad range of techniques to measure the physical response of an applied oscillatory strain, with samples typically consisting of strips, fibres or rods as opposed to a fluid.[20,120]

In torsional mechanical analysis, the dynamic loss modulus, *G"*, is often associated with molecular motions, transitions and morphology.[120] The dynamic storage modulus, *G'*, is often associated with the stiffness of the material and is related to the Young's Modulus, *E*, by:

$$E = 2G'(1 + \nu) \qquad 2.49$$

where ν is the Poisson's Ratio, a measure of the ratio of lateral or transverse strain to the longitudinal strain, given as 0.46 for HDPE.[121]

2.12.2 Measurement Conditions – Tensile Testing

Specimens for tensile testing were prepared by the Couette cell (Section 2.6) to a thickness of 0.5 mm. Five 'dog-bone' samples were manually cut for each set of shear conditions with dimensions (excluding the clamping tabs) of 7 mm x 25 mm (width x length). These samples were subsequently sent to Aliaxis R&D (Vernouillet, France) for tensile testing in accordance with ISO 527.[122] Upon receipt, the samples were conditioned for 24 hours at 23 °C. An Instron AVE 2 Video Extensometer, equipped with Zwick grips 500 N, was used to measure each sample at a rate of 20 mm min^{-1} to deduce the elongation at break values.

2.12.3 Measurement Conditions – Dynamic Mechanical Analysis

SPC composite samples for measurement were prepared as described in Section 2.10.

A Thermo Scientific HAAKE MARS III, equipped with solid clamps, was used for these experiments. The dimensions were measured and loaded between the grips to give a sample length of 30 mm. A torsional oscillatory frequency sweep between ω = 100 – 0.06283 rad s^{-1} at 1 % strain was applied in each case. All measurements were performed at 25 °C.

2.13 Conclusions

Numerous techniques have been used and adjusted throughout this work to characterise and investigate the structural details and mechanical behaviour of samples after SIC or SPC fabrication. Various sample preparation methods were required to fabricate test specimens including hot pressing, MeltPrep VCM, Couette cell shearing and parallel-plate shearing. This latter technique was also used to probe the shear flow behaviour of PE1 and PE2. Through GPC and DSC, important details of the MWDs and thermal behaviours of PE1 and PE2 were obtained. Measurements of the isothermal crystallisation of PE1 and PE2 were also performed using DSC to observe the effect of shearing upon the crystallisation kinetics. Mechano-optical SIPLI measurements assisted in determining critical work parameters for shearing and SAXS was used to observe the resulting morphology from shearing experiments in parallel-plate shearing and Couette cell shearing. Rheology and associated DMA testing gave valuable data regarding the linear viscoelastic behaviour of PE1 and PE2 melts and SPCs fabricated with UHMWPE and aluminium foil inter-layer tapes.

Most significantly for this work, a high temperature Couette cell was fabricated with a removable stator to retrieve the crystallised material for further measurements. Samples from this cell were cut into specimens for tensile testing and permeation measurements, which provided important information regarding the effect of oriented morphology and SPCs upon mechanical properties and resistance to permeation of xylene.

2.14 References

1 *BorSafe PE pipe materials – made for generations*, Borealis AG, Data Sheet, 2016.

2 *ELTEX B4922N3004*, Ineos Olefins & Polymers Europe, Data Sheet, 2009.

3 F. A. Morrison, *Understanding Rheology*, Oxford Univesity Press, Oxford, 2001.

4 H. A. Barnes, *A Handbook of Elementary Rheology*, The University of Wales Institute of Non-Newtonian Fluid Mechanics, Aberystwyth, 2000.

5 W. Chen, Q. Zhang, J. Zhao and L. Li, *J. Appl. Phys.*, 2020, **127**, 241101.

6 C. Macosko, *Rheology: Principles, Measurements and Applications*, Wiley VCH, New York, 1996, vol. 86.

7 M. Couette, in *CR Acad Sci 107*, 1888, pp. 388–390.

8 O. O. Mykhaylyk, P. Chambon, C. Impradice, J. P. A. Fairclough, N. J. Terrill and A. J. Ryan, *Macromolecules*, 2010, **43**, 2389–2405.

9 J. A. Odell, D. T. Grubb and A. Keller, *Polymer (Guildf).*, 1978, **19**, 617–626.

10 H. A. Barnes, J. F. Hutton and K. Walters, *An Introduction to Rheology*, Elsevier Science Publishers, Amsterdam, 3rd edn., 1993.

11 W.-F. Su, in *Principles of Polymer Design and Synthesis*, ed. W.-F. Su, Spinger, Berlin, Heidelberg, 2013, pp. 9–26.

12 T. Williams, *J. Mater. Sci.*, 1970, **5**, 811–820.

13 J. M. Evans, *Polym. Eng. Sci.*, 1973, **13**, 401–408.

14 T. G. Scholte, N. L. J. Meijerink, H. M. Schoffeleers and A. M. G. Brands, *J. Appl. Polym. Sci.*, 1984, **29**, 3763–3782.

15 *Polystyrene and Polyethylene Calibrants in Gel Permeation Chromatography with TCB*, Agilent Technologies Application Notes, Technical Overview, 2015.

16 J. V. Dawkins, *Science*, 1977, **13**, 837–839.

17 H. L. Wagner, *J. Phys. Chem. Ref. Data*, 1985, **14**, 611–617.

18 B. K. Varma, Y. Fujita, M. Takahashi and T. Nose, *J. Polym. Sci. Part A-2, Polym. Phys.*, 1984, **22**, 1781–1797.

19 H. S. Tseng and D. R. Lloyd, *J. Appl. Polym. Sci.*, 1985, **30**, 1815–1826.

20 A. J. Peacock, *Handbook of Polyethylene*, Marcel Dekker, New York, 2000.

21 A. Boborodea, *Evaluation of Polyethylene Type Using High Temperature Gel Permeation Chromatography with Triple Detection*, Agilent Technologies, 2013.

22 R. Salovey and M. Y. Hellman, *Polym. Lett.*, 1967, **5**, 647–651.

23 C. Schick, *Anal. Bioanal. Chem.*, 2009, **395**, 1589–1611.

24 ASTM, *E473-18: Standard Terminology Relating to Thermal Analysis and Rheology*, 2018.

25 J. D. Menczel and R. B. Prime, *Thermal Analysis of Polymers: Fundamentals and Applications*, Wiley, Hoboken, New Jersey, 2009.

26 E. Verdonck, *Differential Scanning Calorimetry (DSC) Advanced Training Course*, TA Instruments, 2020.

27 A. P. Melnikov, M. Rosenthal and D. A. Ivanov, *ACS Macro Lett.*, 2018, 1426–1431.

28 J. N. Hay and P. J. Mills, *Polymer*, 1982, **23**, 1380–1384.

29 E. Piorkowska and G. C. Rutledge, *Handbook of Polymer Crystallization*, Wiley, Hoboken, NJ, USA, 2013.

30 B. Wunderlich and G. Czornyj, *Macromolecules*, 1977, **10**, 906–913.

31 H. Marand, J. Xu and S. Srinivas, *Macromolecules*, 1998, **31**, 8219–8229.

32 E. Földes, G. Keresztury, M. Iring and F. Tüdős, *Die Angew. Makromol. Chemie*, 1991, **187**, 87–99.

33 Y. Kong and Y. N. Hay, *Polymer*, 2002, **43**, 3873–3878.

34 Y. Furushima, C. Schick and A. Toda, *Polym. Cryst.*, 2018, **1**, 10005.

35 Y. Kong and J. N. Hay, *Eur. Polym. J.*, 2003, **39**, 1721–1727.

36 F. P. Price, *J. Chem. Phys.*, 1951, **19**, 973–973.

37 R. Blaine, *TA123: Determination of Polymer Crystallinity by DSC*, TA Instruments, 2010.

38 D. J. Bundell, D. R. Beckett and P. H. Willcocks, *Polym. Reports*, 1981, **22**, 704–707.

39 R. L. Blaine, *TN048: Polymer Heats of Fusion*, TA Instruments Thermal Applications Note.

40 B. Wunderlich and T. Davidson, *J Polym Sci Part A-2 Polym Phys*, 1969, **7**, 2043–2050.

41 T. Davidson and B. Wunderlich, *J Polym Sci Part A-2 Polym Phys*, 1969, **7**, 2051–2059.

42 R. B. Prime and B. Wunderlich, *J Polym Sci Part A-2 Polym Phys*, 1969, **7**, 2099–2113.

43 R. B. Prime and B. Wunderlich, *J Polym Sci Part A-2 Polym Phys*, 1969, **7**, 2073–2089.

44 R. B. Prime, B. Wunderlich and L Melillo, *J Polym Sci Part A-2 Polym Phys*, 1969, **7**, 2091–2097.

45 B. Wunderlich and C. M. Cormier, *J. Polym. Scince Part A-2*, 1967, **5**, 987–988.

46 K. W. Hall, T. W. Sirk, S. Percec, M. L. Klein and W. Shinoda, *Polymers*, 2020, **12**, 447.

47 T. Verho, A. Paajanen, J. Vaari and A. Laukkanen, *Macromolecules*, 2018, **51**, 4865–4873.

48 L. Feng and M. R. Kamal, *Int. Polym. Process.*, 2006, **21**, 402–411.

49 B. Wunderlich, *Macromolecular Physics*, Elsevier Inc., New York, 1980, vol. 3.

50 R. Hooke, *Lectures de Potentia Restitutiva*, 1678.

51 I. Newton, *The Principia*, 1687.

52 M. Okura, *The Control of Structural Morphology of Polyethylene by Shear-Induced Crystallisation*, PhD Thesis, University of Sheffield, 2010.

53 C. D. C. Erbetta, G. F. Manoel, A. P. L. R. Oliveira, M. E. S. R. e Silva, R. F. S. Freitas and R. G. Sousa, *Mater. Sci. Appl.*, 2014, **05**, 923–931.

54 M. Yamamoto, *J. Phys. Soc. Japan*, 1958, **13**, 1200–1211.

55 K. Weissenberg, *Nature*, 1947, **159**, 310–311.

56 D. Doraiswamy, *Rheol. Bull.*, 2002, **71**, 1–9.

57 A. J. Franck, *AN007: Normal stresses in shear flow*, TA Instruments, 2014.

58 H. De Cagny, M. Fazilati, M. Habibi, M. M. Denn and D. Bonn, *J. Rheol.*, 2019, **63**, 285–290.

59 J. M. Dealy and J. Wang, in *Melt Rheology and its Applications in the Plastics Industry*, Springer, Dordrecht, 2nd edn., 2013, pp. 19–47.

60 D. I. Verrelli and A. R. Kilcullen, *Adv. Condens. Matter Phys.*, 2016, **1716598**, 1–21.

61 R. B. Bird, R. C. Armstrong and O. Hassager, *Dynamics of polymeric liquids - Vol. 1: Fluid Mechanics*, Wiley VCH, Weinheim, 1987, vol. 91.

62 P. Sunthar, in *Rheology of Complex Fluids*, eds. A. P. Deshpande, J. M. Krishnan and

S. Kumar, Springer, New York, 2010, pp. 171–191.

63 S. A. McGlashan, V. T. O'Brien, K. Awati and M. E. Mackay, *Polymer Rheology*, 1998, vol. 37.

64 M. M. Cross, *J. Colloid Sci.*, 1965, **20**, 417–437.

65 T. C. Le, B. D. Todd, P. J. Daivis and A. Uhlherr, *J. Chem. Phys.*, 2009, **131**, 044902.

66 W. P. Cox and E. H. Merz, *Am. Soc. Test. Mater. Spec. Tech. Publ.*, 1958, **247**, 178–188.

67 W. P. Cox and E. H. Merz, *J. Polym. Sci.*, 1958, **28**, 619–622.

68 T. Osswald and N. Rudolph, *Polymer Rheology: Fundamentals and Applications*, Hanser Publishers, Munich, 2015.

69 H. Markovitz, *J. Polmer Sci.*, 1975, **50**, 431–456.

70 J. Dealy and D. Plazek, *Rheol. Bull.*, 2009, **78**, 16–21; 30–31.

71 J. D. Ferry, *J. Res. Natl. Bur. Stand. (1934).*, 1948, **41**, 53–62.

72 M. L. Williams, R. F. Landel and J. D. Ferry, *J. Am. Chem. Soc.*, 1955, **77**, 3701–3707.

73 P. E. Rouse, *J. Chem. Phys.*, 1953, **21**, 1272–1280.

74 P. G. de Gennes, *Nature*, 1979, **282**, 367–370.

75 A. A. Cuadri and J. E. Martín-Alfonso, *Polym. Degrad. Stab.*, 2017, **141**, 11–18.

76 M. D. Wallis and S. K. Bhatia, *Polym. Degrad. Stab.*, 2007, **92**, 1721–1729.

77 D. S. Kalika, L. Nuel and M. M. Denn, *J. Rheol.*, 1989, **33**, 1059–1070.

78 J. Aho, *Rheological Characterization of Polymer Melts in Shear and Extension: Measurement Reliability and Data for Practical Processing*, D.Sc Thesis, Tampere University of Technology, 2011.

79 D. F. Griffiths and K. Walters, *J. Fluid Mech.*, 1970, **42**, 379–399.

80 J. E. Mark, *Physical Properties of Polymers Handbook*, Springer, New York, 2nd edn., 2007.

81 F. A. Morrison, *Michigan Technol. Univ. Coursew.*, 2014, 20141–20144.

82 O. O. Mykhaylyk, *Soft Matter*, 2010, **6**, 4430–4440.

83 H. Janeschitz-Kriegl, *Polymer Melt Rheology and Flow Birefringence*, Springer Berlin Heidelberg, Berlin, Heidelberg, 1983, vol. 6.

84 O. O. Mykhaylyk, N. J. Warren, A. J. Parnell, G. Pfeifer and J. Laeuger, *J. Polym. Sci. Part B Polym. Phys.*, 2016, **54**, 2151–2170.

85 B. Crist and J. M. Schultz, *Prog. Polym. Sci.*, 2016, **56**, 1–63.

86 J. J. Lissauer and I. De Pater, *Fundamental Planetary Science: Physics, Chemistry and Habitability*, 2019.

87 O. Glatter and O. Kratky, *Small Angle X-Ray Scattering*, Academic Press, London, 1982.

88 H. Schnablegger and Y. Singh, *The SAXS Guide: Getting Aquainted With The Principles*, Anton Paar GmbH, Graz, 3rd edn., 2013.

89 R. J. Roe, J. E. Mark, K. Binder and B. Erman, *Methods of X-ray and Neutron Scattering in Polymer Science*, Oxford University Press, New York, 2000, vol. 3.

90 G. R. Strobl and M. Schneider, *J. Polym. Sci. Polym. Phys.*, 1980, **18**, 1343–1359.

91 G. Strobl, *The Physics of Polymers*, Springer, 3rd edn., 2007.

92 B. D. Cullity, *Elements of X-Ray Diffraction*, Addison-Wiley Publishing Company Inc., Reading, Massachusetts, 1956, 531.

93 J. Ilavsky, P. R. Jemian, A. J. Allen, F. Zhang, L. E. Levine and G. G. Long, *J. Appl. Crystallogr.*, 2012, **45**, 324–328.

94 J. Ilavsky, P. R. Jemian, L. Kissel, E. P. Gilbert, M. Rutnakornpituk, Q. Zhang, J. S. Riffle, S. Fang and P. Lawton, *J. Appl. Crystallogr.*, 2009, **42**, 347–353.

95 J. M. Lagaron, A. K. Powell and G. Bonner, *Polym. Test.*, 2001, **20**, 569–577.

96 M. H. Klopffer, B. Flaconneche and P. Odru, *Plast. Rubber Compos.*, 2007, **36**, 184–189.

97 V. Siracusa, *Int. J. Polym. Sci.*, 2012, **302029**, 1–11.

98 A. Fick, *Ann. Phys.*, 1855, **170**, 28.

99 J. Comyn, *Polymer Permeability*, Chapman & Hall, London, 1994.

100 A. S. Michaels and H. J. Bixler, *J. Polym. Sci.*, 1961, **50**, 393–412.

101 A. S. Michaels and R. B. Parker, *J. Polym. Sci.*, 1959, **41**, 53–71.

102 A. S. Michaels and H. J. Bixler, *J. Polym. Sci.*, 1961, **50**, 413–439.

103 P. Kofinas, R. E. Cohen and A. F. Halasa, *Polymer*, 1994, **35**, 1229–1235.

104 A. Grüniger and P. R. Von Rohr, *Thin Solid Films*, 2004, **459**, 308–312.

105 *ISO 12572: Hygrothermal Performance of Building Materials and Products — Determination of Water Vapour Transmission Properties — Cup Method*, 2016.

106 *E96/E96M: Standard Test Methods for Water Vapor Transmission of Materials*, 2000.

107 *ISO 2528: Sheet materials — Determination of Water Vapour Transmission Rate (WVTR) - Gravimetric (Dish) Method*, 2017, vol. 2017.

108 P. Atkins and J. de Paula, *Physical Chemistry*, Oxford University Press, Oxford, 9th edn., 2009.

109 T. Boublik, V. Fried and E. Hala, *The Vapor Pressures of Pure Substances*, 1973, vol. 517.

110 R. M. Barrer, *Trans. Faraday Soc.*, 1939, **35**, 628–643.

111 G. J. Van Amerongen, *J. Appl. Phys.*, 1946, **17**, 972–985.

112 S. W. Rutherford and D. D. Do, *Adsorption*, 1997, **3**, 283–312.

113 M. K. Lenzi, M. F. Cunningham, E. L. Lima and J. C. Pinto, *Ind. Eng. Chem. Res.*, 2005, **44**, 2568–2578.

114 Z. Zhai, J. Morthomas, C. Fusco, M. Perez and O. Lame, *Macromolecules*, 2019, **52**, 4196–4208.

115 J. N. Hay, *Pure Appl. Chem.*, 1995, **67**, 1855–1858.

116 R. Zhao, Z. Chu and Z. Ma, *Polymer*, 2020, **12**, 2571–2582.

117 M. J. Hill and A. Keller, *J. Macromol. Sci. Part B*, 1969, **3**, 153–169.

118 J. Milisavljević, E. Petrović, I. Ćirić, M. Mančić, D. Marković and M. Dordević, in

29th DANUBIA-ADRIA Symposium on Advances in Experimental Mechanics, DAS 2012, 2012, **vol. 29**, pp. 266–269.

119 G. Dean and B. Read, *Polym. Test.*, 2001, **20**, 677–683.

120 G. W. Ehrenstein, G. Riedel and P. Trawiel, in *Thermal Analysis of Plastics: Theory and Practice*, Hanser, 2004, pp. 236–299.

121 A. Pawlak and A. Galeski, *Macromolecules*, 2005, **38**, 9688–9697.

122 *ISO 527-1:2019 - Plastics — Determination of Tensile Properties — Part 1: General Principles*, 2019.

Chapter 3

Characterisation of the Materials Used in the Study

3.1 Introduction

Two commercial-grade, unpigmented HDPE resins were obtained, designated as PE1 and PE2 in the subsequent text. Both materials were designed for use in the transport of drinking water with a bimodal MWD, offering excellent resistance to stress crack propagation and growth and good processing properties through extrusion.[1–3]

Bimodal MWDs can be manufactured via two routes: single-reactor, multi-site Ziegler-Natta catalysis or by multiple-cascading reactors.[4,5] They are particularly useful in pipe manufacture, offering a balance of good processability and mechanical properties.[4–6] Pipe manufactured from such bimodal blends allows for higher pressure ratings and longer service lifetimes, with the current generation identified as PE-100.[6] This stipulates that a pipe must withstand a hoop stress of 10 MPa at 20 °C for up to 50 years.[7] The previous generation of PE-80 resins were only able to withstand 8 MPa under the same conditions.

Due to the higher-pressure rating of PE-100 pipes, the pipe wall thickness can be decreased, compared to PE-80 pipes, for the same nominal pressure. Crucially, PE-100 pipe offers a balance between 3 key properties for successful pipe manufacture: pressure, stress cracking and impact resistance.[8] PE1 was optimised for high stress crack resistance and low sag; produced in two reactors, separated by flash evaporation to remove unreacted hydrocarbons, chains grow on the same catalyst particle to form an interpenetrating network of LMW and HMW chains.[9] PE2 was specifically designed for extrusion applications making use of hexene co-monomer polymerisation to achieve a bimodal MWD and impart SCB.[2]

The HMW component imparts increased stiffness and exceptional resistance to slow crack growth and creep, but also causes an increase in melt viscosity and thus processing difficulties.[4] The low molecular weight (LMW) component alleviates this by acting as a ‘lubricant’ in the amorphous regions of the semicrystalline morphology to increase the processability.[4,5] The molecular origins of these improved properties lie in the high degree of short chain branching on the longest chains.[7] This is in contrast to the PE-80 resins in which branching was concentrated in the shortest chains.[7] Increased branching of the longer chains increases the concentration in the amorphous region, thus increasing the likelihood of their action as tie molecules and an overall increase in the strength of the polymer matrix.[7] The type and amount of co-monomer used during the synthesis of branched PEs strongly affects the degree of branching and crystallinity resulting in different structural morphologies, mechanical behaviour and rheology.[10,11] It is generally regarded that the MWD and degree of branching

are the key variables in determining material performance.[11] Increasing the degree of branching will cause a corresponding decrease in crystallinity (LCB < SCB < linear) for the same M_w as the branches increase the mobility of the amorphous regions and entanglement points.[12] SCB increases the temperature sensitivity and flow activation energy under shear by hindering molecular mobility and, therefore, a larger thermal activation is required for segment motion.[13] LCB has been shown to affect the crystallinity, tensile modulus and other mechanical and rheological properties.[10] LCB affects polymer viscosity in two ways. Greater molecular entanglement (compared with a linear polymer of the same molecular weight) causes the viscosity of branched polymers to be higher at low shear rates. However, shear-thinning behaviour is more apparent when LCB is increased due to improved disentanglement under shear.[10] Wood-Adams *et al.* also showed that increasing the LCB content also increased the zero-shear activation energy[14] and Mendelson showed that elastic deformation decreases with LCB.[15] Nevertheless, PE-100 resins cannot easily be used in large diameter, thick-wall pipes owing to sagging before complete crystallisation – the lack of LCB decreases the melt elasticity.[7]

UHMWPE resins typically have viscosities much greater than linear HDPE and, as such, this can make pipe manufacture from such materials difficult.[16,17] However, UHMWPE can be drawn into tapes and fibres through gel-spinning or mechanical drawing, imparting high degrees of orientation in the process and thus offering a method of potentially incorporating UHMWPE into pipe manufacture.[16] Three UHMWPE tapes were obtained from Teijin Aramid: Endumax TA23, XF23 & S1. TA23 was fabricated by compacting of PE powder with subsequent rolling and stretching. An additional uni-directional laying and cross-plying step occurs to fabricate XF23 after the same initial fabrication steps. No manufacturing details could be obtained for tape S1, but it was regarded by industrial collaborators from Aliaxis/GPS PE Pipe Systems as an intermediate stretching step towards the fabrication of TA23.[18]

Key physical properties were obtained through GPC, DSC, rheology and SAXS techniques to establish a relationship between the MWD and physical-structural properties - in particular, how the materials form oriented lamellar morphology under flow conditions.

3.2 Molecular Weight Distribution

Knowledge of the MWD was important for interpreting subsequent flow behaviour and the resulting degree of orientation. HT-GPC (Section 2.3.2) of both PE1 and PE2 was performed

at 160 °C with 1,2,4-trichlorobenzene as the eluent with the results averaged over duplicate runs (Table 3.1 and Figure 3.1).

	M_w (kDa)	M_n (Da)	M_z (kDa)	M_w/M_n
PE1	264.5	7.91	2094.4	33.5
PE2	227.5	7.93	1858.0	28.5

Table 3.1: Obtained results from HT-GPC analysis of two separate HDPE blends (PE1 and PE2). Results have been averaged over duplicate runs. M_w is the weight-average molecular weight, M_n is the number-average molecular weight, M_z is the z-average molecular weight and M_w/M_n is the dispersity. M_z is more sensitive to longer chains present in the melt

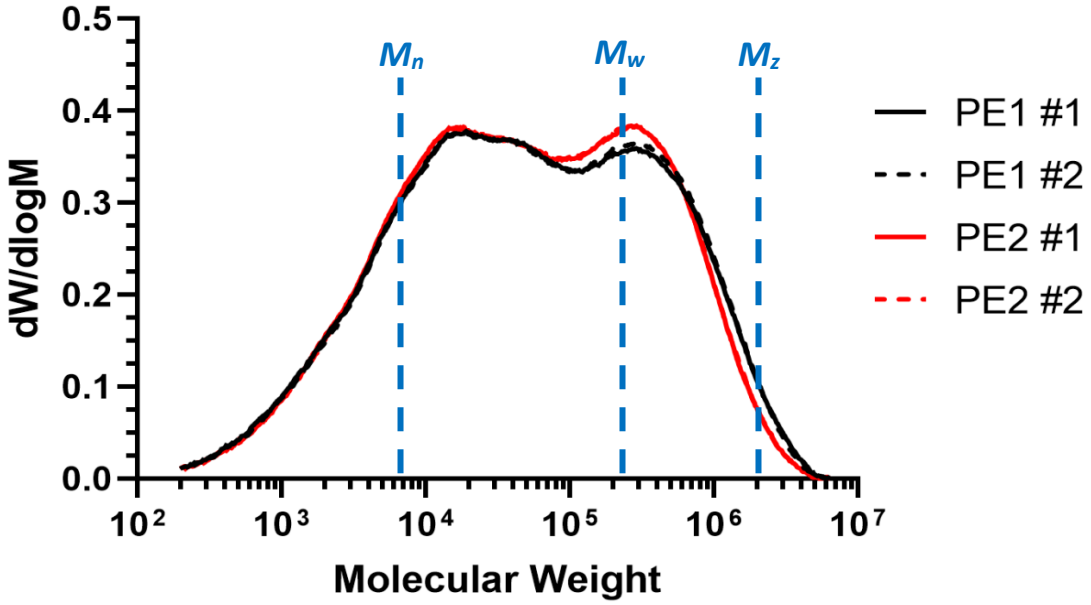

Figure 3.1: Molecular weight distribution of two HDPE blends (PE1 and PE2) obtained by HT-GPC analysis shown on a linear-log scale. The plots are normalised with respect to area, with the y-axis a function of weight fraction. Data for PE1 is shown in black and data for PE2 is shown in red. The solid lines indicate initial sample measurements (also denoted with #1) and the dashed lines indicate the duplicate runs (also denoted with #2). Approximate locations of M_n, M_w and M_z are highlighted.

GPC analysis confirmed that both PE1 and PE2 were bimodal with broad MWD and high dispersity (Table 3.1). The LMW (10^2 – 10^5 Da) regions of both distributions displayed near identical behaviour and therefore exhibited very similar processing properties. At $10^5 \leq M_W \leq 10^6$ Da, PE2 displayed a slightly larger fraction of HMW chains than PE1 at the second peak

suggesting that mechanical strength could be greater compared to PE1. However, PE1 showed a slightly larger fraction of ultra-high molecular weight (UHMW) chains at $M_W > 10^6$ Da. This was confirmed by the larger M_z values, which are more sensitive to the higher molecular weight chains in the sample (it is measured within the high molecular weight region – Figure 3.1), for PE1 compared to PE2. Further evidence was apparent in viscosity measurements (Section 3.4.2) where PE1 displayed slightly higher viscosity than PE2, however it did not adversely affect the processing. As the mechanism for FIC (Figure 1.17) shows, the longest chains in a melt stretch and align under flow first and initiate FIC due to their longest relaxation times.[19] Therefore, it was expected that the greater fraction of UHMW chains in PE1 would result in stronger orientation in shearing experiments compared to PE2.

HDPE resins are typically made using either titanium-based Ziegler-Natta or Chromium-based Phillips catalysts which allow for the reaction process to be tuned according to the desired properties of the end-use product.[17,20] A balance is needed between density, molecular weight and MWD. By adding small amounts of short chain olefins to the reaction vessel, a degree of SCB occurs, increasing the spacing between chains and decreasing the density which improves the resistance to SCG.[17] A higher average molecular weight improves mechanical properties and melt strength, the ability with which a melt resists deformation by sagging during cooling, and typical molecular weights for pipe manufacture are over 100 kDa. However, the corresponding increase in viscosity must be balanced to achieve optimal extrusion conditions and throughput.[17,21]

Producing HDPE resins leads to different chain lengths due to the multiple active site nature of the catalysts, which results in a molecular weight that is different for each molecular chain.[17] A narrow MWD indicates chains with a fairly uniform length, whereas a broader distribution indicates a range of different chain lengths.[17] A broad MWD typically offers good processability, but at the expense of stiffness and impact strength.[17] To circumvent this issue, two or more different resin blends may be mixed to create a final batch combining the optimum properties of broad MWDs at lower and higher molecular weights (Figures 3.2 and 1.2).

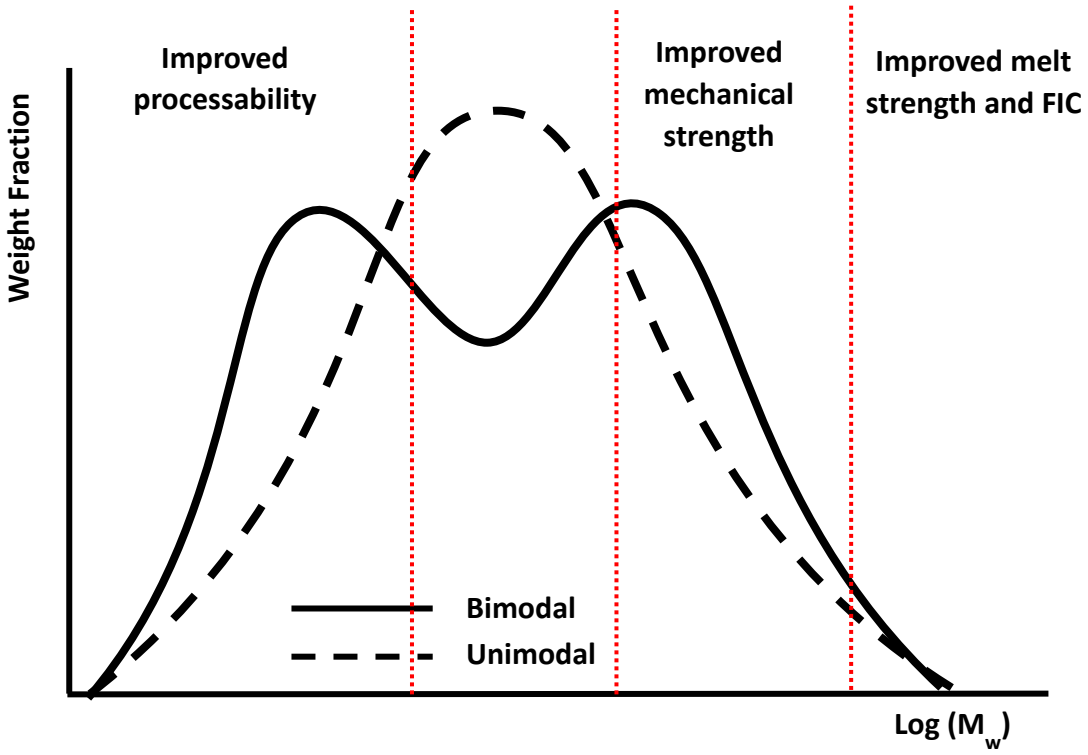

Figure 3.2: A schematic comparison of a typical unimodal and bimodal molecular weight distribution. The bimodal distribution incorporates the optimum properties from different molecular weight regions (such a processability or mechanical strength) into a single blend. Adapted from Ref 22.

A single peak in a MWD is termed unimodal, with several peaks termed multimodal. Typically, bimodal MWDs are used for pipe manufacture as the LMW (and shorter chain components) exhibit improved processability and the HMW (and hence longer chains) exhibit better mechanical strength (Figure 3.2). The chains with the highest molecular weight, often termed a 'high molecular weight tail' (HMWT), impart melt strength.

3.3 Differential Scanning Calorimetry

3.3.1 HDPE

DSC obtained the onset and peak of the melting and crystallisation temperatures of both PE1 and PE2 (Figures 3.3 and 3.4, respectively) in order to understand the thermal properties and establish temperature protocols for polymer processing.

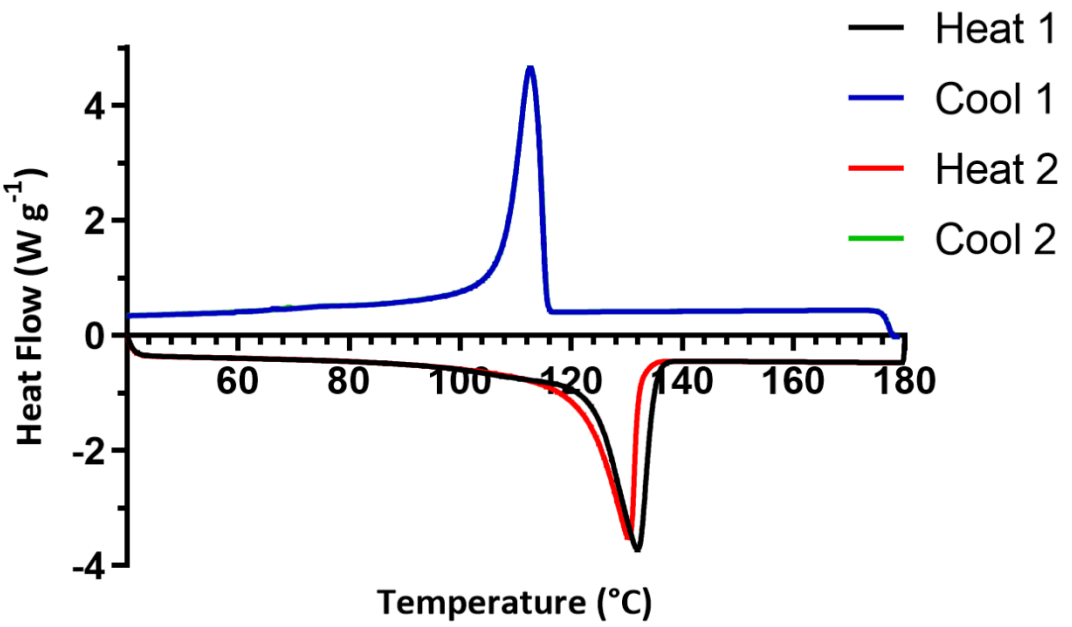

Figure 3.3: DSC curves showing melting endotherms (down) and crystallisation exotherms (up) for PE1. Measurements consisted of two consecutive cycles between 40 – 180 – 40 °C at a heating/cooling rate of 10 °C min^{-1} with 5-minute isothermal holds at each terminal temperature. The blue (Cool 1) and green (Cool 2) curves overlap exactly, hence why the latter cannot be observed on the graph.

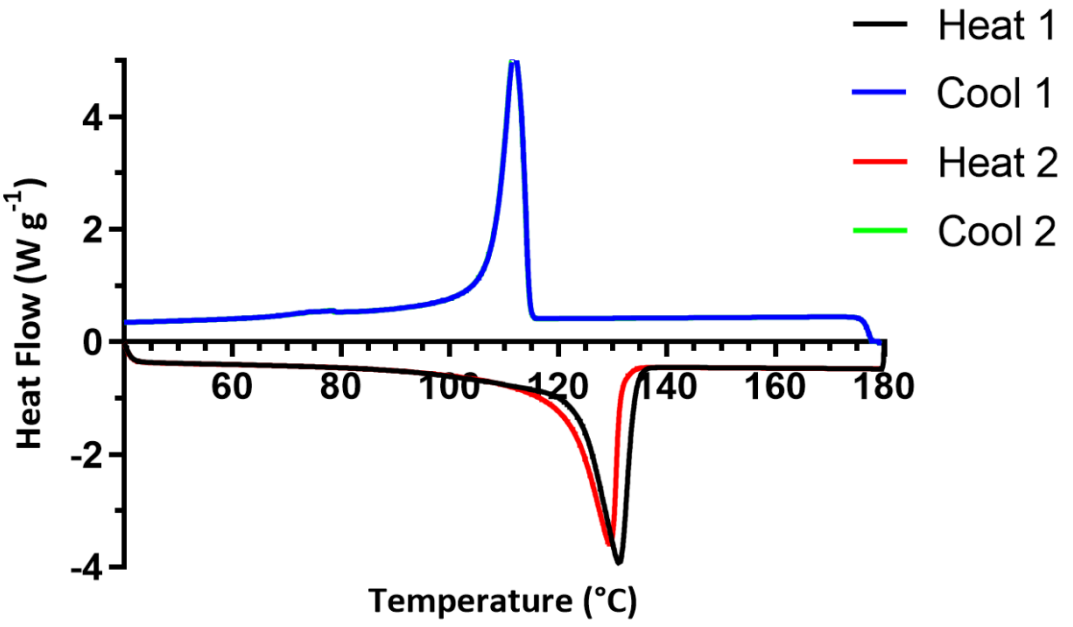

Figure 3.4: DSC curves showing melting endotherms (down) and crystallisation exotherms (up) for PE2. Measurements consisted of two consecutive cycles between 40 – 180 - 40 °C at a heating/cooling rate of 10 °C min^{-1} with 5-minute isothermal holds at each terminal

temperature. The blue (Cool 1) and green (Cool 2) curves overlap exactly, hence why the latter cannot be observed on the graph.

Each sample was subjected to the same heat-cool temperature profile: 40 - 180 - 40 °C at a heating/cooling rate of 10 °C min^{-1} with a 5-minute isothermal hold at each terminal temperature (Section 2.4.3). This profile was repeated twice in succession for each sample: the first to remove any residual thermal or processing history and the second to observe the melting properties of the polymers (Table 3.2).

	Melting				**Crystallisation**			
	Onset/ °C	**Peak/ °C**	**X_c/ %**	**ΔH / J g^{-1}**	**Onset/ °C**	**Peak/ °C**	**X_c/ %**	**ΔH / J g^{-1}**
PE1								
1st Cycle	122.9	131.9	65.4	188.2	118.1	116.7	62.0	178.6
2nd Cycle	*121.5*	*130.3*	*63.2*	*182.1*	*118.1*	*116.7*	*61.4*	*176.9*
PE2								
1st Cycle	122.8	131.2	65.1	187.4	117.3	115.8	58.0	167.1
2nd Cycle	*120.6*	*129.4*	*65.0*	*187.2*	*117.2*	*115.8*	*57.1*	*164.5*

Table 3.2: Values for the onsets, peak melting temperatures, peak crystallisation temperatures, percentage crystallinity (X_c) and enthalpy of transition (ΔH) of PE1 and PE2 obtained by DSC measurements. Two consecutive temperature cycles (40 – 180 – 40 °C at 10 °C min^{-1}) were performed with five-minute isothermal holds at each terminal temperature. X_c and ΔH values were obtained by integrating the melting and crystallisation peaks.

Melting in semicrystalline polymers is a complex process compared to small organic molecules. Due to the distribution of crystallite sizes, the melting peak is not sharp and a broad temperature range is observed.[23] Literature values of PE melting points cover a broad range between 110 – 150 °C with values obtained between 130 – 132 °C for PE1 and 129 – 131 °C for PE2 which were consistent with literature values.[20,24–26] Upon melting, the crystallites binding the solid state together melt to become a viscous liquid.[20] In contrast to small molecules, however, the melting point of polymers is not fixed and can be influenced by molecular composition, thermal history and heating rate.[27] Due to chain entanglement, crystallisation of polymers is slow and kinetically controlled[28] and thus the degree of crystallisation can be affected by the cooling rate. Generally speaking, faster cooling rates result in lower crystallinity as the molecular segments have insufficient time to arrange into

lamellae.[27] A large number of small crystals, with a high surface to volume ratio, and therefore a relatively high surface energy, are formed when the cooling rate is high. Larger crystals are energetically favoured over smaller ones as the surface energy is reduced[29] and thus melting occurs at higher temperatures – rapid cooling therefore leads to reduced melting temperatures and a broad melting range because crystals of many different sizes are formed, each with a unique melting temperature.[27] Note the very rapid onset of crystallisation, yet no change in crystallisation temperature was observed for both cycles for both materials. Due to supercooling effects, which is a consequence of the large energy barrier to the formation of an ordered crystalline phase, the melting temperature will lie above the crystallisation temperature, which was consistent with these results.[30]

Small shifts were seen in the melting points between first and second heating cycles. The first heating step is regarded as the melting of nascent crystals, whereas the second heating is regarded as the melting of a melt-crystallised sample.[23] The peak melting of the latter sample has been shown to be lower than the nascent melting temperature at any heating rate.[23] According to the LH Theory, the thickening of the lamellae formed at the crystallisation temperature accounts for the difference in observed melting temperature peaks.[31]

PE is known to crystallise into chain-folded lamellae, with a range of lamellae thicknesses, the thin nature of which causes the melting point to be depressed below the equilibrium melting point, T_m^0 (145.5 °C for HDPE).[27,32] Assuming, therefore, that a specific melt temperature depends upon lamellae thickness, a correlation may be established between an observed melt temperature with the thickness of lamellae at a specific temperature.[32] There is a thermodynamic driving force towards lamellae thickening caused by the minimising of the total free energy and, consequently, an increase in lamellae thickness (and also the degree of crystallinity), causes the melt temperature to be increased.[32]

Imperfections, such as crystal defects or high surface energies, within the crystal are attributed to the depression of polymeric melting points from T_m^0. A high surface-to-volume ratio exists due to the lamellar morphology and a relation between the melting point depression, $T_m^0 - T_m$ and lamellar thickness, *l*, is given by:

$$l = \frac{2\sigma_e T_m^0}{\Delta H_f (T_m^0 - T_m)} \qquad 3.1$$

where σ_e is the free energy of formation of the lamellae surface and ΔH_f is the bulk heat of fusion.[32] This equation also shows that an increase in *l*, and hence degree of crystallinity, results

in higher peak melting temperatures.[32] The ratio $\sigma_e/\Delta H$ was estimated by Eby and Brown to be 2.04 x 10^{-8} cm.[33] Assuming a value of $T_m^0 = 145.5\ °C$, the lamellar thickness of PE1 and PE2 can be obtained from the melting peaks (Table 3.3). The Gibbs-Thomson equation predicts a thickness of 25 nm for a peak melting temperature of 131 °C (for linear PE with M_n = 9 kDa at a heating rate of 1 °C min^{-1}).[23,34] The large difference in average M_W between theoretical values and these commercial blends and the faster cooling rate likely account for this discrepancy. An increased number of chain entanglements, owing to the HMW, will hinder chain folding into lamellae and, given that crystallisation is a kinetically-controlled process, the higher heating rate will have the effect of 'freezing' chains in place before they can adopt an ideal, lower energy folded conformation.[35]

	Peak Melt/ °C	**Lamellar Thickness/ nm**
	PE1	
1st cycle	131.9	2.18
2nd cycle	*130.3*	*1.95*
	PE2	
1st cycle	131.2	2.08
2nd cycle	*129.4*	*1.84*

Table 3.3: The lamellae thickness calculated from the peak melting temperature for each melting endotherm for PE1 and PE2. Thicker lamellae cause higher peak melting temperatures.

As is evident, the slight decrease in melting peak between successive cycles can be attributed to the decrease in lamellae thickness caused by surface melting and reorganisation.[36] Wunderlich *et al.* observed smoothing of the surface morphology, occurring by a two-step process: melting and then recrystallisation into folded-chain lamellae.[36] By slicing crystals, they observed that an increased surface area resulted in an enhanced melting rate, itself dependent on the time to melt a single chain and thus lamellae thickness.[36] The heating rate of 10 °C min^{-1} was sufficiently high to reduce chain reorganisation on heating.[36] Comparing PE1 and PE2, PE1 maintained a slightly thicker lamellae than PE2 which was consistent with the X_c values obtained from DSC (Table 3.2).

Polymer crystallinity can be obtained by quantifying the heat associated with fusion (melting) of HDPE, reported as a percentage crystallinity, X_c, by normalising the observed heat of melting with that of a 100 % crystalline sample of the same polymer.[37] X_c values were calculated using a value of 293 J g^{-1} as the standard enthalpy of fusion of a 100 % crystalline PE crystal (Table 3.2).[38] For crystals displaying polymorphism, phase transitions between the respective polymorphs can be identified by DSC, as each crystal form typically melts at a different temperature.[2] Measuring X_c for such polymorphic crystals requires values of a 100 % crystalline sample for each polymorph.[2] SAXS/WAXS measurements are often favoured instead to calculate X_c and determine the respective crystal structure. Comparing X_c values of the crystallisation exotherms for PE1 and PE2 (Table 3.2), the crystallinity was similar for both materials, with PE1 showing slightly greater *crystallinity* than PE2 in all cases except the second heating. PE2 showed a significantly lower crystallinity during crystallisation in comparison to the melting, which was not observed with PE1. PE2 was synthesised with a degree of hexene co-monomer[2] to achieve the desired characteristics of the MWD and it was likely that these branches were contributing to the decrease in the crystallinity at this step.[20]

3.3.2 UHMWPE

DSC was used to obtain the onset and peak of the melting and crystallisation temperatures (Table 3.4 and Figures 3.5–3.8) of three UHMWPE oriented tapes (TA23, XF23 and S1) in order to establish conditions for fabricating SPCs. The same heat-cool protocol as for the previous HDPE measurements was used (Section 2.4.3).

All UHMWPE tapes were obtained from Teijin Aramid Endumax brand. TA23 was fabricated by compacting, rolling and stretching of PE powder to a thickness of 60 μm and a density of 46.6 g m^{-2}. XF23 was fabricated in the same manner, but with additional uni-directional laying and cross-plying steps of 4 x TA23 layers (0°/90°/0°/90°), bonded together with Kraton adhesive, with an areal density of 198 g m^{-2}. S1 was a 170 μm thick, non-commercial grade, regarded by industrial colleagues to refer to an intermediate stretching stage of the production of TA23.[18] Further specific manufacturing details could not be obtained.

°C	PE1	PE2	TA23	XF23	S1
1st Heat	131.9	131.2	147.8, 152.8, 160.5	128.8, 147.6 149.0	145.0
1st Cool	118.1	115.8	116.5	119.4	120.5
2nd Heat	*130.3*	*129.4*	*138.0*	*134.9*	*135.3*
2nd Cool	*118.1*	*115.8*	*116.0*	*119.1*	*120.2*

Table 3.4: Peak melting and crystallisation temperatures for HDPE and three UHMWPE tapes. Two consecutive temperature cycles (40 – 180 – 40 °C at 10 °C/min) were performed with five-minute isothermal holds at each terminal temperature.

Rastogi *et al*. showed that solid state drawing of UHMWPE could be achieved across a broad temperature range, below $T_m^0(PE)$, through reactor synthesis using a nanoparticulate-supported Ziegler-Natta catalyst system in order to significantly reduce the entanglement density.[39,40] The disentangled solid state is attractive for making high-modulus and high-strength fibres due to its easier drawability than the corresponding entangled state.[41] However, upon heating above the melting point, such disentangled chains will re-entangle and lose the processability and mechanical benefits.[41] Solid-state drawing of UHMWPE tapes is both economically and environmentally attractive as the use of flammable and toxic solvents is not necessary, as is the case for solution-/gel-spinning of fibres.[40] In composite manufacture, tapes are generally preferred over fibres because the performance is enhanced owing to the lower surface to volume ratio of the former.[40,41] An absence of strain hardening upon deformation, indicates the presence of disentangled chains.[41] High modulus values are obtained for such mechanically drawn UHMWPE tapes caused by the orientation of the molecular chains and the subsequent greater van der Waals interactions between them.[41]

Most polymers are only partially crystalline which results in a broad melting temperature range and melting points significantly lower than the equilibrium melting point, T_m^0 (145.5 °C for HDPE).[27] Multiple melting peaks are common, and may be caused by:

1. Recrystallisation during melting
2. Different crystal forms (or different polymer morphologies)
3. Crystal-crystal transitions
4. Annealing or heat treatment causing changes to crystal size and perfection

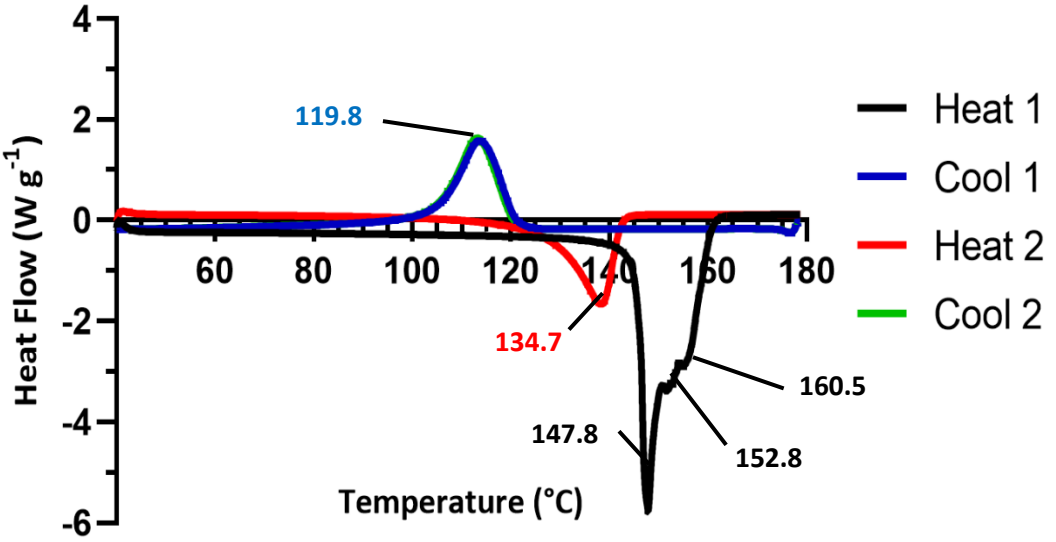

Figure 3.5: DSC curves showing melting endotherms (down) and crystallisation exotherms (up) for UHMWPE tape TA23. Measurements were performed in duplicate and consisted of two consecutive cycles between 40 – 180 – 40 °C at 10 °C min^{-1} with 5-minute isothermal holds at each terminal temperature.

Multiple melting endotherms were observed in the DSC curves for TA23 (Figure 3.5), with similar multiple melting endotherms for drawn UHMWPE fibres observed by several research groups.[42,45–48] Consider that the spherulitic melting point (T_{ms}) of HDPE was 129 - 132 °C and that all melting endotherms in the first heating were greater even than $T_m^0\ (PE)$ = 145.5 °C, which highlighted the effect of orientation upon melting temperatures.[42]

Orthorhombic crystals typically melt at 137 °C,[42] however Ratner observed that abnormally high melting temperatures (greater than T_m^0) arose from constrained orthorhombic crystals caused by the stabilisation of the phase by applied stress (i.e. drawing and orientation) – lower entropy, extended chains are preferred over higher entropy entangled chains.[45,49] Yeh *et al.* demonstrated that the main melting endotherm could be pushed to higher temperatures (from 131 °C to 140 °C) by increasing the draw ratio.[42] Schulte *et al.* and Stern *et al.* independently proposed a combination of both fibre relaxation and crystal form transformation and melting.[43,44] They suggested that the first small shoulder related to fibre relaxation, the second peak arose due to partial melting and solid-state phase transformation of orthorhombic to hexagonal crystal forms and the final peak resulted from the transition to the hexagonal phase.[43]

The peak melting endotherm at approximately 153 °C was attributed to the solid-phase transition of crystal phases from constrained orthorhombic to hexagonal or pseudohexagonal.[42] This transition only occurs for constrained fibres[50] and this new phase subsequently melts at

temperatures around 159 °C.[50,51] A melting temperature range of 155 – 176 °C has been reported for this final phase, indicating that preparation methods, molecular weight and mode of constraining can all have an impact.[51] Modulated-DSC (MDSC) could be used to observe if these transitions are reversible or irreversible.

Polymers drawn into fibres typically display crystallinities, melting points and melting enthalpies that are much greater than the equilibrium melting point and bulk polymer properties.[27,52,53] This was evident with the materials used in this work, as all UHMWPE tapes had a peak melting greater than 145.5 °C, with TA23 reaching a maximum of 160.5 °C. Aligning and stretching the chains produces thermodynamically more stable crystals than conventionally crystallised melts, thus leading to higher melting temperatures, T_m.[52] Considering Gibbs free energy relations, the melting point is given by $T_m = \Delta H/\Delta S$, where ΔH and ΔS are the enthalpy and entropy difference between crystal and liquid phases respectively.[52] The entropy is determined by the chain conformations and the enthalpy by the interaction between chains.[20,27,52] Therefore, controlling or changing either ΔH or ΔS could alter the crystalline melting behaviour.[52] The shift in T_m is the result of decreasing entropy effects upon stretching and orienting the chains, as both the bulk unstretched and oriented chains have similar enthalpies of melting, thus increasing T_m.[52] Increasing the draw ratio, and hence orientation, will also increase the crystallinity as the improved ordering allows for closer chain packing.[52,54]

The shift in T_m arises due to an entropy effect, as the enthalpy of melting will be the same regardless of whether the fibres are constrained or not. Chains in the constrained fibres have no freedom to relax and so any gain in entropy per monomer unit is reduced compared to the unconstrained fibres.[52] Since $T_m = \Delta H/\Delta S$, T_m tends towards higher temperatures as ΔS decreases upon constraining.[52] Constraining the fibre in a DSC pan above the melt temperature, and therefore partially restricting thermal relaxation of the stretched chains, was achieved by using very shallow pans (Figure 3.6). The tape could be pressed flat against both surfaces and a single melting peak appeared at 146.9 °C with a small shoulder at 151.8 °C, suggesting that the majority of crystals remained in the constrained orthorhombic phase.[42]

Upon second heating of all of the unconstrained UHMWPE tapes, the peak melting endotherm reduced in value to around 135 °C, indicating a return to a random coil conformation.[52] Molecules will attempt to regain the preferred isotropic structure on heating and so relaxation will occur.[52]

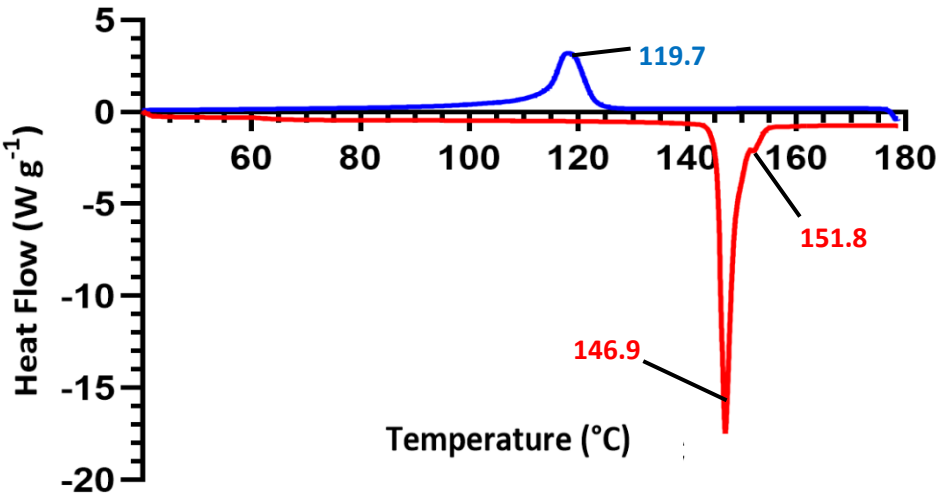

Figure 3.6: DSC curves showing melting endotherms (heating step, red) and crystallisation exotherms (crystallisation step, blue) for constrained UHMWPE tape TA23. Measurements were performed in duplicate and consisted of two consecutive cycles between 40 – 180 – 40 °C at 10 °C min^{-1} with 5-minute isothermal holds at each terminal temperature.

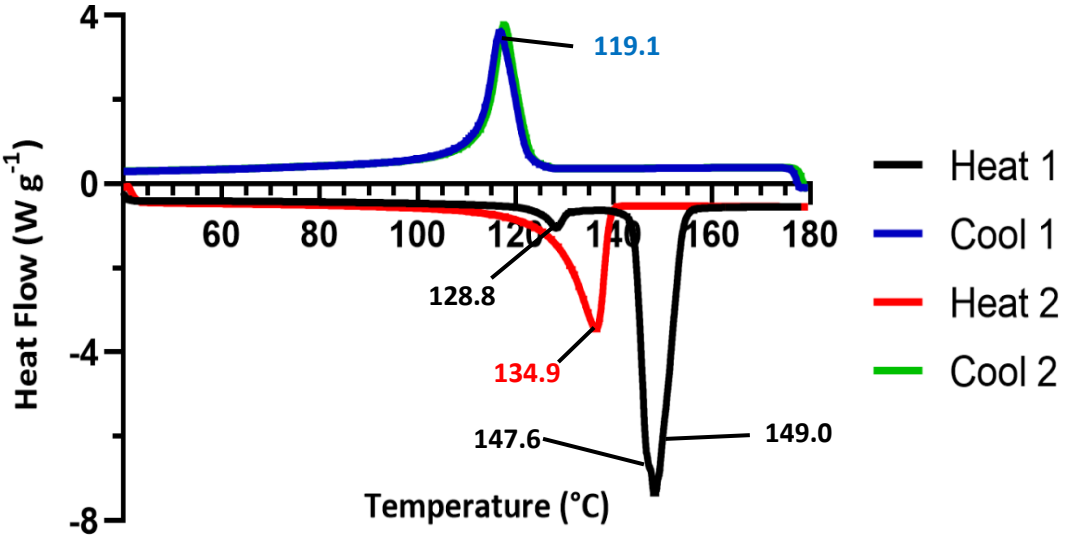

Figure 3.7: DSC curves showing melting endotherms (down) and crystallisation exotherms (up) for UHMWPE tape XF23. Measurements were performed in duplicate and consisted of two consecutive cycles between 40 – 180 – 40 °C at 10 °C min^{-1} with 5-minute isothermal holds at each terminal temperature.

During the first heating cycle for XF23, the main melting endotherm occurred at 149.0 °C in addition to a small shoulder at 147.6 °C and a much smaller peak at 128.8 °C (Figure 3.7). This particular tape was constructed of UHMWPE tape or fibres encased in a PE matrix. Therefore, this small peak was likely to be the HDPE melting, and the subsequent peaks from the UHMWPE, which was partially constrained by entanglements with the surrounding HDPE

matrix and, therefore, unable to transition from the constrained orthorhombic phase.[42] Upon second heating, these peaks coalesced into a single peak at 134.9 °C, also suggesting that the stretched chains had relaxed and entangled in the melt.

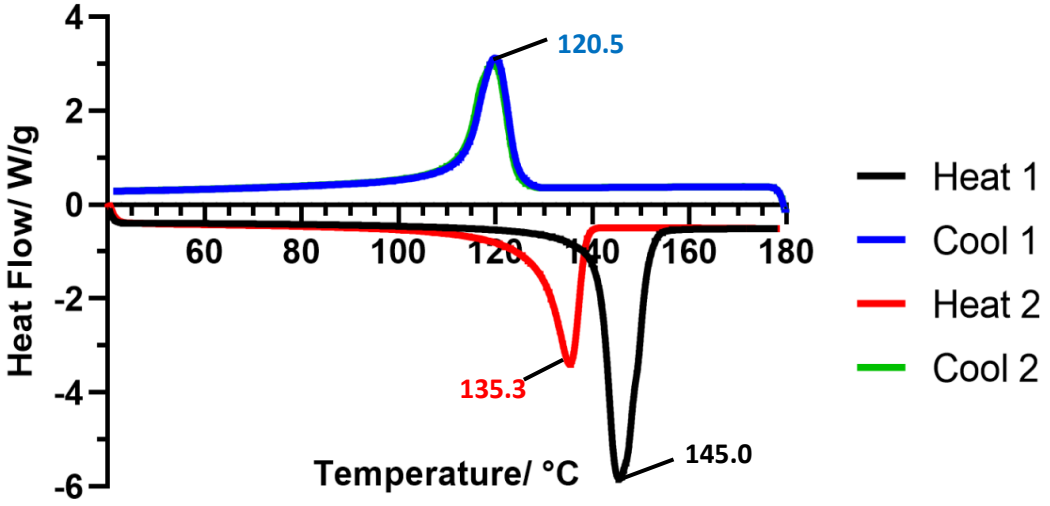

Figure 3.8: DSC curves showing melting endotherms (down) and crystallisation exotherms (up) for UHMWPE tape S1. Measurements were performed in duplicate and consisted of two consecutive cycles between 40 – 180 – 40 °C at 10 °C min^{-1} with 5-minute isothermal holds at each terminal temperature.

The initial peak melting temperature was greater than T_m^0, which suggested that the polymer chains were oriented.[52] No additional peaks were seen for S1, due to the fact that there were no individual fibres in the tape, as in TA23 and XF23 (Figure 3.8). Therefore, the appearance of any multiple peaks was attributed to the presence of UHMWPE fibres. Upon second heating, the peak melting endotherm of this tape reduced to 135.3 °C, which indicated chain relaxation also occurred with this material.[52]

The large shifting of peak melting points indicated a large degree of thermal relaxation of the polymer chains, and the effect of orientation upon melting behaviour.[20,27,52] Melting points for the second heating of each tape were very similar to those of bulk, entangled HDPE. Crucially, these measurements gave a temperature window for SPC fabrication of 136 – 144 °C with a temperature of 140 °C chosen. This ensured that only the HDPE matrix melted whilst the orientation of UHMWPE fibres was preserved. Exceeding the melting point of the UHMWPE resulted in a rapid loss of orientation as the tape contracted back into an entangled melt, which was most apparent for TA23. The crystallisation temperatures for each tape were consistent with those for HDPE.[20]

3.4 Rheology

Rheological measurements were primarily used to gather information about the viscosity and moduli components: viscous and elastic. For the PE melts in question, a series of measurements were performed to obtain information regarding the viscosity behaviour with respect to shear rate.

3.4.1 Amplitude Sweeps

Amplitude sweeps (Section 2.5.7) were an essential first step in assessing rheological behaviour as they ascertained the upper limit of sample integrity and described the deformation behaviour in this range.

According to DSC measurements, the spherulitic melting points of the studied PEs were 129 – 132 °C and the equilibrium melting point (from literature) was 145.5 °C.[27] Thus, the rheology measurements of HDPE were performed at significantly higher temperatures: 150 °C, 170 °C and 190 °C. At each temperature, a strain sweep from 100 - 0.01 % strain was undertaken for PE1 (Figures 3.9 – 3.11) to find the LVR at five angular frequencies, ω, between 0.06283 – 628.3 rad s^{-1} (Section 2.5.7). All measurements were performed in duplicate and averaged. The angular frequency refers to the frequency of a sinusoidal waveform in oscillation, given by $\omega = 2\pi f$ where f is the frequency in s^{-1} and ω is measured in radians per second (rad s^{-1}).[55-57] The LVR is the area in which the microstructure responds linearly to the magnitudes of stress and strain over time, such that *G'*, *G''* and η^* show a linear response to temperature and angular frequency. [58,59]

Cox and Merz devised an empirical relationship of great importance. They observed that the steady state shear viscosity, η, plotted against shear rate, $\dot{\gamma}$, corresponded with a plot of complex viscosity, $|\eta^*|$, against angular frequency, ω: $\eta^* = G^*/i\omega$ where G^* is the complex modulus. Thus $\eta(\dot{\gamma}) = \eta^*(\omega)$ at $\dot{\gamma} = \omega$.[61,62] In order to successfully use this rule, steady state values must be used – any transient effects arising from secondary flows, such as start-up flow or inertia, must have fully decayed and the flow has to be laminar.[63] This rule is especially useful for polymer melts, as the steady state viscosities are difficult to measure at high shear rates on highly viscous materials due to sample fracture or turbulent flow.[63] Therefore, predictions of $\eta(\dot{\gamma})$ can be made from oscillatory measurements and such data are usually more reliable.[61,64]

A constant viscosity against strain indicates the linear region,[60] and therefore a 1 % strain was chosen for subsequent oscillation frequency sweeps.

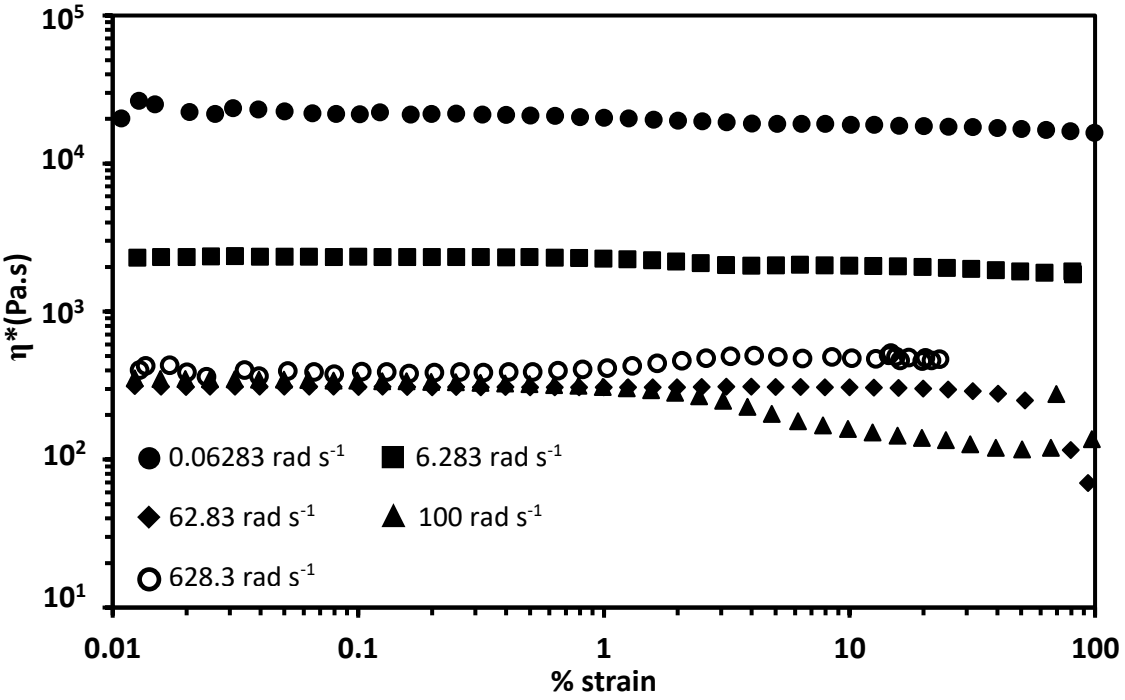

Figure 3.9: Modulus of complex viscosities, η^*, of PE1 at 150 °C measured by amplitude sweeps at ω = 0.06283 rad s^{-1}, 6.283 rad s^{-1}, 62.83 rad s^{-1}, 100 rad s^{-1} and 628.3 rad s^{-1}.

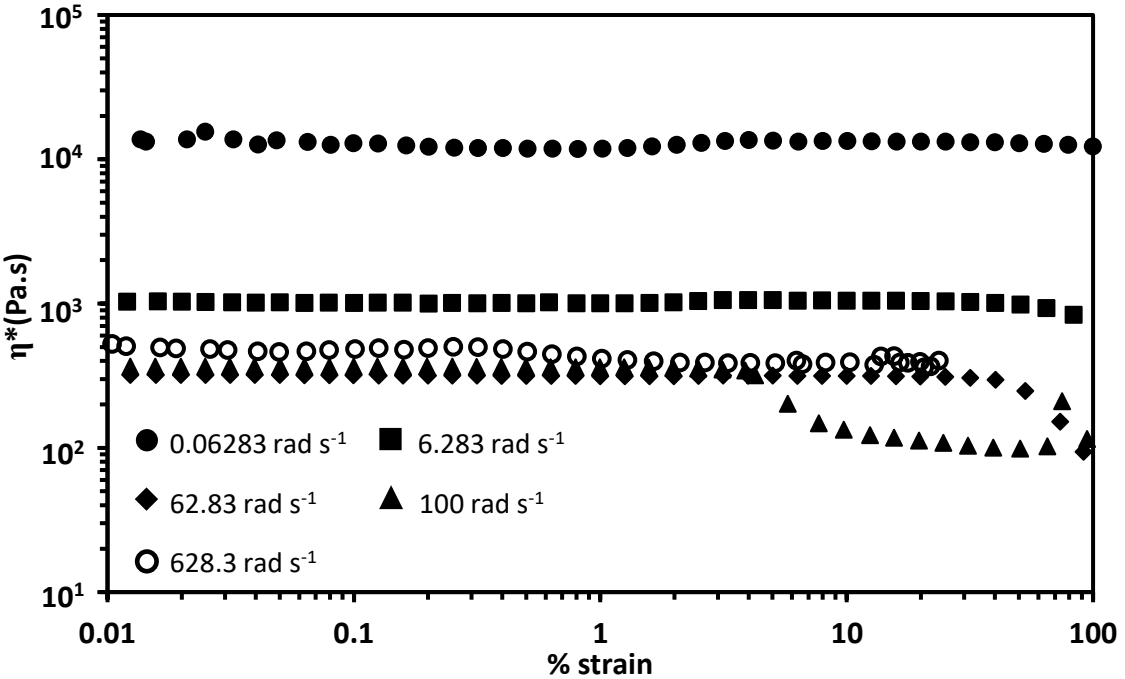

Figure 3.10: Modulus of complex viscosities, η^*, of PE1 at 170 °C measured by amplitude sweeps at ω = 0.06283 rad s^{-1}, 6.283 rad s^{-1}, 62.83 rad s^{-1}, 100 rad s^{-1} and 628.3 rad s^{-1}.

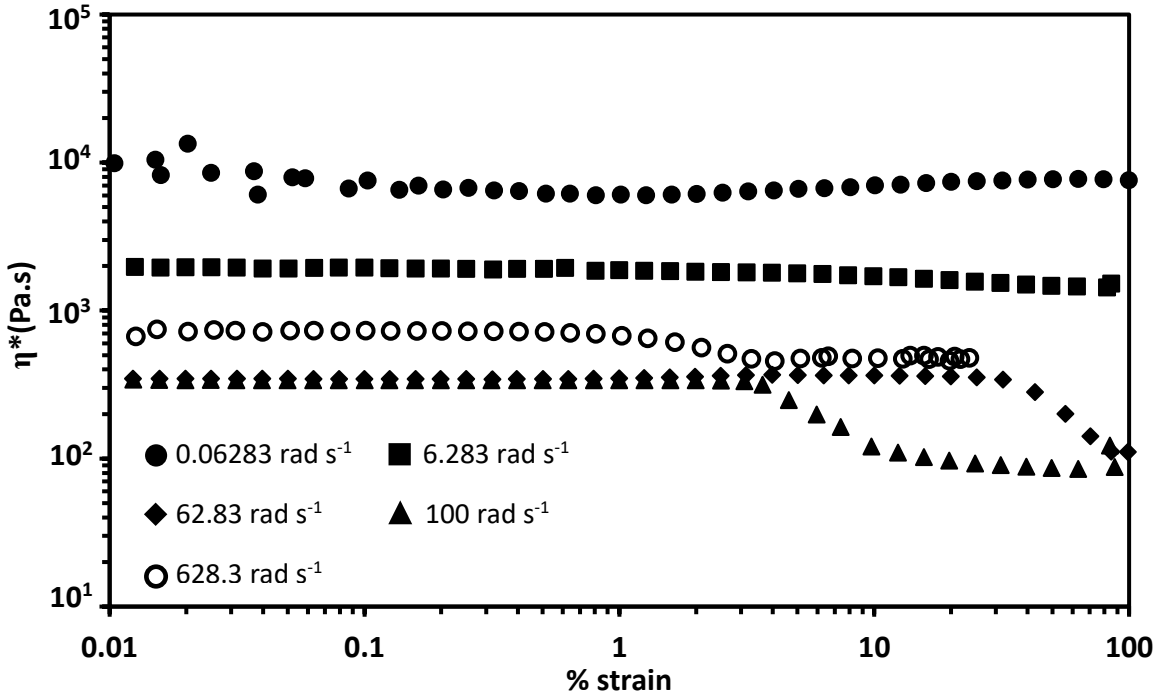

Figure 3.11: Modulus of complex viscosities, η^*, of PE1 at 190 °C measured by amplitude sweeps at ω = 0.06283 rad s^{-1}, 6.283 rad s^{-1}, 62. 83 rad s^{-1}, 100 rad s^{-1} and 628.3 rad s^{-1}.

The same procedure was applied to PE2 and a 1 % strain also selected for future frequency sweeps (Figures 3.12 – 3.14).

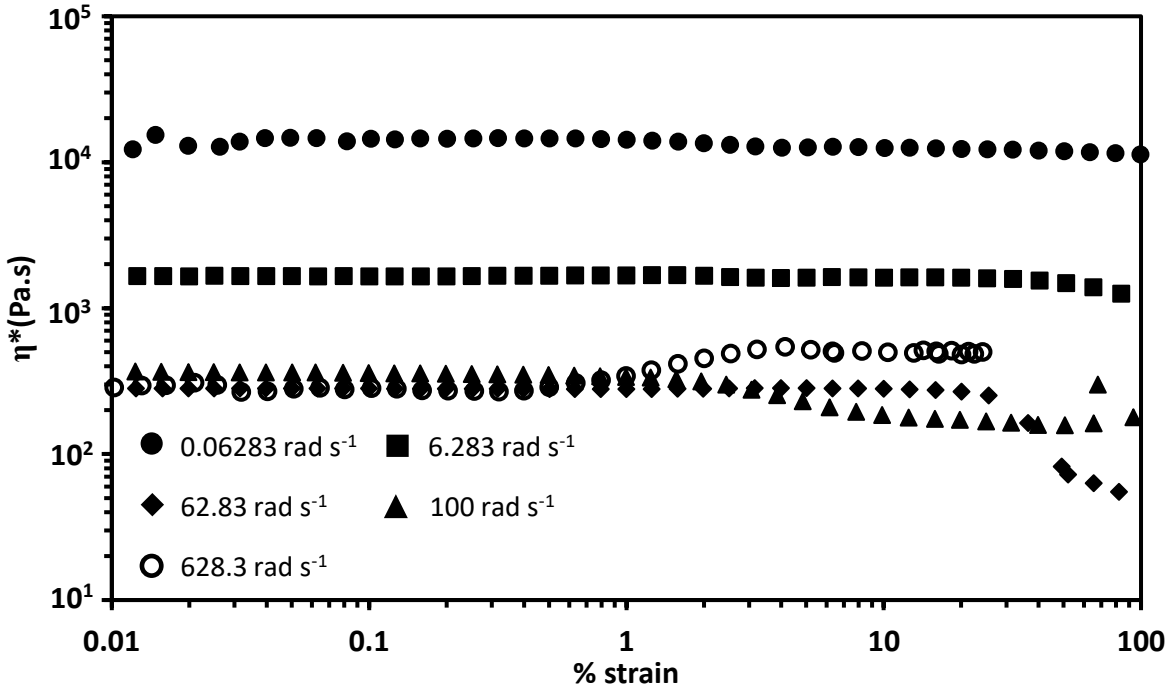

Figure 3.12: Modulus of complex viscosities, η^*, of PE2 at 150 °C measured by amplitude sweeps at ω = 0.06283 rad s^{-1}, 6.283 rad s^{-1}, 62.83 rad s^{-1}, 100 rad s^{-1} and 628.3 rad s^{-1}.

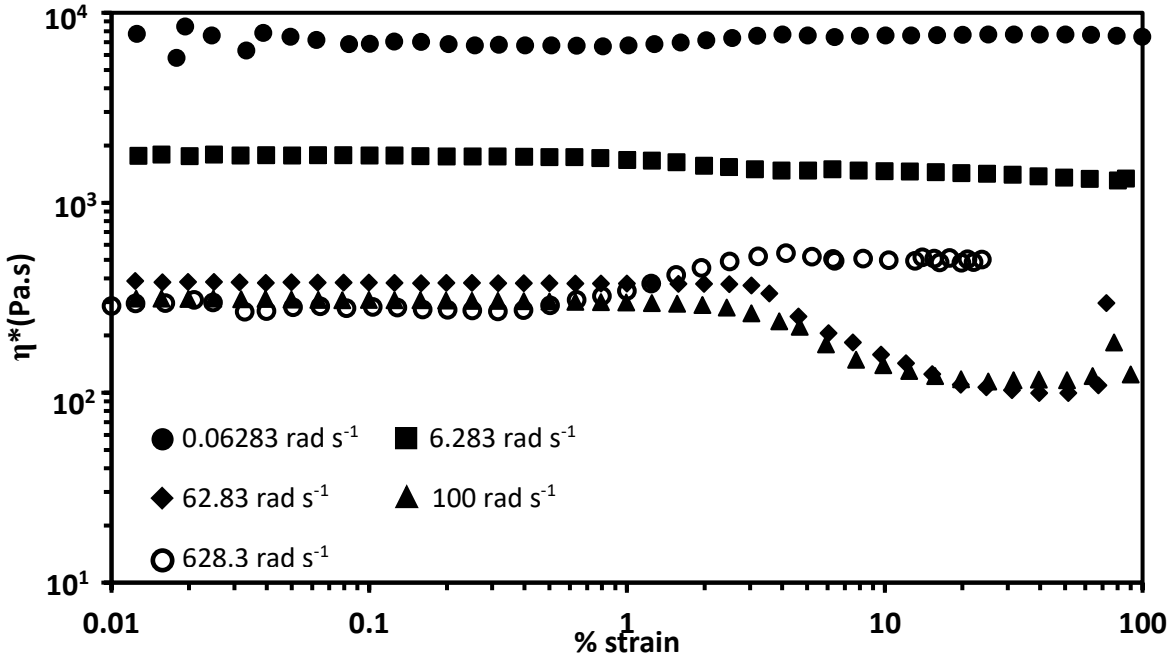

Figure 3.13: Modulus of complex viscosities, η^*, of PE2 at 170 °C measured by amplitude sweeps at ω = 0.06283 rad s^{-1}, 6.283 rad s^{-1}, 62.83 rad s^{-1}, 100 rad s^{-1} and 628.3 rad s^{-1}.

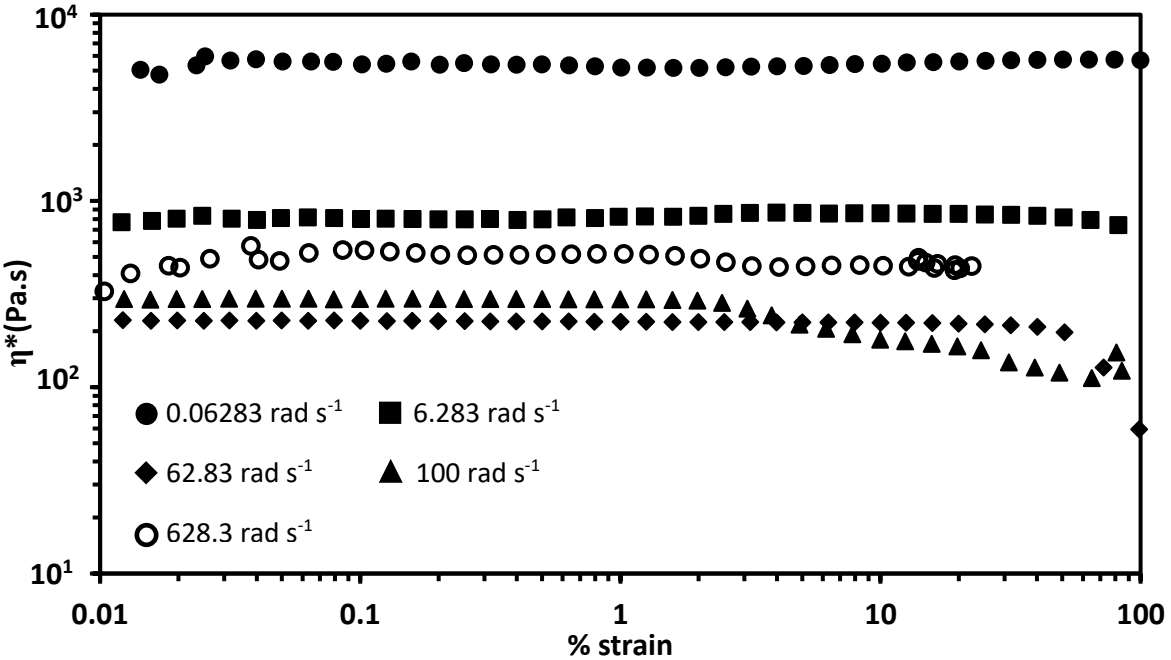

Figure 3.14: Modulus of complex viscosities, η^*, of PE2 at 190 °C measured by amplitude sweeps at ω = 0.06283 rad s^{-1}, 6.283 rad s^{-1}, 62.83 rad s^{-1}, 100 rad s^{-1} and 628.3 rad s^{-1}.

It was evident that the highest angular frequency (628.3 rad s^{-1}) showed non-linear behaviour at both low and high % strains respectively. All 628.3 rad s^{-1} sweeps displayed viscosity values equal to or greater than the preceding data at 62.83 rad s^{-1} in both initial and repeat measurements. The reason why was unclear, as the highest frequency curves should display

the lowest viscosities due to shear thinning.[20] A possible explanation was the build-up of stress during the measurement.[65] Data for 628.3 rad s^{-1} also showed points aggregating and not progressing beyond 50 % strain which suggested a critical amplitude was reached, above which non-linearities emerged and large-scale, irreversible sample deformation occured.[65] The noise present at low strain was attributed to low torque and therefore reduced measurement sensitivity.[60] The deviations at higher percentage strains were most likely the result of emerging inertial effects (manifest as slow flow)[63], which can arise from the centrifugal effects of the periodic acceleration and deceleration of the motor shaft.[66] Prior to the measurements, the moment of inertia of the tool fixture was calculated by the software and applied as a correction to the results. However, if this correction becomes too large, secondary flows are present in the sample (i.e. sample inertia) which, in some cases, can cause the observed viscosity to increase slightly.[58] Barnes noted that inertia can cause issues during high frequency oscillatory measurements, especially when approaching frequencies of 100 s^{-1}.[58] As the flow becomes increasingly non-linear, these inertial effects are amplified.[58,66]

3.4.2 Frequency Sweeps

Initial frequency sweep measurements between ω = 628.3 – 0.06283 rad s^{-1} caused an inflection in the complex viscosity at high frequency, the cause of which was unclear (Figure 3.15) since PE is a known shear-thinning melt.[20] Since the measurements were performed under nitrogen atmosphere to minimise oxidative degradation at temperatures 50 °C lower than the typical industrial processing temperature, it was unlikely that thermal decomposition of the sample was the cause of the observed phenomenon. Additionally, both materials had antioxidant additives to prevent this degradation.

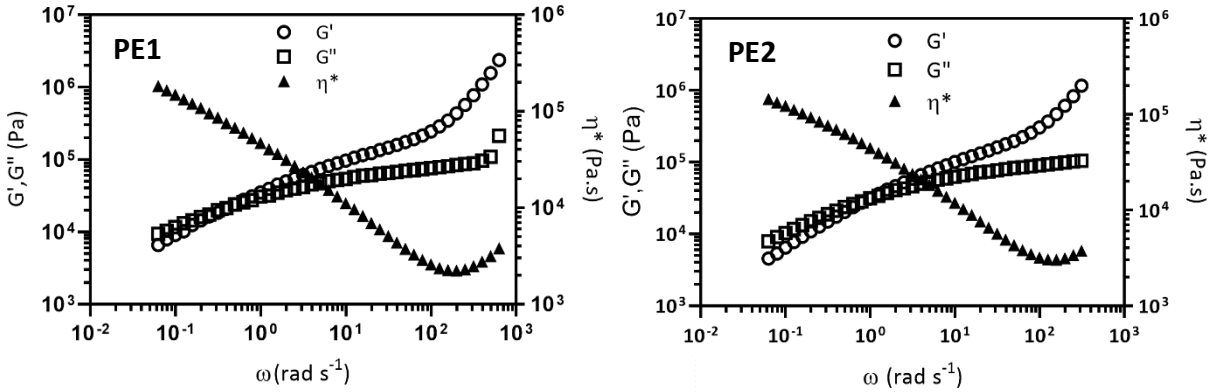

Figure 3.15: Frequency sweep of PE1 (left) and PE2 (right) at 150 °C with 8 mm parallel plate geometry, 0.5 mm gap, 1% strain amplitude and angular frequency, ω = 628.3 rad s^{-1}. The inflection in η^* was present in all measurements at ω > 100 rad s^{-1}. Open circles show data for

G' (storage modulus), open squares show the data for *G''* (loss modulus) and the filled triangles show the data for η^*(modulus of complex viscosity).

The inflection was still present, even after repeating this measurement at different % strains and performing both high-low and low-high sweeps. Temperature effects were also discarded as the inflection was present across all temperatures 150 – 200 °C. Other factors, such as dilatancy above a critical shear rate, solidification under pressure or inertial effects could have contributed to the inflection.[66] Correlating with the amplitude sweep data, the beginning of the inflection arose as the sample approached a deformation of 100 % strain at angular frequencies greater than 100 rad s^{-1}, therefore suggesting some form of irreversible sample deformation was occurring.[58,66] At 1 % strain at 628.3 rad s^{-1} the data was non-linear and beginning to inflect, thus suggesting this was not within the LVR. A significant upturn was also seen in G' and G" for PE1 and G' for PE2. Stadler *et al.* concluded that an upturn in G" at $\omega > 100$ rad s^{-1} was caused by inertia and the onset of Rouse motions.[67] By reducing the maximum frequency from 628.3 rad s^{-1} to 100 rad s^{-1}, the inflection was not observed (Figure 3.16). The temperature range was extended to 200 °C with measurements taken at each 10 °C increment (Figure 3.16).

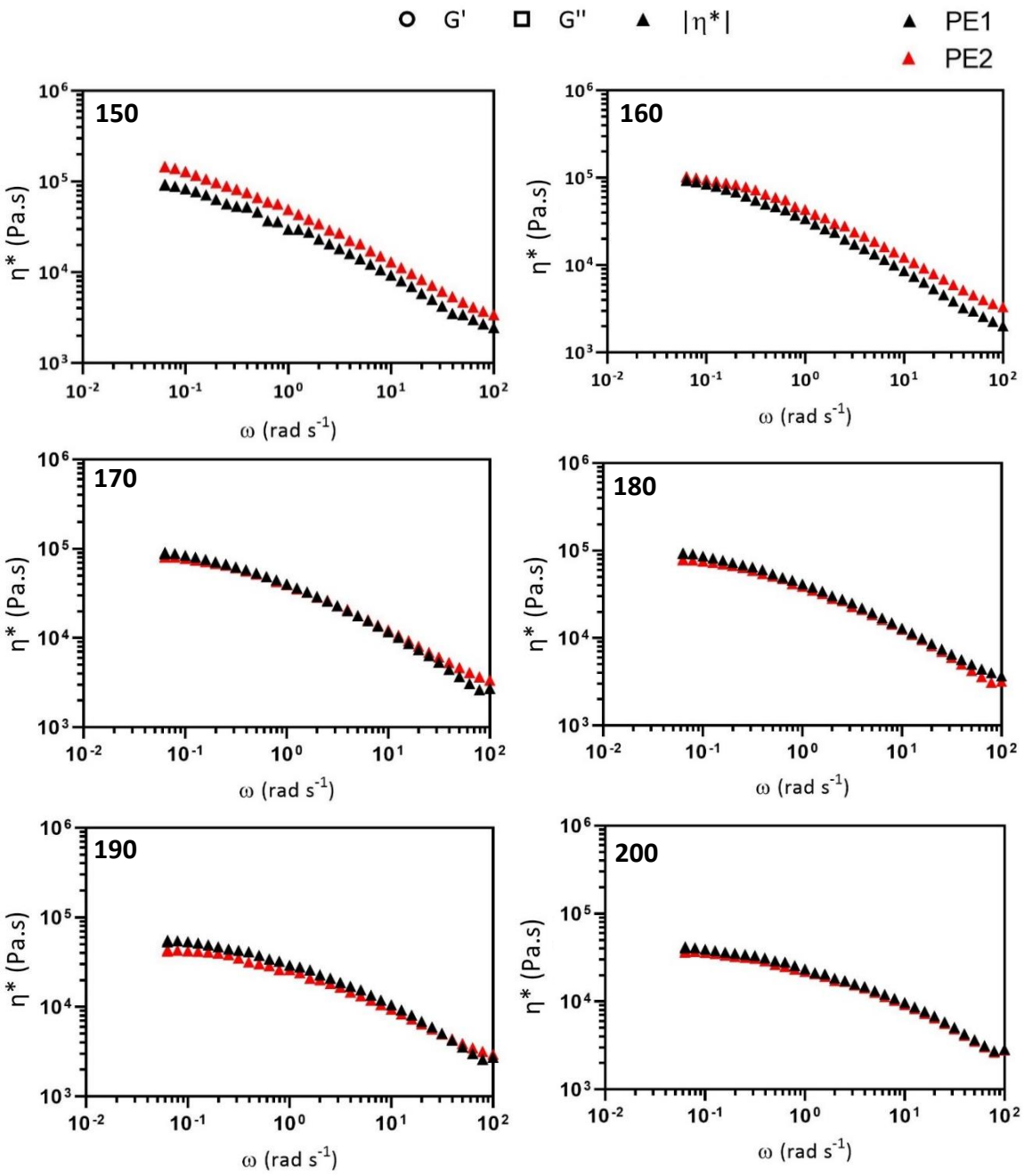

Figure 3.16: Frequency sweeps for PE1 and PE2 showing η^* (modulus of complex viscosity) curves at temperatures between 150 – 200 °C, 1 % strain amplitude and ω = 100 – 0.0628 rad s^{-1}. Black triangles represent PE1 and red triangles represent PE2.

For both PE1 and PE2, the viscosity curves at each temperature were merged using a reference temperature of 170 °C and shifted to 130 °C by performing a TTS to generate viscosity mastercurves (Figure 3.17). By fitting the Cross model (Eq. 2.10) to each mastercurve, a shear-rate dependent viscosity, $\eta(\dot{\gamma})$, value of $\eta(\dot{\gamma})$ = 59 786 ± 3 886 Pa s was obtained for PE1 and $\eta(\dot{\gamma})$ = 71 954 ± 13 592 Pa s for PE2. The fitting of the model at the highest shear rates deviated in a slight upwards curvature for PE2, hence the larger error observed for this material.

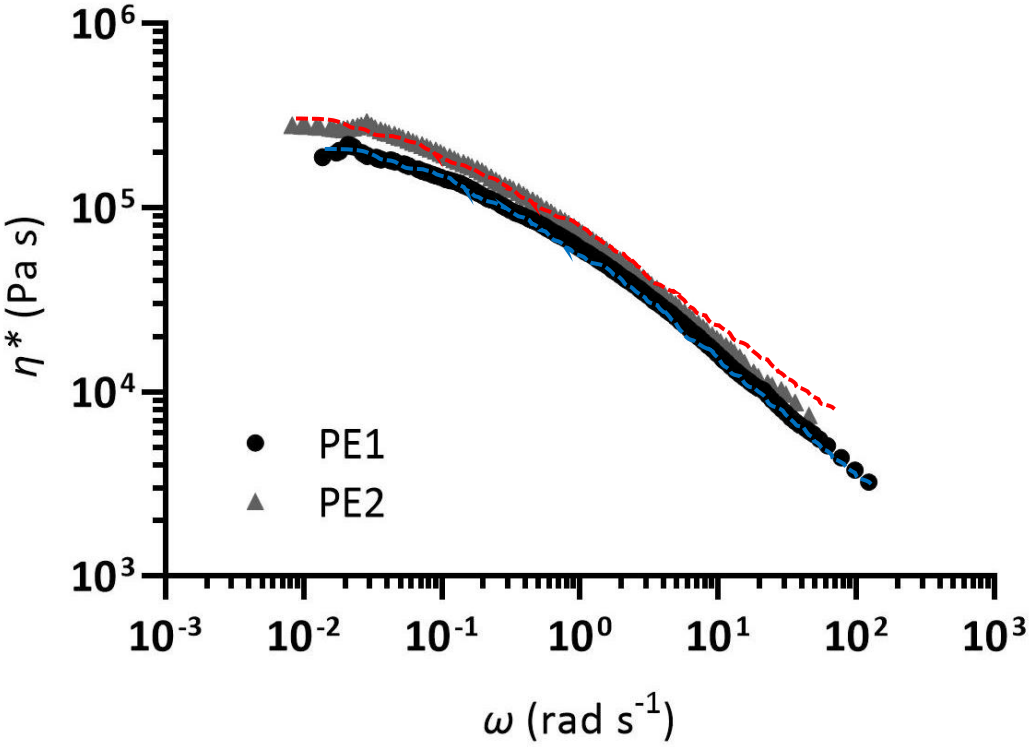

Figure 3.17: The shear-dependent viscosity mastercurves of PE1 (black circles) and PE2 (grey triangles) shifted to 130 °C after performing a time-temperature superposition. Fitting with the Cross model to PE1 (blue dashed line) and PE2 (red dashed line) gave values for the shear-rate dependent viscosity, $\eta(\dot{\gamma})$, of 59 786 Pa s and 71 954 Pa s respectively. The inset table displays the a_T shift factors obtained from the time-temperature superposition.

As expected from the previous GPC measurements (Figure 3.1), PE1 showed slightly higher viscosity at both η_0 and η_∞ regions, owing to the HMWT present in this material (Table 3.5 and Figure 3.20). Despite being manufactured by different suppliers, both materials showed similar rheology and TTS behaviour (Figure 3.20).

	PE1	PE2
η_0 **(Pa s)**	1.82 x 10^5	1.45 x 10^5
η_∞ **(Pa s)**	3790	3748

Table 3.5: Values of the zero-shear viscosity, η_0, and infinite-shear viscosity, η_∞, plateaus as obtained from Cross Model fitting of the time-temperature superposition mastercurves of PE1 and PE2 shifted to 130 °C.

The applicability of the TTS to HDPE melts has been widely researched and shown to work across a wide range of temperatures.[69,70] The a_T values obtained for these materials are consistent with previous works, and have been shown to be independent of MWD.[69] Therefore, these materials can be classified as thermo-rheologically simple on account of obeying the TTS principle.[71]

3.4.3 Linear Viscoelastic Behaviour

Additionally, from the above measurements, plots of G' and G" against ω were created at each temperature for both PE1 and PE2 (Figure 3.18). The crossover points (when $G' = G''$) for each material were largely consistent at all temperatures, which indicated that the materials relaxed along similar timescales.[58] In all cases, $G'' > G'$ at lower frequencies indicating liquid-like behaviour, which became more solid-like after the crossover point as $G' > G''$.[58]

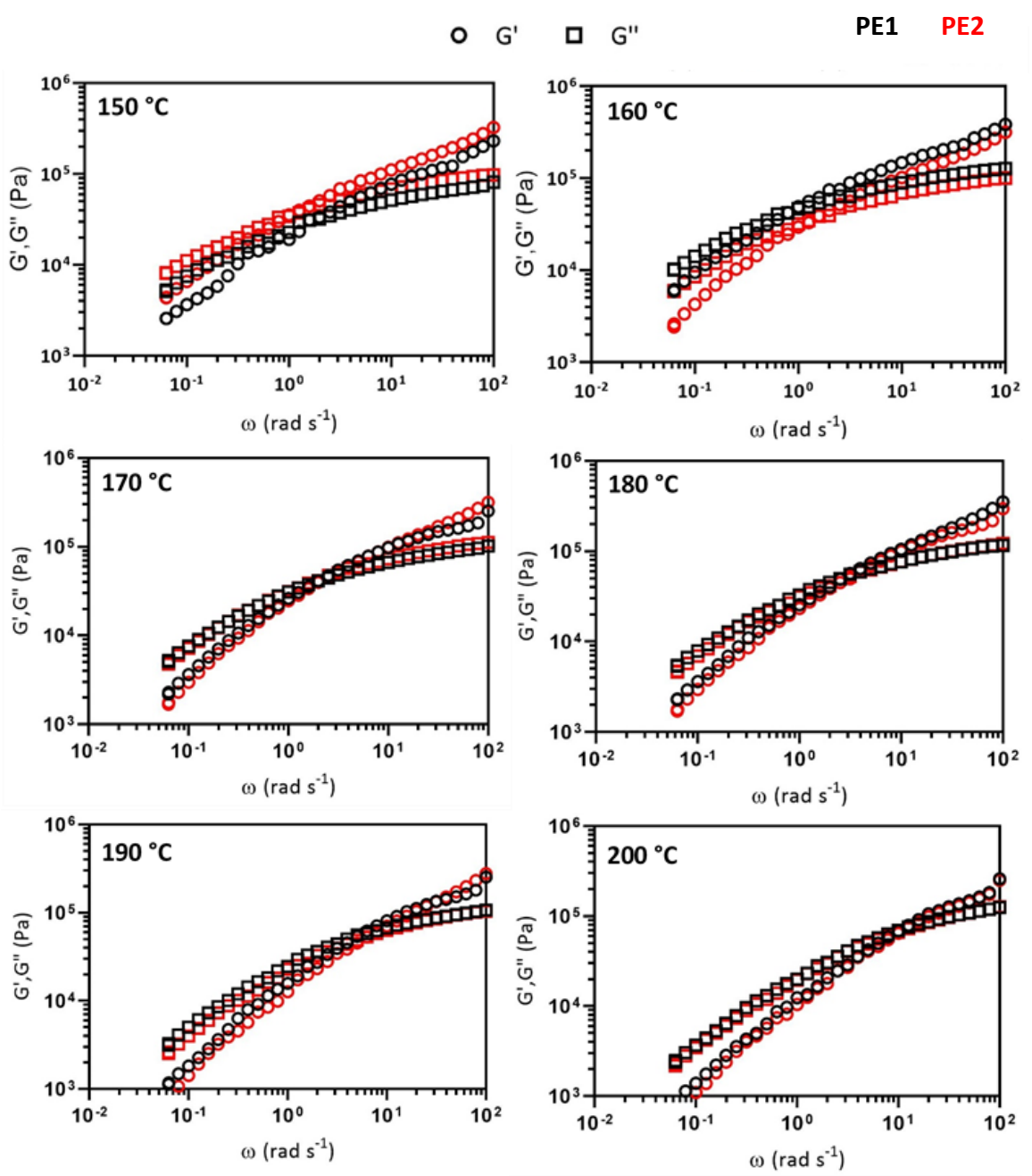

Figure 3.18: Frequency sweeps for PE1 and PE2 showing *G'* (storage modulus) and *G''* (loss modulus) curves at temperatures between 150 – 200 °C, 1 % strain amplitude and ω = 100 – 0.0628 rad s^{-1}. Black symbols represent PE1 and red symbols represent PE2.

A TTS was applied to the *G'/G"* data for PE1 and PE2 using a reference temperature of 170 °C and shifted to 130 °C (Figure 3.19 and Table 3.6). However, across all of the temperatures measured, the *G'/G"* behaviour for each material was very similar hence why the mastercurves do not appear to have covered any greater range of angular frequencies.

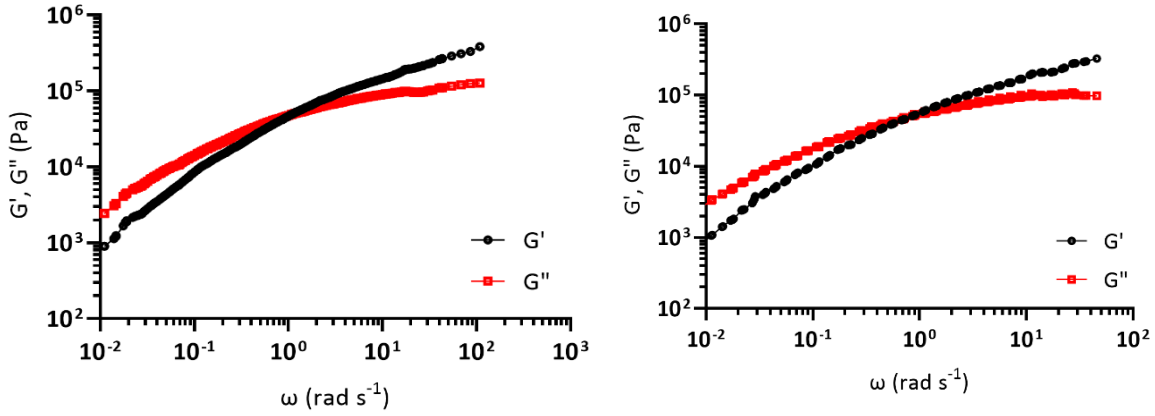

Figure 3.19: Mastercurves of *G'* (black) and *G"* (red) for PE1 (left) and PE2 (right) shifted to 130 °C.

	PE1		PE2	
	τ_i	G_i	τ_i	G_i
1	62.41	2 483.63	185.08	725.21
2	7.45	14 745.00	23.02	7 278.68
3	0.89	64 718.40	2.86	38 696
4	0.11	121 748.00	0.36	100 465.00
5	0.01	202 731.00	0.04	186 792

Table 3.6: Values of τ_i (relaxation time) and G_i (complex modulus) for PE1 and PE2 across the 5 Maxwell modes applied to each *G'/G"* mastercurve.

A Maxwell model of 5 modes was applied to the TTS *G'/G"* mastercurves of PE1 and PE2 (Figure 3.19 and Table 3.6). Polydisperse materials have a range of relaxation time scales.[72] Crossover points of *G'* and *G"* are useful indicators of relaxation times through the reciprocal of the *G'/G"* crossover frequency, $\omega = 1/\tau$,[58] and M_w, with a longer relaxation time referring to a higher M_w (Table 3.7).[58,73]

	PE1	PE2
Crossover Modulus, *G'* = *G"* (Pa)	49 158.90	50 627.00
Crossover Frequency, ω (rad s^{-1})	1.08	0.85
Relaxation Time, τ (s)	0.93	1.18

Table 3.7: Crossover values of the storage, *G',* and loss, *G",* moduli and angular frequency, ω, for PE1 and PE2 which lead to characteristic relaxation times.

HDPE of M_w = 224 000, but a relatively narrow MWD (= 3.0), has been calculated in the literature to have a relaxation time of 4.1 x 10^{-4} s.[67] However, given the narrow MWD compared to both materials used in this study, it was difficult to draw a direct comparison. Considering that the longest chains in a melt have longer relaxation times due to an increased number of entanglements,[74] and the MWDs of both materials, it could be anticipated that PE1 should have the longer relaxation time. However, whilst this material did possess a slightly larger fraction of the highest molecular weight material, the HMW peak in the distribution for PE2 was greater (Figure 3.1). Therefore, this suggested that PE2 on average had a larger proportion of longer, HMW chains, whereas PE1 contained the longest, UHMW chains. The rheology results showed that both PE1 and PE2 were similar in terms of relaxation time and viscosity, which roughly correlated with the MWD.

3.5 SAXS of HDPE and UHMWPE

SAXS provided a valuable insight into the structural morphology of the studied polymers after shearing. Herman's Orientation Function, *P2*, was used in each case to quantify the degree of orientation Section 2.8).

3.5.1 Lamellar Morphology and Degree of Orientation: HDPE

During shearing experiments, two morphologies were visible from a 2D SAXS acquisition (Figure 3.22). The halo pattern was indicative of isotropic morphology (Figure 3.20 left), whereas the two-lobe 'tear-drop' pattern represented anisotropic morphology (Figure 3.20 right), corresponding to a stack of parallel lamellae.[75] As has previously been reported from work involving polyolefins crystallised from oriented melts under shear and melt-spinning, 2D SAXS images can be interpreted in terms of a two-phase lamellar system where the stacks of lamellae are perpendicular to the flow/elongation direction (Figure 3.21).[72,75–79]

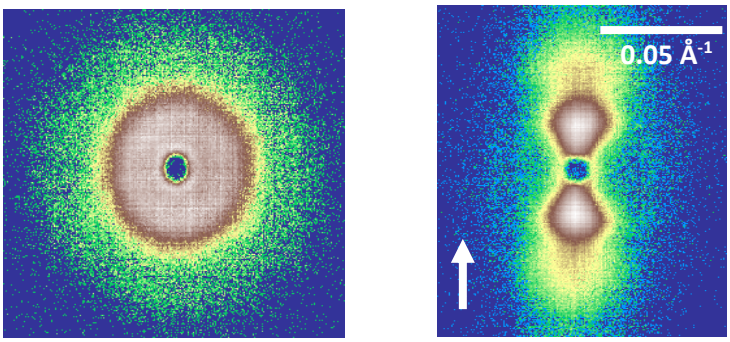

Figure 3.20: Two types of morphology visible in a 2D SAXS pattern: isotropic (left) and anisotropic (right). The arrow in the right image indicates the direction of flow.

2D SAXS patterns gave information regarding the polymer morphology (Figure 3.21), such as the halo (Figure 3.21A) from isotropic spherulites (also seen in the left image of Figure 3.20). The tear-drop shaped meridional lobes (Figure 3.21B, and also seen in the right image of Figure 3.20) arise from a stack of parallel lamellae with a distribution of irregular distances and thicknesses between crystaline lamellae and amorphous regions. However, as lamellae spacing becomes increasingly regular, sharp meridional spots (Figure 3.21C) appear. The meridional arcs (Figure 3.21D) arise due to a wide range of lamellae orientations with respect to the flow direction (vertical in this instance). Finally the meridional tear-drop lobes with equatorial streaks (Figure 3.21E) result from highly-oriented *shish-kebab* sructures with irregularly spaced lamellae and a high density of oriented fibre bundles respectively.[75,78] It is worth noting that these are idealised structures and, in many cases, a mixture of structures will be present, with the resulting 2D pattern reflecting as such.

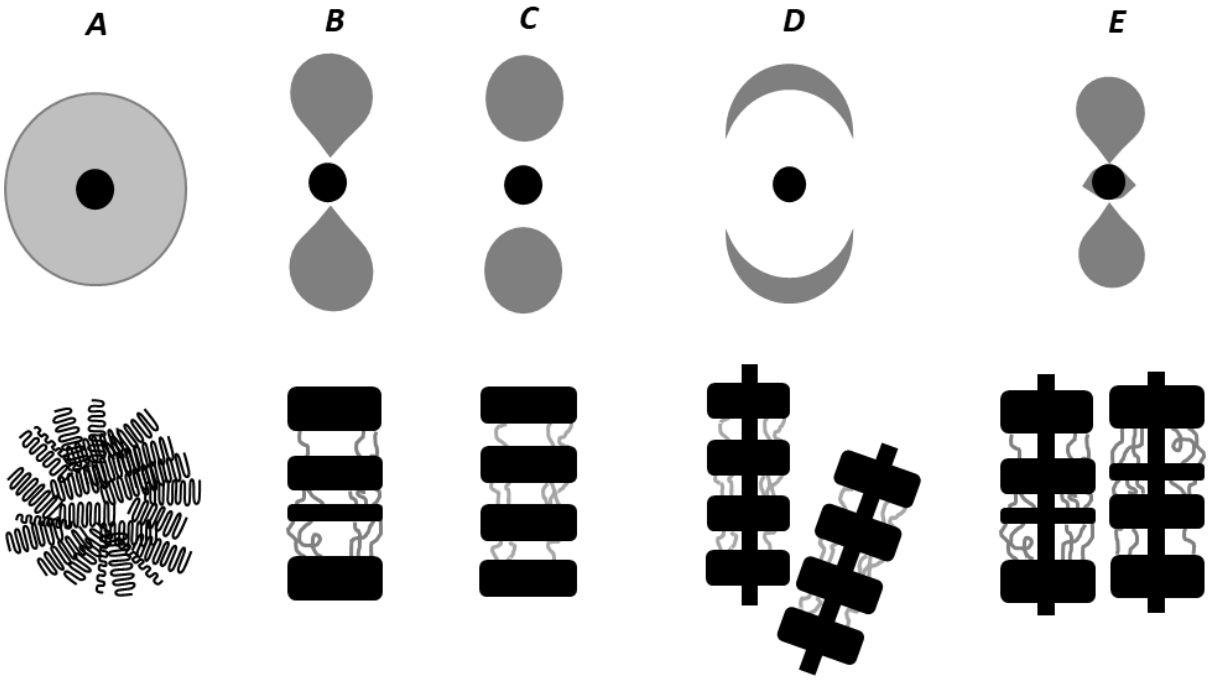

Figure 3.21: Schematic representations of commonly observed 2D SAXS patterns for oriented morphology: A) halo from isotropic polymer chains (i.e. entangled forming a spherulitic morphology); B) tear-drop shaped meridional lobes from irregular distances and thicknesses between crystalline lamellae (black) and amorphous regions (grey); C) sharp meridional spots from regular distances and thicknesses between crystaline lamellae and amorphous regions; D) meridional arcs from lamellae structures with different orientations tilted with respect to the flow direction; E) highly-oriented shish-kebab sructures with irregularly spaced lamellae. The equatorial streaks are indicative of a high density of oriented fibre bundles.[75]

Whilst the latter morphology (Figure 3.21E) indicates highly-oriented *shish-kebabs*, the equatorial streak representing the fibre bundle parallel to the flow direction (*shish*) was not present in this work. Nevertheless, according to the generally accepted mechanism of *shish-kebab* formation (Figure 1.17), they must have been present. Under shear, the longest chains in the melt are stretched and aligned, eventually nucleating and crystallising into fibre bundles (*shish*). This fibre subsequently acts as a nucleation point for the lamellae (*kebabs*), consisting of the remaining chains in the melt, to grow and crystallise. Therefore, *shish* must be present first in order for *kebabs* to form afterwards and produce the tear-drop shaped lobes on the SAXS patterns. It was likely that the number densities of the *shish* were too low to cause significant scattering.[75]

Correlation function analysis allows parameters such as lamellar long period and crystalline and amorphous layer thickness to be determined from a 1D SAXS pattern.[80–83] A Correlation

Function can be envisioned by considering an imaginary line moving through the structure of a sample. $\Gamma_{(x)}$ is the probability that a line of length x has equal electron scattering length density at either end and, hence, a regular structural ordering within the sample will manifest itself as a peak in $\Gamma_{(x)}$. 1D ($\Gamma_{(x)}$) and 3D ($\Gamma_{(x)}$) correlation functions can be obtained, the difference being that the former is only averaged in the plane of the scattering vector.[30] Data are extrapolated to $q \rightarrow 0$, according to the Guinier model, and $q \rightarrow \infty$, according to Porod's law, with the resulting analysis interpreting the results based upon a two-phase lamellar model.[80] The correlation function can be written as:

$$\gamma_1(R) = \frac{1}{Q_s}\int_0^{\infty} I(q)q^2 \cos(qR)\, dq \qquad 3.2$$

where $I(q)$ is the scattering intensity and the invariant, Q_s, is defined as:

$$Q_s(t) = \int_0^{\infty} q^2\, I(q)dq \;\approx\; \int_{q_1}^{q_2} q^2\, I(q)dq \qquad 3.3$$

Integration of the 1D SAXS curve gives Q_s, provided that it is performed between suitable limits of $q = q_1$ (the first reliable data point) and $q = q_2$ (the region where $I(q)$ is constant.

Correlation functions from reduced 1D patterns (Figure 3.22) were performed on isotropic samples of PE1 and PE2 in order to gather the average lamellae long period, average lamellae thickness and degree of crystallinity (Table 3.8). PE samples with M_W = 500 kDa and M_W = 5 MDa (500k and 5M respectively, both of which were used later in Chapter 6 in the fabrication of SPCs) were also measured to show the effect of M_w and crystallinity on morphology. A sample of LDPE was also measured (Lupolen 1840H, Basell, M_n = 17 kDa, M_w = 240 kDa, polydispersity $M_w/M_n \sim 14$, T_{ms} = 111.2 °).[97]

	PE1	**PE2**	**500k**	**5M**	**LDPE**
Average Long period (Å)	170	141	135	124	151
Average Lamellae Thickness (Å)	99.1	67.8	62.0	47.9	65.1
$\boldsymbol{X_c}$	0.58	0.48	0.46	0.39	0.43

Table 3.8: Average long period, average lamellae thickness and degree of crystallinity obtained from correlation funcions of PE1, PE2, 500k, 5M and LDPE.

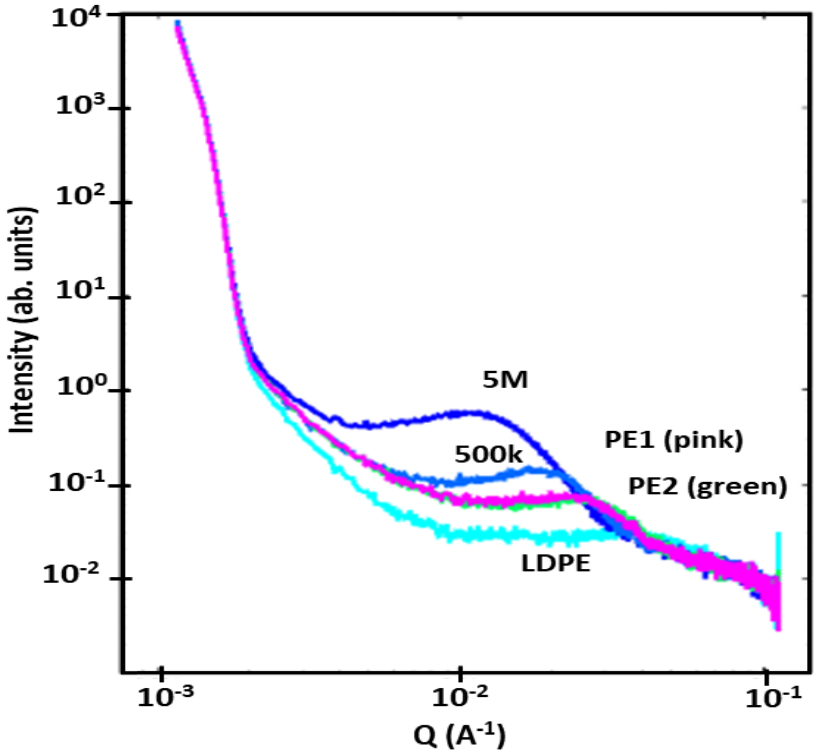

Figure 3.22: 1D SAXS patterns of LDPE, HDPE and UHMWPE samples collected using a Bruker AXS NanoStar.

The long periods obtained (Table 3.8) from the correlation function were consistent with literature values.[84] PE1 displayed larger long periods than PE2 which was consistent with GPC and first-scan DSC measurements. Due to Babinet's principle, and without any prior knowledge, the degree of crystallinity according to the correlation function could have been either 58 % or 42 % for PE1.[85,86] For PE2, the degree of crystallinity could either have been 48 % or 52 %. However, considering the DSC data (Table 3.2), values of 58 % and 52 % for PE1 and PE2 respectively were in corroboration. Crystallinities for 500k and 5M were also in corroboration with DSC measurements.

Cole and Holmes obtained a value of 123 Å for the long period and X_c of 0.45 for a sample of LDPE at room temperature, but with large error ranges.[84,87] The MWDs and increased number of entanglement points with UHMW chains, and hence lower chain mobility to form folded-chain structures, could account for the observed differences.[20] Additionally, Bellare *et al.* discovered that UHMWPE contained a large distribution of lamellae thicknesses and spacings, which could also account for the values obtained here.[88] There was good correlation between the X_c values obtained through the correlation function and those obtained by DSC.

Depending upon the area at which a SAXS acquisition is taken, the lobes arising in an anisotropic 2D image can be arranged parallel to the meridional or equatorial direction (Figure 3.23).

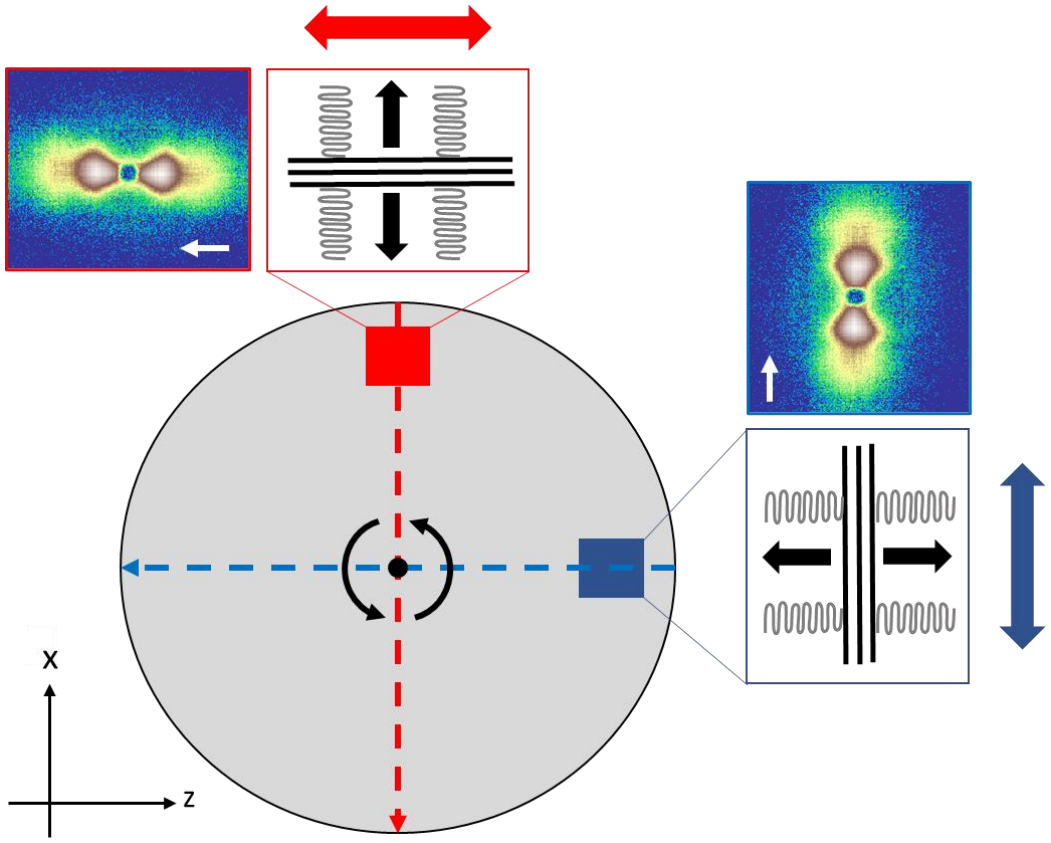

Figure 3.23: The changes in lamellae orientation with respect to taking a SAXS acquisition with the lobes parallel to the meridian (blue) or equatorial (red) directions. Measuring at different points will lead to changes in the direction of the lobes identified on the 2D SAXS scattering pattern. The white arrows in the 2D SAXS images indicate the direction of flow and the grey arrows in the *shish-kebab* diagrams represent the growth direction of lamellae.

The sheared PE disk underwent planar rotational flow, thus a linear distribution of shear rates occurred from a maximum at the disk edge, to zero at the disk centre. By performing an azimuthal integration of the radial 2D SAXS patterns, this orientation was observed quantitatively (Figure 3.24).

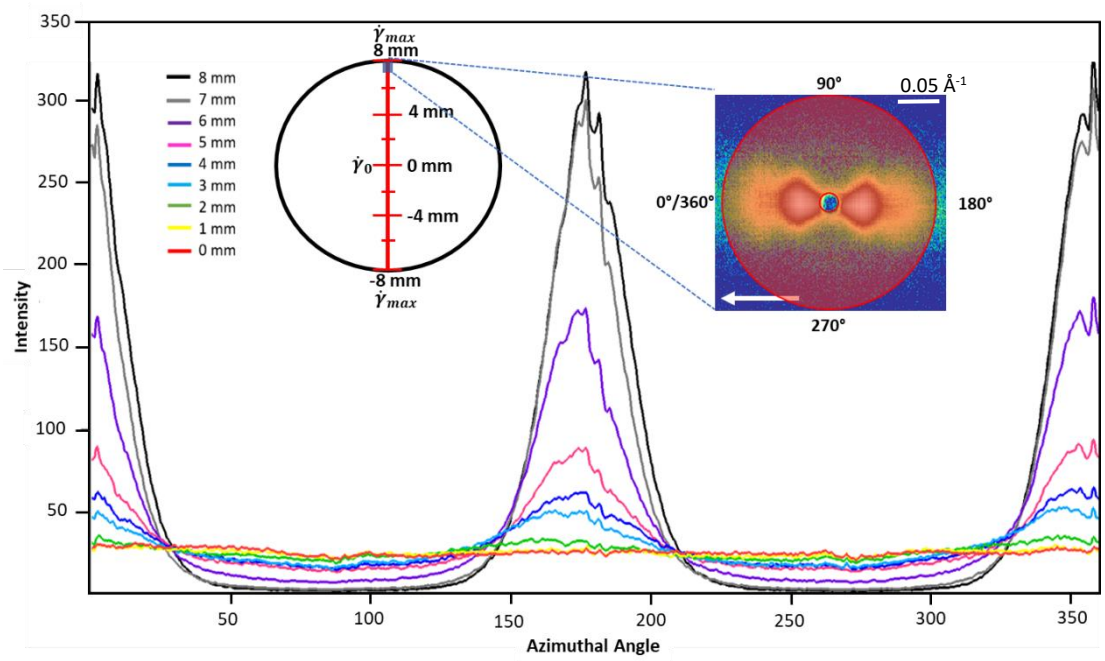

Figure 3.24: Azimuthal integrations of a disk of HDPE at vairous radius intervals (inset white circle) with the area of integration shown in the inset image by the red shadow ring (inset). As the distance from the centre decreases, so also do the intensity peaks and, in the 2D SAXS patterns, the lobes change into a diffuse halo indicating an isotropic region.

3.5.2 Lamellar Morphology and Degree of Orientation: UHMWPE

Three UHMWPE tapes were used to construct SPCs: TA23, XF23 and S1. Each of the three tapes underwent a single SAXS acquisition for 120 seconds in order to understand the underlying morphology (Figure 3.25).

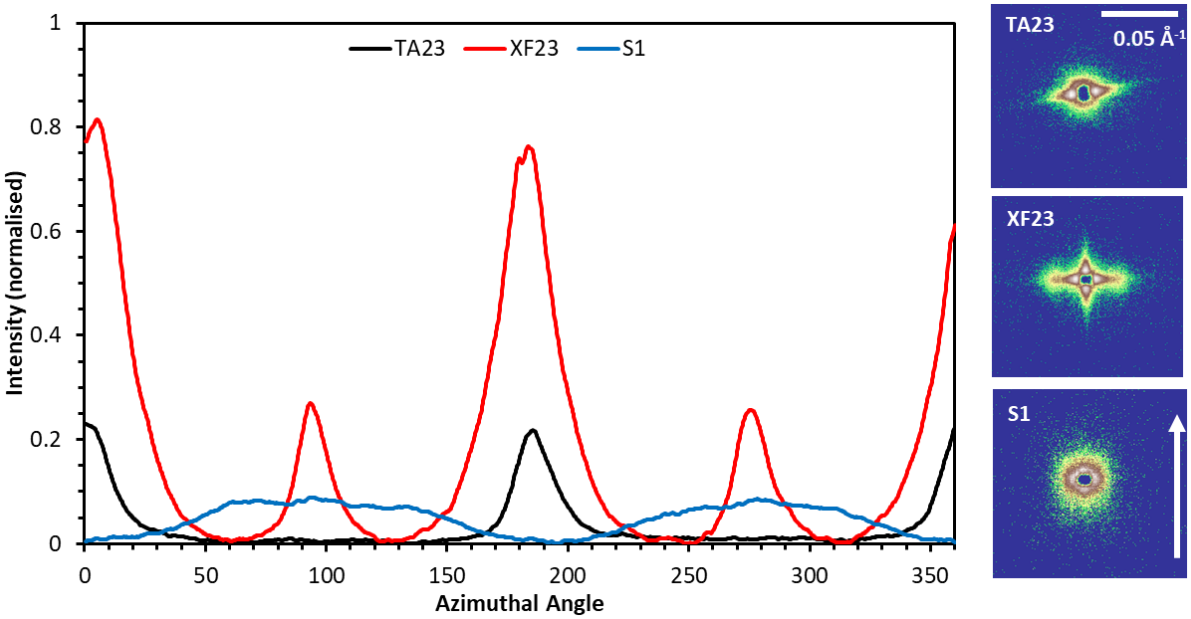

Figure 3.25: 2D SAXS patterns (measured using a Bruker AXS NanoStar) and 1D azimuthal integrations of UHMWPE oriented tapes TA23 (black curve, top image), XF23 (red curve, middle image) and S1 (blue curve, bottom image). The scale bar of 0.05 $Å^{-1}$ in the image of TA23 applies to all images and the white arrow in the image of S1 indicates the direction of fibre orientation for all tapes. In this instance, 0° is taken as the point on the left-hand side of the images, perpendicular to the white arrow (i.e. West if on a compass), working around in a clockwise direction.

Azimuthal integrations of all tapes revealed a degree of orientation with the directions of the azimuthal angles as denoted previously (Figure 3.24). The single equatorial streak in TA23 indicated fibrils oriented in a direction perpendicular to the streak direction (the fibre direction is indicated by the white arrow in Figure 3.25). The two peaks in the azimuthal integration (one peak is located at 180 °, the second is split at 0°/360° – this also occurs for XF23) indicated orientation in one direction. XF23 displayed biaxial orientation, evident by the cross-streak pattern in the 2D image and four peaks present in the integration. The two peaks located at 90° and 270° displayed weaker intensity than the peaks at 0°/360° and 180° which indicated that orientation was stronger in the transverse direction (perpendicular to the white arrow in Figure 3.25). S1 exhibited very weak orientation, which was consistent with the belief that this was an intermediate step towards the fabrication of TA23, in a direction corresponding with the orientation aligned axially (parallel to the white arrow in Figure 3.25).

Due to the high intensity spots visible in TA23 and XF23, there could have been significant void scattering.[89] Due to the mechanical stresses imparted by drawing, these voids would be ellipsoidal with the major axis parallel to the draw direction.[90] The presence of such features

could be explained by the small amount of intermolecular forces between parallel fibrils without significant entanglement.[91] Equatorial streaks have been observed in other highly drawn tapes and were ascribed to voids which imparted a high scattering contribution.[90] Fibres with a *shish-kebab* structure were unable to pack closely due to lamellae overgrowths. Therefore, such a system may be considered as a three-phase model: crystalline, amorphous and voids. However, Yeh *et al.* observed that at high draw ratios, lamellar overgrowths constituting the *kebabs* were pulled into the main *shish* core, whereby *kebabs* could not be observed by SAXS.[42] Given, therefore, the highly drawn nature of these tapes (in particular TA23), it was highly likely that this accounted for the lack of *kebab* lobes present in the 2D SAXS patterns.[29]

3.6 Conclusions

Over the 40 years of HDPE use in plastic pipes, there has been an increasing drive towards higher performance materials, typically expressed as a pressure rating over a typical service lifetime of 50 years.[7] The demands placed upon plastic water pipes during their operational lifetime are such that a somewhat contradictory combination of stiffness (i.e. high modulus) and resistance to environmental stress cracking are key requirements.[92] The dominating features of an HDPE pipe resin that determine the performance in a pipe application are molecular weight and MWD.[17] This, in turn, determines the mechanical and rheological properties of the melt, which translates into the strength characteristics and processing behaviour during manufacture and application.[17] Higher molecular weights generally impart improved mechanical performance at the expense of ease of processing.[17] Two commercial-grade HDPE materials, currently used in the manufacture of plastic water pipes, were obtained and various thermal, rheological and SAXS properties measured.

The average molecular weight and MWD considerably affect the physical properties.[17] MWDs of PE1 and PE2 were obtained by HT-GPC which confirmed that both materials were bimodal and that PE1 had a slightly larger proportion of UHMW material (a HMWT) than PE2. This small tail drives much of the mechanism of FIC.[93] The average molecular weights of PE1 and PE2 were 264.5 kDa and 227.5 kDa respectively with dispersity values of 33.5 Da and 28.5 Da respectively. Typical literature M_w values for HDPE are in the range 10^4 - 10^5 Da, however, the studied materials were speciality polymers and literature values of similar M_w and dispersity for comparison could not be obtained.[92]

DSC measurements gave the key melting and crystallisation points for both materials, with melting point values between 120 - 132 °C and degree of crystallinity values consistent with literature values for HDPE.[20,24–26] By repeating each thermal cycle twice, the effect of surface interfaces upon the measured temperature values was elucidated. Knowledge of the peak crystallisation and melting temperatures, along with the respective onsets, allowed temperature protocols to be established for polymer processing. The melting of highly crystalline, oriented UHMWPE tapes revealed three distinct peaks, most likely caused by a combination of fibre constraint and crystal melting and transitions.[94,95] By constraining the fibre, a single peak appeared at 146.9 °C with a small shoulder at 151.8 °C. Therefore, the multiple melting peaks were only possible for unconstrained UHMWPE fibres, consistent with the literature.[42,49]

Rheological measurements revealed that both materials displayed similar rheological properties in terms of viscosity and relaxation times, which correlated with the MWD obtained by HT-GPC. Creating *G'/G"* mastercurves determined the relaxation times from *G'/G"* crossover points as 0.93 s and 1.18 s for PE1 and PE2 respectively. By performing frequency sweeps at temperatures 150 - 200 °C, and conducting a TTS on the resulting η^* data, mastercurves shifted to 130 °C were obtained for both PE1 and PE2. Applying the Cross model to these mastercurves gave shear-rate dependent viscosity values, $\eta(\dot{\gamma})$, of 59 786 ± 3 886 Pa s and 71 954 ± 13 592 Pa s for PE1 and PE2 respectively. These values were consistent with GPC measurements which revealed that PE2 had a greater amount of HMW material (as identified in the second peak of the bimodal distribution) compared to PE1.

SAXS analysis of HDPE samples allowed for the determination of the underlying crystal morphology. Isotropic samples showed a 2D pattern consisting of a diffuse halo around the beamstop, whereas anisotropic samples displayed a distinct two lobe pattern centred around the beamstop.[80] Azimuthal integrations of these patterns determined the degree of orientation according to Herman's Orientation Function, *P2*. The distinct two-lobe pattern of sheared samples pointed towards an oriented morphology, indicative of chains that have stretched and aligned during processing.[60] This correlated with polymer processing techniques, such as injection moulding and extrusion, which result in a degree of stretching and aligning of polymer chains through the movement of the melt. Therefore, control of the magnitude of shearing during polymer processing could impart beneficial properties, such as enhanced mechanical behaviour, to end-use products.[96] Correlation function analysis revealed differences in the long periods, lamellar thicknesses and degrees of crystallinity between PE1 and PE2. The former

showed larger values of each measured property which was consistent with GPC and DSC measurements. Long periods were also consistent with literature values.

3.7 References

1 *BorSafe PE pipe materials – made for generations*, Borealis AG, Data Sheet, 2016.

2 *ELTEX B4922N3004*, Ineos Olefins & Polymers Europe, Data Sheet, 2009.

3 Z. Zhai, C. Fusco, J. Morthomas, M. Perez and O. Lame, *ACS Nano*, 2019, **13**, 11310–11319.

4 H. Shen, B. Xie, W. Yang and M. Yang, *Polym. Test.*, 2013, **32**, 1385–1391.

5 G. Pircheraghi, A. Sarafpour, R. Rashedi, K. Afzali and M. Adibfar, *Express Polym. Lett.*, 2017, **11**, 622–634.

6 Plastics Pipe Institute (PPI), in *PPI Handbook of Polyethylene Pipe*, 2nd edn., 1950, pp. 43–103.

7 P. J. DesLauriers, M. P. McDaniel, D. C. Rohlfing, R. K. Krishnaswamy, S. J. Secora, E. A. Benham, P. L. Maeger, A. R. Wolfe, A. M. Sukhadia and B. B. Beaulieu, *Polym. Eng. Sci.*, 2005, **45**, 1203–1213.

8 *HDPE Performance Pipes*, Ineos Olefins and Polymers, Technical Data Sheet, 2014.

9 *BorSafe^{TM} Polyethylene*, Borealis AG, Technical Data Sheet, 2007.

10 M. A. Parvez, M. Rahaman, J. B. P. Soares, I. A. Hussein and M. A. Suleiman, *Polym. Sci. Ser. B*, 2014, **56**, 707–720.

11 F. M. Rugg, J. J. Smith and L. H. Wartman, *Ann. N. Y. Acad. Sci.*, 1953, **57**, 398–416.

12 D. E. Kline, J. A. Sauer and A. E. Woodward, *J. Polym. Sci.*, 1956, **22**, 455–462.

13 F. J. Stadler, C. Gabriel and H. Münstedt, *Macromol. Chem. Phys.*, 2007, **208**, 2449–2454.

14 P. Wood-Adams and S. Costeux, *Macromolecules*, 2001, **34**, 6281–6290.

15 R. A. Mendelson and F. L. Finger, *J. Appl. Polym. Sci.*, 1973, **17**, 797–808.

16 Á. Kmetty, T. Bárány and J. Karger-Kocsis, *Prog. Polym. Sci.*, 2010, **35**, 1288–1310.

17 J. A. P. Caceres, Virginia Polytechnic Institute and State University, 2019.

18 Teijin Aramid BV, *An Ultra-Strong Performance Film*, Technical Data Sheet, 2020.

19 L. Balzano, *Flow Induced Crystallisation of Polyolefins*, PhD Thesis, Eindhoven University of Technology, 2008.

20 A. J. Peacock, *Handbook of Polyethylene*, Marcel Dekker, New York, 2000.

21 R. K. Krishnaswamy, D. C. Rohlfing, A. M. Sukhadia and K. R. Slusarz, *Polym. Eng. Sci.*, 2004, **44**, 2266–2273.

22 H.-T. Liu, C. R. Davey and P. P. Shirodkar, *Macromol. Symp.*, 2003, **195**, 309–316.

23 A. Pandey, A. Toda and S. Rastogi, *Macromolecules*, 2011, **44**, 8042–8055.

24 M. H. Nafar Sefiddashti, B. J. Edwards and B. Khomami, *Phys. Rev. Res.*, 2020, **2**, 013035.

25 V. B. F. Mathot and M. F. J. Pijpers, *J. Therm. Anal.*, 1983, **28**, 349–358.

26 B. Wunderlich and C. M. Cormier, *J. Polym. Scince Part A-2*, 1967, **5**, 987–988.

27 J. D. Menczel and R. B. Prime, *Thermal Analysis of Polymers: Fundamentals and Applications*, Wiley, Hoboken, New Jersey, 2009.

28 J. Xu, S. Srinivas, H. Marand and P. Agarwal, *Macromolecules*, 1998, 31, 8230–8242.

29 G. C. Oppenlander, *Science*, 1968, **159**, 1131–1319.

30 G. R. Strobl, M. J. Schneider and I. G. Voight-Martin, *J. Polym. Sci. Part A-2, Polym. Phys.*, 1980, **18**, 1361–1381.

31 H. Marand, J. Xu and S. Srinivas, *Macromolecules*, 1998, **31**, 8219–8229.

32 J. J. Weeks, *J. Res. Natl. Bur. Stand. Sect. A Phys. Chem.*, 1963, **67A**, 441.

33 R. G. Brown and R. K. Eby, *J. Appl. Phys.*, 1964, **35**, 1156–1161.

34 V. K.-H. Illers and H. Hendus, *Die Makromol. Chemie*, 1968, **113**, 1–22.

35 T. Verho, A. Paajanen, J. Vaari and A. Laukkanen, *Macromolecules*, 2018, **51**, 4865–4873.

36 B. Wunderlich, L. Melillo, C. M. Cormier, T. Davidson and G. Snyder, *J. Macromol.*

Sci. Part B, 1967, **1**, 485–516.

37 R. Blaine, *TA123: Determination of Polymer Crystallinity by DSC*, TA Instruments, 2010.

38 M. Rezaei, N. G. Ebrahimi and M. Kontopoulou, *J. Appl. Polym. Sci.*, 2006, **99**, 2344–2351.

39 S. Ronca, G. Forte, H. Tjaden, Y. Yao and S. Rastogi, *Polymer*, 2012, **53**, 2897–2907.

40 D. Romano, N. Tops, J. Bos and S. Rastogi, *Macromolecules*, 2017, **50**, 2033–2042.

41 S. Rastogi, Y. Yao, S. Ronca, J. Bos and J. Van Der Eem, *Macromolecules*, 2011, **44**, 5558–5568.

42 J. T. Yeh, S. C. Lin, C. W. Tu, K. H. Hsie and F. C. Chang, *J. Mater. Sci.*, 2008, **43**, 4892–4900.

43 T. Stern and G. Marom, *J. Compos. Part A*, 1997, **28A**, 437–444.

44 F. V. Lacroix, J. Loos and K. Schulte, *Polymer*, 1998, **40**, 843–847.

45 S. Ratner, A. Weinberg, E. Wachtel, P. M. Moret and G. Marom, *Macromol. Rapid Commun.*, 2004, **25**, 1150–1154.

46 J. T. Yeh and S. S. Chang, *J. Appl. Polym. Sci.*, 2001, **79**, 1890–1901.

47 J. T. Yeh, Y. T. Lin and K. N. Chen, *J. Appl. Polym. Sci.*, 2003, **89**, 3728–3738.

48 S. Tsubakihara, A. Nakamura and M. Yasuniwa, *Polym. J.*, 1996, **28**, 489–495.

49 S. Ratner, A. Weinberg and G. Marom, *Polym. Compos.*, 2003, **24**, 422–427.

50 Y. K. Kwon, A. Boller, M. Pyda and B. Wunderlich, *Polymer*, 2000, **41**, 6237–6249.

51 I. Chodák, *Prog. Polym. Sci.*, 1998, **23**, 1409–1442.

52 N.-M. Barkoula, T. Peijs, T. Schimanski and J. Loos, *Polym. Compos.*, 2005, **26**, 114–120.

53 N. J. Capiati and R. S. Porter, *J. Mater. Sci.*, 1975, **10**, 1671–1677.

54 Y. You, X. Huang, Z. Pu, K. Jia and X. Liu, *J. Polym. Res.*, 2015, **22**, 1–9.

55 C. Vasile, *Handbook of Polyolefins*, Marcel Dekker Inc., New York, 2nd edn., 2000.

56 Q. Guo, *Polymer Morphology: Principles, Characterisation and Processing*, Wiley, Hoboken, NJ, USA, 2016.

57 K. Cummings and D. Halliday, *Understanding Physics*, Wiley, New Delhi, 2007.

58 H. A. Barnes, *A Handbook of Elementary Rheology*, The University of Wales Institute of Non-Newtonian Fluid Mechanics, Aberystwyth, 2000.

59 J. E. Mark, *Physical Properties of Polymers Handbook*, Springer, New York, 2nd edn., 2007.

60 M. Okura, *The Control of Structural Morphology of Polyethylene by Shear-Induced Crystallisation*, PhD Thesis, University of Sheffield, 2010.

61 W. P. Cox and E. H. Merz, *J. Polym. Sci.*, 1958, **28**, 619–622.

62 T. S. R. Al-Hadithi, H. A. Barnes and K. Walters, *Colloid Polym. Sci.*, 1992, **270**, 40–46.

63 C. Macosko, *Rheology: Principles, Measurements and Applications*, Wiley VCH, New York, 1996, vol. 86.

64 W. P. Cox and E. H. Merz, *Am. Soc. Test. Mater. Spec. Tech. Publ.*, 1958, **247**, 178–188.

65 H. A. Barnes, J. F. Hutton, K. Walkters, A*n Introduction to Rheology*, Elsevier Science Publishers, 1993, 201.

66 E. Verdonck, *BROC Module 3 - Oscillation: Amplitude and Frequency*, TA Instruments, 2020.

67 F. J. Stadler and T. Mahmoudi, *Korea Aust. Rheol. J.*, 2011, **23**, 185–193.

68 M. M. Cross, *J. Colloid Sci.*, 1965, **20**, 417–437.

69 R. A. Mendelson, *Trans. Soc. Rheol.*, 1965, **9**, 53–63.

70 M. van Gurp and J. Palmen, *J Rheol Bull*, 1998, **65**, 5–8.

71 M. Ansari, S. G. Hatzikiriakos, A. M. Sukhadia and D. C. Rohlfing, *Rheol. Acta*, 2011, 50, 17–27.

72 E. L. Heeley, C. M. Fernyhough, R. S. Graham, P. D. Olmsted, N. J. Inkson, J. Embery,

D. J. Groves, T. C. B. McLeish, A. C. Morgovan, F. Meneau, W. Bras and A. J. Ryan, *Macromolecules*, 2006, **39**, 5058–5071.

73 E. A. Andablo-Reyes, E. L. de Boer, D. Romano and S. Rastogi, *J. Rheol.*, 2014, **58**, 1981–1991.

74 P. G. de Gennes, *Phys. Today*, 1983, **36**, 33–39.

75 E. L. Heeley, T. Gough, D. J. Hughes, W. Bras, J. Rieger and A. J. Ryan, *Polym.*, 2013, **54**, 6580–6588.

76 J. M. Samon, J. M. Schultz, B. S. Hsiao, S. Seifert, N. Stribeck, I. Gurke, G. Collins and C. Saw, *Macromolecules*, 1999, **32**, 8121–8132.

77 Z. Jiang, Y. Tang, J. Rieger, H. F. Enderle, D. Lilge, S. V. Roth, R. Gehrke, Z. Wu, Z. Li, X. Li and Y. Men, *Eur. Polym. J.*, 2010, **46**, 1866–1877.

78 J. M. Schultz, B. S. Hsiao and J. M. Samon, *Polymer*, 2000, **41**, 8887–8895.

79 G. Kumaraswamy, *J. Macromol. Sci. - Polym. Rev.*, 2005, **45**, 375–397.

80 E. L. Heeley, T. Gough, D. J. Hughes, W. Bras, J. Rieger and A. J. Ryan, *Polymer*, 2013, **54**, 6580–6588.

81 P. Debye, H. R. Anderson and H. Brumberger, *J. Appl. Phys.*, 1957, **28**, 679–683.

82 C. G. Vonk and G. Kortleve, *Kolloid-Zeitschrift Zeitschrift für Polym.*, 1967, **220**, 19–24.

83 W. Ruland, *Colloid Polym. Sci.*, 1977, **255**, 417–427.

84 E. A. Cole and D. R. Holmes, *J. Polym. Sci.*, 1960, **147**, 245–256.

85 A. J. Ryan, W. Bras, G. R. Mant and G. E. Derbyshire, *Polymer*, 1994, **35**, 4537–4544.

86 A. J. Ryan, J. L. Stanford, W. Bras and T. M. W. Nye, *Polymer*, 1997, **38**, 759–768.

87 G. R. Strobl and M. Schneider, *J. Polym. Sci. Polym. Phys.*, 1980, **18**, 1343–1359.

88 A. Bellare, H. Schnablegger and R. E. Cohen, *Macromolecules*, 1995, **28**, 7585–7588.

89 Y. Tang, Z. Jiang, Y. Men, L. An, H. F. Enderle, D. Lilge, S. V. Roth, R. Gehrke and J. Rieger, *Polymer*, 2007, **48**, 5125–5132.

90 W. Hoogsteen, G. Ten Brinke and A. J. Pennings, *J. Mater. Sci.*, 1990, **25**, 1551–1556.

91 F. Rybnikar, M. Kaszonyiova, R. Cermak, V. Habrova and M. Obadal, *J. Appl. Polym. Sci.*, 2013, **128**, 1665–1672.

92 B. L. L. Bohm, H. F. Enderle and M. Fleisner, *Adv. Mater.*, 1992, **4**, 234–238.

93 M. Okura, P. Chambon, O. O. Mykhaylyk, J. P. A. Fairclough and A. J. Ryan, *J. Polym. Sci. Part B Polym. Phys.*, 2011, **49**, 621–628.

94 F. V. Lacroix, J. Loos and K. Schulte, *Polymer*, 1999, **40**, 843–847.

95 T. Stern, G. Marom and E. Wachtel, *J. Compos. Part A*, 1997, **444**, 437–444.

96 Z. Bashir, J. A. Odell and A. Keller, *J. Mater. Sci.*, 1986, **21**, 3993–4002.

97 O. O. Mykhaylyk, P. Chambon, C. Impradice, J. P. A. Fairclough, N. J. Terrill, A. J. Ryan, *Macromolecules*, 2010, **43**, 2389-2405

Chapter 4

Controlling the Structural Morphology Through Shear-Induced Crystallisation

4.1 Introduction

Pennings and Keller were one of the first to conclude that *shish-kebab* formation depended upon a HMWT in the MWD, and that these longest chains must be stretched and elongated at a critical rate.[1–5] Subsequent work found that oriented structures could only be created through flow when the shear rate (often applied through mechanical work) was greater than the inverse Rouse time (the relaxation time of the longest chains in the melt or solution), $\dot{\gamma} > 1/\tau_r$.[6–8] Mykhaylyk *et al.* expanded on this, using parallel plate shear geometry combined with polarised light imaging and SAXS measurements, to reveal the relationship between the degree of orientation in the sample and the critical shear rate at which orientation could occur.[7]

In order to assess the effectiveness of using SIC as a viable method to increase pipe permeation resistance and mechanical strength, the critical shear rate and critical work for the formation of oriented morphologies in PE used for pipe production needed to be measured. An important distinction must be made between FIC and SIC. The impact of shear flow or extensional flow upon chain conformation is fundamentally the same, thus FIC is a general term covering different kinds of flow, including shear and extensional.[9,10] SIC refers specifically to shear-flow conditions for inducing crystallisation and so applies to this work.

4.2 Temperature-Shear Protocol

A temperature-shear profile typically consists of three key steps: initial removal of thermal history by melting of the polymer at temperatures greater than the equilibrium melting point; cooling the polymer to the shearing temperature and application of a shear pulse; crystallisation of the polymer, either isothermally or non-isothermally.[6] Therefore, characteristic temperatures such as melting point and crystallisation point were measured by DSC (Section 3.3.1) prior to developing the profile.

To ensure all morphology arising from the thermal processing history is erased prior to starting measurements, the polymer should be heated above T_m^0 for a duration longer than the disengagement time of the longest chains, τ_d, which can be estimated from the crossover of *G'* and *G"* (Table 3.7).[6] T_{ms} can be obtained from DSC measurements as the peak melting endotherm in a DSC measurement.[6] After a controlled melting and cooling protocol, spherulites have been observed to melt and recrystallise in the same place, as the nuclei from which the spherulite grows survive the melting process.[11] Within the range between T_{ms} and T_m^0, *shish* nuclei, precursors to oriented *shish-kebab* morphology, can be stable. The presence

of *shish* nuclei influences the final crystallised morphology and the memory effect of these nuclei can be exploited to analyse their thermal stability.[6,12] If the melting temperature of *shish* nuclei, T_{mo}, is greater than T_{ms}, then these flow-induced nuclei should survive at temperatures $T_{ms} < T_{mo} < T_m^0$ and act as oriented nucleating agents to direct the crystallising morphology.[6]

Previous work has shown that samples with an oriented morphology created by FIC have confirmed thermal stability of the *shish* at temperatures higher than T_{ms}.[6,13] Therefore, it was important to understand the thermal stability of oriented morphology nucleated within PE1 and PE2. The conditions used ($\dot{\gamma}$ = 10 s^{-1}; t_s = 10 s; T = 130 °C), were shown to induce orientation by post-shear SAXS measurements (Figure 4.7).

As defined from DSC measurements (Section 3.3.1, Table 3.2), a crystallisation temperature of 114 °C was selected with an initial melting temperature of 134 °C, increasing by 2 °C per cycle to a final temperature of 150 °C. Heating and cooling rates were 10 °C min^{-1} with isothermal holds of 6 minutes at 114 °C and 4 minutes at each melting temperature. SAXS acquisitions were taken consecutively every 120 seconds with selected images taken at each melting and crystallisation temperature displayed (Figures 4.1 and 4.2).

The SAXS patterns obtained for PE1 at temperatures greater than T_{ms}, (Figure 4.1, even-numbered images 2 - 18) showed no orientation suggesting the *kebabs*, representing the formation of oriented structures, had melted. However, upon cooling the melt to the crystallisation temperature, the emergence of an oriented structure returned even up to melting temperatures of 140 °C (Figure 4.1, image 9). This was consistent with the trend seen by plotting the degree of orientation P_2 function against time (Figure 4.1, black filled circles) which showed that orientation was maintained until melting at 140 °C, with a small amount remaining after melting at 142 °C (Figure 4.1, image 11). After melting at 146 °C, no orientation was detected in the crystallised state as evidenced in the 2D SAXS patterns (odd-numbered images 13 – 19) and the P_2 function. Thermal relaxation of the polymer chains caused a relaxation of the *shish-kebab* structures to an entangled melt.[12] Therefore, this proved that the melting temperature of *shish* nuclei was between 144 – 146 °C for PE1 and that thermal treatment at temperatures below 144 °C would not erase the oriented structure.

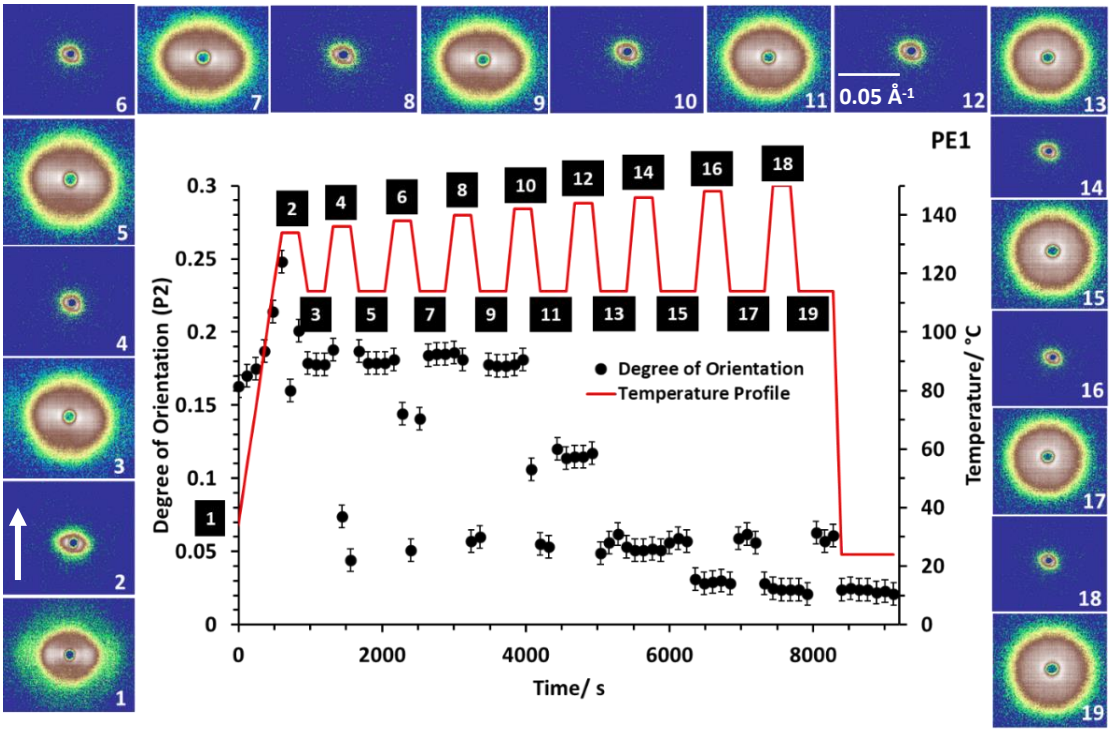

Figure 4.1: Detection of the melting point of oriented *shish* nuclei created in PE1 during shear-induced crystallisation measured by the decrease of the degree of orientation with temperature (filled symbols). Heat-treatment cycles were applied to a sample of PE1 crystallized after a shear pulse $\dot{\gamma}$ = 10 s^{-1} for t_s = 10 s at 130 °C and encapsulated in an aluminium DSC pan with Kapton windows. The heating protocol (red line) was stepped in increasing increments of 2 °C (134 °C, 136 °C etc.) alternated by cooling to below the temperature of spherulite crystallization), 114 °C. No orientation (P_2 = 0) was observed in the sample crystallized after heating to 146 °C (pattern 16 and corresponding time-temperature range in the graph). The orientation of the lamellar stacking (SAXS) was parallel to the direction of the shear flow (indicated by the white arrow in image 2), applied at 130 °C before crystallization. All of the SAXS patterns shown (1 - 19) have the same q scale (the scale bar is in pattern number 12).

Mykhaylyk *et al.* demonstrated that this was a temperature-dependent effect, caused by the temperature oscillations, and not a time-dependent kinetic process.[6] Oriented samples were held at temperatures greater than T_{ms}, but below T_{mo}, for 10 hours and upon crystallisation the oriented structure was still present, suggesting that such a long thermal treatment at temperatures greater than T_{ms} did not erase the *shish* nuclei.[6] Thus the memory effect of *shish* nuclei demonstrated that they could survive at temperatures greater than the melting point of spherulites ($T_{mo} > T_{ms}$).[6] Hsiao *et al.* presented a mechanism for the thermal relaxation of *shish-kebabs* subjected to a similar melting-recrystallisation procedure.[12] They postulated that the stability was dependent upon the relaxation dynamics of the stretched, UHMW chains forming

the *shish*, the time scales of which were an order of magnitude higher than those for the *kebabs*.[12] These stretched chains could, therefore, remain so during the time scale of the experiment and quickly nucleate the growth of *kebabs* upon cooling to the crystallisation temperature. As the temperature was increased, however, gradual relaxation of the stretched chain components occurred after each thermal cycle.[12] Consequently, as the concentration of stretched chain segments decreased, so too did the amount of *shish* re-formation and hence fewer *kebabs* recrystallised.[12] The point at which no orientation was observed indicated that the stretched chains had relaxed completely to the entangled network.

A sample of oriented PE2 was also subjected to the same melting and recrystallisation procedure. Similar to PE1, the SAXS patterns obtained at temperatures greater than the spherulitic melting temperature (Figure 4.2, even-numbered images 2 - 18) showed no orientation suggesting the *kebabs* were also in the melt state. Upon cooling the melt to the crystallisation temperature, the emergence of an oriented structure also returned but only up to melting temperatures of 136 °C (Figure 4.2, image 9). This was consistent with the trend seen by plotting the degree of orientation P_2 function against time (Figure 4.2, black filled circles) which confirmed that orientation remained until melting at 136 °C, with a small amount remaining after melting at 136 °C (Figure 4.2, image 3). After melting at 138 °C, no orientation was detected in the crystallised state as evidenced in the 2D SAXS patterns (odd-numbered images 5 – 19) and the P_2 function. Therefore, this suggested that the melting temperature of *shish* nuclei was between 134 – 136 °C and that thermal treatment at temperatures below 136 °C would not erase the oriented structure.

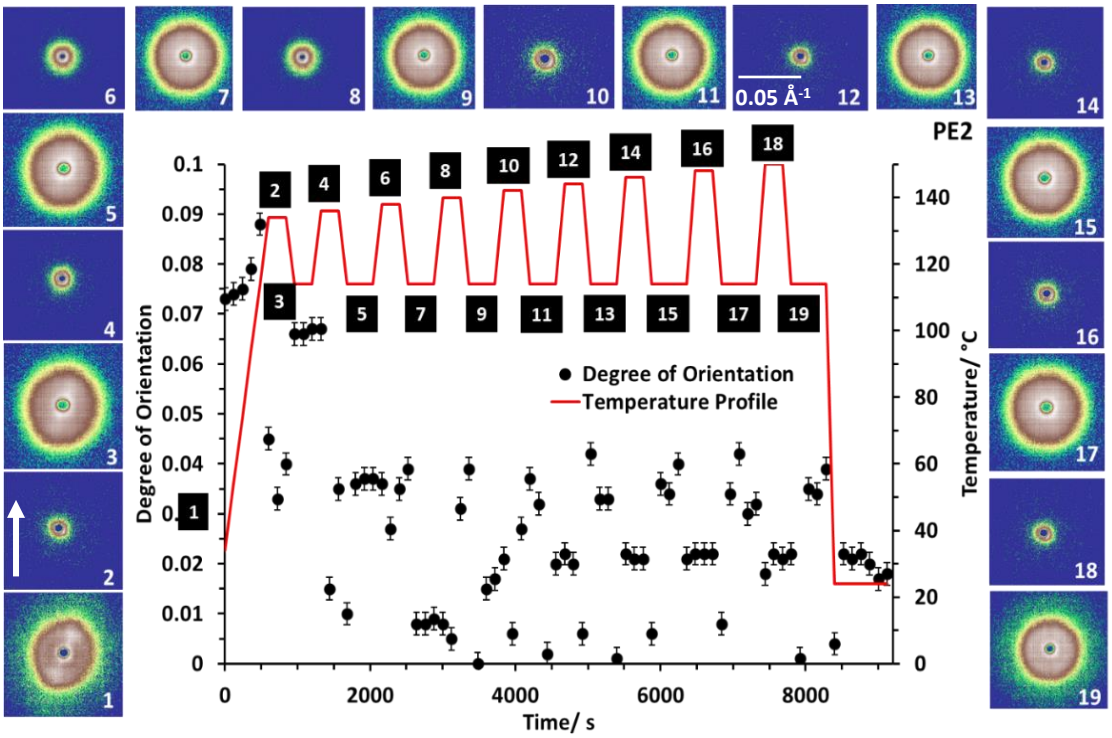

Figure 4.2: Detection of the melting point of oriented *shish* nuclei created in PE2 during shear-induced crystallisation measured by the decrease of the degree of orientation with temperature (filled symbols). Heat-treatment cycles were applied to a sample of PE2 crystallized after a shear pulse $\dot{\gamma}$ = 10 s^{-1} for t_s = 10 s at 130 °C and encapsulated in an aluminium DSC pan with Kapton windows. The heating protocol (red line) was stepped in increasing increments of 2 °C (134 °C, 136 °C etc.) alternated by cooling to below the temperature of spherulite crystallization), 114 °C. No orientation (P_2 = 0) was observed in the sample crystallized after heating to 136 °C (pattern 4 and corresponding time-temperature range in the graph). The orientation of the lamellar stacking (SAXS) is parallel to the direction of the shear flow (indicated by the white arrow in image 2), applied at 130 °C before crystallization. All of the SAXS patterns shown (1 - 19) have the same q scale (the scale bar is in pattern number 12).

There was clearly a significant difference between the thermal stability of oriented structures between PE1 and PE2, with the former displaying thermal stability of the oriented morphology to higher temperatures. As shown by GPC measurements (Section 3.2, Figure 3.1), PE1 possessed a larger fraction of UHMW material in the MWD. Therefore, the chain relaxation dynamics would have been longer than those for PE2 and the corresponding thermal stability greater.[14]

The onset and peak melting and crystallisation temperatures were obtained by DSC for both PE1 and PE2 (Section 3.3.1, Table 3.2) to assist in constructing a temperature-shear profile

(Figure 4.3). Spherulitic melting temperatures, T_{ms}, of PE1 and PE2 were 129 - 132 °C and crystallisation temperatures were 116 - 118 °C. Therefore, an initial melting temperature of 150 °C was selected in order to be certain that the previous thermal history had been erased (by melting at temperatures greater than T_m^0).[6] A shearing temperature of 130 °C was chosen at the melting point of spherulites and significantly above the crystallisation temperature under quiescent conditions. This choice was also consistent with the early experimental work showing that this temperature was an appropriate value for studying FIC of HDPE.[15]

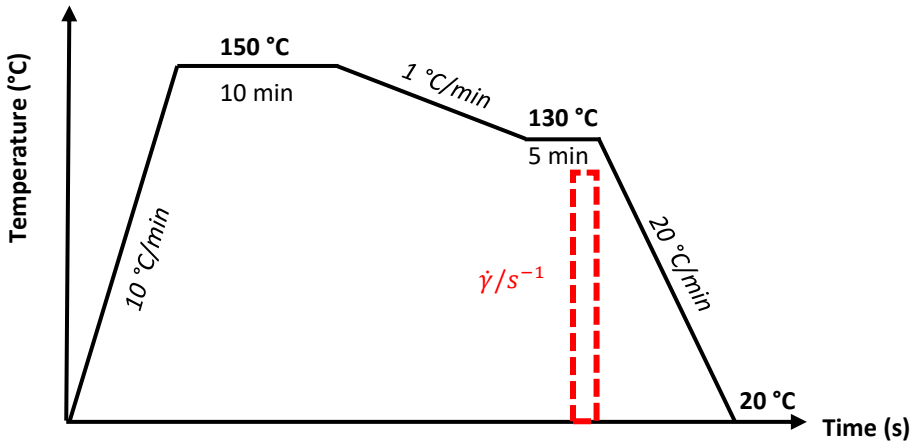

Figure 4.3: The initial temperature-shear protocol created from DSC data and SAXS measurements of the *shish* melting temperature. An initial heating step to 150 °C at 10 °C min^{-1} was followed by a 10-minute isothermal hold to erase thermal history. Cooling at 1 °C min^{-1} to the shear temperature of 130 °C, with a 5-minute isothermal hold, during which a shear pulse was applied. The final cooling step to room temperature occurred at 20 °C min^{-1}.

A risk with using parallel plate geometries was the influence of secondary, turbulent flows, caused by elastic instabilities, displacing the newly formed *shish* nuclei into the centre of the sample disk.[16–18] Unlike LMW liquids, polymer melts are known to develop elastic flow instabilities, which are often a limiting factor in fabrication processes.[22] Elastic instabilities in polymer melts arise because of the viscoelastic nature of such fluids and the non-linear response to deformation – elastic energy is stored (rheologically classified by *G'*) during deformation and subsequently released (through chain relaxation), thus causing turbulence to existing laminar flows.[19–21] The general criterion for instability onset is a certain critical value of the Weissenberg number as a measure of the melt elasticity.[21,23] By shearing at higher temperatures, relatively low shear rate and strain (shearing time), the effect of elastic instabilities was minimised.[7] These flow instabilities are a known phenomenon in a range of processing techniques, including extrusion where linear polymers such as HDPE can exhibit

instabilities in shear flow in the die.[23,24] For example, melt fracture during extrusion occurs above a critical output rate resulting in an apparent wave-like defect pattern on the surface of extruded products.[24] These industrial polymers were designed to have a high melt elasticity, making them stable during processing but potentially leading to problems such as die swell.[25,26] Above a certain strain, distortions to the symmetric shearing caused spiral flow through the disk which was identified by a tilting in the 2D SAXS pattern, indicating an uneven flow distribution (Figure 4.4).[6] A four-spot 2D SAXS pattern was also indicative of tilting of the crystalline lamellae (Figure 4.4, image 18).[27]

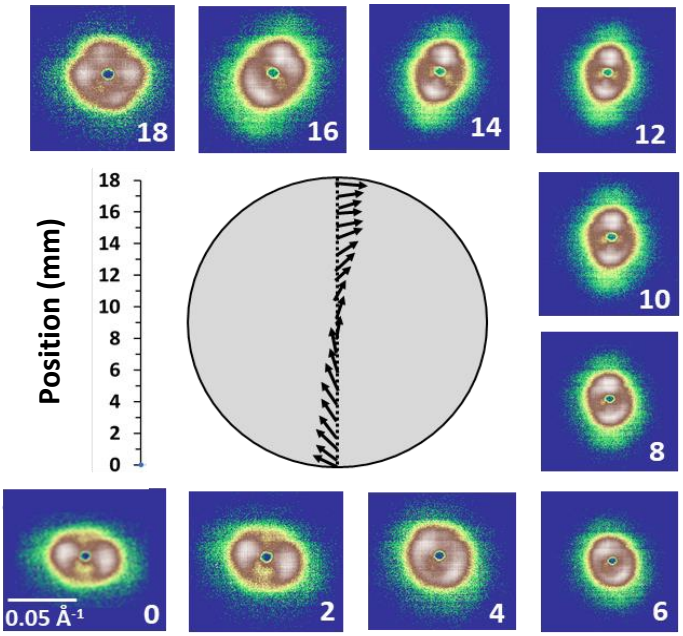

Figure 4.4: A diagram of spiral shear flow during torsional parallel plate shearing ($\dot{\gamma}$ = 10 s^{-1}, t_s = 10 s, T = 130 °C) displaying elastic instabilities, as observed by the 2D SAXS images taken along the sample diameter. The tilting of the 2D SAXS patterns was indicative of flow instabilities. The arrows indicate the approximate direction of flow within the sample and the numbers correspond to the radial position in mm at which the SAXS measurement was taken along the diameter of the disk.

In this work, appropriate conditions were chosen to avoid flow instabilities by shearing at higher temperatures, relatively low shear rate and strain (shearing time).[7] Thus a disk of PE1 (16 mm diameter) was subjected to the temperature-shear protocol (Figure 4.3, see also Section 2.2) with a shear pulse applied: $\dot{\gamma}$ = 10 $^{-1}$, t_s = 10 s, T = 130 °C. After unloading the disk from the shear cell, a radial SAXS scan was performed in 0.5 mm intervals with the resulting 2D

SAXS patterns. Calculating and plotting the degree of orientation, P_2, against the radial position gave a quantitative distribution of the orientation across the disk (Figure 4.5).

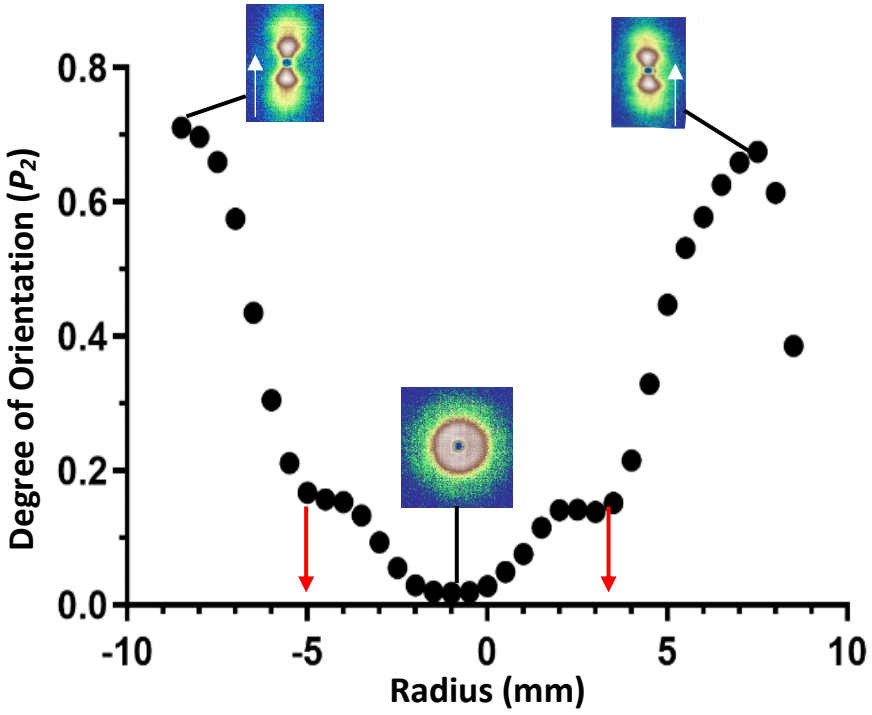

Figure 4.5: Plots of the degree of orientation of PE1 calculated from SAXS patterns (Bruker AXS NanoStar) measured along the diameter of the samples after shearing ($\dot{\gamma}$ = 10 s^{-1} for a shear time of 10 s at 130 °C). The zero-radius position corresponds to the centre of the sample, the negative values of the radius correspond to the left-hand side of the sample and the positive to the right-hand side of the samples. The white arrows on the SAXS patterns indicate the flow direction. The red arrows indicate the approximate regions at which significant orientation onset occurred. Selected 2D SAXS patterns are included to show the change in morphology at the highest and lowest shear rates.

There was a clear difference in the two morphologies identified by SAXS: the two-lobe spots indicated oriented structure formation and the isotropic halo indicated unoriented material.[28] It was clear that as the shear rate decreased towards the centre of the disk (as $\dot{\gamma} \rightarrow 0$), P_2 tended towards zero. Thus, a clear boundary was observed between oriented and unoriented material, indicated by the red arrows (Figure 4.5). Therefore, under the shear conditions used here, PE1 could form oriented morphology.

Another interesting feature was the plateau region just after the degree of orientation increased from zero (Figure 4.5). The radial distribution of shear rates in parallel plate shearing (Figure 2.2, Section 2.2) leads to an increased density of oriented nuclei at the disk edge and a faster

rate of crystallisation which creates an annular-shaped crystallisation front, identified by polarised light imaging (Figure 4.6).[6] Therefore, as the crystallisation front proceeded from the disk edge to the centre upon cooling, the molten centre was confined by the shear plates and experienced compression due to shrinkage of the crystallised annulus (Figure 4.6).[6]

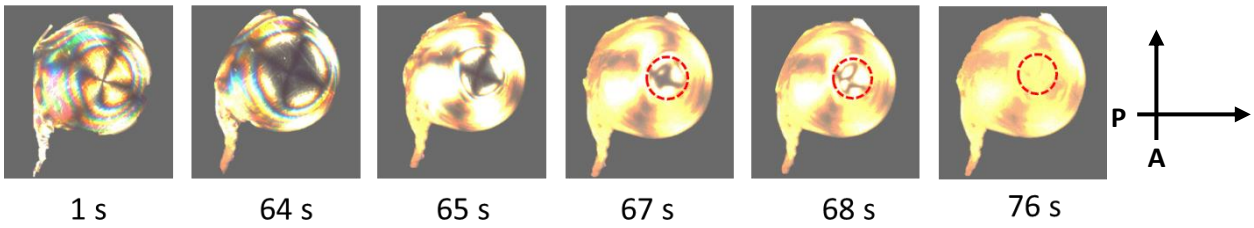

Figure 4.6: Selected polarised light images of PE1 taken at 1 s intervals after the cessation of shear ($\dot{\gamma}$ = 10 s^{-1}, t_s = 10 s, T = 130 °C) during cooling at 20 °C min^{-1}. The faint Maltese Cross indicates the formation of oriented morphology and the red circles represent the boundary between oriented and unoriented material. The directions of the crossed polariser and analyser are indicated.

The circular fringe surrounding the Maltese cross was caused by two forces originating from shrinkage of the crystallised polymer annulus and compressibility of the melt in the centre of the sample.[6] Eventually, complete crystallisation occurred as the sample continued to be cooled, however some orientation at the fringe was lost due to local motion of the chains.[6] The location of the fringes was also identified from SAXS measurements by the plateaus in the degree of orientation (black (PE1) and red (PE2) arrows in Figure 4.7).[6] PE2 was also subjected to the same temperature-shear profile (Figure 4.3) and a subsequent radial SAXS scan in 0.5 mm intervals performed to plot P_2 against radial position (Figure 4.7).

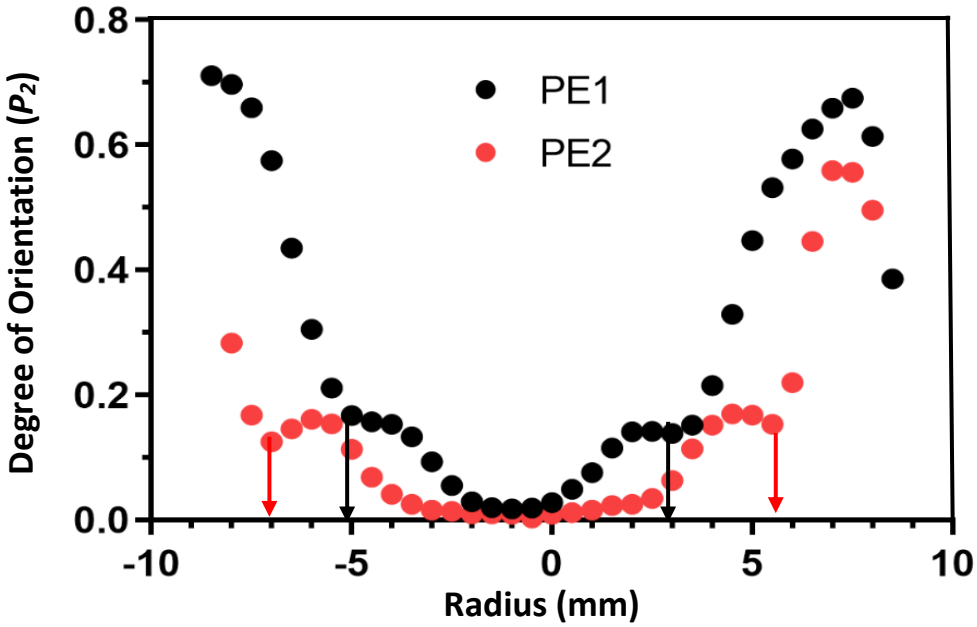

Figure 4.7: Comparison plots of the degree of orientation of PE1 (black) and PE2 (red) measured (Bruker AXS NanoStar) along the diameter of the samples after shearing ($\dot{\gamma}$ = 10 s^{-1}, t_s = 10 s, T = 130 °C). The zero-radius position corresponds to the centre of the samples, the negative values of the radius correspond to the left-hand side of the samples and the positive to the right-hand side of the samples. The black and red arrows indicate the onset of the plateaus in orientation caused by the moving crystallisation front for PE1 and PE2 respectively.

Considering the linear distribution of shear rates in parallel plate shear, the zone of no orientation indicated the region in which the shear rate was insufficient to stretch and orient the polymer chains.[6,7] Above this shear rate, the stretching and orientation caused oriented morphology formation upon crystallisation – oriented structures can only be formed if a polymer is sheared at a rate greater than the inverse Rouse time, τ_R, of the longest chains in the melt ($\dot{\gamma} > 1/\tau_R$) and has experienced mechanical work greater than a threshold value.[6] For blends with a large polydispersity (Table 3.1), the Rouse time, and hence $\dot{\gamma}_{min}$, should be regarded as an ensemble value for the molecules in the melt.[9] A distribution of polymer chain lengths is present in any polymer melt, as evidenced by a broad MWD obtained through GPC measurements (Figure 3.1). The breadth of this distribution can also affect the rheology behaviour, especially with regard to shear-thinning. In particular, melts with a larger molecular weight and broader MWD exhibit greater shear-thinning than melts with a narrower MWD at similar molecular weights.[54] Additionally, melt relaxation times of melts with a broader MWD have been shown to be larger than narrow MWD counterparts.[55]

Under quiescent conditions, nucleation of HMW chains is largely independent of chain length.[7] However, flow supplies conformational order to chains by stretching and thus delivering one stretched segment to another via a collision.[7] These collisions can continue until the aggregated segment size is larger than the critical nucleus size and so stable *shish* nuclei are formed.[7,9] Longer molecules are likely to contain a greater number of stretched segments under flow and, therefore, more intrachain contacts can occur to further stabilise the emerging nuclei. Consequently, chains with a large radius of gyration (the UHMW chains) are a necessary component of a polymer system for the formation of stable *shish* nuclei.[7] By way of increasing the shear rate, the frequency of segment collisions can be increased and thus also the probability of *shish* nuclei forming. Hence flow is integral and impacts upon the nucleation process only above a critical shear rate, whereby the flow stretches and elongates the polymer chains to form these segments.[7] The number of stretched segments required to form the *shish* nuclei depends upon the critical size of the stable nucleus and stretched segment length, the latter of which is dependent both upon the MWD and molecular weight of the longest chains in the melt.[7,9] Thus, a critical nucleation density exists at which the flow causes the stretched segments to aggregate at a critical size and not immediately relax upon cessation of shear.[6,7,9]

During SAXS measurements, x-rays interact with electrons and thus an electron density difference must be present in order to establish contrast between the background and the sample.[6,28] The greater number of electrons that are present within the sample volume (the electron density) the greater the scattering and hence the contrast. Therefore, as the stretched segments aggregate into *shish* nuclei, the electron density contrast increases until scattering reaches the detection limit at which morphological features can be observed by SAXS.[6,7,28]

PE2 displayed a much broader zone of no orientation and lower peak orientation at the edges compared to PE1, due to the differences in MWD. PE1 had a higher fraction of UHMW material (Figure 3.3, Section 3.2), the relaxation times of which were longer, and this has been shown to play an essential role in the formation of oriented *shish* nuclei.[12] Therefore, a larger fraction of long chains resulted in greater orientation overall, as a higher concentration of *shish* nuclei could be formed initially.[29] An increased fraction of HMW chains, as was the case for PE1, also required a lower shear rate for the onset of oriented morphology and hence displayed a smaller zone of no orientation.[6,7]

4.3 Critical Shear Rate – Polarised Light Imaging and Boundary Conditions

The critical shear rate was an important parameter for understanding the behaviour of a material undergoing SIC as it was the shear rate above which the chains, oriented by flow, began to stretch. Below this critical shear rate, chains cannot stretch and form oriented nuclei thus SIC cannot occur and only spherulitic morphology will be produced during crystallisation.

A useful technique for quantifying the shear flow parameters that govern the formation of oriented morphology was SIPLI (Section 2.7.2).[7,16,30] During shear, PLIs display a clear boundary between oriented and unoriented zones of the sample; the boundary between these two zones corresponds to the shear rate above which oriented morphology can be created.[7] Birefringence of PE melts under flow can originate from stretched molecules and nucleating crystals, hence anisotropy in both refractive index and stress caused by flow are mutually related through a linear stress-optical relationship.[16] Therefore, a connection between melt motion under flow and structural response can be established through this technique.[16]

For PE1 and PE2, it was important to understand the critical shear rate above which oriented morphology formation could occur. A lower shear rate was used (to reduce the possibility of the Weissenberg effect occurring upon shearing these materials at higher shear rates) in 25 mm parallel plate rotational rheology with all other conditions as per the previous temperature-shear protocol: $\dot{\gamma}_{max}$ = 0.5 s^{-1}, t_s = 10 s, T = 130 °C.

An indication of the Weissenberg effect was apparent in initial measurements at $\dot{\gamma}_{max}$ = 10 s^{-1}, t_s = 180 s and T = 130 °C (Figure 4.8). $\dot{\gamma}$ did reach $\dot{\gamma}_{max}$ = 10 s^{-1} after 40 seconds of shearing, however this would not have been convenient or practical for further rheology measurements. Additionally, the viscosity and shear rate showed corresponding maxima and minima respectively between 0 – 40 seconds of shearing which suggested that the flow behaviour was non-laminar within this timeframe.[6,7] The first small plateau (at 25 – 30 seconds) suggested a build-up of stress with prolonged shearing which could have been released by slippage between the sample and disk or, as was observed, a gradual expulsion of the sample through the gap.[6,7] As a greater volume of sample was expelled, the normal stresses diminished sufficiently so that $\dot{\gamma}_{max}$ could be reached. Gradual shear-thinning was apparent once a steady rotational flow had been achieved.

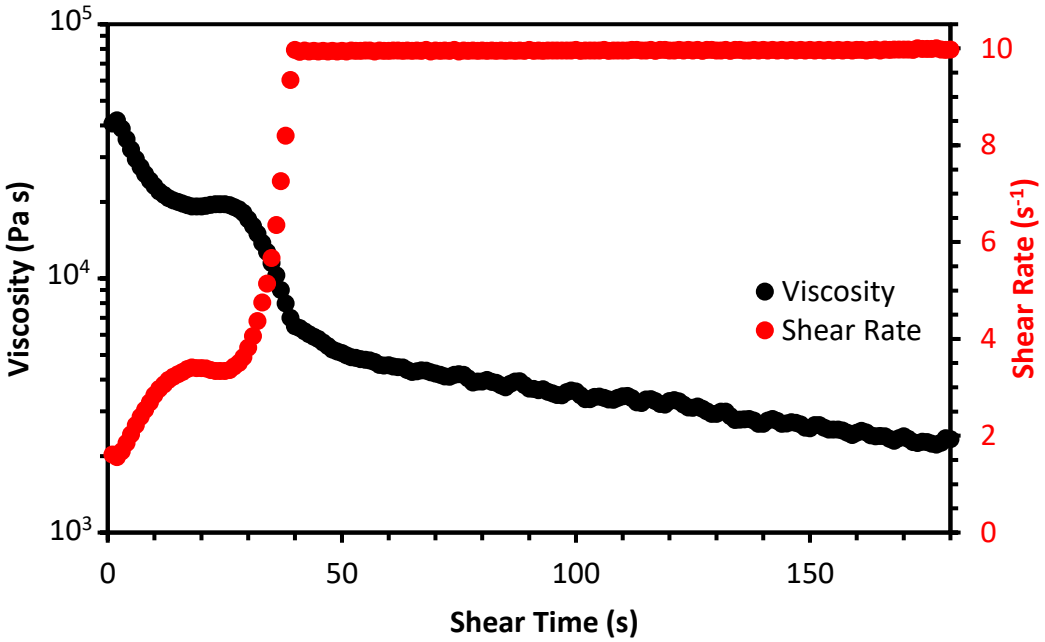

Figure 4.8: Viscosity and shear rate against time (on log-linear and linear-linear scales respectively) for a sample of PE1 sheared at $\dot{\gamma}_{max}$ = 10 s^{-1}, t_s = 180 s, T = 130 °C using 25 mm parallel plates. The $\dot{\gamma}_{max}$ was achieved only after 40 seconds of shearing.

Images were recorded at 0.5 second intervals (Figures 4.9 and 4.10). The PLIs for PE1 (Figure 4.9), with corresponding times indicated, displayed an opaque Maltese cross. The central opaque zone corresponded to a non-birefringent region, indicating that this region had experienced little shear and hence the isotropic polymer melt contained no oriented nuclei formed under the shear.[6,16] Conversely, the outer bright zone indicated that at higher shear rates birefringent material corresponding to oriented nuclei was formed under shear.[6]

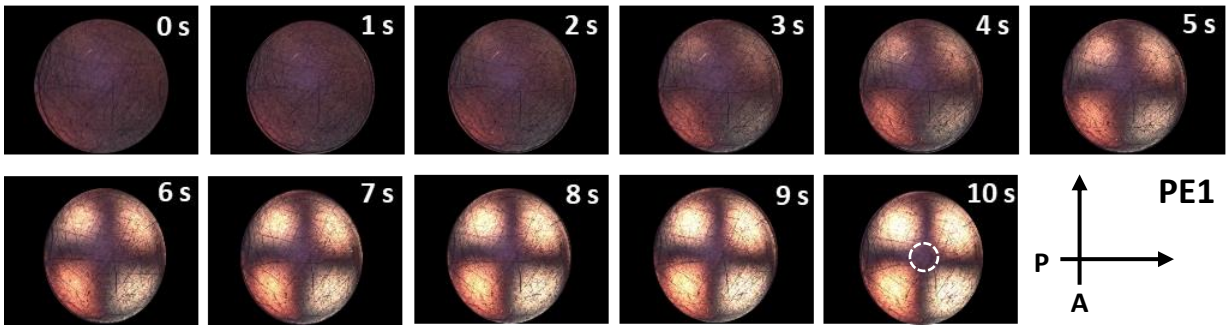

Figure 4.9: Polarised light images of PE1 during shearing ($\dot{\gamma}_{max}$ = 0.5 s^{-1}, t_s = 10 s, T = 130 °C) measured at 0.5 second intervals. The white circle in the 10 second image indicates the boundary between unoriented (dark, inner, non-birefringent region) and oriented material (outer, light, birefringent regions).

After less than a second of shear flow (image not displayed), faint translucent outer zones emerged which continued to grow in intensity throughout the time of shearing until a maximum was reached at approximately 8 seconds of shear. A clear boundary between the light and dark regions emerged with growing intensity. This boundary, indicated by the dashed circle in the 10 second PLI (Figure 4.9), marked the transition from unoriented to oriented material. By measuring the position of the boundary relative to the disk edge (and hence maximum shear rate) through image processing, a critical shear rate of 0.14 s^{-1} was obtained.[6]

The same shearing and PLI procedure were applied to PE2 (Figure 4.10).

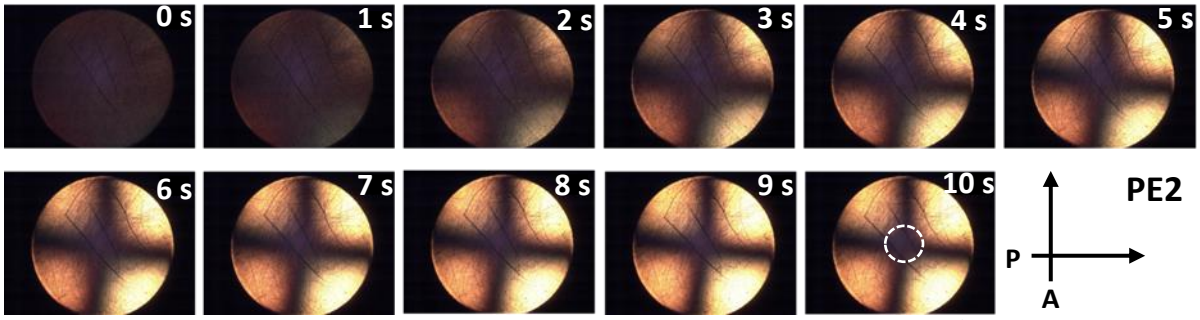

Figure 4.10: Polarised light images of PE2 during shearing ($\dot{\gamma}_{max}$ = 0.5 s^{-1}, t_s = 10 s, T = 130 °C) measured at 0.5 second intervals. The white circle in the 10 second image indicates the boundary between unoriented (dark, inner, non-birefringent region) and oriented material (outer, light, birefringent regions).

After 1 second of shearing, faint translucent outer zones emerged and continued to grow in intensity throughout the time of shearing until a maximum was reached at approximately 9 seconds of shear. A clear boundary between the light and dark regions emerged with growing intensity. This boundary, indicated by the dashed circle in the 10 second PLI (Figure 4.7), marked the transition from unoriented to oriented material. By measuring the position of the boundary relative to the disk edge (and hence maximum shear rate) through image processing, a critical shear rate of 0.24 s^{-1} was obtained.[6]

Note that the orientation increased with the time of shearing, indicating that it took a certain amount of time at the shear rate of interest to stretch and build oriented nuclei under flow – a specific amount of work was required.[6] The lower work observed for PE1 can be explained by again considering the MWD and the increased fraction of HMW material present in PE1. These longest chains will have the greatest relaxation times, and an increased concentration of long chains in the melt requires a smaller applied strain to stretch and align these chains.[7] A similar

study performed by Mykhaylyk *et al.* determined a critical shear rate for an industrial HDPE (of similar molecular weight but narrower dispersity) of 2 s^{-1}.[30]

4.4 Critical Work Parameters for Oriented Morphology Formation

The critical work is a key parameter to predict the formation of an oriented morphology. According to the hypothesis of Janeschitz-Kriegl, the morphology of a sheared polymer melt can be controlled by the amount of mechanical work performed by flow on the system.[31] The specific work *w* can be calculated as (Eq. 4.1):

$$w = \int_0^{t_s} \eta[\dot{\gamma}(t)]\dot{\gamma}^2(t)\mathrm{d}t \qquad 4.1$$

where the integration is over the entire time of shearing, t_s, $\dot{\gamma}$ is the shear rate and $\eta[\dot{\gamma}(t)]$ is the shear-rate dependent viscosity.[6,7,31] This equation demonstrates that both the shear rate and shear time are important for the respective stretch and growth of the *shish* morphology.[32] When a relatively high angular speed is used and/or the polymer has a high viscosity, there is an unavoidable acceleration period before the maximum angular velocity is reached, thus changing the shape of the shear pulse from rectangular to trapezoidal (Figure 4.3).[6] This effect can be used, through a programmed slow acceleration, to bring two experimental benefits: sample damage during shear at high shear rates can be minimised and the stress overshoot caused by a nonlinear response during start-up shear is reduced.[6] Consequently, the shear rates are no longer constant and, therefore, calculating the specific work requires integration over the total flow taking into account the dependence of the viscosity upon shear rate.[6] However, if the acceleration period is negligible then the shear pulse can be assumed to be rectangular in shape and, from Eq. 4.1, the shear rate and viscosity can be assumed constant ($\dot{\gamma}(t) = \dot{\gamma}$ and $\eta[\dot{\gamma}(t)] = \eta(\gamma)$ respectively).[6] Subsequently, multiplication of the parameters can be utilised in place of the integration over the shearing time, t_s:[6]

$$w_c = \eta(\dot{\gamma}).\dot{\gamma}^2.t_s \qquad 4.2$$

where $\eta(\dot{\gamma})$ is the shear-rate dependent viscosity (this was obtained from the modulus of complex viscosity mastercurves shifted to 130 °C by applying TTS coefficients and subsequent Cross model fitting – Section 3.4.2), with all terms as previously defined.[7] Consequently, with an increasing fraction of HMW material, the critical work, w_c, for oriented structure formation

decreases and has been shown to be approximately inversely proportional to the concentration of long chains in the blend.[7]

Flow has a significant impact upon nucleation in undercooled polymer melts to the extent that considerable numbers of nuclei, comparable to those obtained from quiescent melts at undercoolings greater than 100 °C, can be obtained by applying moderate amounts of mechanical work and undercooling.[31] An increase in the number of nuclei with the applied mechanical work was observed by Janeschitz-Kriegl *et al.*[31] This was built upon by Mykhaylyk *et al.* to show that oriented structures were only obtained if the applied work was greater than a critical threshold value at shear rates greater than the inverse Rouse time, $\dot{\gamma} > 1/\tau_R$.[6,7] Therefore, chains with a longer relaxation time, the longest chains in the melt, have to be stretched by the applied shear to form *shish* nuclei upon which the remaining chains in the melt can crystallise as *kebabs*.[7] As both the chemical structure and MWD affect the relaxation times, the magnitude of the specific work required to create oriented structures is dependent upon these factors also.[6,7] For the bimodal blends used in this work, PE1 was shown by GPC analysis (Section 3.2, Figure 3.1) to possess a larger fraction of UHMW material than PE2 which indicated initially that the former material would display a lower critical work for oriented structure formation.

A combination of techniques was required to obtain the critical work values for the materials used herein. By performing SIC in parallel plate shear, and then unloading the samples from the shear device, a boundary could be detected between oriented and unoriented material by an increase in the P_2 function, calculated from radial SAXS measurements (Figures 4.5 and 4.7).[6] Given a distribution of shear rates is present in parallel-plate shear (Section 2.2.1, Figure 2.1), the radius at which the boundary occurs can be recalculated into a boundary shear rate, $\dot{\gamma}_b$.[6]

Under the shear conditions used ($\dot{\gamma}$ = 0.5 s^{-1}, t_s = 10 s, T = 130 °C), boundary shear rates, $\dot{\gamma}_b$, were calculated to be 4.7 s^{-1} and 5.6 s^{-1} for PE1 and PE2 respectively (Figure 4.7). Shear-rate dependent viscosity values, $\eta(\dot{\gamma})$, of 59 786 Pa s and 71 954 Pa s were obtained from the viscosity master curves measured for PE1 and PE2 respectively (Table 4.1 and Figures 3.17 & 3.19, Section 3.4.2).

	$\dot{\gamma}_b$ (s^{-1})	$\eta(\dot{\gamma})$ (Pa s)	M_w (kDa)	M_n (Da)	M_z (kDa)
PE1	4.7	59 786	264.5	7.91	2094.4
PE2	5.6	71 954	227.5	7.93	1858.0

Table 4.1: Boundary shear rates as obtained from the degree of orientation as measured by SAXS and shear-rate dependent viscosity values as obtained from application of a time-temperature superposition of oscillatory frequency sweeps and fitting with the Cross Model. M_n, M_w and M_z values as measured by GPC (Figure 3.1 and Table 3.1) are included to highlight the importance of the UHMW chain present in the melt.

Using these values with Eq. 4.2 gave $w_c(PE1) = 13.21 \pm 1.61$ MPa and $w_c(PE2) = 22.56 \pm 4.67$ MPa.[7] Previous work by Mykhaylyk *et al.* obtained values of the same order of magnitude for a number of LDPE and model PE samples with similar molecular weights and dispersity.[6] These results were consistent with GPC measurements which showed that PE1 had a HMWT present in the blend and, therefore, the critical work required to form oriented morphology was smaller than that for PE2.[7] The larger value obtained for PE2 was related to the viscosity and MWD of the melt. The viscosity of PE2 was fractionally lower than PE1 (Table 3.6, Section 3.4.2) due to the smaller fraction of UHMWPE in the melt. However, the GPC measurements indicated that the rest of the PE2 blend (especially the HMW content constituting the second peak in the bimodal distribution) was of a greater molecular weight (Figure 3.1, Section 3.2) which explained why a greater amount of work was required to overcome the viscosity barrier to flow.[7]

As the M_n and M_w of both materials were similar (Section 3.2, Table 3.1), it was expected that similar viscosity and relaxation times, averaged by the rheology measurement, would be obtained. This, however, did not correlate with critical specific work, w_c, as the values for both materials were very different (PE1 = 13.21 MPa, PE2 = 22.56 MPa) which was likely explained by the difference in M_z values which are more sensitive to longer chains (M_z is measured in the high molecular weight region) .[7] However, the w_c values correlated well with the HMWT observed for PE1 in the MWD. The longest chains in a melt enhance the flow-induced nucleation and, therefore, less work was required for PE1 to produce an oriented morphology.[7] Therefore, rheology alone was not indicative or conclusive for the prediction of the behaviour of flow-enhanced nucleation. Differences in relaxation dynamics between different molecular weight components may well have complicated matters.[33]

4.5 Optimisation of Processing Parameters

4.5.1 Effect of Shearing Temperature on Degree of Orientation

In order to further test the thermal stability of oriented structures, a series of experiments were conducted at different shearing temperatures whilst maintaining the shear rate and shear time: $\dot{\gamma}$ = 10 s^{-1} and t_s = 10 s. 130 °C was taken as the benchmark temperature at which it was known orientation could be achieved. For each subsequent shearing experiment, the temperature was increased in 10 °C increments up to 160 °C. After shearing, each sample was unloaded and measured with a radial SAXS scan (Figures 4.11a and 4.11b) to obtain the degree of orientation, P_2, against radial position for PE1 and PE2 at each temperature.

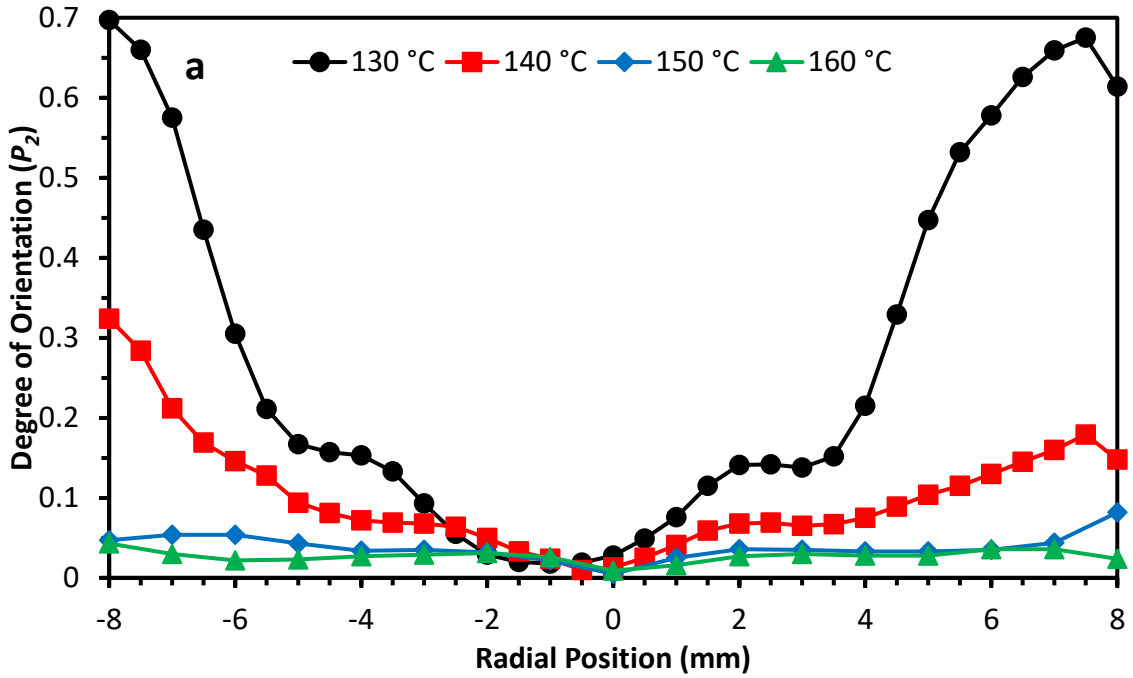

Figure 4.11a: Degree of orientation against radial position for a) PE1 and b) PE2 at shear temperatures increasing in 10 °C increments from 130 – 160 °C. The shear rate and time were kept consistent across the temperature range: $\dot{\gamma}$ = 10 s^{-1} and t_s = 10 s.

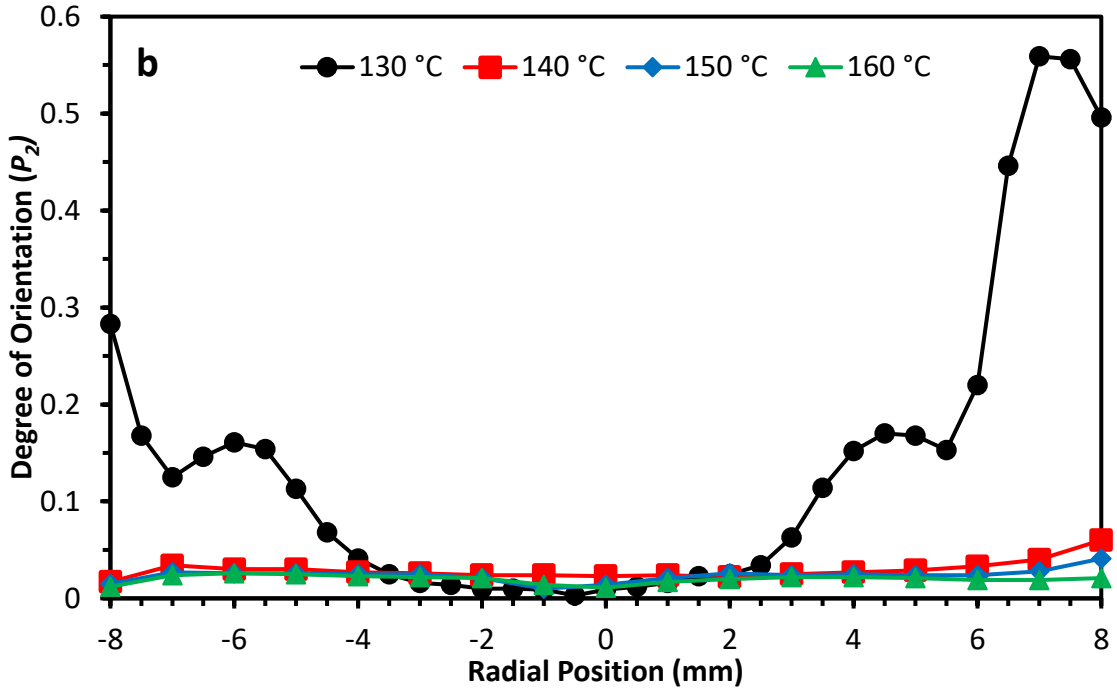

Figure 4.11b: Degree of orientation against radial position for a) PE1 and b) PE2 at shear temperatures increasing in 10 °C increments from 130 – 160 °C. The shear rate and time were kept consistent across the temperature range: $\dot{\gamma}$ = 10 s^{-1} and t_s = 10 s.

Some orientation was clearly visible for PE1 at 140 °C, but significantly less than at 130 °C at the maximum shear rates at the disk edges. No orientation was observed for PE2 at the same temperature. At temperatures greater than 140 °C, polymer relaxation outpaced crystallisation and any oriented nuclei formed relaxed back to the entangled melt state. This was consistent with the melting behaviour and thermal stability of oriented morphology during thermal cycling experiments (in Section 4.2.1, Figures 4.1 and 4.2). Oriented structures in PE1 were stable until 144 – 146 °C, whereas oriented structures in PE2 were only stable until 134 – 136 °C due to the longer relaxation times of the UHMW fraction in PE1. This was particularly important for consideration when designing future industrial processes as PE is often processed at high temperatures close to 200 °C. Therefore, if SIC was desired, a method of cooling the process to suitable temperatures would need to be incorporated.

4.5.2 Effect of Shearing Time upon Degree of Orientation

The shearing time, t_s, was another important parameter for controlling the formation of oriented structures in polymer melts.[32] In order to probe this, a series of samples were sheared at a consistent shear rate ($\dot{\gamma}$ = 10 s^{-1}) and temperature (130 °C) with only the length of shear time varied. The samples were imaged *in-situ* using polarised light imaging in order to observe orientation in each sample (Figure 4.12).

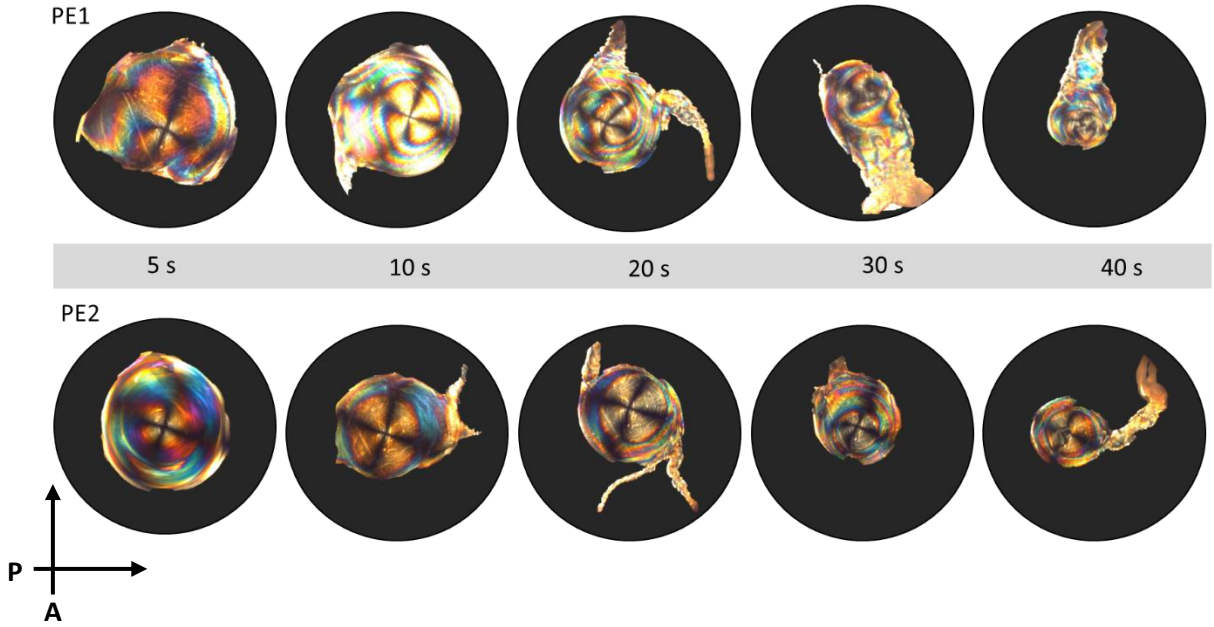

Figure 4.12: Polarised light images of PE1 (top) and PE2 (bottom) taken immediately after the cessation of shear at different shearing times. The shear rate and temperature were kept constant ($\dot{\gamma}$ = 10 s^{-1}, T = 130 °C).

Time intervals of 5-, 10-, 20-, 30- and 40-seconds shearing time were selected and the samples sheared in a Linkam CSS450 shear cell with the top plate replaced with a glass viewing window and polarised camera optics (experimental details can be found in Section 2.7.2.1). A Maltese cross was visible in images taken at lower shear times, with increasing distortions as the shear time increased. A clear boundary was also seen at lower shear times between the Maltese cross and brightly coloured outer fringes which were caused by the increasing stress-induced birefringence towards the disk edge.[16] For both PE1 and PE2, increasing the shear time from 5 seconds to 10 seconds caused the diameter of the unoriented zone (indicated by the Maltese cross) to correspondingly decrease in size. This indicated that the amount of orientation increased with an increasing shear time. However, as the time of shearing increased further for PE1, the oriented zone grew smaller, identified by the decreasing diameter of the Maltese cross region, with a corresponding increase in the highly coloured outer regions, suggesting that

elastic instabilities (additional turbulent flows arising from the release of stored elastic energy from melt deformation by shear) were becoming increasingly dominant in the flow. [16–18] For shear times greater than 30 seconds for PE1, the Maltese Cross disappeared completely with only the brightly coloured stress birefringence observed, suggesting that the oriented structures formed previously had been displaced due to the dominant elastic instabilities.[6] The Maltese cross was visible for PE2 throughout all shearing times, but the diameter of this zone did diminish with increasing time, also suggesting that elastic instabilities were becoming increasingly dominant.[6] The extreme distortions observed at longer shearing times for PE1 were not observed to the same extent for PE2 at corresponding times, which suggested that PE1 had exceeded an upper strain limit to forming oriented morphology. Chains with the longest relaxation times and narrow MWDs are most susceptible to elastic instabilities.[6] The greater, but narrow (relative to the MWD of PE2) fraction of UHMW chains present in the MWD of PE1 could explain why this melt exhibited greater susceptibility to elastic instabilities.

After shearing, each sample was cooled to room temperature and unloaded from the shear cell to perform a radial SAXS scan in 1 mm intervals across the diameter of each disk (Figures 4.13a and 4.13b).

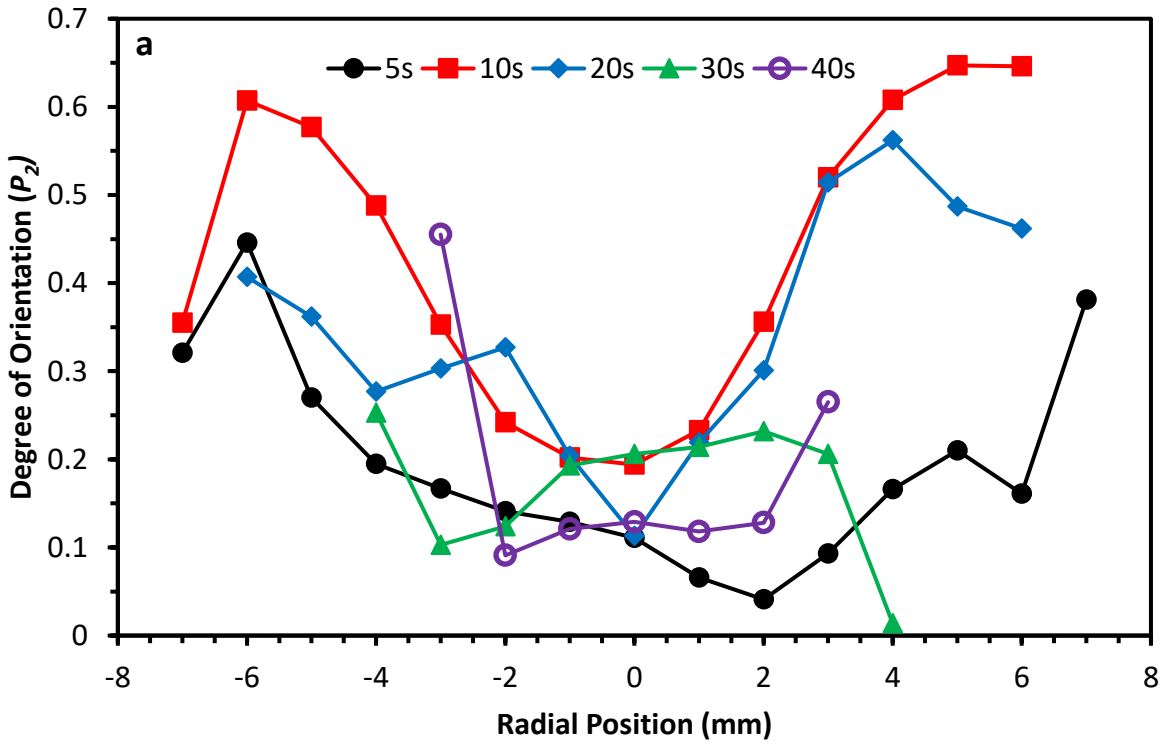

Figure 4.13a: The degree of orientation plotted against disk radius for a) PE1 and b) PE2 showing the effect of shear time upon degree of orientation. Shear times of 5 s, 10 s, 20 s, 30 s and 40 s were measured with $\dot{\gamma}$ = 10 s^{-1} at a shear temperature of 130 °C.

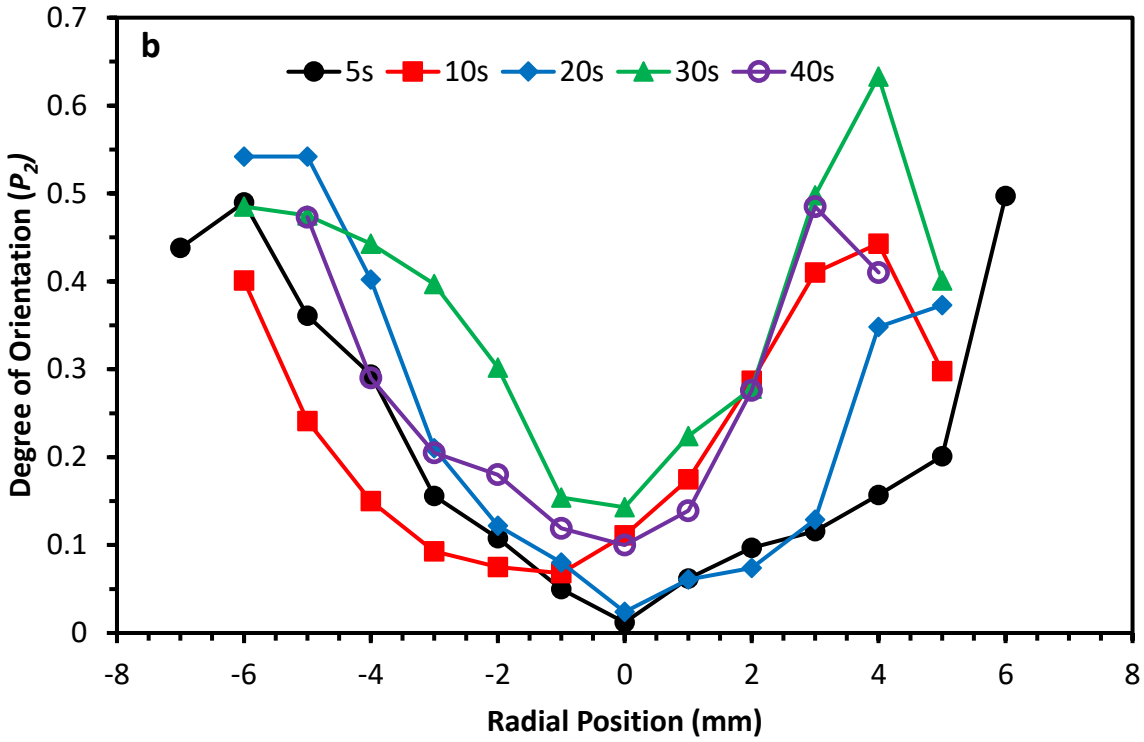

Figure 4.13b: The degree of orientation plotted against disk radius for a) PE1 and b) PE2 showing the effect of shear time upon degree of orientation. Shear times of 5 s, 10 s, 20 s, 30 s and 40 s were measured with $\dot{\gamma}$ = 10 s^{-1} at a shear temperature of 130 °C.

By plotting the degree of orientation, P_2, against radial position, a picture of the distribution of orientation was obtained. For both PE1 and PE2, elastic flow instabilities complicated the interpretation. The increase in orientation by increasing the shearing time from 5 seconds to 10 seconds was clear for PE1 (Figure 4.13a), whereas the same increase in shear time for PE2 appeared minimal. The impact of elastic instabilities was evident from a shearing time of 30 seconds onwards for PE1 as the P_2 curves displayed an uneven distribution of orientation with no increase observed upon increasing for longer shear times. Whilst elastic instabilities were evident in the P_2 plots of PE2, only minor increases in the degree of orientation were evident (Figure 4.13b). Thus, both the PLI images and SAXS measurements corroborate each other.

Previous work has indicated the presence of a minimum threshold value for the mechanical work required to form oriented structures - such oriented morphology will only form above this critical specific work.[6,7,34] These results presented in Sections 4.3 and 4.4 also point to a critical amount of work required to form oriented structures. However, this recent work would suggest the presence of an upper limit above which elastic instabilities dominated the flow and distorted the orientation distribution through the sample, which was especially apparent for

PE1. Therefore, these results indicated that a saturation point in the degree of orientation was achieved for PE1 but not for PE2. Prolonged shearing above this saturation point evidently had the effect of initiating elastic flow instabilities which displaced/destroyed the oriented structures.[6]

In a quality control setting, these elastic instabilities would result in fatal product flaws that would not pass quality control assessment. Therefore, it is important for manufacturers to understand the full flow behaviour of the material in question. It was clear that in order to achieve oriented morphology a balance between shear rate, time and temperature should be met. All three were equally important in controlling the FIC process and due care must be taken when designing any future industrial processes.

4.6 Crystallisation Kinetics

Several studies have shown the impact of orientation upon the enhancement of crystallisation kinetics for polymer melts.[12,35,36] Comparing the isothermal crystallisation kinetics of sheared and unsheared HDPE through Avrami analysis gave an insight into the crystallisation kinetics for PE1 and PE2.

Isotropic samples were cut from melt pressed films of 0.5 mm thickness and anisotropic samples were obtained by shearing using the Couette cell ($\dot{\gamma}$ = 10 s^{-1}, t_s = 20 s, T = 130 °C) before cutting, ensuring that stator segment joints and other defects were avoided. The measurement protocol for the anisotropic samples was composed of isothermal melting at 136 °C for 1 minute before rapid cooling at 100 °C min^{-1} to crystallisation temperatures, T_c, of 120 – 110 °C, where the temperature was maintained for 10 minutes before cooling at 20 °C/min to room temperature. For the isotropic samples, initial isothermal melting occurred at 150 °C for 10 minutes to erase thermal history,[6] before cooling to the crystallisation temperatures as mentioned. An isothermal melting temperature of 136 °C was selected to ensure that the oriented morphology was not destroyed by thermal relaxation.[12]

4.6.1 The Avrami Model

Application of the Johnson-Mehl-Avrami-Kolmogorov (JMAK) model (often simply shortened to the "Avrami Model") is commonly used in order to understand isothermal crystallisation kinetics.[37–39] The model is based upon crystalline volume fractions and the subsequent change of these fractions over time.[40] A sample is heated above the equilibrium

melt temperature, held isothermally to erase thermal history and then cooled rapidly to the isothermal crystallisation temperature until crystallisation is complete.

The Avrami equation is valid for such isothermal conditions providing that the following assumptions are met: 1) crystallisation is isothermal; 2) nucleation is random; 3) growth rate is dependent only upon temperature, not on time (linear growth rate).[41–43] The general form of this equation is:

$$1 - X_t = exp(-Kt^n) \tag{4.3}$$

where X_t is the degree of crystallinity at time *t*, *K* is the crystallisation rate constant and *n* is the Avrami exponent.[41–44] This exponent provides information regarding the overall rate of crystallisation and growth dimension of the crystalline material[45] and can either be found from:

$$n = -t\frac{dX_t}{dt}(X_\infty - X_t)ln(1 - X_t)^{-1} \tag{4.4}$$

or graphically from a double logarithm plot of *ln {ln (1 - Xt)}* against *ln t*, since:[41]

$$ln\{-ln(1 - X_t)\} = n \ln t + \ln K \tag{4.5}$$

where *n* is the gradient and *K* the intercept. Alternatively, *K* can be calculated from the average value for *n* and the crystallisation half-life, $t_{1/2}$:

$$K = \frac{ln2}{t_{1/2}^n} \tag{4.6}$$

The Avrami exponent *n* reveals information regarding the nucleation type, growth geometry and growth velocity[46] within the sample (Table 4.2), with an increasing exponent value indicating an increase in the dimension of crystal growth.[45]

Avrami Exponent, *n*	**Dimensions and type of crystal growth**
1	Fibrils from instantaneous nucleation
2	Fibrils from sporadic nuclei or disks from instantaneous nuclei
3	Disk from sporadic nuclei or spherulites from instantaneous nuclei

Table 4.2: Avrami exponents *n* for various types of nucleation and crystal growth.

Relating these values to the morphology, values approaching $n = 3$ indicate a large number of spherulites; values approaching $n = 2$ indicate an unordered lamellae morphology; values

approaching n = 1 indicate ordered fibrils.[47] Values greater than 3 are typically not observed for HDPE.[45,47] Deviations from the Avrami model, which manifest as nonlinear plots or non-integer n values, are often attributed to the simultaneous or consecutive growth of crystalline units or other inappropriate assumptions in the Avrami model.[47]

4.6.2 Avrami Model Analysis of PE1 and PE2

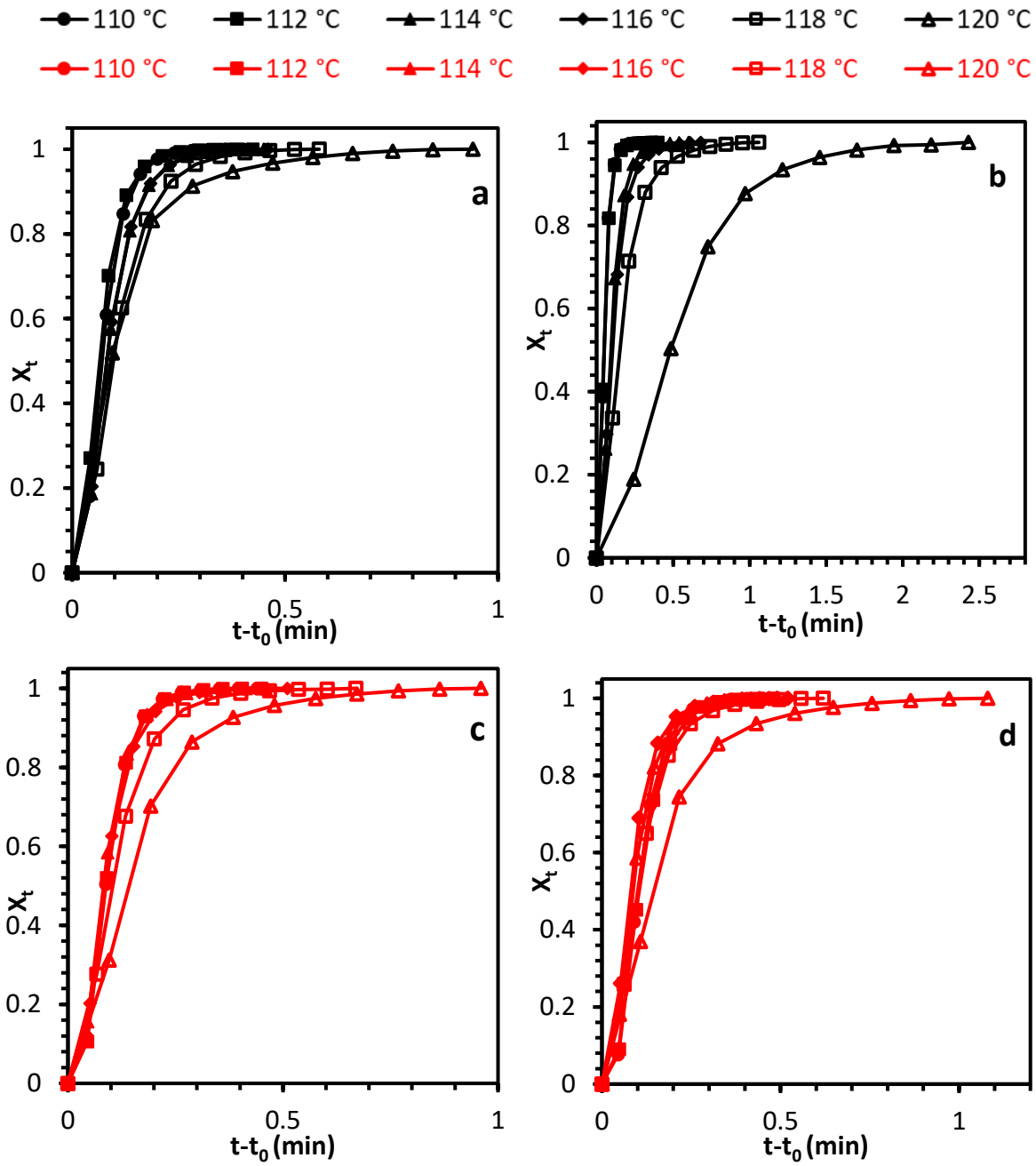

Figure 4.14: Plots of X_t vs crystallisation time for isothermal crystallisation at temperatures betwween 120 – 110 °C as measured by DSC. The black curves denote unoriented PE and the red curves denote oriented PE: unsheared PE1 (a), unsheared PE2 (b), sheared PE1 (c) and sheared PE2 (d).

The relative crystallinity plotted against time (Figure 4.14) displayed an initial linear portion before plateauing between X_t values 0.7 – 1.0 which indicated that crystal growth slowed. HDPE is known to crystallise rapidly[48], as evidenced by the rapid crystallinity development over time for both PE1 and PE2 (Figure 4.14). For the unsheared samples in each case, however, the highest crystallisation temperature (120 °C) showed significantly longer crystallisation times than the lower temperatures. In addition, the time for complete crystallisation at this temperature for PE2 was approximately over 1 minute longer than the corresponding conditions for PE1. It is known that at higher crystallisation temperatures the overall crystallisation rate is determined mainly by the nucleation rate which tends to be lower than the crystal growth rate at such temperatures.[14] Song *et al.* determined that a small amount of UHMWPE dispersed in the HDPE matrix was likely to induce a greater amount of nuclei thus leading to an enhanced overall crystallisation rate.[14] Therefore, the greater fraction of UHMW chains in PE1 was also likely to induce greater nucleation and hence a faster overall crystallisation rate than PE2 at the highest T_c.[14]

Crystallisation after shear was faster for a given crystallisation temperature and showed lower Avrami *n* values than the corresponding quiescent temperature (Figure 4.15 and Table 4.3). The general decreasing trend with increasing temperature was consistent with a shift from sporadic to instantaneous nucleation.[45] A change in the crystalline morphology was also observed – lower *n* values correspond to the formation of fewer spherulites and more fibrils.[47] All of the sheared Avrami exponents gave values of approximately $n = 1$ which was consistent with the growth of a fibril.[45] The corresponding unsheared samples all had values approaching $n = 2$, which indicated an unordered lamellae morphology.[47] In all cases, the values of *K* decreased with increasing T_c. These values were related to nucleation rate and growth processes, hence this data confirmed that both of these processes were arrested somewhat at higher temperatures.[45] Significantly, shearing led to a decrease in *K* values except for the highest T_c for PE2. This extremely low crystallisation rate constant could indicate that crystallisation was extremely slow and unfavourable at this temperature due to very low nucleation rates.[45] Therefore, for both PE1 and PE2, shearing changed the growth from spherulitic to fibrillated.[45,49]

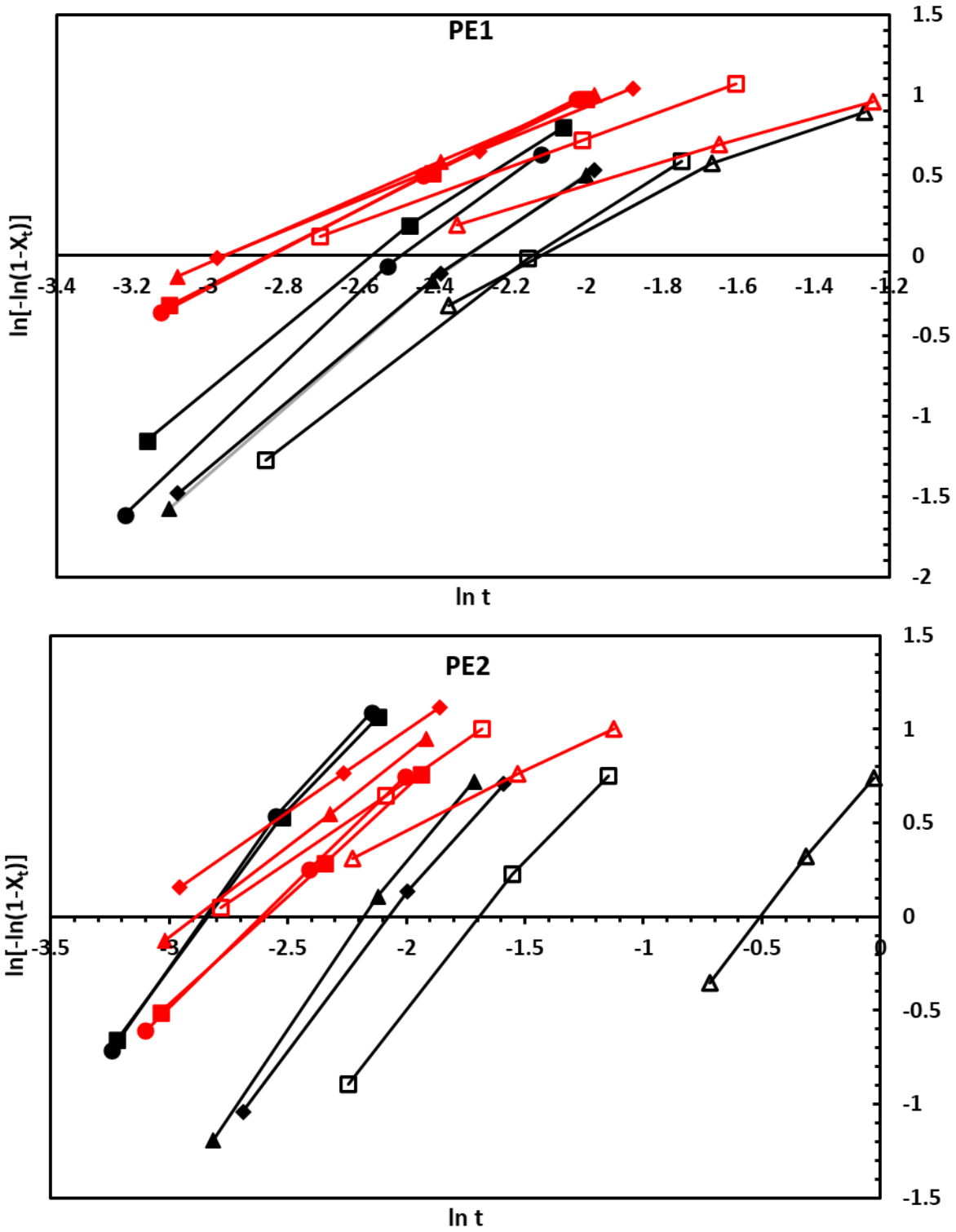

Figure 4.15: Plots of *ln[-ln(1 - X_t)]* versus *ln t* (crystallisation time) for PE1 (top) and PE2 (bottom) under isothermal crystallisation at different crystallisation temperatures. The black curves denote unoriented PE and the red curves denote oriented PE.

		110	112	114	116	118	120
		(°C)					
PE1 (Unsheared)	*n*	2.1	1.8	1.9	1.8	1.7	1.1
	K (min^{-1})	*5.1*	*4.5*	*4.4*	*4.2*	*3.6*	*2.4*
PE2 (Unsheared)	*n*	1.7	1.6	1.8	1.6	1.5	1.6
	K (min^{-1})	*4.7*	*4.5*	*3.8*	*3.3*	*2.5*	*0.8*
PE1 (Sheared)	*n*	1.2	1.2	1.0	1.0	0.9	0.7
	K (min^{-1})	*3.4*	*3.3*	*3.0*	*2.9*	*2.5*	*1.8*
PE2 (Sheared)	*n*	1.2	1.2	1.0	0.9	0.9	0.6
	K (min^{-1})	*3.2*	*3.0*	*2.8*	*2.7*	*2.5*	*1.7*

Table 4.3: Avrami exponents *n* and crystallisation rate constants *K* from fitting the Avrami equation to the isothermal crystallization DSC results of unsheared and sheared samples of PE1 and PE2 (Figure 4.14).

Enhanced crystallization arises from rapid nucleation of many small crystallites, followed by subsequent growth of crystalline material around these nucleation sites. In contrast, nucleation in quiescent melts is typically sporadic and slow.[45] It is hypothesised that deformation, due to shearing, leads to rapid homogeneous nucleation during flow with subsequent growth proceeding centered on these newly-established nucleation sites.[45,50–53] A direct correlation was made by Gholami *et al.* between isothermal crystallisation and resistance to SCG for a series of PE-100 resins.[47] They noted that higher Avrami exponents correlated with an increased amount of spherulites. Resins that displayed higher Avrami values, and hence greater amounts of spherulitic morphology, displayed easier crack growth because the spherulitic boundary acted as a weak region in front of the propagating crack.[47] Therefore, the lower *n* values of sheared PE1 and PE2 would indicate that the SCG resistance would be improved compared to the unsheared blends.

4.7 Conclusions

The physical, thermal and mechanical properties of semicrystalline polymers depend on the morphology, degree of crystallinity and crystallisation rate.[49] The latter two points in particular can have a significant effect upon the final crystalline morphology, and hence the physical

properties. Quite often, the rate of cooling determines the crystallisation rate and consequently the degree of crystallinity. SIC offers another way by which the morphology can be controlled and influenced.

The primary morphology of samples that have undergone SIC is the *shish-kebab*, which has been demonstrated to remain thermally stable at temperatures greater than the melting temperature of spherulitic morphology. Subjecting pre-sheared samples of PE1 and PE2 to a repeated melting-recrystallising temperature protocol, with *in-situ* SAXS measurements, demonstrated enhanced thermal stability of the *shish-kebab* morphology. These structures did not melt until 144 – 146 °C for PE1 and 134 – 136 °C for PE2. Due to the greater fraction of UHMW material present in the MWD of PE1, the relaxation times of the longest chains comprising the *shish* were greater hence the enhanced thermal stability observed. The presence of this UHMW fraction influenced many of the optimisation parameters in subsequent work.

Shearing PE1 and PE2 under the same conditions ($\dot{\gamma}$ = 10 s^{-1}, t_s = 10 s, T = 130 °C) and performing radial SAXS scans across the disk diameter revealed similar results. The degree of orientation, measured by Herman's Orientation Function, *P2*, showed greater values at the disk edges (the highest shear rates) for PE1 and a smaller zone of no orientation towards the centre of the disk (where shear rates tended to $\dot{\gamma} = 0$). This was further confirmation of the importance of the role of UHMW chains in the formation of oriented morphology by SIC.

A critical shear rate, $\dot{\gamma}_c$, and critical work, w_C, exist for the onset of stretching and aligning the longest chains in the melt for the formation of oriented morphology by SIC. Shearing below this critical value would not form oriented nuclei, and consequently oriented morphology upon full crystallisation. The critical shear rates for PE1 and PE2 were obtained through SIPLI and were 0.14 s^{-1} and 0.24 s^{-1} respectively. The lower value for PE1 was further confirmation of the role of the greater fraction of UHMW material in the melt. By using the shear-rate dependent viscosity values, $\eta(\dot{\gamma})$, the critical work for the onset of oriented morphology formation were obtained: PE1 = 13.21 ± 1.61 MPa and PE2 = 22.56 ± 4.67 MPa. The lower value for PE1 indicated that less work was required to produce oriented nuclei under shear. These values correlated well with the larger fraction of UHMW material (the UHMWT) present in PE1 and, therefore, less work input would be required to obtain oriented morphology. Therefore, rheology alone was not indicative or conclusive for the prediction of the behaviour of flow-enhanced nucleation.

The temperature of shear also had a significant effect upon the formation of oriented morphology and the overall degree of orientation. Shearing at different temperatures from 130 – 200 °C, and performing post-shear radial SAXS measurements, demonstrated that orientation decreased with increasing temperature, with no orientation present at $T \geq 150$ °C for PE1 and $T \geq 140$ °C for PE2. Thermal relaxation caused the oriented morphology to relax back to the entangled state before crystallisation could be completed. This was particularly important for the consideration of the design of future industrial processes as typical processing temperatures are at least 200 °C. Therefore, a method of cooling the production line to 130 – 140 °C before applying shear would need to be devised.

Controlling the time of shearing also affected the resulting crystalline morphology. The shear time was increased in increments of 5-, 10-, 20-, 30- and 40-seconds with the shear rate and temperature constant ($\dot{\gamma} = 10$ s^{-1}, $T = 130$ °C). Polarised light images were taken during shear and post-shear radial SAXS measurements were also performed. It was shown that no noticeable increase in orientation was seen by shearing for longer, instead elastic instabilities began to dominate the flow at increasing shear times and ultimately distort or destroy the oriented morphology. This effect was particularly apparent for PE1 at shear times greater than 20 seconds, suggesting that the oriented nuclei formation had become saturated by this time and further shearing caused the morphology to be destroyed.

Finally, isothermal crystallisation kinetics measurements were performed by DSC and analysed using the Avrami equation. The Avrami exponents n were approximately $n = 1$ for the sheared samples and $n = 2$ for the unsheared samples, which indicated fibrillar and unordered lamellae growth respectively. In all cases, the values of K decreased with increasing T_c which suggested that slower crystallisation occurred because the nucleation rate was low due to a low thermodynamic driving force.[14,54]

4.8 References

1 A. J. Pennings and A. M. Kiel, *Kolloid-Zeitschrift Zeitschrift fur Polym.*, 1965, **205**, 160–162.

2 A. J. Pennings, J. M. A. A. van der Mark and A. M. Kiel, *Kolloid-Zeitschrift Zeitschrift fur Polym.*, 1970, **237**, 336–358.

3 A. Keller and M. J. Machin, *J. Macromol. Sci. Part B*, 1967, **1**, 41–91.

4 M. J. Hill and A. Keller, *J. Macromol. Sci. Part B*, 1971, **5**, 591–615.

5 M. R. Mackley and A. Keller, *Polymer*, 1973, **14**, 16–20.

6 O. O. Mykhaylyk, P. Chambon, C. Impradice, J. P. A. Fairclough, N. J. Terrill and A. J. Ryan, *Macromolecules*, 2010, **43**, 2389–2405.

7 O. O. Mykhaylyk, P. Chambon, R. S. Graham, J. P. A. Fairclough, P. D. Olmsted and A. J. Ryan, *Macromolecules*, 2008, **41**, 1901–1904.

8 J. van Meerveld, G. W. M. Peters and M. Hütter, *Rheol. Acta*, 2004, **44**, 119–134.

9 M. Okura, O. O. Mykhaylyk and A. J. Ryan, *Phys. Rev. Lett.*, 2013, **110**, 1–5.

10 M. Stadlbauer, H. Janeschitz-Kriegl, G. Eder and E. Ratajski, *J. Rheol.*, 2004, **48**, 631–639.

11 H. Janeschitz-Kriegl, *Monatshefte fur Chemie*, 2007, **138**, 327–335.

12 F. Zuo, J. K. Keum, L. Yang, R. H. Somani and B. S. Hsiao, *Macromolecules*, 2006, **39**, 2209–2218.

13 J. K. Keum, F. Zuo and B. S. Hsiao, *Macromolecules*, 2008, **41**, 4766–4776.

14 S. Song, P. Wu, M. Ye, J. Feng and Y. Yang, *Polymer*, 2008, **49**, 2964–2973.

15 H. Marand, J. Xu and S. Srinivas, *Macromolecules*, 1998, **31**, 8219–8229.

16 O. O. Mykhaylyk, *Soft Matter*, 2010, **6**, 4430–4440.

17 F. A. Morrison, *Understanding Rheology*, Oxford Univesity Press, Oxford, 2001.

18 G. Eder, H. Janeschitz-Kriegl and S. Liedauer, *Prog. Polym. Sci.*, 1990, **15**, 629–714.

19 A. Groisman and V. Steinberg, *Nature*, 2001, **405**, 53–55.

20 A. Groisman and V. Steinberg, *Nature*, 2001, **410**, 905–908.

21 P. Pakdel and G. McKinley, *Phys. Rev. Lett.*, 1996, **77**, 2459–2462.

22 R. Kupferman, *J. Comput. Phys.*, 1998, **147**, 22–59.

23 R. G. Larson, *Rheol. Acta*, 1992, **31**, 213–263.

24 C. J. S. Petrie and M. M. Denn, *AIChE J.*, 1976, **22**, 209–236.

25 A. Franck, *Understanding Rheology of Thermoplastic Polymers*, TA Instruments, 2004, vol. AAN013.

26 B. Maxwell, *Polym. Eng. Sci.*, 1973, **13**, 227–230.

27 Y. Tang, Z. Jiang, Y. Men, L. An, H. F. Enderle, D. Lilge, S. V. Roth, R. Gehrke and J. Rieger, *Polymer*, 2007, **48**, 5125–5132.

28 E. L. Heeley, T. Gough, D. J. Hughes, W. Bras, J. Rieger and A. J. Ryan, *Polymer*, 2013, **54**, 6580–6588.

29 R. H. Somani, L. Yang, L. Zhu and B. S. Hsiao, *Polymer*, 2005, **46**, 8587–8623.

30 O. O. Mykhaylyk, N. J. Warren, A. J. Parnell, G. Pfeifer and J. Laeuger, *J. Polym. Sci. Part B Polym. Phys.*, 2016, **54**, 2151–2170.

31 H. Janeschitz-Kriegl, E. Ratajski and M. Stadlbauer, *Rheol. Acta*, 2003, **42**, 355–364.

32 M. Dhaese, O. O. Mykhaylyk and P. Van Puyvelde, *Macromolecules*, 2011, **44**, 1783–1787.

33 E. A. Andablo-Reyes, E. L. de Boer, D. Romano and S. Rastogi, *J. Rheol.*, 2014, **58**, 1981–1991.

34 K. Cui, Z. Ma, Z. Wang, Y. Ji, D. Liu, N. Huang, L. Chen, W. Zhang and L. Li, *Macromolecules*, 2015, **48**, 5276–5285.

35 L. Balzano, Z. Ma, D. Cavallo, T. B. Van Erp, L. Fernandez-Ballester and G. W. M. Peters, *Macromolecules*, 2016, **49**, 3799–3809.

36 D. Mi, F. Hou, M. Zhou and J. Zhang, *Eur. Polym. J.*, 2018, **101**, 1–11.

37 A. N. Kolmogorov, *Bull. Acad. Sci URRS (Ci. Sci. Math. Nat)*, 1937, **3**, 355.

38 M. Avrami, *J. Chem. Phys.*, 1939, **7**, 1103–1112.

39 W. A. Johnson and R. F. Mehl, *Trans. Am. Inst Min. Engin.*, 1939, **135**, 416.

40 E. Piorkowska and G. C. Rutledge, *Handbook of Polymer Crystallization*, Wiley, Hoboken, NJ, USA, 2013.

41 A. Booth and J. N. Hay, *Polymer*, 1982, **23**, 1380–1384.

42 H. Shan and G. C. Lickfield, *Int. J. Polym. Anal. Charact.*, 2007, **12**, 327–338.

43 M. Avrami, *J. Chem. Phys.*, 1939, **7**, 1103–1112.

44 Z. H. Stachurski, Y. Long and R. A. Shanks, *Prog. Polym. Sci.*, 1995, **20**, 651–701.

45 E. L. Heeley, C. M. Fernyhough, R. S. Graham, P. D. Olmsted, N. J. Inkson, J. Embery, D. J. Groves, T. C. B. McLeish, A. C. Morgovan, F. Meneau, W. Bras and A. J. Ryan, *Macromolecules*, 2006, **39**, 5058–5071.

46 J. K. Keum, R. H. Somani, F. Zuo, C. Burger, I. Sics, B. S. Hsiao, H. Chen, R. Kolb and C.-T. Lue, *Macromolecules*, 2005, **38**, 5128–5136.

47 F. Gholami, G. Pircheraghi, R. Rashedi and A. Sepahi, *Polym. Test.*, 2019, **80**, 106128.

48 A. T. Lorenzo, M. L. Arnal, J. Albuerne and A. J. Müller, *Polym. Test.*, 2007, 26, 222–231.

49 X. Chen, J. Shi, L. Wang, H. Shi, Y. Liu and L. Wang, *Polym. Compos.*, 2011, 101–113.

50 A. Keller and H. W. H. Kolnaar, in *Materials Science and Technology: Processing of Polymers*, ed. H. E. H. Meijer, Wiley-VCH, Weinheim, 1997, **vol. 18**, pp. 191–266.

51 J. A. Kornfield, G. Kumaraswamy and A. M. Issaian, *Ind. Eng. Chem. Res.*, 2002, **41**, 6383–6392.

52 G. Kumaraswamy, R. K. Verma, J. A. Kornfield, F. Yeh and B. S. Hsiao, *Macromolecules*, 2004, **37**, 9005–9017.

53 G. Kumaraswamy, *J. Macromol. Sci. - Polym. Rev.*, 2005, **45**, 375–397.

54 A. J. Peacock, *Handbook of Polyethylene*, Marcel Dekker, New York, 2000.

55 T. H. Yu and G. L. Wilkes, *J. Rheol.*, 1996, **40**, 1079-1093

Chapter 5

Polymer Processing under Controlled Flow Conditions to Improve the Barrier and Mechanical Properties

5.1 Introduction

A custom built Couette flow cell (Section 2.6) was used to obtain larger oriented film samples with different degrees of oriented morphology in order to investigate the effect of SIC upon permeability and mechanical properties respectively. Couette flow can be classified as a drag flow with no pressure gradient and, if the inner cylinder is rotated with the outer fixed, the flow can be described as laminar with circular stream lines.[1,2] Thus, samples with a relatively uniform distribution of orientation were produced because they experienced a constant shear rate in the Couette shear cell geometry.

Shish-kebabs, the resultant morphology from a melt that has undergone SIC, have been shown to exhibit improved mechanical properties compared to quiescent melts.[3,4] The final mechanical properties of a product depend upon the respective morphologies of the amorphous and crystalline regions, which in turn are dependent upon thermal history and deformation during processing.[5] Hence for the *shish-kebab* morphology, mechanical properties are greatly enhanced along the length of the *shish*, parallel to the flow direction.[4]

Similarly, the crystalline morphology has a direct correlation to the diffusivity, and hence permeability, of organic vapours through semicrystalline polymers.[6] Previous work has shown that such vapours are essentially insoluble in the crystalline regions which act as impermeable barriers.[7,8] Furthermore, the barrier properties of semi-crystalline polymers can be influenced by crystallite size, shape and degree of crystallinity.[7] Therefore, the *shish-kebab* morphology offered a promising path to increasing the mechanical strength and barrier properties of PE-100 pipe resins.

5.2 Preparation of Oriented PE Samples

Using prior SIPLI and critical work measurements (Section 4.4 – 4.5), a range of shear rates and times were selected to obtain samples of PE1 with varying degrees of anisotropy (Table 5.1). Shear rates greater than 0.14 s^{-1} and 0.24 s^{-1} for PE1 and PE2 respectively were shown to be necessary to stretch polymer chains and form an oriented morphology (Section 4.3.1). Additionally, applying strain $\varepsilon > 400$ through shear to the melt was shown to increase the dominance of elastic flow instabilities (Section 4.5.2). Boundary shear rates for oriented morphology formation of 4.7 s^{-1} and 5.6 s^{-1} were obtained for PE1 and PE2 respectively (Table 4.1); however, it was posited that shearing for longer times at shear rates lower than these boundary rates (i.e. conditions A & B) could supply enough work to stretch and orient the chains.

After isothermal melting at 150 °C for 30 mins to erase thermal history, shear pulses were applied at 130 °C (the melting point of spherulites and significantly above the crystallisation temperature of the polymers under quiescent conditions). In addition, shearing at temperatures greater than 130 °C had been shown previously to result in lower degrees of orientation due to competing thermal chain relaxation (Section 4.5.1, Figure 4.10a & 4.10b).[9] Subsequent sample naming follows the pattern *HDPE-shear_rate-shear_time-strain.*

	Sample Name	**Shear Rate (s^{-1})**	**Shear Time (s)**	***Strain (ε)***
A	PE1-1-150-150	1	150	*150*
B	PE1-1-300-300		300	*300*
C	PE1-10-10-100	10	10	*100*
D	PE1-10-20-200		20	*200*
E	PE1-10-30-300		30	*300*
F	PE1-10-40-400		40	*400*
G	PE1-20-10-200	20	10	*200*

Table 5.1: Shear rate and shear time conditions, with corresponding strain applied in each case, selected for measurements in the Couette shear cell. Sample naming follows the pattern *HDPE - shear_rate - shear_time - strain.* The grey shading identifies those samples which exceeded the critical work threshold and formed oriented morphology under shearing.

This range of shear rates and times were selected in order to give a good insight into the flow behaviour under different conditions and strain values. After shearing, each sample was removed from the cell and subjected to SAXS measurements, in 10 mm intervals along the length of the sample (parallel with the flow direction), to ascertain the degree of orientation using Herman's Orientation Function, P_2. (Figure 5.1).

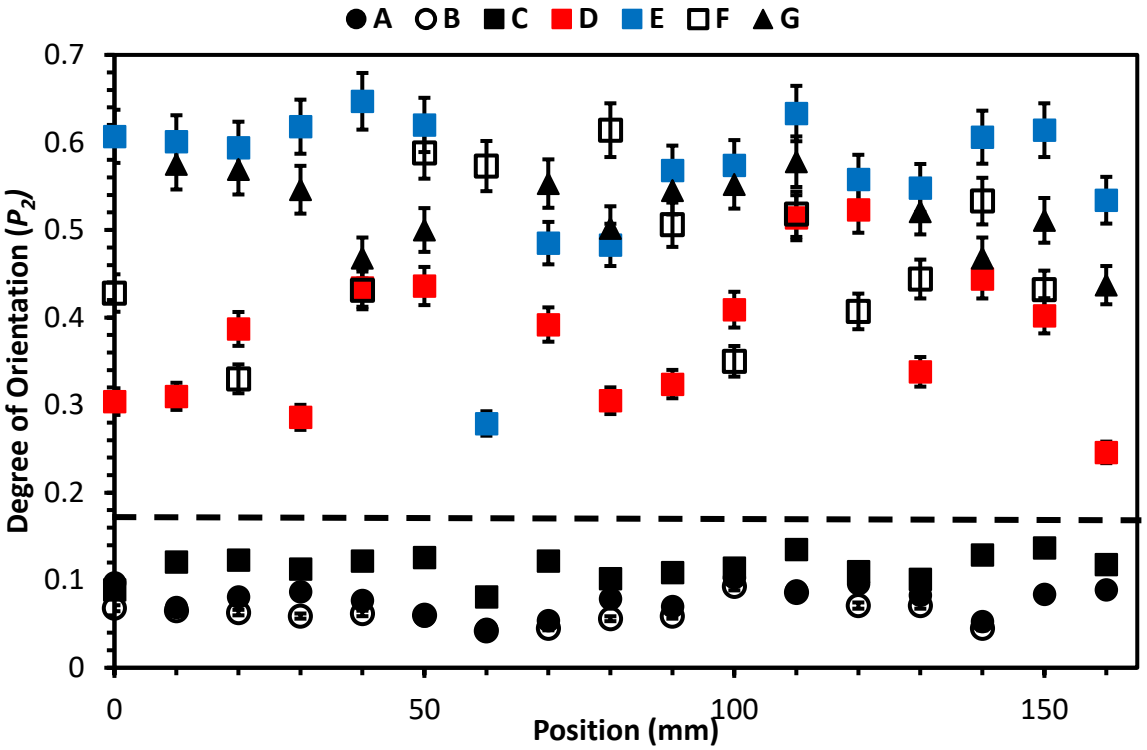

Figure 5.1: Degree of orientation, P_2, plotted against measurement position of PE1 samples sheared in duplicate and averaged for the Couette cell for conditions A – G (full sample names are given in Table 5.1). Error bars are also fitted to conditions A – C but are not visible due to their magnitude. The dashed black line indicates the critical work above which oriented morphology can form.

Weak orientation was observed for conditions (Table 5.1) A and B, with shear rates of $\dot{\gamma}$ = 1 s^{-1}, with degrees of orientation comparable to condition C. Conversely, condition G showed a degree of orientation similar to conditions E and F (both with $\varepsilon \geq 200$) which further confirmed the existence of an upper strain limit (Section 4.5.2).[10] The dashed black line (Figure 5.1) indicates the critical work threshold above which oriented morphology could be created (Section 4.4) . The critical work for conditions A – C was therefore below the threshold and so no orientation was observed by SAXS.

Conditions C - F gave a good range of strain values and these conditions were selected to shear samples of PE1 and PE2 for further mechanical and permeation measurements (Figure 5.2).

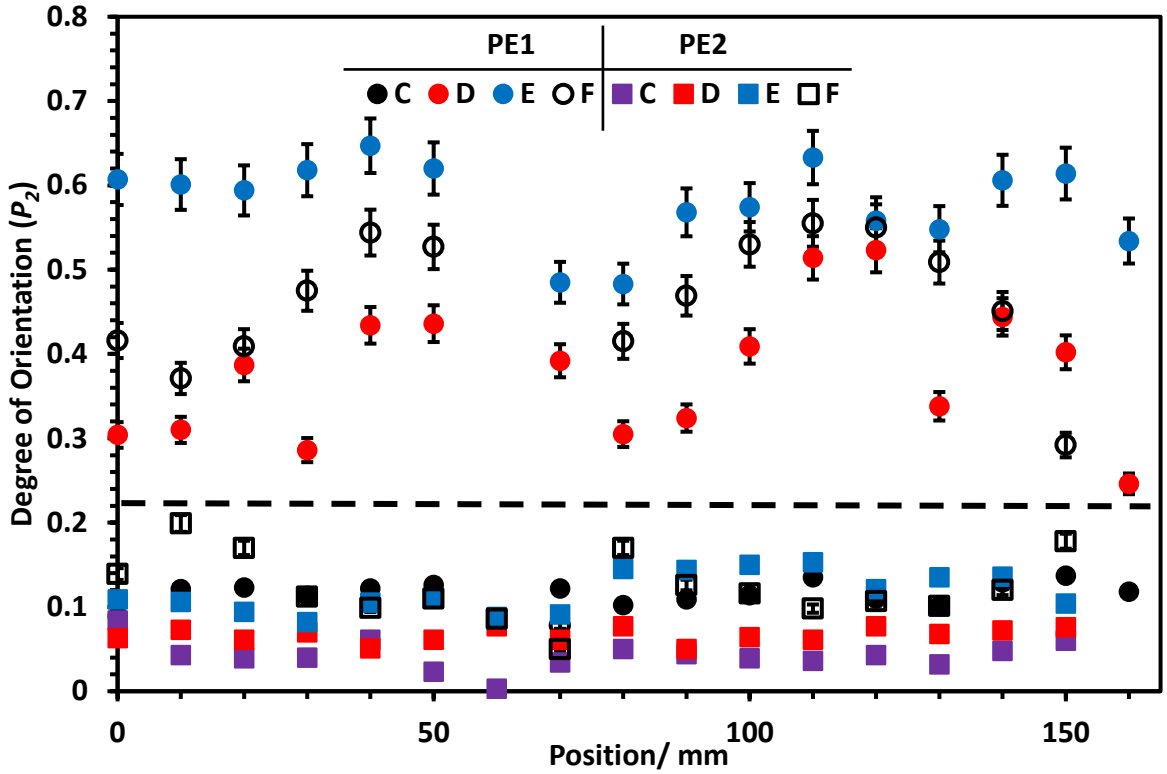

Figure 5.2: Degree of orientation, P_2, plotted against Couette cell sample position for shear conditions (measured in duplicate and averaged) C, D, E and F for PE1 (circles) and PE2 (squares). Error bars are also fitted to condition C (PE1) and conditions C – F (PE2) but are not visible due to their magnitude. The dashed black line indicates the critical work above which oriented morphology can form.

Significant differences in the degrees of orientation were observed between PE1 and PE2 under shear conditions C - F (Figure 5.2). Even at the longest shear times, the degree of orientation for PE2 did not greatly exceed the shortest shear time for PE1, further demonstrating the importance of a HMWT in the blend (Section 3.2, Figure 3.1) for SIC and oriented morphology formation.[11] The dashed black line (Figure 5.2) indicates the critical work threshold (Section 4.4) above which oriented morphology formation occurred. All shear conditions (Table 5.1) for PE2 were below this threshold and of comparable orientation to the only condition of PE1 that was below the threshold (condition C: $\dot{\gamma}$ = 10 s^{-1}, t_s = 10 s). Given the similarity in MW between PE1 and PE2, this was further confirmation of the significance of the UHWMT present in PE1 for the formation of oriented morphology.[6,7]

2D SAXS images showed distinct orientation in the direction of flow with very little lamellae tilting under all conditions across the sample length for PE1 (Figures 5.3 & 5.4). The intensity of the two-lobe spot pattern increased with increasing shear time for PE1, but was fairly consistent in intensity for PE2 (Figure 5.5) which corroborated with the P_2 data (Figure 5.2). Sharp drops in the orientation were noted around 60 – 70 mm and 120 - 130 mm, especially at higher shear rates. This was likely due to the construction of the stator consisting of four equal segments, into which small amounts of molten polymer could leak between the joints and stagnate. Thermal transfer through the polymer within these regions would have been more efficient due to the very small gap (and hence very thin amounts of PE material) between stator segments and so thermal relaxation was likely to be especially prevalent, hence a reduction in the observed orientation.

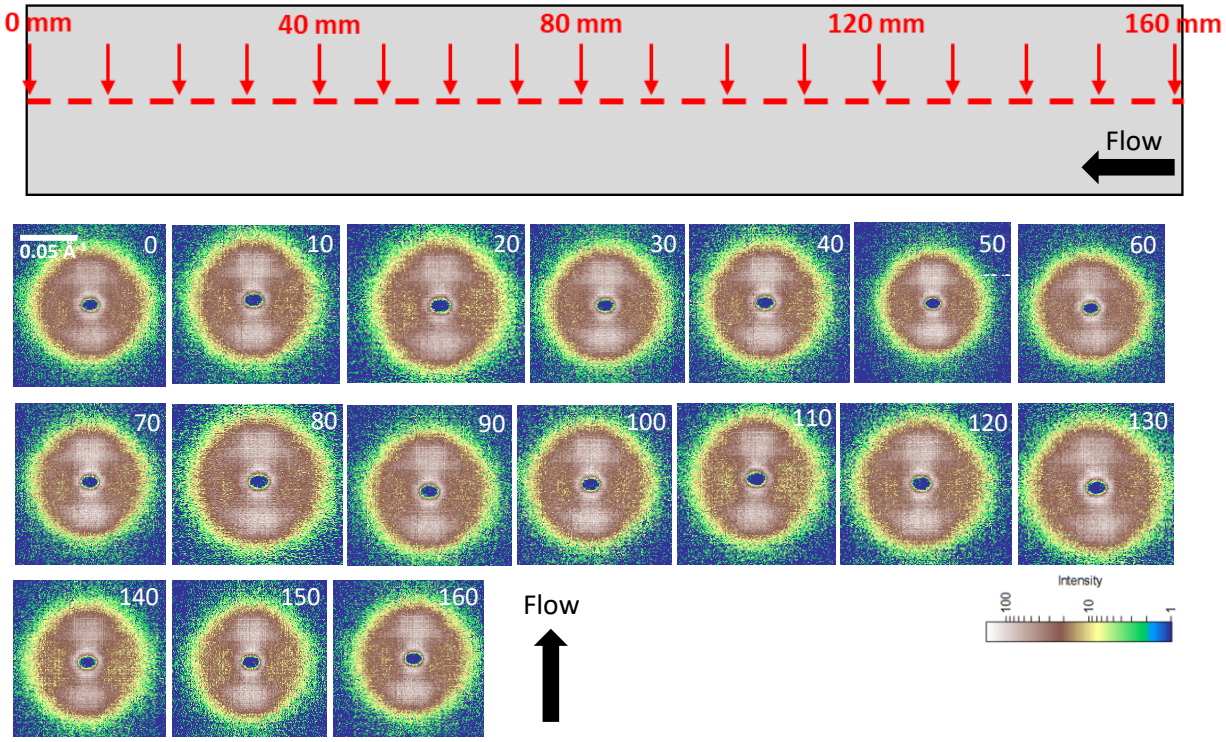

Figure 5.3: 2D SAXS patterns taken from an oriented Couette sample of PE1 at 10 mm intervals – the 'map' above the images denotes the approximate locations of each measurement interval. $\dot{\gamma}$ = 10 s^{-1}, t_s = 10 s and T = 130 °C (Table 5.1, condition C). The numbers in the top right-hand corner of image denote the position in mm at which each image was acquired with the black arrow indicating the direction of flow. A scale bar is shown in image 0. No images were acquired at the stator segment joints.

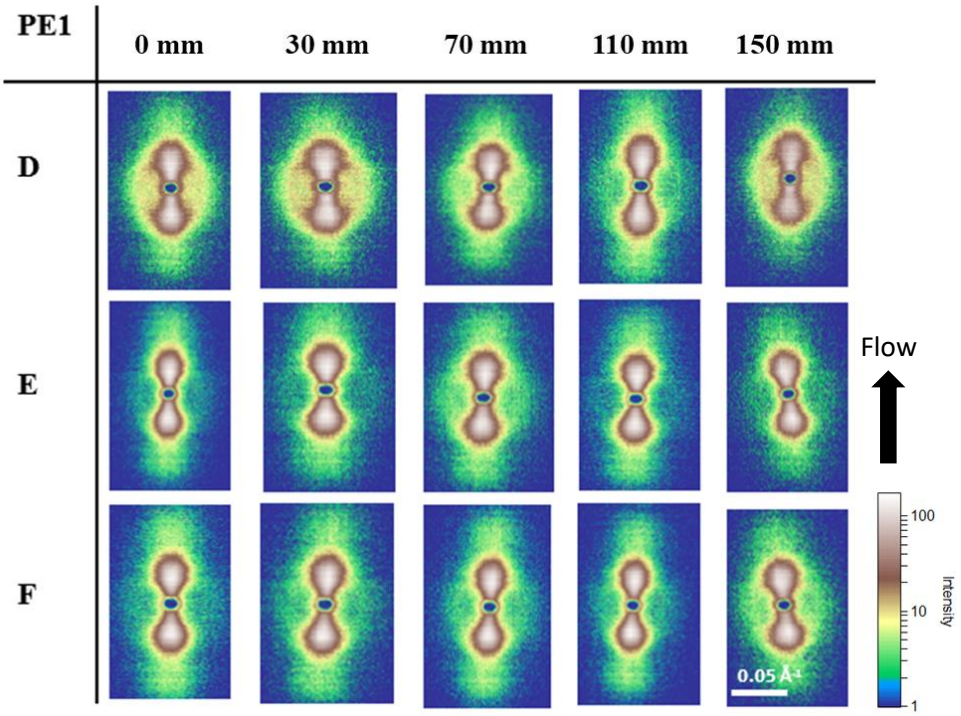

Figure 5.4: 2D SAXS patterns (120 seconds acquisition) taken from selected locations along a Couette-sheared sample of PE1 for conditions D - F at 130 °C.

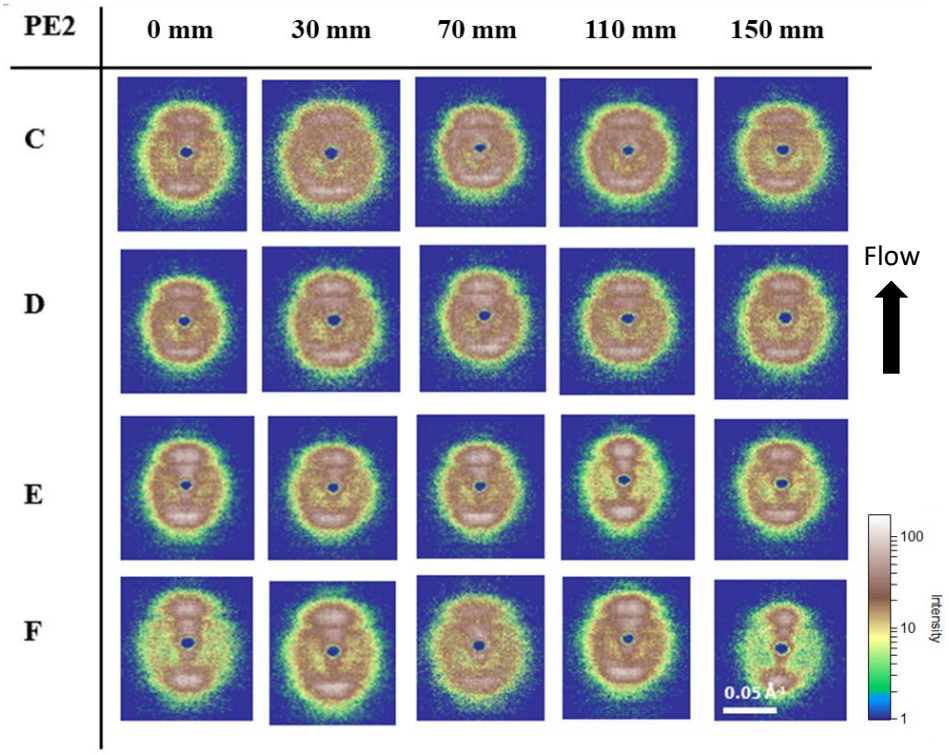

Figure 5.5: 2D SAXS patterns (120 seconds acquisition) taken from selected locations along a Couette-sheared sample of PE2 for conditions C – F at 130 °C.

5.3 Permeation Testing

A key research objective of this work was to investigate whether the *shish-kebab* morphology, induced by SIC, displayed decreased permeability, and hence improved barrier properties to hydrocarbons, for use in PE-100 pipes. Such properties can be influenced by degree of chain branching, molecular structure, cross-linking and the degree of crystallinity.[12] Previous research has shown that higher crystallinities displayed reduced permeation to gases because high levels of crystalline chain packing reduce the free volume for gases to permeate.[12]

5.3.1 Sealing Tests

In order to ensure adequate sealing of the test cell, and confirm that any weight loss occurred through the sample and not as a result of leaking through the sealing lid, a washer was needed between the base and sample. A comparison of copper and rubber washers was performed by using a 3 mm thick aluminium disk as a sample and 5 mL of xylene. Conditions C – H had either silicone grease or PTFE tape applied to the lid screw thread (see Figure 2.31, Section 2.11 for reference). Samples were weighed at regular intervals for 14 days (Table 5.2 and Figure 5.6).

	Sealing method
A	Copper washer
B	Rubber washer
C	Silicone grease only, no washer
D	PTFE tape only, no washer
E	Polished copper washer, silicone grease
F	Polished copper washer, PTFE tape
G	Rubber washer, silicone grease
H	Copper foil washer, silicone grease

Table 5.2: Methods of sealing the permeation cells tested during the initial cell sealing trials. Conditions C – H had either silicone grease or PTFE tape applied to the lid screw thread.

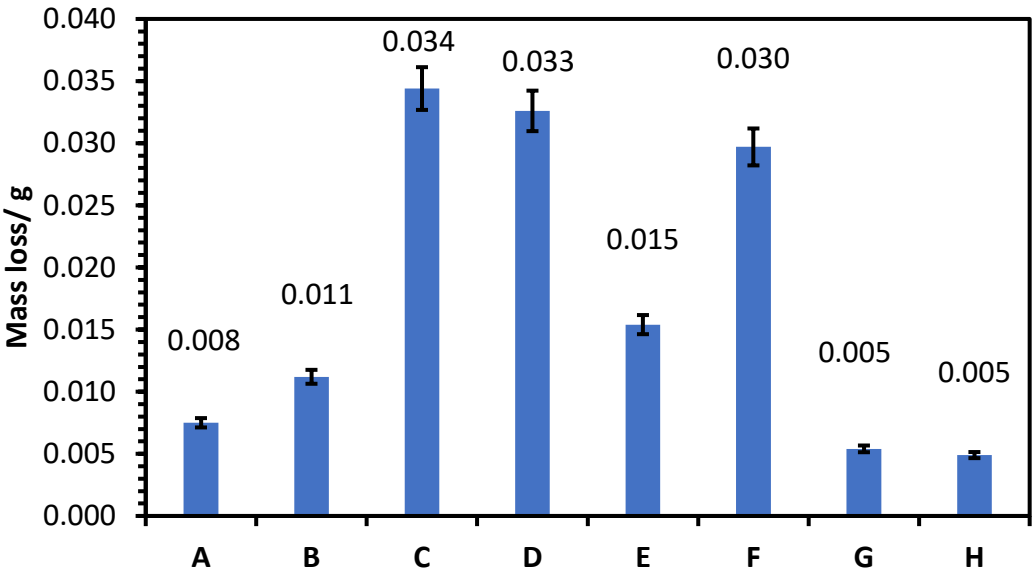

Figure 5.6: Mass lost over 14 days from sealing methods A-H to test the effectiveness of sealing of the permeation cells. All samples were measured in duplicate and a 95 % confidence interval is fitted to each sample.

By comparing each sealing method, the most effective was identified. Copper washers were investigated because they are used for certain high vacuum applications. Upon annealing, the soft nature of the metal allows for a perfectly tight seal as the two components are screwed together. The circumferential thickness of the original washers (condition A, as purchased) ranged between 1.40 - 1.42 mm. This discrepancy in size was most likely sufficient for vapour transmission and loss. The polished washers had a consistent circumferential thickness of 1.40 mm (conditions E and F). Concurrently, copper film of 0.1 mm thickness was obtained and punched to create washers. Another variable to consider was the sealing of the thread bearing – either silicone grease or PTFE tape was used.

By removing the first 4 days of measurements, the permeation at a steady state was reached (Figure 5.6). The highest rates of vapor transmission were observed for conditions C - D. Whilst the rubber washer (G) and the copper foil (H) gave similar permeation results, the latter showed slightly less permeation, and so it was decided to pursue copper foil owing to ease of fabrication and time available. In all cases, sealing with silicone grease and not PTFE tape proved most beneficial. This could be due to problems arising during the sealing of the test cells – the PTFE tape was harder to apply to the screw thread and was prone to tearing.

Three samples per set of shear conditions were tested alongside unoriented specimens and averaged over a period of 130 days (Figure 5.7 and Table 5.3).

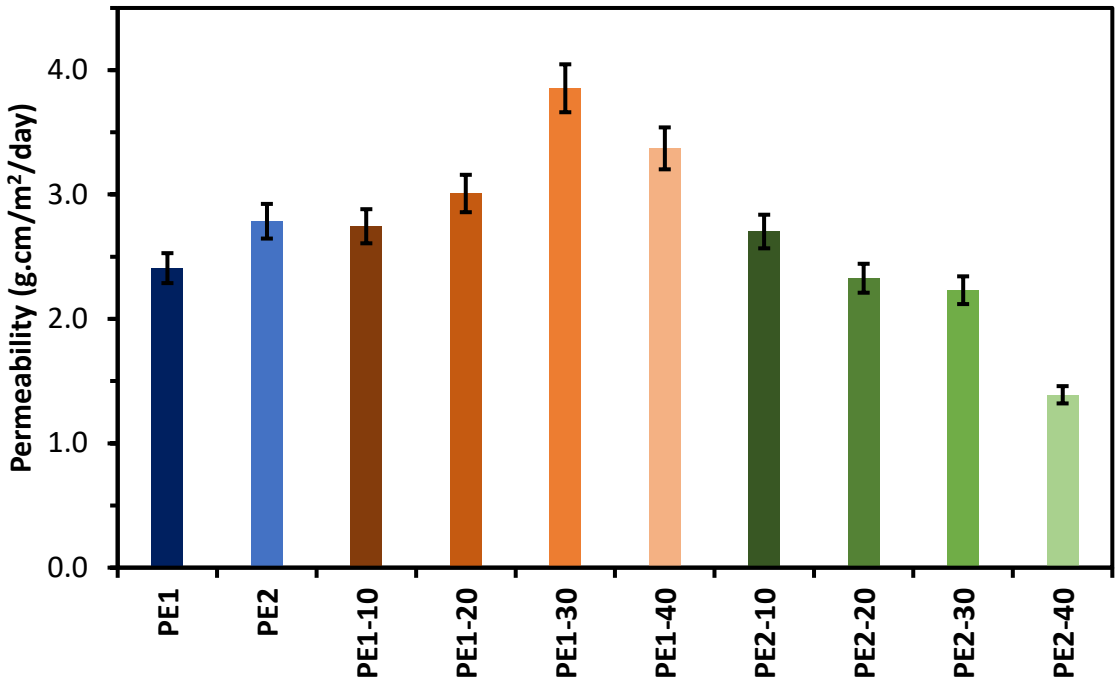

Figure 5.7: Average permeability (measured in duplicate) of PE1 and PE2 samples sheared at $\dot{\gamma}$ = 10 s^{-1} for times of 0 s, 10 s, 20 s, 30 s and 40 s. PE1-30 exhibited the highest orientation upon shearing (Figure 5.2).

g cm m^{-2} day^{-1}	**0 s**	**10s**	**20s**	**30s**	**40s**
PE1	2.41	2.74	3.01	3.85	3.37
PE2	2.79	2.70	2.33	2.23	1.39

Table 5.3: Average permeability coefficients of PE1 and PE2 samples sheared at $\dot{\gamma}$ = 10 s^{-1} for times of 0 s, 10 s, 20 s, 30 s and 40 s.

There was a noticeable change in permeability by shearing for different times. Unsheared PE1 and PE2 displayed similar values with the former showing slightly lower permeability. The crystallinities as measured by DSC (Section 3.3.1) were similar, although PE1 did display slightly greater crystallinity than PE2 (61.4 % and 57.1 % respectively). Therefore, the increased crystallinity resulted in lower permeability as the permeable, amorphous free volume available for a permeant molecule to diffuse through was reduced.[6,13–15]

5.3.2 Permeability of Sheared PE1

Samples of PE1 were sheared at times of 10 – 40 seconds at a shear rate of $\dot{\gamma}$ = 10 s^{-1} at 130 °C with three samples measured and averaged per shear time (Figure 5.8).

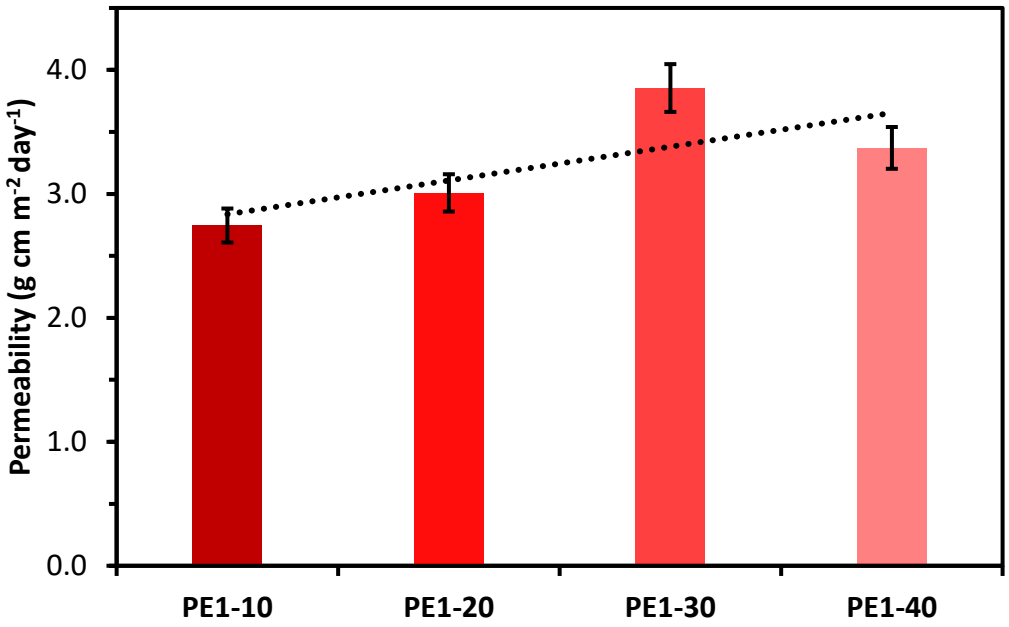

Figure 5.8: Average permeability (measured in duplicate) of PE1 samples sheared at $\dot{\gamma}$ = 10 s^{-1} for times of 10 s, 20 s, 30 s and 40 s. The numbers denote the time of shearing.

The overall trend showed that increasing the shear time caused a corresponding increase in the permeability, with the highest rate after shearing for 30 seconds. It was postulated that increasing the shear time would lead to an increased concentration of *shish-kebab* morphology and, hence, a decrease in the permeability because of the greater crystalline volume fraction.[8] However, this was not observed for PE1 due to the direction of the *shish* compared to the solvent flux (Figure 5.9). Further information regarding the orientation of *shish-kebabs* during shearing can be found within Section 1.4.4, Figure 1.17 and Section 3.5, Figure 3.25.

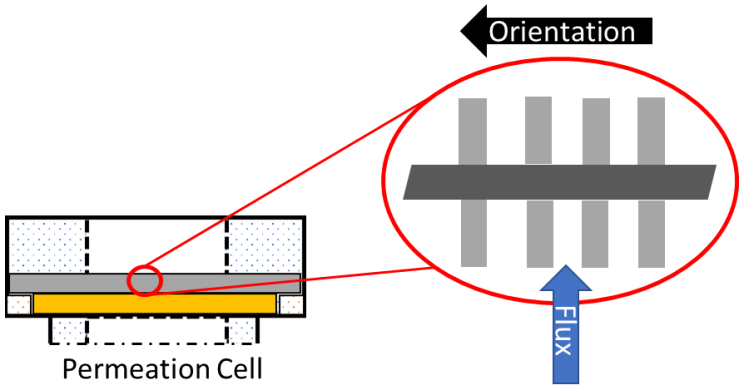

Figure 5.9: The directions of oriented morphology (represented by *shish-kebabs*) orientation and solvent flux (right) during a permeability test using a permeation cell (left – the solvent reservoir is not shown).

The oriented morphology was formed in the direction of shearing (as confirmed by SAXS, Figures 5.3 – 5.5), however, measurements were performed such that this orientation direction lay perpendicular to the solvent flux. Therefore, minimal permeability resistance was likely to have been supplied by the inter-locking *kebabs*, and the permeant vapour could penetrate through the voids between adjacent *kebabs*, thus giving rise to the observed increase in permeability. As the orientation increased, more oriented morphology was created and hence greater permeability was observed.

Considering the degree of orientation as measured by SAXS (Figure 5.2) for each of the conditions tested, the peak orientations increased with longer shear times. Prior investigations into the effect of shearing time upon orientation (Section 4.5.2) also revealed that increasing the shear time of PE1 caused an increase in elastic flow instabilities, which increased in dominance and distorted the oriented structures (Section 4.2, the discussion preceding Figure 4.4) .[10] However, the 2D SAXS images showed minimal tilting of the lamellae which suggested that the flow was relatively homogeneous.[16] Therefore, elastic instabilities were unlikely to contribute further to the increased permeability. The HMWT present in the MWD of PE1 (Figure 3.1, Section 3.2) would cause an increased number of entanglements (and hence an increased amount of amorphous material) which could have prevented close chain packing into crystalline regions under these conditions and thus may have also been a contributary factor to the increased permeability.[17] If the permeant molecular size is small enough, these entanglements are weak barriers to permeation.[18]

5.3.3 Permeability of Sheared PE2

As for PE1, samples of PE2 were sheared at times of 10 – 40 seconds at a shear rate of $\dot{\gamma}$ = 10 s^{-1} at 130 °C with three samples measured and averaged per shear time (Figure 5.10).

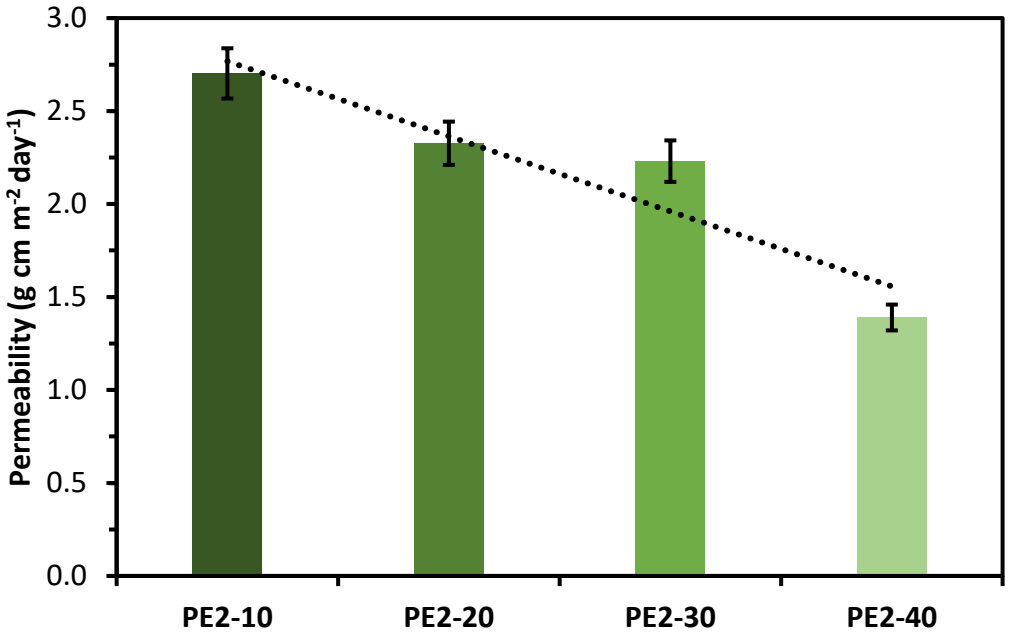

Figure 5.10: Average permeability (measured in duplicate) of PE2 samples sheared at $\dot{\gamma}$ = 10 s^{-1} for times of 10 s, 20 s, 30 s and 40 s. The numbers denote the time of shearing.

Conversely to PE1, the overall trend showed a decrease in permeability with increasing shear time, with a shear time of 40 s displaying the lowest permeability overall.

The degree of orientation as measured by SAXS (Figure 5.2) showed that peak orientation was much lower overall than PE1, however the distribution was more homogeneous as evidenced by the much flatter degree of orientation curves and lack of sharp drops around the stator joining lines (as seen for PE1, Figure 5.2). Furthermore, previous measurements to investigate the effect of shear time upon orientation (Section 4.5.2) showed that elastic instabilities did not dominate the flow behaviour of PE2 to the same extent as PE1. Thus, the flow was more homogeneous and the oriented morphology likely was not disturbed. The increased concentration of oriented morphology caused by shearing would result in a decrease in the amorphous volume fraction and hence a corresponding decrease in permeability. Therefore, these results demonstrated that increasing the orientation through longer shear times did result in a corresponding decrease in permeability. This was because of the increased sample crystallinity and increased tortuosity of the permeant diffusion path.[15,19]

5.3.4 Degree of Crystallinity and Permeability

In order to ascertain whether an increased crystallinity caused by shearing accounted for the observed permeability behaviour, DSC measurements were performed (60 – 180 °C at 10 °C min^{-1}) on each sample after permeability testing had concluded to ascertain the degree of crystallinity (averaged in triplicate, Figure 5.11).

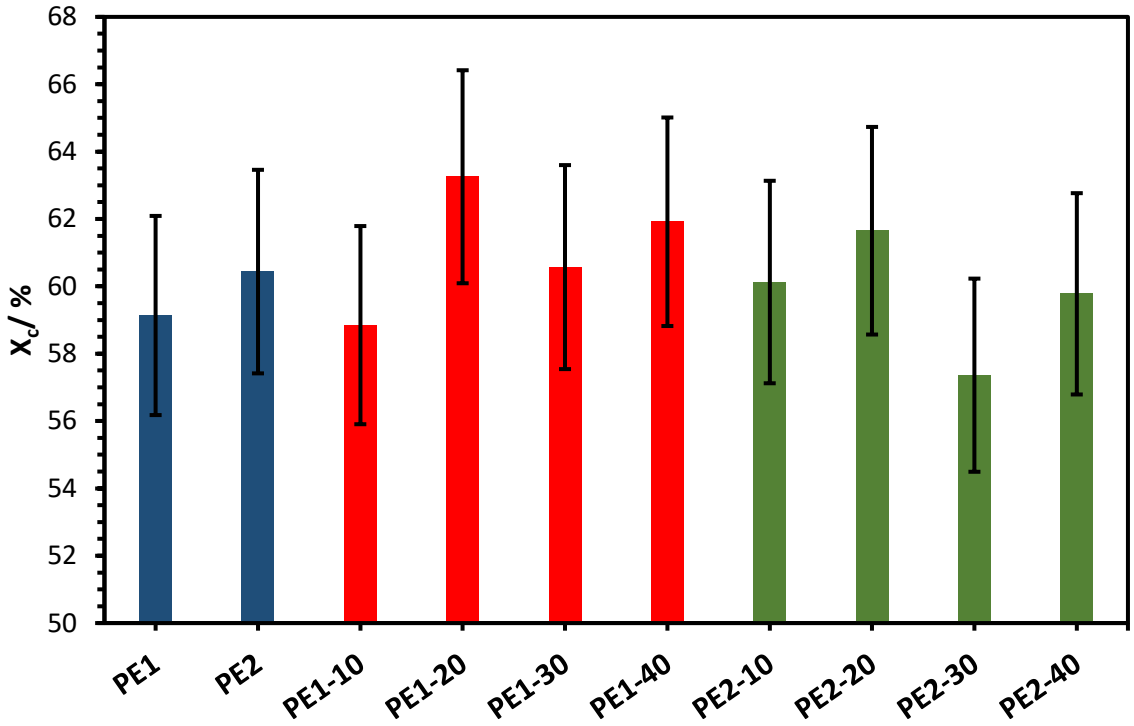

Figure 5.11: Average degree of crystallinity (X_c) as measured by DSC for samples after permeability testing had concluded. All samples were measured in triplicate and averaged. The numbers denote the time of shearing and the error bars display a 95 % confidence interval.

Given the very slight differences in crystallinity, and significant overlap between the errors, observed by DSC across the samples, this indicated that neither the shear time nor the HPDE grade had a significant impact upon the total degree of crystallinity. Thus, total crystallinity was not the dominating factor in resisting permeation. However, these two factors did have a clear effect upon the morphology (Figure 5.2) which did show evidence as the dominating factor for resisting permeation (Figures 5.8 and 5.10).

5.4 Mechanical Testing

The semicrystalline morphology of PE, particularly the degree of crystallinity,[20,21] can explain many of the observed physical and mechanical properties: crystalline fractions impart rigidity and amorphous fractions impart toughness (Section 1.4.1, Figure 1.12).[22] The mechanical

response of PE samples subjected to mechanical testing involves the rearrangement of molecules or distortion of the morphology after a load is applied, such as tension.[17] Typically, PE deforms via a mechanism of yielding, necking and strain hardening before sample failure, all of which can be observed in a typical stress-strain curve (Figure 2.32, Section 2.12.1.2).[17,23,24] It should be noted that no universal shape for the stress-strain curve of PE exists.[17] Within the low strain region, properties such as yield stress and Young's Modulus are obtained, with morphological features controlling this behaviour; at high strain the ultimate tensile strength and elongation at break are obtained, with molecular characteristics controlling this behaviour.[17] When a tension load is applied to a sample, homogeneous deformation initially occurs until one cross-sectional slice yields independently. The onset of this heterogeneous deformation marks the yield point.[17] Further deformation causes the newly formed neck to grow until it encompasses the entire sample. Subsequent deformation is homogeneous and strain hardening occurs until the sample breaks.[17,25] On a morphological level, the onset of plastic deformation corresponds to deformation of the crystallites – reorientation of chain-folded lamellae towards the tensile deformation direction and fragmentation of the largest crystallites.[23,26]

Oriented morphologies and *shish-kebabs* have been shown to improve the mechanical performance, such as stiffness, of polymer products due to load transfer by the oriented fibres.[3,27] High modulus and tensile strength are known for highly oriented fibrillated polymer chains due to the covalent bonding along the chain length.[28] Perpendicular to this chain direction, however, the moduli are typically two orders of magnitude lower.[28] When a tensile stress is applied to a semi-crystalline polymer, two modes of deformation act: lamellae slip and chain slip.[26,28] The enhancement of modulus seen with the *shish-kebab* morphology arises due to the *shish* fibre and inter-locking nature of the *kebabs* caused by the close proximity of neighbouring chains during growth.[28–30] Additionally, the intermeshing of *shish-kebab* structures has the effect of increasing lateral cohesion in the mechanical response, in comparison to fibrillated structures mentioned previously.[28,29] Furthermore, an increased fraction of HMW material has been shown to further enhance the mechanical response.[29,31]

Samples of PE1 were sheared using the Couette cell at $\dot{\gamma}$ = 10 s^{-1}, 130 °C and t_s = 10 – 40 s in 10 second increments. After cutting tensile testing bars with gauge length dimensions 7 mm x 25 mm (Figure 5.12), the samples were outsourced for tensile testing at Aliaxis R&D (Vernouillet, France) in accordance with ISO Standard 527.[32] Five samples were tested per shear condition with the exception of PE1 where only three specimens were tested. All samples

were tested at 20 mm min^{-1} in the direction of flow/orientation. Slower draw rates give rise to decreased elastic moduli, lower yield stresses, higher yield elongations, broader yield peaks in the force versus elongation curve, and a less well-defined neck as observed visually.[17]

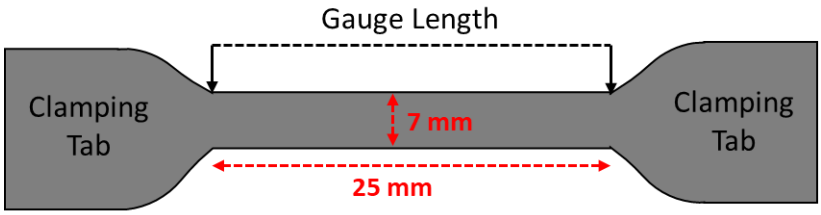

Figure 5.12: Schematic of the 'dog-bone' samples used for tensile testing with dimensions of 7 mm x 25 mm manufactured to a thickness of 0.5 mm.

5.4.1 Young's Moduli

The Young's modulus, *E*, or elastic modulus, can be determined from the initial slope of the stress-strain curve (Figure 2.32, Section 2.12.1.2). This deformation prior to yield is homogeneous and largely recoverable if the stress is removed.[17] Thus the Young's modulus is a measure of stiffness of a sample – larger moduli correspond to stiffer samples.[17] A strong dependence of Young's modulus and molecular orientation has been found for HDPE elongated to various draw ratios.[17,33] The Young's modulus was obtained for each shear condition from the stress-strain curves of PE1 (Figure 5.13 and Table 5.4) and PE2 (Figure 5.14 and Table 5.4).

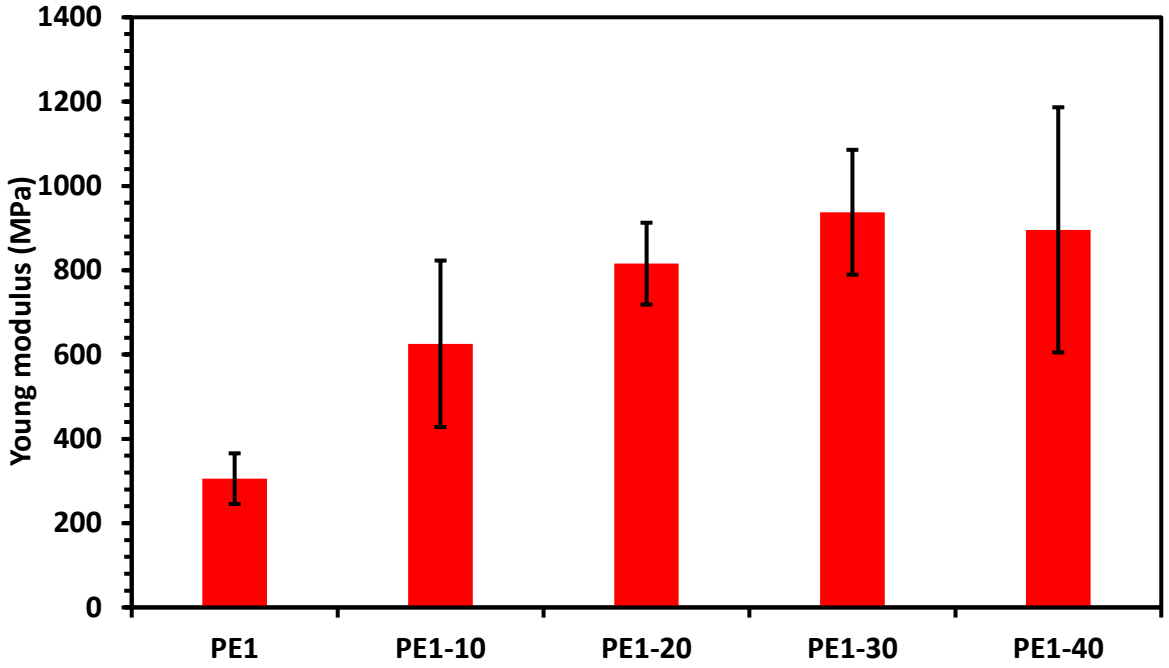

Figure 5.13: Young's moduli in tension obtained from stress-strain curves at different shear times for PE1. All measurements were performed 20 mm min^{-1} on 5 specimens, with the exception of PE1 where only 3 specimens were tested, and averaged. The numbers in each sample title denote the time of shearing.

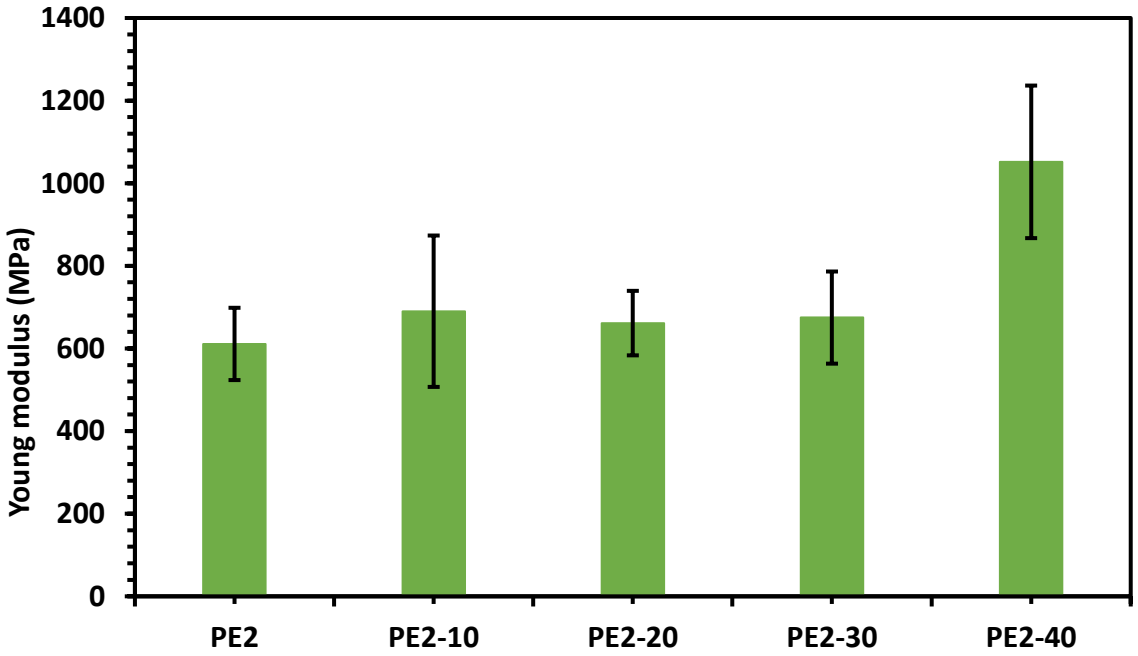

Figure 5.14: Young's moduli in tension obtained from stress-strain curves at different shear times for PE2. All measurements were performed at 20 mm min^{-1} on 5 specimens and averaged. The numbers denote the time of shearing. The numbers in each sample title denote the time of shearing.

	PE1	PE1-10	PE1-20	PE1-30	PE1-40
Young's Modulus (MPa)	306	626	816	938	896
Error	*60*	*198*	*97*	*148*	*291*

	PE2	PE2-10	PE2-20	PE2-30	PE2-40
Young's Modulus (MPa)	611	690	661	675	1052
Error	*87*	*183*	*78*	*112*	*185*

Table 5.4: Young's Moduli in tension at different shear times for PE1 and PE2. All measurements were performed at 20 mm min^{-1} on 5 specimens with the exception of PE1 where only 3 specimens were measured. The numbers in each sample title denote the time of shearing.

Unoriented bulk PE typically displays a value of 1000 MPa, which was not fully consistent with this work.[28,34] It was noted that many of the isotropic samples had surface defects or bubbles (especially for PE2, but PE1 also) arising due to the processing which may have had an impact. However, as all failure strains were >100 %, this could not have been the case as *E* was measured prior to yielding. Therefore, this suggested that low crystallinity within the samples contributed to the observed literature discrepancies.[32]

For the oriented PE1 samples, the Young's modulus increased between 0 – 30 seconds shear time before plateauing at 40 seconds (Figure 5.13 and Table 5.4) – there was a large degree of uncertainty for this final measurement, however, and the general trend was one of increasing with longer shear times. All sheared values were greater than the isotropic sample, suggesting that shearing and subsequent crystalline orientation had increased the Young's Modulus. For PE2, shear times between 0 – 30 seconds displayed a plateau before increasing significantly at a shear time of 40 seconds (Figure 5.14 and Table 5.4). All values were greater than the isotropic PE2 sample, but only weakly oriented (Figure 5.2) which could explain the close nature of these values. A greater orientation or concentration of *shish-kebabs* generally causes an increase in the Young's Modulus as an increased amount of the material in the melt can intermesh and act as a load-bearing feature.[17,35] *Shish-kebabs* formed from dilute solutions, with mutually parallel fibre axes, at crystallisation temperatures greater than 124 °C exhibit Young's moduli $E > 140$ GPa. From the melt, however, chain entanglements reduce the

network mobility and thus the values obtained will be lower.[26,36] As was evident from the results for PE1, increasing shear time caused increased anisotropy (Figure 5.2) and an increase in the Young's modulus. The effects of shearing for longer times were less apparent for PE2 which was reflected in the fairly consistent values for the Young's Moduli. The degree of orientation as measured by SAXS for PE2 across all shear times (Figure 5.2) was of similar magnitude to PE1-10 (the number denotes the time of shearing in seconds), hence the similarity in Young's Moduli values observed across these samples when compared with PE1-10 (Table 5.3).

Calculated values, from theory and simulation, have predicted a maximum value for the Young's Modulus of fully extended PE chains to be greater than 300 GPa.[37] Experimentally, the highest values achieved in the literature thus far are 230 – 264 GPa.[17,38] Compared to isotropic samples, the values for the Young's Modulus were significantly higher. Smaller amounts of deformation under tension are required at low strains to stretch the random coil in isotropic samples, which is largely facilitated by bond rotations.[17] The chains in anisotropic PE samples, however, are already stretched and, therefore, larger amounts of deformation under tension are required to stretch these chains further, typically due to bond elongation and an increase in the C-C-C dihedral angle.[17] Generally, high molecular orientation is necessary for a high Young's modulus, with an increased fraction of oriented crystalline material contributing to higher moduli.[17,35]

5.4.2 Stress at Yield and Maximum Strain at Break

Yielding occurs in samples when deformation changes from homogeneous to hetergeneous, after which point the deformation is no longer elastic and the strain is irrecoverable.[17] An increased yield stress has been observed for polymers with increasing degrees of crystallinity.[20,26,36,39–42] Yielding has been attributted to the crystalline fraction in the sample because, at ambient temperature, the amorphous fraction is rubbery in nature and so does not contribute to the yield stress.[20,26,36,39–42] Thus the stress at yield is the force at which a sample yields divided by its cross-sectional area.[17] For isotropic samples, this values correlates strongly with the degree of crystallinity; greater degrees of crystallinity contribute to a greater yield stress – however, at crystallinites over 80 % samples tend to be brittle.[17] From a practical perspective, the yield stress determines the maximum applicable load a sample could withstand during service. The maximum strain at break refers to the strain within the sample at the point of sample failure under tension, expressed as a percentage elongation with respect to the original length.[17] The molecular characteristics that develop high degrees of crystallinity are

similar to those that facilitate large strains at break.[17] Features that hinder the slippage of chains past one another during crystallisation, such as branching and entanglements, also reduce the strain at break.[17] Thus, the intermeshed nature of *shish-kebabs* will also hinder chain slippage and should reduce the strain at break.[28–30] Comparing oriented and isotropic samples, those with greater initial orientaion should display lower strains at break.[17] However, the maximum strain at break is inversely proportional to orientation, with ultra-oriented fibres exhibiting values approaching 10 %.[17]

For PE1, increasing the shear time beyond PE1-20 resulted in an increase in the stress at yield and a corresponding linear decrease in the maximum strain at break (Figure 5.15 and Table 5.5). The observed consistency in stress at yield values for 10 seconds of shear (PE1-10) and 20 seconds of shear (PE1-20) samples suggested that the concentrations of oriented morphology in the anisotropic samples were insufficient to impact the stress at yield. Given that an increased shear time corresponded with an increase in anisotropy, the greater concentration of oriented morphology would have intermeshed more significantly and thus restricted the mobility of the network under deformation thus resulting in lower strains at break.[17,19,26,28–30]

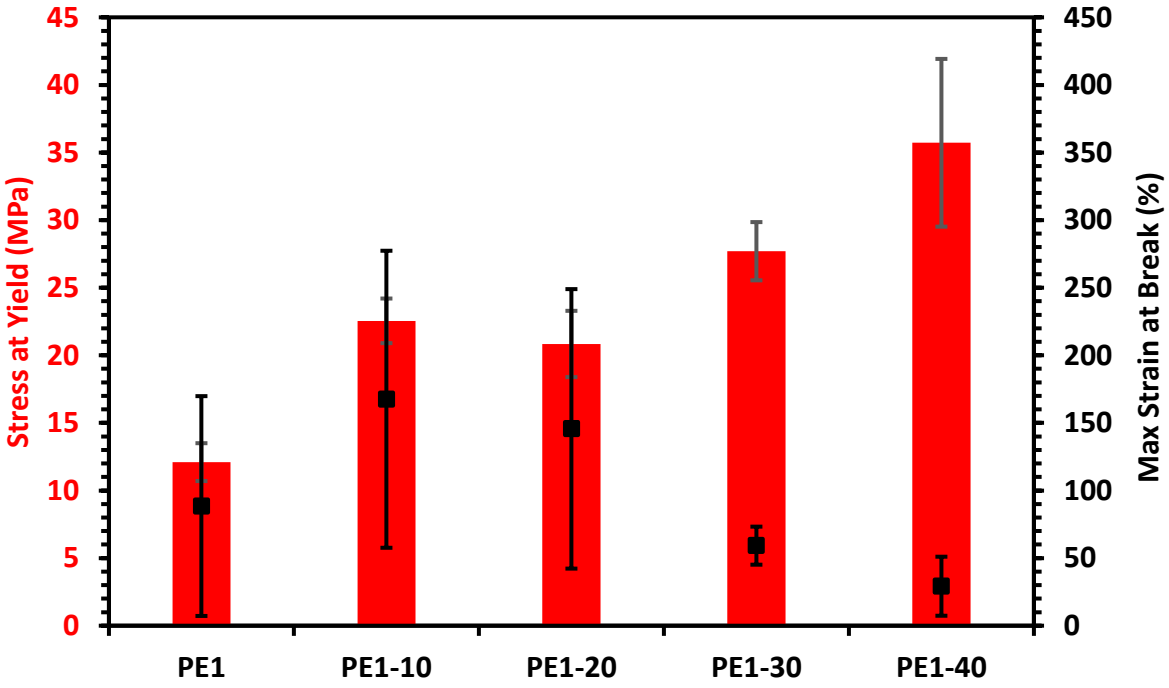

Figure 5.15: Stress at yield (orange bars) and maximum strain at break (black squares) in tension at 20 mm min^{-1} for different shearing times of PE1. The numbers in each sample title denote the time of shearing.

	PE1	PE1-10	PE1-20	PE1-30	PE1-40
Max strain at break (%)	294	168	146	59	29
Error	*40*	*110*	*103*	*14*	*22*
Stress at yield (MPa)	22	23	21	28	36
Error	*1.0*	*1.7*	*2.5*	*2.2*	*6.2*

Table 5.5: The maximum strain at break and stress at yield in tension at different shear times for PE1. The numbers refer to the shearing time ($\dot{\gamma}$ = 10 s^{-1}, T = 130 °C). The numbers in each sample title denote the time of shearing.

For PE2, negligible increases were seen for the stress at yield with increasing shear time (Figure 5.16 and Table 5.6), most likely due to the minimal orientation in this material. The value for PE2-40 was comparable to that for PE1-10 as both samples had similar degrees of orientation (Figure 5.2). The effect of a lack of orientation was clear as the 10 – 30 s (PE2-10, PE2-20, PE2-30) shear time samples displayed similar degrees of orientation and stress at yield to isotropic PE2. The strain at break values, therefore, were also generally consistent with the isotropic sample. The large value for the strain at break for PE2-40 was most likely due to deformation occurring in a region outside the gauge length (Figure 5.12) - an assumption in calculating the maximum strain at break is that all deformation occurs within the gauge length.[17]

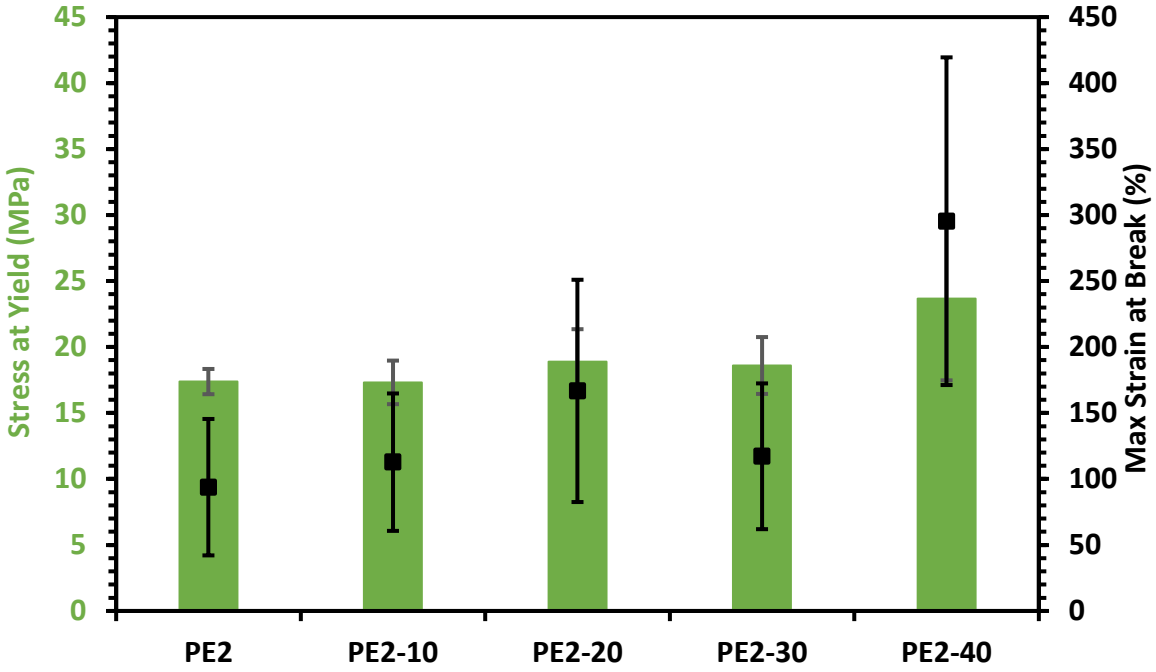

Figure 5.16: Stress at yield (green bars) and maximum strain at break (black squares) in tension at 20 mm min^{-1} for different shearing times of PE2. The numbers in each sample title denote the time of shearing.

	PE2	PE2-10	PE2-20	PE2-30	PE2-40
Max strain at break (%)	94	113	167	117	295
Error	*52*	*52*	*84*	*55*	*124*
Stress at yield (MPa)	17	17	19	19	24
Error	*3.3*	*1.9*	*2.1*	*2.4*	*3.5*

Table 5.6: The maximum strain at break and stress at yield in tension at different shear times for PE2. The numbers refer to the shearing time ($\dot{\gamma}$ = 10 s^{-1}, T = 130 °C). The numbers in each sample title denote the time of shearing.

Both isotropic samples displayed stress at yield behaviour that was consistent with literature.[34] In both cases, however, shearing and orientation did increase the stress at yield and Young's Moduli compared to the isotropic samples.[19]

5.5 Comparison of Orientation, Young's Modulus and Permeability

A comparative plot of shear-induced orientation (through Couette shear and measured by SAXS), Young's Modulus and permeability for PE1 and PE2 highlights the importance of the critical work (black dashed line in Figure 5.17) for the formation of orientated morphology and the subsequent effect upon mechanical and permeability properties (Figure 5.17 and Table 5.7).

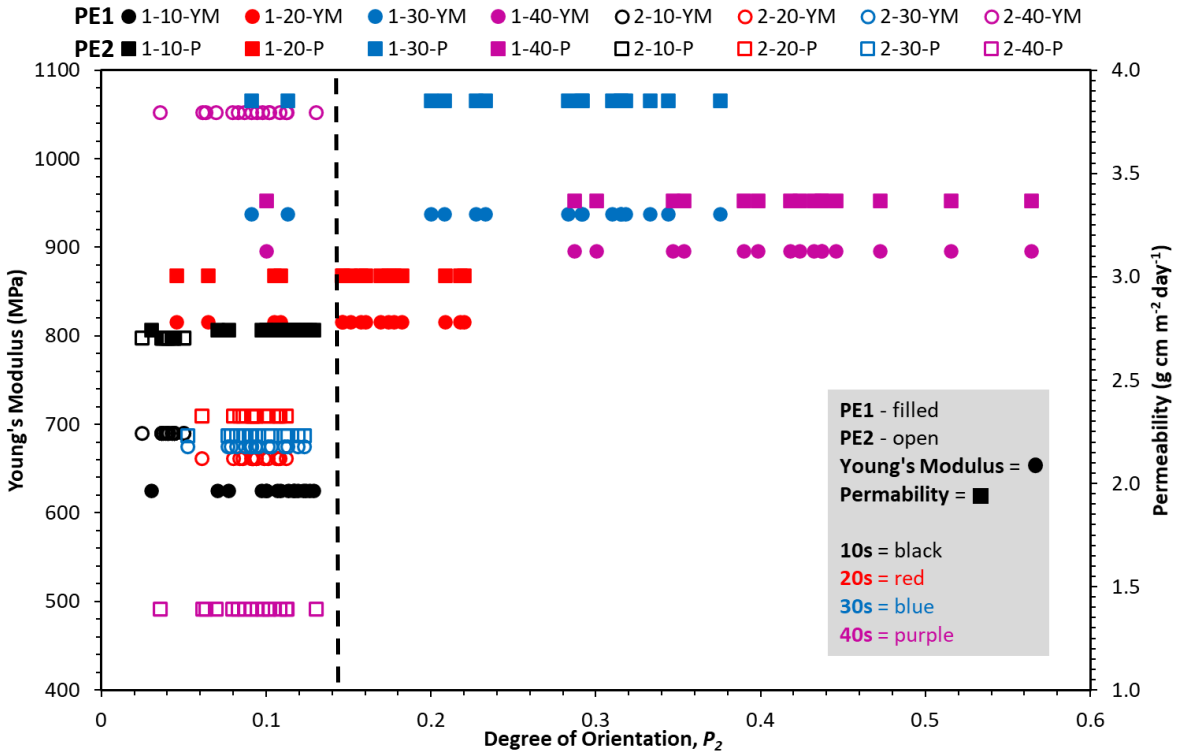

Figure 5.17: A comparative plot of shear-induced orientation (through Couette shear and measured by SAXS), Young's Modulus (left *y-axis*) and permeability (right *y-axis*) for PE1 (filled symbols) and PE2 (open symbols). Symbols for Young's Modulus are denoted by circles and those for permeability by squares. The colours correspond to the increasing amounts of shear time, and hence orientation, imparted to each sample during shearing: 10 seconds = black; 20 seconds = red; 30 seconds = blue; 40 seconds = purple. The sample naming given by the key follows the pattern *[1]* or *[2]-[time of shearing]-[YM]* or *[P]*, where *1* or *2* refers to the *PE* material, the following numbers refer to the time of shearing and *YM* or *P* refer to *Young's Modulus* or *Permeability* respectively (Table 5.7). The black dashed line highlights the critical work above which oriented morphology is formed and impacts upon the mechanical properties and permeation behaviour.

Name	HDPE	Shear Time (s)	Young's Modulus or Permeability	Name	HDPE	Shear Time (s)	Young's Modulus or Permeability
1-10-YM	PE1	10	YM	**2-10-YM**	PE2	10	YM
1-20-YM	PE1	20	YM	**2-20-YM**	PE2	20	YM
1-30-YM	PE1	30	YM	**2-30-YM**	PE2	30	YM
1-40-YM	PE1	40	YM	**2-40-YM**	PE2	40	YM
1-10-P	PE1	10	P	**2-10-P**	PE2	10	P
1-20-P	PE1	20	P	**2-20-P**	PE2	20	P
1-30-P	PE1	30	P	**2-30-P**	PE2	30	P
1-40-P	PE1	40	P	**2-40-P**	PE2	40	P

Table 5.7: A guide to the naming of the samples given in Figure 5.17 indicating the HDPE grade, shear time and measure of either the Young's Modulus (Y) or Permeability (P).

As the orientation increased for PE1 (filled symbols, Figure 5.17), both the Young's modulus and permeability also increased up to 30 seconds of shear (1-30-YM and 1-30-P) but with a decrease at a shear time of 40 seconds (1-40-YM and 1-40-P). None of the PE2 samples (2-10-YM/P) displayed an orientation greater than the critical work and thus the impact of orientation upon physical properties was not observed as clearly. The sample sheared for 40 seconds displayed the greatest orientation and, correspondingly, the largest Young's modulus (2-40-YM) and lowest permeability (2-40-P), which indicated that oriented morphology in this sample was beginning to impact upon the properties, but not at significant levels above the critical work.

Considering the MWDs of PE1 and PE2 (Figure 3.1), PE1 had a larger fraction of UHMW material and consistently showed greater degrees of orientation than PE2 because of this UHMWT (Figures 4.7, 4.11 & 5.2). Therefore, a lower critical work was required to produce oriented morphology upon shearing under the same conditions as PE2 (Section 4.4). Only the 10 second sample for PE1 received insufficient work for oriented morphology formation, however all samples of PE2 received insufficient work.

Oriented morphology has been shown to increase the Young's modulus, therefore the 40 second sample for PE1 (1-40-YM) should have displayed the greatest modulus. However, the orientation of this sample was lower than the preceding (30 seconds shear) and so the Young's modulus (1-30-YM) and permeability (1-30-P) decreased accordingly. Elastic flow instabilities (Section 4.2) have been observed for PE1 at shear times greater than 30 seconds (Section 4.5.2), therefore these same flow instabilities could have arisen during Couette shearing of PE1 at 40 seconds of shear. However, only minimal titling of the 2D SAXS patterns was observed (Figure 5.4) which suggested that elastic instabilities were not a significant issue. High viscosity and

high shear strain, supplied through the action of shearing in Couette flow, can cause viscous shear (or frictional) heating, whereby the low thermal conductivity of PE causes a viscous dissipation of heat and a rise in temperature of the melt.[17,45] Indeed, shear heating is the principal method of melting HDPE within a single-screw extruder.[46] As viscosity decreases with increasing temperature, a subsequent reduction in shear strain occurs, and hence the work supplied to the melt is reduced which causes a lower than expected degree of orientation.[17,45] This increase in heat could also have caused partial thermal relaxation of oriented morphology. The UHMWT present in the MWD of PE1 (Figure 3.1, Section 3.2) would cause an increased number of entanglements (and hence an increased amount of amorphous material) which could have prevented close chain packing into crystalline regions under these conditions and thus may have also been a contributary factor to the reduced Young's modulus and increased permeability.[17]

The oriented morphology was formed in the direction of shearing (as confirmed by SAXS, Figures 5.3 – 5.5), however, measurements were performed such that this orientation direction lay perpendicular to the solvent flux (Section 5.3.2, Figure 5.9). Therefore, as the concentration of oriented morphology increased, the permeability also increased.

5.6 Conclusions

By using a Couette cell that could be disassembled, it was possible to prepare large area samples processed at homogeneous shear conditions and recover them from the cell for further structural analysis and mechanical testing. The samples were sheared at different shear times, with shear rate and shear temperature constant, to achieve varying degrees of orientation. SAXS measurements showed that the orientation within each condition was relatively homogeneous, however the effects of shear time were more evident for PE1 than PE2 due to the HMWT in the MWD of the former.[11] From these samples, specimens were cut for further permeation and mechanical testing measurements. Previous research has shown that the *shish-kebab* morphology, arising from shearing and present in these samples, can improve the tensile deformation properties because of the stretched *shish* fibrils and intermeshed nature of the *kebab* lamellae overgrowths.[17,43] The crystalline regions in semicrystalline polymers are impermeable to permeant gases and, therefore, the *shish-kebab* morphology was investigated as a means to increase the barrier properties of HDPE for use in PE-100 plastic pipes.[8,12,14,44]

The degrees of orientation as measured by SAXS showed a clear increase in orientation with increasing time of shear for PE1, whereas this was less evident for PE2 – even at the longest

shear times, the degree of orientation was comparable to just 10 seconds for PE1. This was attributed to the increased fraction of HMW chains present in the MWD of PE1; a greater fraction of UHMW material in the MWD has been shown to facilitate orientation at lower shear rates or strains due to the longer relaxation times of these chains.[11]Three samples per shear condition were measured in permeation cells that had been fabricated previously by utilising a method similar to the time-lag method. Samples of isotropic PE1 and PE2 were also tested for comparison. Anisotropic PE1 samples showed evidence of increasing permeability with increasing shear rate which was attributed to the direction of polymer chain orientation and permeant flux during the measurement – orientation was perpendicular to the flux. As the number of *shish-kebabs* increased with shear time, the number of voids between *kebab* lamellae overgrowths also increased thus facilitating a higher permeability. A greater number of entanglements preventing close chain packing into crystalline domains may also have contributed.[10] Conversely, PE2 displayed decreasing permeability for an increase in the shear time which indicated that the increased concentrations of oriented crystalline morphology did reduce the permeability. DSC measurements concluded that the oriented morphology, and not the total crystallinity, was the dominating factor in determining permeation resistance.

Tensile testing measurements were outsourced to Aliaxis R&D, with the Young's modulus, stress at yield and maximum strain at break reported. The Young's moduli for PE1 increased as shear time increased which confirmed that the oriented morphology did enhance the mechanical properties. This did not correlate with the permeation results obtained for this material (as highlighted previously) – increasing Young's modulus with increasing permeability. This was attributed to a relaxation of the oriented morphology via shear heating and an increased concentration of voids between lamellae *kebabs*. This same effect was not observed for PE2 which was because of the generally lower degrees of orientation across all shear conditions which were below the critical work for oriented morphology formation. However, the permeability results for PE2 did correlate well with the Young's modulus as predicted – increasing orientation (albeit minor) led to decreasing permeability. The stress at yield values across all samples for both materials were greater than the corresponding isotropic samples. The maximum strain at break values decreased linearly for oriented PE1 with the lowest values observed at the highest shear times which was consistent with trends as reported in the literature. As the orientation in the PE2 samples was lower and of comparable magnitude, the strain at break values showed consistency across shear times up to 30 seconds. A much

greater value was noted at 40 seconds shear time which was likely as a result of sample failure outside of the gauge length.

Overall, oriented morphology with possible *shish-kebab* formation has been shown to have an impact upon the barrier properties and mechanical deformation behaviour. It was evident, that the samples with the greatest orientation displayed the greatest improvements in tensile deformation behaviour, but suffered from increased permeability. At these highest shear times, the entangled *shish-kebab* network was capable of resisting deformation up to higher strains but likely suffered from an increased void concentration and hence weaker barrier properties. PE2 was unable to be oriented to the same degrees as PE1 owing to the decreased fraction of UHMW material in the blend, however, it did show increased barrier properties with increasing shear time. The weaker orientation was clearly reflected in the mechanical behaviour. It was clear that further optimisation of the shear rate, time and temperature would be necessary to achieve the optimum balance of mechanical strength and barrier properties.

5.7 References

1 C. J. S. Petrie and M. M. Denn, *AIChE J.*, 1976, **22**, 209–236.

2 R. G. Larson, *Rheol. Acta*, 1992, **31**, 213–263.

3 R. Zhao, Z. Chu and Z. Ma, *Polymer*, 2020, **12**, 2571–2582.

4 M. J. Hill and A. Keller, *J. Macromol. Sci. Part B*, 1969, **3**, 153–169.

5 I. J. Rao and K. R. Rajagopal, *Z. Angew. Math. Phys.*, 2002, **53**, 365–406.

6 C. E. Rogers, V. Stasnett and M. Szwarc, *Journl Polym. Sci.*, 1960, **XLV**, 61–82.

7 M. Hedenqvist and U. W. Gedde, *Science*, 1996, **21**, 299–333.

8 A. S. Michaels and H. J. Bixler, *J. Polym. Sci.*, 1961, **50**, 393–412.

9 S. Song, P. Wu, M. Ye, J. Feng and Y. Yang, *Polymer*, 2008, **49**, 2964–2973.

10 O. O. Mykhaylyk, P. Chambon, C. Impradice, J. P. A. Fairclough, N. J. Terrill and A. J. Ryan, *Macromolecules*, 2010, **43**, 2389–2405.

11 L. Balzano, *Flow Induced Crystallization of Polyolefins*, PhD Thesis, Eindhoven University of Technology, 2008.

12 M. Kuzmanovic, L. Delva, L. Cardon and K. Ragaert, *Adv. Mater.*, 2020, **32**, 2003938.

13 D. H. Weinkauf and D. R. Paul, in *Barrier Polymers and Structures - ACS Symposium Series*, ed. W. J. Koros, Austin, Texas, 1990, pp. 60–91.

14 A. S. Michaels and R. B. Parker, *J. Polym. Sci.*, 1959, **41**, 53–71.

15 P. S. Holden, G. A. J. Orchard and I. M. Ward, *J. Polym. Sci. Part A-2, Polym. Phys.*, 1985, **23**, 709–731.

16 O. O. Mykhaylyk, P. Chambon, R. S. Graham, J. P. A. Fairclough, P. D. Olmsted and A. J. Ryan, *Macromolecules*, 2008, **41**, 1901–1904.

17 A. J. Peacock, *Handbook of Polyethylene*, Marcel Dekker, New York, 2000.

18 S. J. Doong and W. S. W. Ho, *Ind. Eng. Chem. Res*, 1998, **31**, 1050–1060.

19 S. Srinivas, P. Brant, Y. Huang and D. R. Paul, *Polym. Eng. Sci.*, 2003, **43**, 831–849.

20 M. F. Butler, A. M. Donald and A. J. Ryan, *Polymer*, 1998, **39**, 39–52.

21 M. A. Parvez, M. Rahaman, J. B. P. Soares, I. A. Hussein and M. A. Suleiman, *Polym. Sci. Ser. B*, 2014, **56**, 707–720.

22 Z. Jiang, Y. Tang, J. Rieger, H. F. Enderle, D. Lilge, S. V. Roth, R. Gehrke, Z. Wu, Z. Li and Y. Men, *Polymer*, 2009, **50**, 4101–4111.

23 S. J.-F. Rottler, Joerg Rottler, O. Lame, A. Makke, M. Perez and J.-L. Barrat, *ACS Macro Lett.*, 2015, **4**, 147–151.

24 D. A. Şerban, G. Weber, L. Marşavina, V. V. Silberschmidt and W. Hufenbach, *Polym. Test.*, 2013, **32**, 413–425.

25 J. Milisavljević, E. Petrović, I. Ćirić, M. Mančić, D. Marković and M. Dordević, in *29th DANUBlA-ADRIA Symposium on Advances in Experimental Mechanics, DAS 2012*, 2012, **vol. 29**, pp. 266–269.

26 R. Hiss, S. Hobeika, C. Lynn and G. Strobl, *Macromolecules*, 1999, **32**, 4390–4403.

27 M. J. Hill and A. Keller, *J. Macromol. Sci. Part B*, 1969, **3**, 153–169.

28 J. A. Odell, D. T. Grubb and A. Keller, *Polymer*, 1978, **19**, 617–626.

29 Z. Bashir, J. A. Odell and A. Keller, *J. Mater. Sci.*, 1984, **19**, 3713–3725.

30 Z. Bashir, J. A. Odell and A. Keller, *J. Mater. Sci.*, 1986, **21**, 3993–4002.

31 S. H. Burstein, Y. Lin, W. Wu and Q. Ge, *Polymer*, 2020, **213**, 123210.

32 *ISO 527-1:2019 - Plastics — Determination of Tensile Properties — Part 1: General Principles*, 2019.

33 P. Smith and P. J. Lemstra, *J. Mater. Sci.*, 1980, **15**, 505–514.

34 Q. Guan, F. S. Lai, S. P. McCarthy, D. Chiu, X. Zhu and K. Shen, *Polymer*, 1997, **38**, 5251–5253.

35 M. J. Hill, P. J. Barham and A. Keller, *Colloid Polym. Sci. Kolloid-Zeitschrift Zeitschrift für Polym.*, 1980, **258**, 1023–1037.

36 M. A. Kennedy, A. J. Peacock, M. D. Failla, J. C. Lucas and L. Mandelkern, *Macromolecules*, 1995, **28**, 1407–1421.

37 A. S. Deazle, B. J. Howlin, C. Lekakou, G. J. Buist, J. R. Jones and J. M. Barton, *J. Chem. Crystallogr.*, 1994, **24**, 17–20.

38 P. J. Lemstra and L. A. Kleintjens, *Integration of Fundamental Polymer Science and Technology—2*, Springer Netherlands, Dordrecht, 1988.

39 J. Clements, S. A. Jawad, G. R. Davies, I. M. Ward and G. Capaccio, *Polymer*, 1986, **27**, 363–368.

40 W. J. O'kane, R. J. Young and A. J. Ryan, *The Effect of Annealing on the Structure and Properties of Isotactic Polypropylene Films*, 1995, vol. 34.

41 G. Capaccio and I. M. Ward, *J. Polym. Sci. Part A-2, Polym. Phys.*, 1984, **22**, 475–484.

42 B. Na, R. Lv, Q. Zhang and Q. Fu, *Polym. J.*, 2007, **39**, 834–840.

43 D. T. Grubb and M. J. Hill, *J. Cryst. Growth*, 1980, **48**, 321–333.

44 A. S. Michaels and H. J. Bixler, *J. Polym. Sci.*, 1961, **50**, 413–439.

45 C. Macosko, *Rheology: Principles, Measurements and Applications*, Wiley VCH, New York, 1996, **vol. 86**.

46 Chris Rauwendaal, *Polymer Extrusion*, Hanser Publishers, Munich, 5th edn., 2014.

Chapter 6

Fabricating Single-Polymer Composites to Improve the Barrier and Mechanical Properties

6.1 Introduction

The advantages of polymer materials are often a result of their low cost, low weight, easy processability and physical properties.[1] However, in order to tailor the material properties to specific applications, techniques such as melt blending are employed to improve properties such as stiffness, toughness and chemical and thermal resistance.[1] The microstructure of such blends has been shown to link directly to the mechanical and physical properties.[1–4] Processing methods have a direct impact upon the dispersion of the immiscible blend and previous work has shown that well-dispersed particles displayed improved matrix impact strength,[5] sheet-like dispersions improved barrier properties[6] and fibrillar morphologies increased the unidirectional strength.[5]

Further improved mechanical properties have been obtained using carbon-fibre or glass-fibre polymer composites.[1] However, such composites are associated with high manufacturing costs, complex production methods and challenging end-of-life recycling - not only to separate the fibre and matrix from carbon- and glass-fibre composites, but they are also reported to be quite abrasive to recycling equipment.[1] This has led to the development of SPCs where both the fibre and matrix are thermoplastic in nature and made from similar polymer, therefore, end-of-life recycling may be easier compared to carbon- or glass-fibre composites as the fibres and matrix are both thermoplastic.[1,7,8]

In particular, HDPE-UHMWPE SPCs have seen considerable interest.[8,10,11] The high strength and modulus of extended chain PE fibres are attributed to their HMW, crystallinity and degree of orientation.[9] UHMWPE fibres possess an impressive list of beneficial properties: high impact resistance, high cut and abrasion tolerance, excellent chemical resistance, low dielectric constant, good UV resistance, low moisture absorption, excellent vibration damping capability, low coefficient of friction and self-lubricating properties.[9] Therefore, SPCs could offer another solution to increase mechanical strength and permeability resistance of PE-100 pipes. Such composites have been shown to exhibit mechanical strengths between that of glass-reinforced polyester and epoxy resins.[12] Designing and manufacturing a new extrusion head can be extremely expensive, whereas a more simple tape-wrapping procedure could be incorporated into the existing manufacturing architecture, saving development time and money.

With regard to permeation, previous research has shown that the crystalline regions are impermeable to the vapour of small organic molecules.[13] Addition of highly-crystalline UHMWPE oriented tapes should significantly improve the permeation resistance of PE-100

pipes and should also improve the mechanical properties.[14,15] A strong and stable interface, created by inter-diffusion of molecular chains into the corresponding layers, between the matrix and fibre interlayer allows for load transfer from the weaker matrix to the stronger fibre under mechanical deformation resulting in increased mechanical strength.[16,17] Processing conditions have a great impact upon the efficiency of the fusion bonding between the matrix and fibre interlayer: high temperatures, such that the interfacial temperature is greater than the melting temperature, and high contact pressures induce efficient bonding.[16] Under these conditions, polymer chains can inter-diffuse across the interface in three stages: 1) polymer surfaces rearrange and approach each other; 2) the two surfaces begin to approach and wet; 3) completion of wetting, making good contact, and chain inter-diffusion marked by the disappearance of the interface boundaries.[16] The potential barriers at the interfaces are removed as the polymer chains are free to move from one surface to another.[16]

Three UHMWPE tapes were selected for use as barrier layers in SPCs, with PE1 and PE2 acting as the matrix. In order to fabricate SPCs, it was necessary to find the temperature window in which the matrix (HDPE) would melt and the fibre (UHMWPE) would remain oriented. At high temperatures, polymer chains relax to the coiled state and lose any anisotropy.[18] After construction of mono-layer and crossed bi-layer SPCs, they were subjected to permeation measurements and mechanical testing with comparison to aluminium foil composites currently used.

6.2 Single-Polymer Composite Fabrication

Fabrication of SPCs can be challenging. Despite the beneficial properties of UHMWPE fibres, a major limitation is the difficulty in bonding to other substrates and forming a stable interface due to the chemical inertness and lack of functional groups of the fibre.[9,16,19] Several methods have been developed over the years in order to overcome this difficulty, often by pre-treatment of the fibres:[9] increasing the surface roughness by chemical etching, plasma or corona treatments (with O_2 or CO_2);[20] introducing surface functional groups through chain scission and substitution.[9,21] Whilst these approaches have been observed to significantly increase bonding, the cost is a degradation of the physical properties.[9]

An alternative approach regards the exploitation of the thermoplastic nature of PE. Through careful application of heat and pressure, surface melting and recrystallisation can be used to melt the fibre surface and fuse with an HDPE matrix.[9,19] This method of melt pressing has been

used extensively in the literature to fabricate SPCs because the fibre orientation can be carefully controlled.[1,22–25]

Orienting polymer chains (for example, by mechanical drawing) causes a small difference between the melting temperatures, T_m, of stretched and unstretched polymers.[19,26] This is caused by orientation of the polymer chains resulting in a corresponding reduction in entropy and, given that the ΔH of melting is the same regardless of orientation and $T_m = \Delta H/\Delta S$, the melting temperature increases as ΔS decreases.[27] Stretched chains form more thermodynamically stable crystals and, therefore, exhibit a higher melting point than conventional melts.[12] Folded lamellae essentially melt into an entangled coil, so ΔS is larger than that for unentangled oriented chains which melt into a rotator phase. This needs to be exploited in order to melt the surrounding HDPE matrix, but not the fibres themselves.[12,27] Pressure needs also to be applied in order to cause wetting of the fibres and matrix and good adhesion between the two.[26] Thus, two compression moulding fabrication methods were investigated: melt pressing and VCM.

6.2.1 Melt Pressing

From DSC measurements (Section 3.3.2), the fabrication temperature window was established to be 136 - 144 °C and a temperature of 140 °C chosen as the fabrication temperature. In order to find the optimum pressing force, three different forces (6 MPa, 16 MPa, 32 MPa) were applied at times of 30 seconds and 60 seconds (for each pressing force), for both PE1 and PE2. Sections of pre-cut TA23 UHMWPE tape were sandwiched between two HDPE layers (0.55 mm thick), heated to 140 °C and pressed. As soon as the required time for pressing had elapsed, the plates were removed from the press and submerged in cold water to complete crystallisation.

For the lowest pressing force and shortest times, these conditions were insufficient for homogeneous surface melting and bonding and most samples delaminated with relative ease. Studies investigating the sintering of UHMWPE have found that processing temperature, and not heat soak time or pressing force, were the most significant factor in achieving homogeneous melting.[28] However, this application was strictly limited by an upper temperature limit above which the highly oriented fibres in the UHMWPE tape would relax to the entangled state and permanently lose all orientation.[18]

For the remaining samples, no delamination occurred, however significant fibre splaying was evident (Figure 6.1, left). TA23 was a mechanically drawn UHMWPE tape with a very high

crystallinity and degree of orientation in the fibre direction. However, the mechanical strength was considerably weaker in the direction transverse to the fibre orientation. Therefore, due to the viscous nature of the HDPE, and the weak transverse orientation strength,[27,29] the HDPE matrix had pushed through the UHMWPE fibres upon application of pressure splaying them apart (Figure 6.1, left).

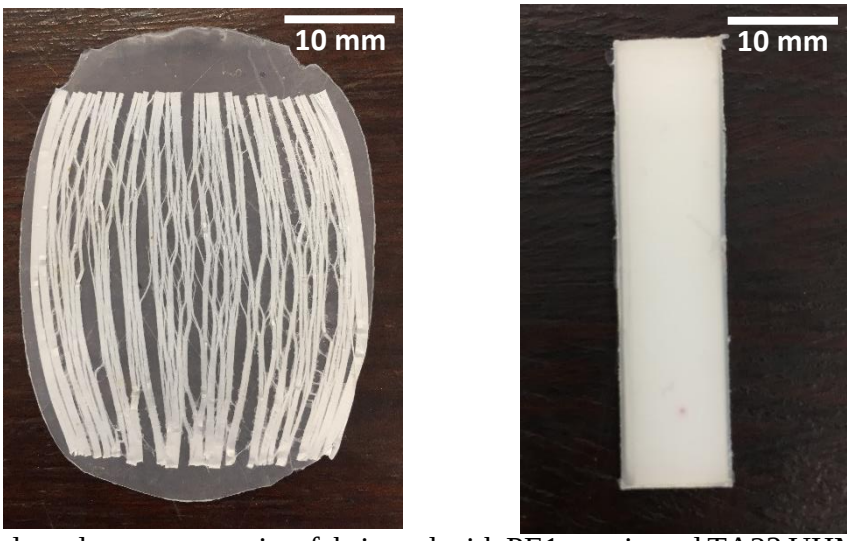

Figure 6.1: Single-polymer composites fabricated with PE1 matrix and TA23 UHMWPE inter-layer, using melt pressing (left) and vacuum compression moulding (right).

Whilst these samples would likely show an increase in tensile strength owing to the UHMWPE fibre reinforcement, the permeation resistance would be similar to that of HDPE, owing to the large gaps between fibres. It was observed in the literature, however, that the majority of compression moulding was performed using a mould that confined the SPC to a shape of set dimensions and/or used woven fabric inter-layers which prevented the fibres from displacing to a large extent.[17,29–31] The lack of constraint and weak transverse strength of the fibres was the cause of fibre splaying. Therefore, a more suitable fabrication method was needed to constrain the fibres.

6.2.2 Vacuum Compression Moulding

A novel apparatus has been introduced by MeltPrep, whereby vacuum compression moulding is used to produce defect-free samples from powder or pellet starting materials (Section 2.10). This was used to create SPCs that did not show evidence of fibre splaying (Figure 6.1, right).

Two 10 mm x 40 mm bars of HDPE (0.55 mm thick) were prepared initially (195 °C, 5 minutes) before the SPC was fabricated (140 °C, 10 minutes) by inserting a pre-cut TA23 layer in between. Samples prepared in this way showed no fibre splaying and bi-layered composites,

with the second fibre interlayer oriented 90° to the first, could be produced with relative ease. However, an additional interlayer of HDPE was needed in order to ensure bonding of the two TA23 layers and prevent delamination. Using this method, 25 mm SPC disks for permeation testing and 10 x 40mm SPC bars for tensile testing were produced using each of the three UHMWPE tapes.

6.3 Permeation Measurements

A key requirement of this work was to understand the permeation resistance of HDPE and HDPE-UHMWPE SPCs and to investigate whether this technology was a viable option for improving the barrier properties of PE-100 pipes compared to FIC. Further details regarding permeation theory of polymers are given in Section 2.11.

For each matrix HDPE (PE1 and PE2), each of the three tapes was used in two configurations: mono-layer (classified 0°) and bi-layer (classified 0°/90°). For the bi-layer samples, the orientation of the second tape layer was 90° perpendicular to the first layer (Figure 6.2). Therefore, 6 samples per matrix HDPE were fabricated to give 12 samples in total (Table 6.2a) with all SPC samples tested in duplicate (24 samples total).

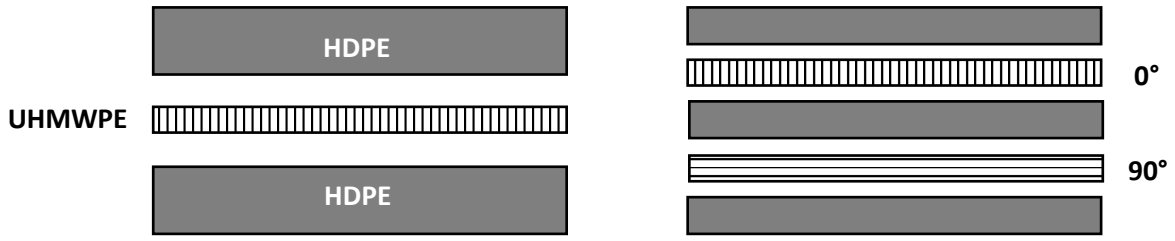

Figure 6.2: A schematic showing the mono-layer (0°) construction (left) and the bi-layer (0°/90°) construction (right) of SPC samples, with the latter having UHMWPE tape orientations crossed at 90°. The dashed lines are included to show the orientation of the UHMWPE tape layers. Both sample configurations were fabricated to the same thickness of 1.5 mm, hence different thicknesses of HDPE layers were required, by taking into account the thickness of each UHMWPE tape.

a	HDPE	UHMWPE	Configuration
1-A	PE1	TA23	0°
1-B	PE1	TA23	0°/90°
1-C	PE1	XF23	0°
1-D	PE1	XF23	0°/90°
1-E	PE1	S1	0°
1-F	PE1	S1	0°/90°
2-A	PE2	TA23	0°
2-B	PE2	TA23	0°/90°
2-C	PE2	XF23	0°
2-D	PE2	XF23	0°/90°
2-E	PE2	S1	0°
2-F	PE2	S1	0°/90°

b	HDPE
PE1	PE1
PE2	PE2
500k	M_w = 500 kDa
5M	M_w = 5 MDa
1-X	PE1-Aluminium foil (mono-layer)
1-Z	PE1-Aluminium foil (bi-layer)
2-X	PE2-Aluminium foil (mono-layer)
2-Z	PE2-Aluminium foil (bi-layer)

Table 6.2: **a)** SPC samples fabricated for permeation testing displaying the matrix HDPE, UHMWPE tape inter-layer and tape layering configuration; **b)** Additional samples fabricated consisting of HDPE of different molecular weights (top) and aluminium foil inter-layers in mono-layer and bi-layer constructions (bottom).

For comparison purposes, samples of 100 % PE1 and PE2 were also included, as well as PE grades with M_w = 500 kDa and M_w = 5 MDa respectively (Table 6.2b). A test cell with an aluminium disk instead of a polymer sample was also measured to monitor vapour loss through the lid screw thread/sealing ring to allow for correction of the data. As a control, aluminium foil, as currently used in the pipe manufacturing process, was obtained and used to make further SPC samples: mono-layer and bi-layer for each HDPE giving four samples in total (Table 6.2b). All samples were manufactured to a thickness of 1.5 mm and all measurements were performed in duplicate with mass measurements taken at regular intervals for 250 – 330 days. By normalising with respect to sample thickness, information regarding the vapour transmission per unit area, and hence the permeability, was obtained from the mass lost per day (Figure 6.3 – 6.4; Figure 6.6; Figures 6.8 – 6.9).

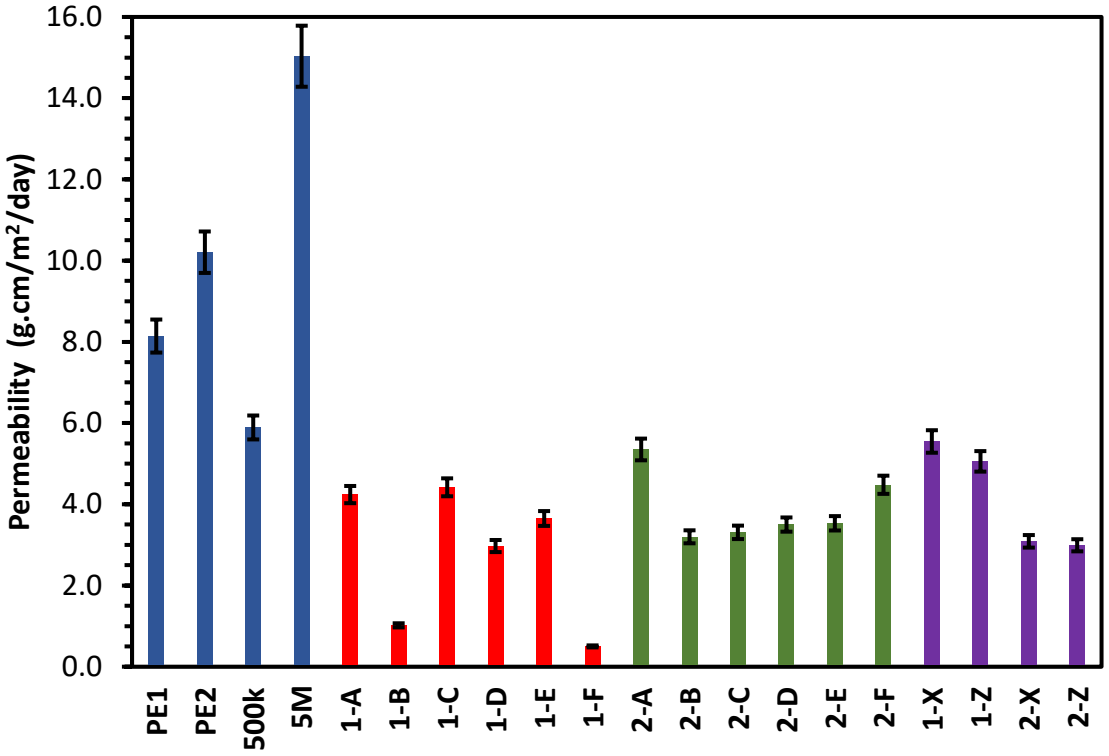

Figure 6.3: Permeability for all samples weighed at regular intervals for 250 – 330 days and normalising for variations in sample thickness. The different colours highlight each different grouping used during the measurements: HDPE (blue); PE1 (red); PE2 (green); aluminium foil (purple). Table 6.2 provides further details regarding the sample construction.

The 5 MDa PE sample showed the highest permeability which was likely due to the fabrication. The viscosity of this material was very high and, therefore, the material flow was much slower than standard HDPE. Using MeltPrep™, any air can be removed from a sample through a combination of heat and pressure. However, the pressure exerted on a sample using the 25 mm disk tool was 1.7 bar which was likely to be insufficient to remove all air in this very viscous sample. With poor material flow, there was also the possibility of holes forming thus allowing for greater permeation. Therefore, this sample was likely to be full of small holes through which the vapour escaped, thus increasing the permeation rate.

Conversely 1-B and 1-F showed the lowest permeability which suggested that these SPCs were strong candidates for further permeation trials. Nevertheless, considering the similarity in behaviour of PE1 and PE2, it was initially unclear why these two samples should significantly outperform (with a reduced permeability) the PE2 counterparts 2-B and 2-F. SAXS measurements would suggest elliptical voids were present (Figure 3.27), yet these should increase the permeability. PE2 did display increased permeability compared to PE1, which could partly account for the discrepancy between samples. Additionally, the similarity of the

permeability rates between samples 2-B, 2-C, 2-D and 2-E indicated that sample preparation issues, such as a poor fibre matrix interface, could have also led to an increased permeability.

In the following sections, the samples have been grouped into 4 sets for a more detailed analysis: HDPE, PE1 SPCs, PE2 SPCs and aluminium foil SPCs. For the PE1 matrix group and aluminium foil group all bi-layer (0°/90°) samples showed decreased permeation compared to the corresponding mono-layer (0°) which was consistent with a greater concentration of crystalline domains and/or the formation of a more tortuous path for the permeant causing a reduction in permeability.[13,32] This effect was less pronounced for the PE2 matrix group. For reasons to be discussed in Section 6.3.4, a comparative study of the SPCs against aluminium foil could not be made. However, this data was still useful in displaying the effect of additional foil inter-layers on the permeability. All of the UHMWPE tapes used in this study were commercial tapes with no similar studies performed using them in the literature.

6.3.1 HDPE Group

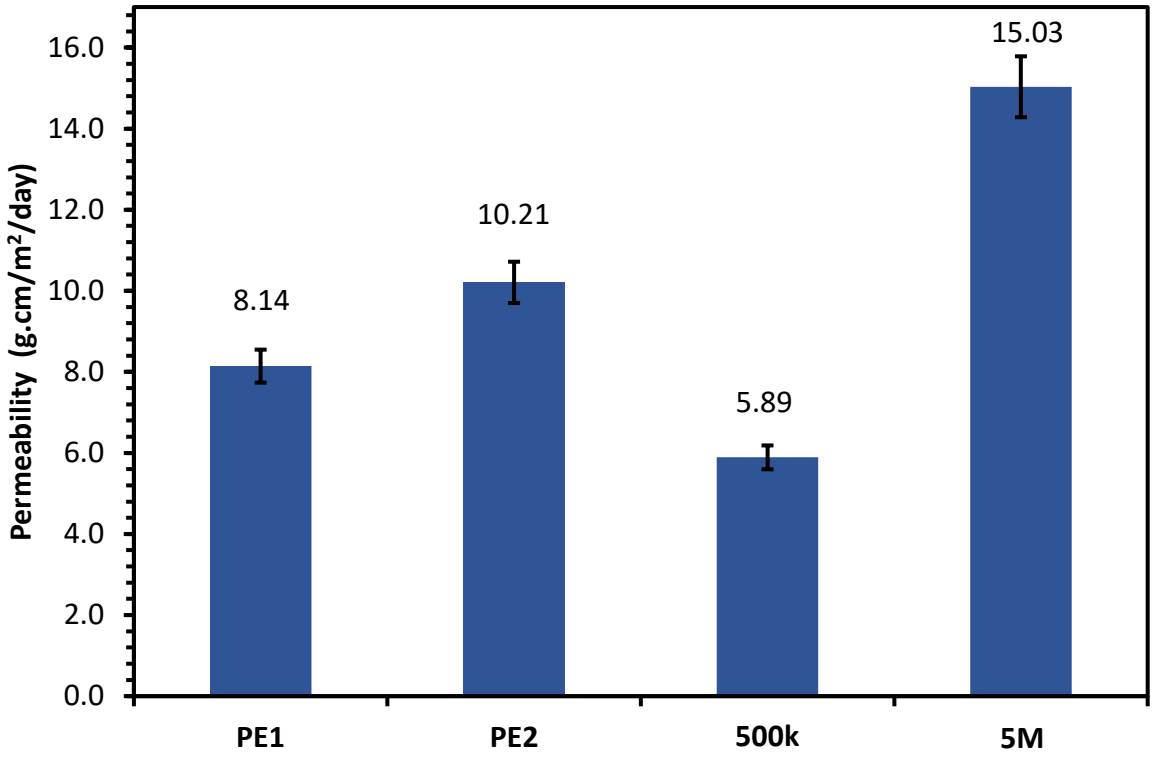

Figure 6.4: Permeability of PE1, PE2 and PE samples with M_w = 500 kDa and M_w = 5 MDa.

Generally, barrier properties can be improved through increased orientation and/or crystallinity because of the increased packing efficiency of the chains into crystalline domains – such domains are insoluble to permeant molecules.[13–15] PE2 displayed a higher permeation than

PE1. From DSC measurements (Section 3.3.1, Table 3.2), the X_c values were 61.4 % and 57.1 % for PE1 and PE2 respectively. The X_c value for the 500 kDa PE sample was 62.9 %; it also displayed the lowest permeability of this group, which suggested that a M_w = of 500 kDa could provide the optimal matrix barrier performance. However, the M_W = 5 MDa sample displayed the highest permeability and an X_c of 46.2 %, which therefore did support literature findings that lower crystallinity correlates to lower resistance to permeation.[14,32] The lower crystallinity, despite the UHMW, was likely due to a limited chain mobility caused by a greater amount of chain entanglements preventing suitable chain folding into crystalline lamellae.[33]

The ratio between the degree of crystallinity (from DSC, Section 3.3.1, Table 3.2) of PE1 (61.4 %) and PE2 (57.1 %) was 1.08 and the ratio of the permeabilities was 1.25 (Figure 6.4) – the cube of the crystallinity ratio. Additionally, a power law relation (Figure 6.5) to the one-third power was established between the permeability (logP) and degree of crystallinity ($LogX_c$) for each of the HDPE samples with different molecular weights.

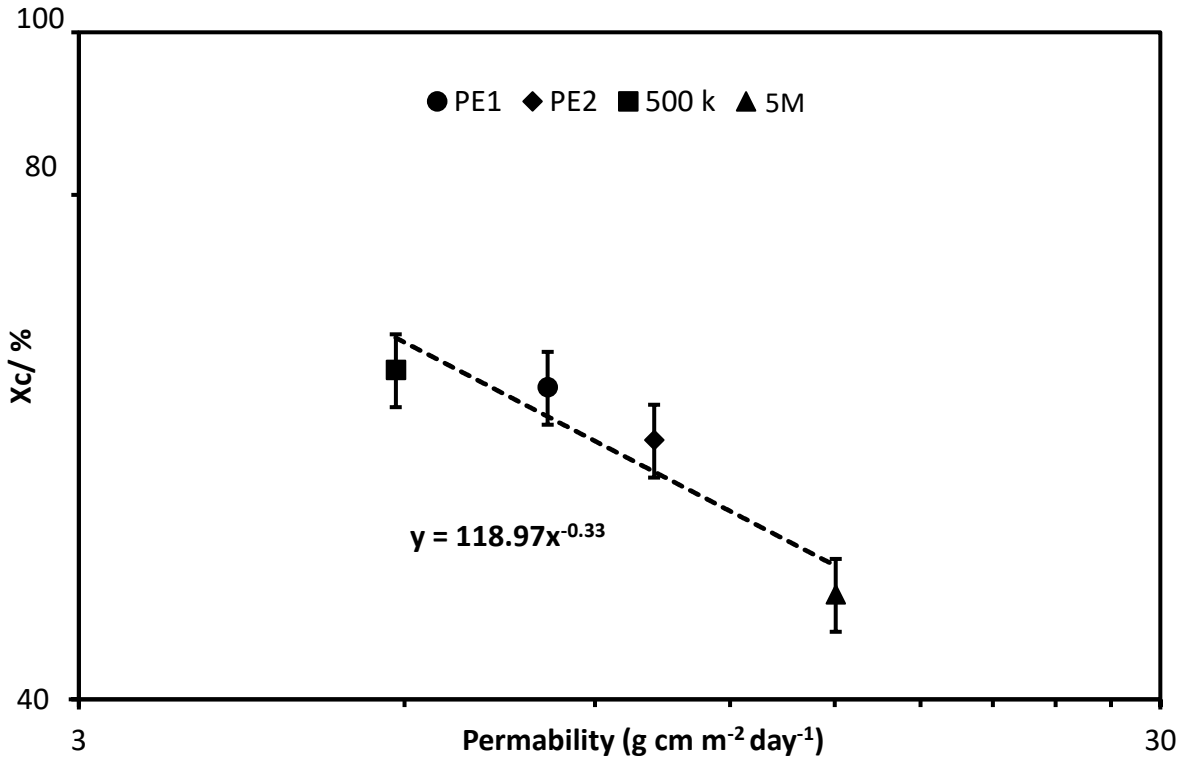

Figure 6.5: A power law relation established between the permeability and degree of crystallinity of HDPE samples with different molecular weights.

Thus, there was a volume effect to the one-third power; if permeation depends on tortuosity, then it should also be dependent on the volume.[34] Diffusion of the permeant gas occurs in the

amorphous, continuous phase with an increased amount of crystalline 'bricks' increasing the tortuosity and hence decreasing the permeability.[13,34] Hence the total crystallinity was the dominating factor in this instance. Crystallite size and shape would also have an impact upon the permeant diffusion and hence overall permeability, with larger, planar crystals acting as a better barrier (compared to smaller, spherical particles) by increasing the totuosity.[34] It could be argued that an increased crystallinity, and hence larger crystalline regions, could have the effect of acting as plate-like barriers.

6.3.2 PE1 SPC Group

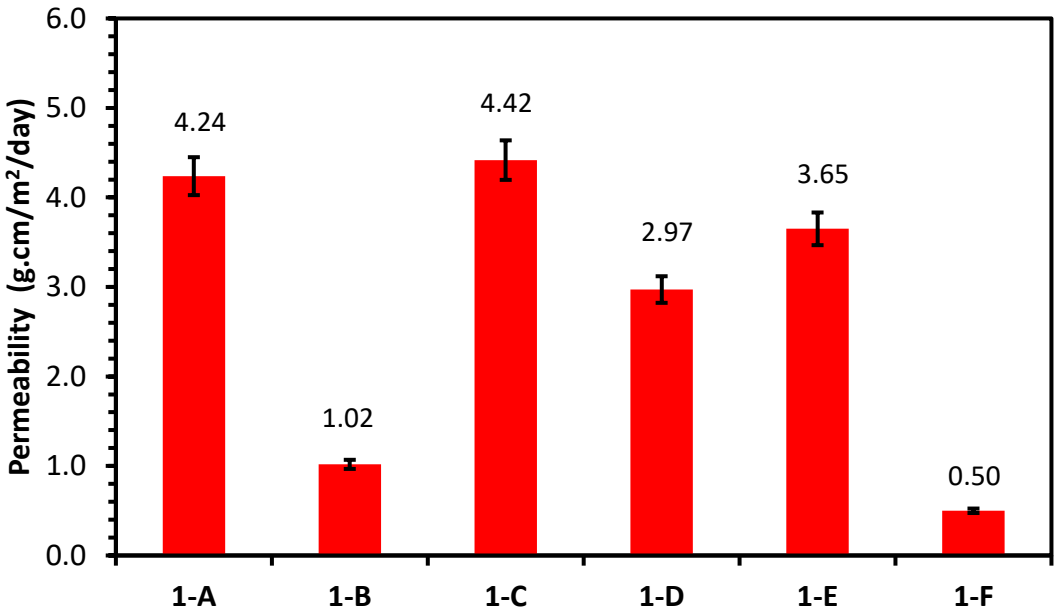

Figure 6.6: Permeability of SPC samples with PE1 as the matrix material. Samples A, C and E were fabricated with a mono-layer construction and samples B, D and F were constructed with a bi-layer construction with the orientation crossed at 90°.

This group was fabricated using PE1 (Figure 6.6) as the matrix with UHMWPE inter-layers constructed as described previously (Table 6.2). In all cases, samples with the 0°/90° bi-layer construction showed lower permeability than the mono-layer counterparts, confirming that additional barrier layers clearly improve permeability resistance. By aligning fibrils perpendicularly to the gas permeation direction, a tortuous path for the permeant molecules was created (Figure 6.7).[1] Thus an additional UHMWPE barrier layer should further increase the tortuous path and bi-layer composites will display lower permeability than the equivalent mono-layer SPC.

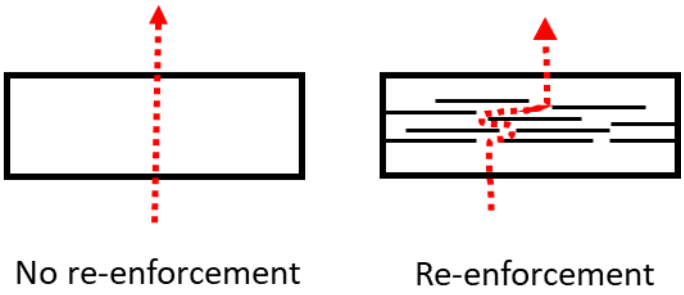

Figure 6.7: The distance a penetrating molecule must travel (highlighted by the red arrow) is influenced by the internal film morphology. Those with reinforcing inter-layers create greater distances and display lower permeability.

Samples 1-B and 1-F, fabricated with UHMWPE tapes TA23 and S1, respectively, displayed the lowest permeability of all SPC samples, which suggested that the combination of PE1 matrix and these two UHMWPE inter-layers provided optimal permeability resistance.

6.3.3 PE2 SPC Group

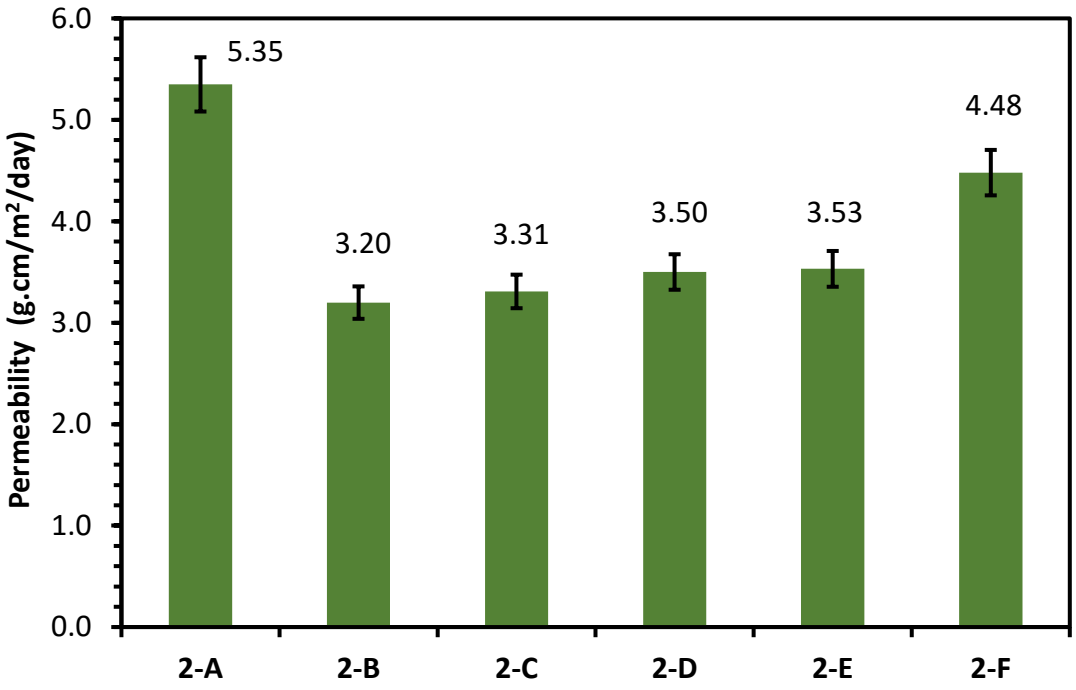

Figure 6.8: Permeability of SPC samples with PE2 as the matrix material. Samples A, C and E were fabricated with a mono-layer construction and samples B, D and F were constructed with a bi-layer construction with the orientation crossed at 90°.

This group was fabricated using PE2 (Figure 6.8) as the matrix with UHMWPE inter-layers constructed as described previously (Table 6.2a and 6.2b). The same trends for the PE1 group were not as clear for the PE2 group as only sample 2-B showed lower permeability compared

to its mono-layer counterpart. This could have been due to sample preparation issues such as a weak interface between the fibres and matrix.

6.3.4 Aluminium Foil Group

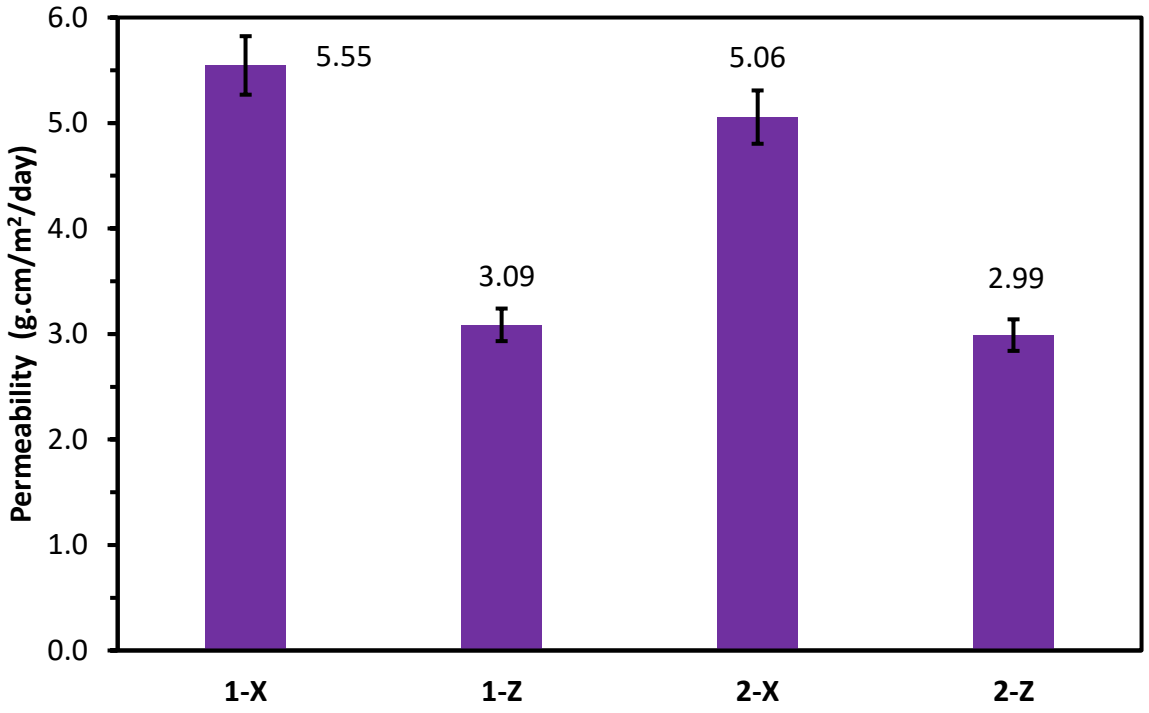

Figure 6.9: Permeability of SPC samples with aluminium foil inter-layers with a mono-layer (X) and bi-layer (Z) construction – the numbers preceding the letters denote the choice of matrix HDPE (either PE1 – "1" or PE2 – "2").

The aluminium foil group (Figure 6.9) was intended to be used as a control to assess the performance of the UHMWPE barrier layers against the current market product barrier layer. Unfortunately, the majority of SPC samples displayed similar or much lower permeability than these foil SPCs, which indicated that the foil results were unreliable – the aluminium foil SPCs should have shown the lowest permeability owing to the continuous nature of the foil compared to UHMWPE tapes with potential voids between the fibres (and thus an increased likelihood of greater permeation).[1] It was concluded that holes, edge leaking or other leaks contributed to this observed behaviour. Nonetheless, a very clear reduction (approximately 40 %) in permeability was observed between the mono-layer and bi-layer samples for both PE1 and PE2. This suggested that these results could be used to show the relative performance enhancement of additional barrier layers but were collectively greater than expected due to an issue with the sealing arrangement. If pinholes had been present in the sample, thus causing increased permeation, then the effect of an additional inter-layer would not have been observed

so clearly. As for the SPCs, this reduction in permeability arose from an increased tortuous path of the permeant molecule (Figure 6.7).[1]

6.4 Mechanical Testing

10 mm x 40 mm bars of each SPC sample condition (Table 6.2a and 6.2b) were fabricated and subjected to oscillatory DMA measurements (Section 2.12.3) to assess the mechanical properties of each SPC fabrication (Figure 6.10).

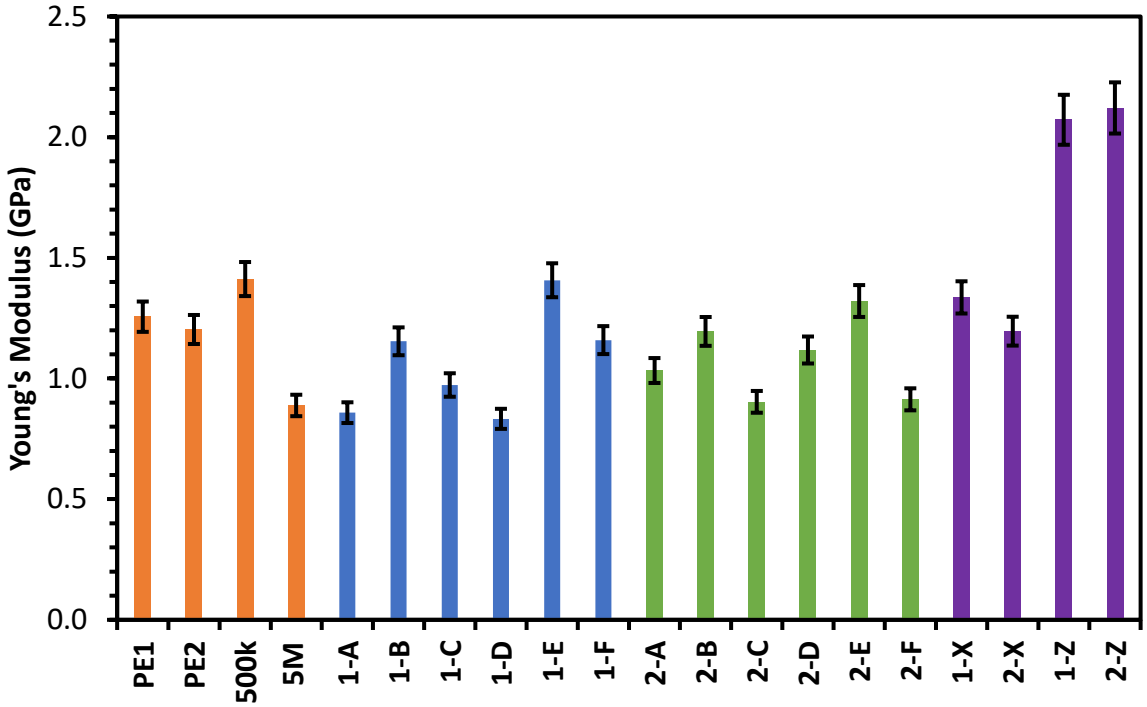

Figure 6.10: Young's moduli calculated from oscillatory DMA frequency sweeps (100 – 0.01 rad s^{-1}; 1 % strain, 25 °C) of each sample listed in Table 6.2 (a and b). Three specimens were measured per SPC sample and averaged.

The Young's modulus, *E*, can be calculated by using *G'* from an oscillatory rheology measurement and Eq. 2.49 with a Poisson's ratio value of 0.46 for HDPE.[35] Thus, for the majority of the SPC samples, the Young's modulus was greater for the bi-layer SPCs than the mono-layer SPCs, which demonstrated that the Young's modulus increased slightly as fibre content increased.[29] However, the bi-layer samples of PE1-S1 (samples 1-E, 1-F) and PE2-S1 (samples 2-E, 2-F) and PE1-XF23 (samples 1-C, 1-D) showed lower values of the Young's modulus. Prior to measurement of these samples, it was noted that some delamination had occurred which required a brief period of remelting to re-bond the HDPE matrix and UHMWPE inter-layers. After the measurements, all samples had partially or fully de-laminated

under the strain. The tensile modulus of the standard TA23 film given by the supplier was 170 GPa.[22] No data could be obtained for XF23 or S1.

The mechanical properties of SPCs are primarily related to three factors: stiffness and strength of the matrix; stiffness and strength of the fibre; the fibre-matrix interface.[1] The formation of a strong and stable interface between the matrix and fibre reinforcement is crucial in determining the eventual performance of SPCs.[1,7] Furthermore, poor interfacial adhesion leads to poor load transfer between the matrix and fibre and so the benefits of adding fibre reinforcement are not observed.[16] Therefore, as these bi-layer samples had a greater interface content (i.e. between both UHMWPE fibre layers and HDPE matrix), this delamination resulted in a decrease of mechanical strength.[16] The HDPE-only samples displayed values comparable to those in the literature, however, those of the SPC were much lower than other self-reinforced composites, likely caused by poor interface adhesion.[17,36]

However, as was evident from the aluminium foil SPCs, the bi-layer significantly increased the Young's moduli compared to the corresponding mono-layer sample. This same enhancement was not observed to the same degree for any of the other SPCs. Therefore, this suggested that the foil inter-layers imparted greater torsional strength than any of the UHMWPE inter-layers.

6.5 Conclusions

SPCs represent an interesting class of composite material. With both matrix and fibre reinforcement of similar thermoplastic material they have been shown to display comparable mechanical properties to typical carbon-fibre and glass-fibre composites.[1] The use of such thermoplastic fibres makes end-of-life recycling much easier than traditional fibre-based composites.[1] In addition, the increased crystallinity of SPC samples, through the use of highly oriented and crystalline fibres, could increase barrier properties by creating a more tortuous path for permeant molecules.[1] Therefore, this technology was explored as a viable option for increasing the mechanical strength and barrier properties of PE-100 pipes. Three UHMWPE inter-layer tapes were selected for mechanical testing and permeability measurements. Alongside these, PEs of different molecular weights and SPCs with aluminium foil inter-layers (as currently used in PE-100 pipe manufacture) were fabricated for comparison.

A significant challenge in the manufacture of SPCs is obtaining good adhesion between the fibre and matrix, as stress transfer from the matrix to the fibre imparts the improved mechanical

properties.[1] Several methods have been researched to improve the interface between the fibre and matrix often involving chemical modification of the respective surfaces.[1] By orienting the thermoplastic fibres, a small temperature window emerges in which the matrix material is able to melt whilst leaving the fibres intact. Melting above this temperature causes a total loss of orientation as the extended chains relax back to their entangled state.[12] The majority of processes to exploit this phenomenon have depended upon hot pressing - the careful application of heat and pressure to a layered composite.

Previous DSC measurements led to a fabrication temperature selection of 140 °C. Attempts to hot press samples of PE1 and TA23 at several pressing forces and times displayed either delamination or significant fibre splaying, both of which would have displayed poor mechanical and barrier properties respectively. By utilising the VCM apparatus, defect-free SPC samples were consistently produced. However, some samples did still delaminate after mechanical testing suggesting that more work would be required to fully optimise the conditions and process. Thus, VCM was shown to be an effective method of SPC fabrication for further measurements. Whilst this method proved very effective on the laboratory scale, it was anticipated that achieving the same levels of control on an extrusion line would prove challenging due to the narrow temperature window.

Novel permeation testing cells were fabricated and samples of each SPC construction underwent permeation testing by measuring the mass lost per day and normalising with respect to the sample thickness. PE1 displayed slightly lower permeability than PE2 and the optimum barrier properties for HDPE-only samples appeared to occur at M_W = 500 kDa with the UHMWPE sample (M_W = 5 MDa) displaying the highest permeability. The decreased permeability was attributed to the increased crystallinity (as measured by DSC) in the samples 500k < PE1 < PE2 < 5M (62.9 % < 61.4 % < 57.1 % < 46.2 %). A power law relation between the resulting permeability and degree of crystallinity was established to the one-third power, which indicated that the total crystallinity was the dominant factor in this instance.

The majority of bi-layer samples (with 90° cross-ply UHMWPE tape orientation) displayed lower permeability than the corresponding mono-layer samples due to the increased tortuous path for the permeant molecules caused by the addition of highly crystalline layers. The samples with the lowest permeability were PE1-TA23 0°/90° (1-B) and PE1-S1 0°/90° (1-F). Comparison with PE1 and PE2 showed that the HDPE-only samples displayed greater permeability as was expected because of the lack of barrier layers. The aluminium foil samples

showed a very clear reduction in permeability between the mono-layer and bi-layer samples, however the data were deemed unreliable and were not used for a comparison with SPC samples. Further optimisation of the sealing process would be required.

Young's moduli were obtained for each sample from DMA measurements. They revealed that the addition of UHMWPE inter-layers had little influence upon the torsional stiffness compared to the nascent PE1 and PE2 matrices. The aluminium foil bi-layer samples showed much improved mechanical properties compared to the corresponding mono-layer samples which suggested that the aluminium foil displayed greater torsional stiffness compared to the UHMWPE tapes. It was also noted that several polymer SPC samples had delaminated as a result of the measurement. The formation of a strong and stable interface between the matrix and fibre reinforcement was crucial for imparting load transfer from the former to the latter.[1,7] Therefore, the weak interface in the polymer SPCs limited the mechanical improvements and further processing and fabrication optimisation would be necessary.

In terms of pipe manufacture, SPC technology was an attractive, lower-cost option than pursuing FIC through novel die-head design by substituting the wrapping of the pipe with the current aluminium foil for one of the UHMWPE tapes selected. However, the fragile nature of UHMWPE tapes (such as TA23) transverse to the orientation direction would have likely resulted in frequent tears and defects in the final product. Additionally, the precise control of temperature and pressure required for good matrix and fibre adhesion (and hence the improvement in mechanical and barrier properties) would be difficult to achieve.

6.6 References

1 M. Kuzmanovic, L. Delva, L. Cardon and K. Ragaert, *Adv. Mater.*, 2020, **32**, 2003938.

2 H. E. H. Meijer and L. E. Govaert, *Prog. Polym. Sci.*, 2005, **30**, 915–938.

3 J. Wang, H. Wu and S. Guo, *RSC Adv.*, 2016, **6**, 1313–1323.

4 S. Joseph and S. Thomas, *Eur. Polym. J.*, 2003, **39**, 115–125.

5 R. J. Shields, D. Bhattacharyya and S. Fakirov, *J. Mater. Sci.*, 2008, **43**, 6758–6770.

6 R. J. Shields, D. Bhattacharyya and S. Fakirov, *Compos. Part A Appl. Sci. Manuf.*, 2008, **39**, 940–949.

7 T. Stern, A. Teishev and G. Marom, *Compos. Sci. Technol.*, 1997, **57**, 1009–1015.

8 M. Deng and S. W. Shalaby, *Biomaterials*, 1997, **18**, 645–655.

9 T. Xu and R. J. Farris, *Polym. Eng. Sci.*, 2007, 1544–1553.

10 T. Stern, G. Marom and E. Wachtel, *J. Compos. Part A*, 1997, **444**, 437–444.

11 C. Gao, L. Yu, H. Liu and L. Chen, *Prog. Polym. Sci.*, 2012, **37**, 767–780.

12 N. J. Capiati and R. S. Porter, *J. Mater. Sci.*, 1975, **10**, 1671–1677.

13 A. S. Michaels and R. B. Parker, *J. Polym. Sci.*, 1959, **41**, 53–71.

14 D. H. Weinkauf and D. R. Paul, in *Barrier Polymers and Structures - ACS Symposium Series*, ed. W. J. Koros, Austin, Texas, 1990, pp. 60–91.

15 C. E. Rogers, V. Stasnett and M. Szwarc, *Journl Polym. Sci.*, 1960, **XLV**, 61–82.

16 D. Chukov, A. Kharitonov, V. Tcherdyntsev, D. Zherebtsov and A. Maksimkin, *J. Compos. Mater.*, 2018, **52**, 1689–1698.

17 T. Ogawa, H. Mukai and S. Osawa, *J. Appl. Polym. Sci.*, 1998, **68**, 1431–1439.

18 F. Zhong, R. Thomann and R. Mülhaupt, *Macromol. Mater. Eng.*, 2018, **303**, 1–8.

19 N. J. Capiati and R. S. Porter, *J. Mater. Sci.*, 1975, **10**, 1671–1677.

20 Y. Lo Hsieh, M. Hartzell and S. Xu, *J. Adhes. Sci. Technol.*, 1991, **5**, 1023–1039.

21 C. Della Volpe, L. Fambri, R. Fenner, C. Migliaresi and A. Pegoretti, *J. Mater. Sci.*, 1994, **29**, 3919–3925.

22 *Endumax: Thin Tape With a High Modulus*, Teijin, Data Sheet, 2016.

23 T. Tam and M. B. Boone, *Patent Application: US 2013/0202844 A1*, USA, 2013.

24 B. Alcock, N. O. Cabrera, N. M. Barkoula, C. T. Reynolds, L. E. Govaert and T. Peijs, *Compos. Sci. Technol.*, 2007, **67**, 2061–2070.

25 T. Boublik, V. Fried and E. Hala, *The vapor pressures of pure substances*, 1973, vol. 517.

26 F. V. Lacroix, J. Loos and K. Schulte, *Polymer*, 1999, **40**, 843–847.

27 N.-M. Barkoula, T. Peijs, T. Schimanski and J. Loos, *Polym. Compos.*, 2005, **26**, 114–120.

28 R. M. Gul and F. J. Mcgarry, *Polym. Eng. Sci.*, 2004, **44**, 1848–1857.

29 K. P. Matabola, A. R. De Vries, F. S. Moolman and A. S. Luyt, *J. Mater. Sci.*, 2009, **44**, 6213–6222.

30 Á. Kmetty, T. Bárány and J. Karger-Kocsis, *Prog. Polym. Sci.*, 2010, **35**, 1288–1310.

31 P. J. Hine, A. P. Unwin and I. M. Ward, *Polymer*, 2011, **52**, 2891–2898.

32 A. S. Michaels and H. J. Bixler, *J. Polym. Sci.*, 1961, **50**, 393–412.

33 A. J. Peacock, *Handbook of Polyethylene*, Marcel Dekker, New York, 2000.

34 E. L. V. Lewis, R. A. Duckett, I. M. Ward, J. P. A. Fairclough and A. J. Ryan, *Polymer*, 2003, **44**, 1631–1640.

35 A. Pawlak and A. Galeski, *Macromolecules*, 2005, **38**, 9688–9697.

36 Q. Guan, F. S. Lai, S. P. McCarthy, D. Chiu, X. Zhu and K. Shen, *Polymer*, 1997, **38**, 5251–5253.

Chapter 7

Conclusions and Future Work

7.1 Conclusions

The aim of this thesis was to find alternative solutions for improving permeability and mechanical properties of HDPE resins of PE-100 grade used for transporting potable water, in order to meet growing requirements for polymer recycling to be more sustainable. In particular, two new routes were explored for replacing the aluminium foil permeation barrier, currently used in PE-100 pipes, by a PE barrier compatible with the bulk HDPE material of the pipes. One of the routes was based on the production of multiple structural morphologies within the pipes using FIC properties of the bulk HDPE material and the other was based on an incorporation of UHMWPE tapes during the pipe manufacturing process producing an SPC pipe.

FIC has been shown through extensive prior literature to induce an oriented crystalline morphology which also increases the mechanical properties in the orientation direction.[1–5] SPCs are an interesting class of fibre-reinforced materials in that both the fibre and matrix are of the same material.[6] As with traditional fibre-reinforced composites, the mechanical properties are improved by the addition of the fibre reinforcement.[6,7] Both technologies had an effect upon the crystallisation behaviour, mechanical properties and permeation barrier properties of two HDPE resins to some extent and showed potential for further application.

Two HDPE resins, currently used in the manufacture of PE-100 pipes, were supplied by Aliaxis R&D (designated as PE1 and PE2) and key molecular characteristics were determined by GPC and DSC measurements. PE1 was observed by GPC to possess a greater fraction of UHMW material in the blend (a HMWT) compared to PE2. Crucially, this HMWT was responsible for the consistently greater degree of orientation for PE1 compared to PE2. DSC measurements were performed to obtain the melting and crystallisation temperatures and the degree of crystallinity of PE1 and PE2, with melting points between 129 - 132 °C and degree of crystallinity values consistent with literature values for HDPE.[8–11] PE2 displayed a lower degree of crystallinity than PE1 upon crystallisation. This was attributed to the hexene co-monomer branches,[12] incorporated to achieve the desired MWD, contributing to the lower crystallinity by preventing close chain packing.[9] The peak crystallisation and melting temperatures, along with the respective onsets, were subsequently used to establish temperature-shear protocols for polymer processing.

In addition, three UHMWPE tapes were obtained from Teijin for the fabrication of SPCs using PE1 and PE2 as the polymer matrices. All tapes showed high degrees of orientation by SAXS

and crystallinity by DSC, caused by the drawing process during manufacture. Multiple melting peaks were evident during DSC measurements for TA23 and XF23, particularly with the former, which arose from a combination of the high orientation of the molecular chains, lack of fibre constraint and crystal melting and transitions.[13–15] By constraining TA23, a single main peak was observed at 146 °C with a small shoulder at 152 °C. Therefore, the multiple melting peaks were an artefact only observable for unconstrained, highly oriented UHMWPE fibres, and consistent with the literature.[16,17]

Through parallel-plate shearing experiments and rheological measurements, key flow parameters governing the molecular stretching and orientation of the polymer chains were determined, namely the critical work and shear-rate dependent viscosity.[18] PE1 consistently showed greater degrees of orientation after smaller amounts of work through shear had been applied, as noted by the earlier onset of a Maltese cross under polarised light imaging after shorter times of shearing.[18,19] The critical work values correlated well with the HMWT observed for PE1 in the MWD. The longest chains in a melt enhance the flow-induced nucleation and, therefore, less work was required for PE1 to produce an oriented morphology.[18,19]

Investigations were also conducted into the optimisation of shear parameters, namely shear time and shear temperature at a constant shear rate. As the shear time increased from 10 seconds to 40 seconds (in 10 second increments), elastic flow instabilities emerged and grew in intensity to ultimately dominate the flow behaviour and destroy/distort the oriented crystalline structures formed, as observed by significant tilting in the 2D SAXS patterns and increasing stress birefringence in the PLIs.[18] This was most apparent for PE1 which was attributed to the saturation of the melt with oriented nuclei which further shearing distorted. For PE2, elastic instabilities only appeared significantly at the longest shear times and the increasing orientation with increasing shear time was most apparent. For both materials, increasing the shear time caused an increase in the resulting orientation until an elastic instability limit. After shearing at temperatures greater than 150 °C (exceeding the equilibrium melting temperature of PE[20]) thermal relaxation of the oriented polymer chains outpaced the crystallisation process and no orientation was observed by SAXS. Thus, it was demonstrated that careful control of shear parameters was necessary to produce highly oriented samples free from elastic flow instabilities. Finally, the crystallisation kinetics of sheared and unsheared samples of PE1 and PE2 were investigated by DSC measurements and fitting with the Avrami model confirmed fibrillar crystal growth for the sheared samples.[21,22]

To investigate the permeation barrier and mechanical properties, larger film samples with an oriented morphology were fabricated. A novel high temperature Couette cell was developed and extensively upgraded to allow for shearing of larger polymer film samples – no such device was known to exist commercially. The cell was constructed with an inner rotor and outer stator consisting of four quadrants which could be removed to release the sample for further measurements. SAXS measurements confirmed a predominantly homogeneous distribution of orientation throughout the samples. By changing the shear time, different amounts of strain could be supplied to the polymer melt and hence samples with different degrees of orientation were obtained. From these films, specimens were cut for tensile testing (at Aliaxis R&D) and permeability testing. The degrees of orientation were consistently greater for PE1 than PE2 due to the HMWT present in the former, for reasons as discussed previously.[18]

Tensile testing revealed that increased orientation correlated with an increased Young's Modulus. For PE2, where the difference in orientation between successive shear times was less pronounced, minimal improvement over the comparative isotropic specimen was observed. In general, all mechanical properties of sheared PE2 samples showed little improvement due to the low orientation. PE1, on the other hand, showed an increasing stress at yield and decreasing strain at break which was consistent with greater amounts of oriented crystalline morphology.[23] Permeation testing revealed that the permeability increased for PE1 samples with increasing shear time, whereas PE2 showed a decreasing permeability with increasing shear time. This was attributed to the direction of the chain orientation in measured samples lying perpendicular to the permeant flux in the permeation test cells. At longer shear times, the orientation for PE1 correspondingly increased along with the number of voids between lamellae *kebabs*. Shear heating through the action of shearing by the Couette cell could also have caused slight thermal relaxation of the oriented morphology,[9] hence the lower Young's Modulus and permeability values for PE1 sheared for 40 seconds. Additionally, an increased probability of elastic instabilities distorting the crystalline morphology, and a greater concentration of chain entanglements, could also have contributed by acting as less effective barriers to diffusing permeant molecules. By plotting the relationship between the degree of orientation, Young's modulus and permeability for each of the sheared samples, the impact of the critical work for oriented morphology formation on physical properties was apparent, especially for PE1 samples above the critical work.

There were crucial differences between oriented and unoriented materials with respect to the permeability behaviour. The four different HPDE grades, covering more than an order of

magnitude in molecular weight and 17 % crystallinity degree variation, indicated that the total crystallinity, and hence the volume of dispersed crystalline regions, was the dominating factor in determining permeability. A one-third power-law relationship was observed between the degree of crystallinity and permeability which essentially confirmed that the diffusion of organic molecules in the amorphous (continuous) phase of PE was greater than that in crystalline PE. For sheared samples, however, measurement of the degree of crystallinity by DSC for each sample after the conclusion of permeation measurements revealed that the total crystallinity or specific HDPE grade was not the dominating factor in determining the permeability – it was the formation of oriented morphology.

SPCs of mono-layer and bi-layer construction (with the tape orientation between layers crossed 90°) were constructed using three UHMWPE tapes (TA23, XF23 and S1) and two HDPE matrices (PE1 and PE2). Composites with aluminium foil inter-layers (as currently used in pipe manufacture) were also prepared to act as control specimens. Samples for mechanical testing were subjected to DMA via an oscillatory frequency sweep. However, results showed that none of the UHMWPE tapes offered significant improvements in the axial strength of PE1 and PE2 (without reinforcement) compared to the aluminium foil composites. Permeation testing revealed decreased permeability (and therefore improved barrier properties) for SPCs compared to the non-composite homopolymer samples. For PE1, the majority of bi-layer samples displayed significantly decreased permeability compared to the mono-layer counterparts, likely due to the increased tortuous path of the permeant molecules. This effect was not as pronounced for PE2. Regardless, several SPCs displayed similar or decreased permeability to the aluminium foil samples, most likely from issues arising from the method of sealing, and thus a direct comparison could not be achieved. Nevertheless, the foil-composites demonstrated that an additional layer of aluminium foil (to fabricate bi-layer samples) decreased the permeability by approximately 40 %, compared to the mono-layer samples, also likely due to the increased tortuous path of the permeant molecules.

Importantly, both technologies showed potential for improving the barrier and mechanical properties of PE-100 plastic pipes as it has been shown that orientation does indeed have an effect upon both properties. Increasing orientation, up to the elastic instability limit, has been shown to increase barrier properties and mechanical strength, but this was not consistent between the two resins supplied. SPC formation initially appeared as the more favourable option for pipe-wrapping extrusion trials as the current aluminium foil could easily be replaced with the necessary UHMWPE tape. However, the practical difficulties in temperature control,

formation of a strong fibre-matrix interface and often delicate handling required (especially in directions transverse to the fibre orientation) would likely have been more difficult to incorporate and control within the existing manufacturing architecture. Additionally, raw material and production costs would be considerably increased. Consequently, SIC was preferred by the industrial collaborators as the approach to pursue further.

7.2 Future Work

Two representative HDPE resins of PE-100 grade used for polymer pipe manufacturing were selected/provided for study in this work. The results obtained have clearly demonstrated that two polymers of the same grade, supposedly designed to produce products with similar physical properties, in fact, result in materials with strikingly different performance because of small differences in their HMW fractions. In this respect, further research should consider expanding the scope of HDPE resins under investigation, with particular focus upon the MWD in the polymer blends. For example, a blend which included the UHMWT of PE1 and the larger amount of HMW material in the second bimodal peak of PE2 would have good FIC characteristics (as per PE1) and a greater resistance to the onset of elastic flow instabilities (as per PE2). The LMW regions in each case would offer good processability. Optimisation of the MWD through custom reactor conditions could also be explored. The disassembling coaxial (Couette) shear cell developed in this work for polymer processing at the melting point provided a unique opportunity to establish structure-property relationships for large polymeric articles processed at precisely-controlled shear flow conditions such as shear rate, time and temperature. Relatively large areas of homogeneously-processed polymer films would enable further experiments on different approaches for permeation and mechanical tests. For permeation testing, further studies should be undertaken to optimise the method of sealing the cells. Moreover, manufactured pipe specimens should be tested by submersion in xylene to further validate the potentially improved barrier properties. As SCG is the primary mechanism of pipe failure, these tests should also be conducted in combination with the other mechanical tests including stress performed at yield, maximum strain at break and Young's Moduli measurements. Crucially, however, both of these next steps would depend upon scale-up to a laboratory extrusion line and a new die head design with a variable temperature gradient across the head, which in itself would be a significant undertaking to optimise the flow conditions.

7.3 References

1 L. Balzano, *Flow Induced Crystallization of Polyolefins*, PhD Thesis, Eindhoven

University of Technology, 2008.

2 I. M. Ward, *Structure and Properties of Oriented Polymers*, Springer, Dordrecht, 2nd edn., 1997.

3 A. Keller and M. J. Machin, *J. Macromol. Sci. Part B*, 1967, **1**, 41–91.

4 M. J. Hill, P. J. Barham and A. Keller, *Colloid Polym. Sci. Kolloid-Zeitschrift Zeitschrift für Polym.*, 1980, **258**, 1023–1037.

5 M. J. Hill and A. Keller, *J. Macromol. Sci. Part B*, 1969, **3**, 153–169.

6 M. Kuzmanovic, L. Delva, L. Cardon and K. Ragaert, *Adv. Mater.*, 2020, **32**, 2003938.

7 K. P. Matabola, A. R. De Vries, F. S. Moolman and A. S. Luyt, *J. Mater. Sci.*, 2009, **44**, 6213–6222.

8 M. H. Nafar Sefiddashti, B. J. Edwards and B. Khomami, *Phys. Rev. Res.*, 2020, **2**, 013035.

9 A. J. Peacock, *Handbook of Polyethylene*, Marcel Dekker, New York, 2000.

10 B. Wunderlich and C. M. Cormier, *J. Polym. Scince Part A-2*, 1967, **5**, 987–988.

11 V. B. F. Mathot and M. F. J. Pijpers, *J. Therm. Anal.*, 1983, **28**, 349–358.

12 *ELTEX B4922N3004*, Ineos Olefins & Polymers Europe, Data Sheet, 2009.

13 N. J. Capiati and R. S. Porter, *J. Mater. Sci.*, 1975, **10**, 1671–1677.

14 F. V. Lacroix, J. Loos and K. Schulte, *Polymer*, 1999, **40**, 843–847.

15 T. Stern, G. Marom and E. Wachtel, *Compos. Part A Appl. Sci. Manuf.*, 1997, **28**, 437–444.

16 S. Ratner, A. Weinberg and G. Marom, *Polym. Compos.*, 2003, **24**, 422–427.

17 J. T. Yeh, S. C. Lin, C. W. Tu, K. H. Hsie and F. C. Chang, *J. Mater. Sci.*, 2008, **43**, 4892–4900.

18 O. O. Mykhaylyk, P. Chambon, C. Impradice, J. P. A. Fairclough, N. J. Terrill and A. J. Ryan, *Macromolecules*, 2010, **43**, 2389–2405.

19 O. O. Mykhaylyk, P. Chambon, R. S. Graham, J. P. A. Fairclough, P. D. Olmsted and A. J. Ryan, *Macromolecules*, 2008, **41**, 1901–1904.

20 B. Wunderlich and G. Czornyj, *Macromolecules*, 1977, **10**, 906–913.

21 A. N. Wilkinson and A. J. Ryan, *Polymer Processing and Structure Development*, Kluwer Academic Publishers, Dordrecht, 1999.

22 M. Avrami, *J. Chem. Phys.*, 1939, **7**, 1103–1112.

23 Z. Bashir, J. A. Odell and A. Keller, *J. Mater. Sci.*, 1986, **21**, 3993–4002.